Brigham Young University
BYU ScholarsArchive

Theses and Dissertations

2018-07-23

Time-Domain Characterization of Nonlinear Propagation in Military Aircraft Jet Noise

Brent Owen Reichman
Brigham Young University

Follow this and additional works at: https://scholarsarchive.byu.edu/etd

BYU ScholarsArchive Citation

Reichman, Brent Owen, "Time-Domain Characterization of Nonlinear Propagation in Military Aircraft Jet Noise" (2018). *Theses and Dissertations*. 9263.
https://scholarsarchive.byu.edu/etd/9263

This Dissertation is brought to you for free and open access by BYU ScholarsArchive. It has been accepted for inclusion in Theses and Dissertations by an authorized administrator of BYU ScholarsArchive. For more information, please contact ellen_amatangelo@byu.edu.

Time-Domain Characterization of Nonlinear Propagation in Military Aircraft Jet Noise

Brent Owen Reichman

A dissertation submitted to the faculty of
Brigham Young University
in partial fulfillment of the requirements for the degree of

Doctor of Philosophy

Kent L. Gee, Chair
Tracianne B. Neilsen
Brian E. Anderson
Ross L. Spencer
Bradley R. Adams
Alan T. Wall

Department of Physics and Astronomy

Brigham Young University

Copyright © 2018 Brent Owen Reichman

All Rights Reserved

ABSTRACT

Time-Domain Characterization of Nonlinear Propagation in Military Aircraft Jet Noise

Brent Owen Reichman
Department of Physics and Astronomy, BYU
Doctor of Philosophy

Nonlinear propagation and shock formation are shown in noise radiated from full-scale military jet aircraft. Perception of sound is not only affected by the overall sound pressure level of the noise, but also characteristics of the sound itself. In the case of jet noise, acoustic shocks within the waveforms result in a characteristic commonly referred to as "crackle." The origin of shocks in the far-field of jet noise is shown to be through nonlinear propagation. Metrics characterizing the shock content of a waveform are explained and given physical significance, then applied to jet noise at various distances and engine conditions to show areas where shock formation is significant. Shocks are shown to develop at different distances from the aircraft, dependent on the amplitude and frequency, and nonlinear propagation is shown to be important in determining time and frequency characteristics of jet noise at distances of up to 1220 m from the aircraft. The shock content is also characterized during flyover experiments, and the shock content between the two scenarios is compared. While some reduction in overall level and shock content is seen in the maximum radiation region, level increases in the forward direction during flight result in increased shock content. Variation at distances of 305 m and beyond is considered and shown as a result of small atmospheric changes. Finally, a nonlinear numerical propagation scheme is used to model the propagation, showing accuracy in predicting frequency-domain and time-domain features that are evidence of nonlinear propagation.

Keywords: jet noise, aeroacoustics, nonlinear propagation, shock, crackle

ACKNOWLEDGMENTS

The people that deserve thanks and recognition for their help in getting me to this point are innumerable, and I am forever grateful for the support that they have given me. It is impossible to overstate the importance of my family over the last five years. To my parents and in-laws, your support and encouragement have meant the world to me, and your pride in my accomplishments has been one of my great motivators. To my siblings and siblings-in-law, your funny texts and messages of encouragement have done more than you know. To my children, you won’t remember much of this time, but your smiles and youthful exuberance have energized and inspired me when I have needed it most. And to my beautiful and selfless wife, I could not have done this without you. You have been by my side every step of the way, celebrating every accomplishment, making our home an incredible place, and helping me enjoy the journey. Thank you for being practically perfect.

My advisor has exemplified all that a mentor should be. Patient when possible, a compelling force when necessary, and always driven to help his students achieve their full potential. In my life he will be the standard of hard work, excellence in his field, and a dedication to helping others that I will be striving to emulate. My unofficial second advisor has demonstrated those same qualities and words cannot express my thanks for the hours of help she has given me, whether directly discussing and answering questions about research or her above-and-beyond editing. The support of these two exceptional professors has helped me get to where I am today.

The long journey of a PhD would have felt much longer without the companionship of others, and I count myself lucky to have developed friendships with many incredible students during my time at BYU. The hours doing homework, discussing research issues, and attending conferences together have helped me emerge from my PhD not only with an amount of expertise

in my field, but as a better person. To those unfortunate enough to have shared the office with me, I express my thanks for the friendship, support, and occasional distractions that helped me enjoy this journey.

This research was supported in part by the appointment of Brent Reichman to the Student Research Participation Program at USAFRL, 711th Human Performance Wing, Human Effectiveness Directorate, Warfighter Interface Branch, Battlespace Acoustics Branch administered by the Oak Ridge Institute for Science and Education through an interagency agreement between the U.S. Department of Energy and USAFRL. (Distribution A: Approved for public release; distribution unlimited. F-35 PAO Cleared **/**/20**; JSF**-****.)

Table of Contents

Table of Contents v
List of Tables ix
List of Figures x
1 Introduction 1
1.1 Basics of nonlinear acoustic propagation 2
1.2 Metrics that characterize shock content 4
1.3 Nonlinearity within jet noise 6
1.4 Measurement Setup 7
1.5 Long-range propagation considerations 9
1.6 Modeling shock formation in the far-field 10
1.7 Objectives and Scope of Work 10
2 Evolution of the Derivative Skewness for Nonlinearly Propagating Waves 12
2.1 Introduction 12
2.2 Derivative Skewness 14
2.2.1 Definition 14
2.2.2 Burgers Equation 15
2.2.3 Earnshaw Solution 16
2.2.4 Fubini Solution 18
2.2.5 Fay Solution 20
2.2.6 Derivative Skewness of Acoustic Shocks 22
2.3 Measurement Considerations 23
2.3.1 Finite Sampling Rate 23
2.3.1.1 Fubini Solution 26
2.3.1.2 Fay Solution 28
2.3.1.3 Recommended Sampling Rates 29
2.3.2 Signal-to-Noise Ratio 30
2.4 Applications 33
2.4.1 Numerical Case Study 33
2.4.2 Plane Wave Tube 37
2.4.2.1 Initially sinusoidal signal 37

2.4.2.2 Broadband noise 39
2.5 Conclusions 45

3 Acoustic shock formation in noise propagation during ground run-up operations of military aircraft 47
3.1 Introduction 47
3.2 Metrics indicative of nonlinear propagation 49
3.2.1 Derivative Skewness 49
3.2.2 ASF 50
3.2.3 Shock Energy Fraction 51
3.3 Measurement Details 55
3.3.1 Setup 55
3.3.2 OASPL 57
3.4 Evidence of Shock Formation 58
3.4.1 Waveform Characteristics 59
3.4.2 Derivative Skewness 66
3.4.3 Average Steepening Factor 68
3.4.4 Shock Energy Fraction 70
3.4.5 Spatial Trend Summary 72
3.5 Nonlinearity Metrics Along Radials 73
3.5.1 Comparison Across ETR 74
3.5.2 Angular Dependence of Nonlinearity Metrics 77
3.5.3 SEF and Shock Thresholds 79
3.6 Conclusions 80

4 Characterizing acoustic shocks in high-performance jet aircraft flyover noise 82
4.1 Introduction 82
4.2 Nonlinearity Metrics 84
4.3 Flyover Measurement Setup 86
4.4 Characterizing Nonlinearity in Flyover Waveforms 87
4.4.1 Waveforms and spectra 89
4.4.2 Flyover waveforms 90
4.4.3 Metrics Characterizing Nonlinear Propagation 94
4.5 Data Analysis 99
4.5.1 Engine Condition 99
4.5.2 Microphone size 102
4.5.3 Sampling Frequency 108
4.5.4 Microphone Height 112
4.6 Conclusions 114

5 Comparison of Noise from High-Performance Military Aircraft for Ground Run-up and Flyover Operations 116
5.1 Introduction 116
5.2 Measurements 118
5.3 Metrics 121
5.3.1 Sound Pressure Level 121
5.3.2 Derivative Skewness 122

5.3.3 Average Steepening Factor ... 122
5.3.4 Example of flyover metrics ... 123
5.4 OASPL Comparison ... 124
5.4.1 Method ... 125
5.4.1.1 Directivity Curves ... 125
5.4.1.2 Comparison of Average Results ... 127
5.4.1.3 Consistency with Aircraft Height ... 127
5.4.1.4 Azimuthal Directivity ... 128
5.5 Field Comparisons ... 132
5.5.1 Method ... 133
5.5.2 OASPL ... 135
5.5.3 Spectra ... 136
5.5.4 Nonlinearity ... 139
5.6 Results at Other Engine Conditions ... 142
5.6.1 OASPL ... 142
5.6.2 Nonlinearity Comparisons ... 144
5.7 Conclusions and Future Work ... 150

6 Atmospheric Conditions and Their Effects on Long-Range Nonlinear Propagation... 152
6.1 Introduction ... 152
6.2 Measurements ... 154
6.3 Metrics ... 156
6.3.1 Derivative Skewness ... 157
6.3.2 Average Steepening Factor ... 158
6.3.3 Shock Energy Fraction ... 158
6.4 Far-Field Variation in Metrics ... 159
6.4.1 Uncertainty with Distance ... 159
6.4.2 Trends at 610 m ... 164
6.4.3 Trends at 1220 m ... 169
6.5 Variation attributable to atmospheric conditions ... 173
6.6 Conclusions and Future Work ... 176

7 Numerically modeling far-field shock formation ... 178
7.1 Introduction ... 178
7.2 Measurement Setup ... 180
7.3 Metrics Indicative of Nonlinear Propagation ... 181
7.3.1 Derivative Skewness ... 181
7.3.2 Average Steepening Factor ... 182
7.3.3 Shock Energy Fraction ... 183
7.4 Spectral Analysis ... 183
7.4.1 Spectral Effects ... 183
7.4.2 Spectral Comparisons ... 185
7.5 Nonlinear Propagation Modeling ... 191
7.5.1 Propagation Algorithm and Spectral Correction ... 192
7.5.2 Nonlinear Prediction Spectral Comparison ... 193
7.5.3 Nonlinear Gain ... 198
7.6 Accuracy of Numerical Modeling in Waveform Characterization ... 201
7.6.1 Waveform Characteristics ... 202

7.6.2 Prediction of Nonlinearity Metrics 206
7.7 Conclusions and Future Work 212
8 Conclusions 213
8.1 Dissertation Summary........ 213
8.2 Recommendations and Future Work 215
References........ 217

List of Tables

Table 1.1. Source material for technical chapters 11
Table 2.1. The number of shocks present in two waveforms of different amplitudes, calculated from the waveforms measured at each of the five microphones. For this table a shock has been defined as a derivative exceeding 20 standard deviations of the waveform derivative. 45
Table 6.1. Weather conditions for all recorded runs at 100% ETR for both measurement days and ranges given in the standard 156
Table 7.1. The frequencies with an absorption length corresponding to measurement locations. The absorption length is calculated using meteorological data from the given measurement time over a range of frequencies, then the data are interpolated to find the frequency with the absorption length at the microphone distances from the MARP. 184
Table 7.2. Microphone heights and expected interference nulls for various distances. The heights of the microphones located in arcs of various radii are listed. These microphone heights are then used with a nozzle height of 1.82 m to calculate the frequency at which an interference null would be expected using a ground flow resistivity of 3,000 rayls 185
Table 7.3. Shock properties in measured and numerically propagated waveforms. Quantities shown are the number of shocks per second, the total pressure change over the shock, ΔP, and the average maximum shock derivative, $\langle(\partial p/\partial t)_{\max}\rangle$ 209

List of Figures

Fig. 1.1 Microphone measurement positions within 305 m of the MARP. The dashed red line shows the $\theta = 135°$ radial....8
Fig. 1.2. Flyover microphone locations. The aircraft flew roughly over the y = 0 line at heights of 76 m or 305 m....9
Fig. 2.1 The analytical derivative skewness of an initially sinusoidal waveform modeled by the Earnshaw solution as a function of σ along with the estimated derivative skewness of the Fubini solution for N terms [see Eq. (2.12)]....20
Fig. 2.2 The derivative skewness of the Fay solution as a function of σ for three values of Gol'dberg number....22
Fig. 2.3 Shock profiles for normalized Fubini (σ = 0.96) and Fay (σ = 260, $\Gamma = 10^3$) solutions with derivative skewness values of 8.9 and 3.9, respectively, shown over a section of the period T. See text for shock definition....23
Fig. 2.4 a) Derivative skewness estimates of the Fubini solution for $f_s/f = 10^1$, 10^2, 10^3, and 10^4 along with the analytical Earnshaw calculation. For each curve, $f_s/2f$ terms were used to compute the estimates. b) Error between the Fubini estimates and the Earnshaw solution....26
Fig. 2.5 Estimates of the derivative skewness for the Fay solution as a function of σ and $f_s/f = 10^1$, 10^2, 10^3, and 104, with a Gol'dberg number of 1000. To calculate the estimates, $(f_s/f)/2$ terms were used. The exact derivative skewness derived from continuous sampling is plotted for comparison....28
Fig. 2.6 Derivative skewness error for an initial sinusoid propagated to a distance of a) σ = 0.75 and b) σ = 30 for Γ = 1000 with band-passed noise added to the signal at various SNR. The calculated derivative skewness with infinite SNR are a) 2.51 and b) 12.23....32
Fig. 2.7 Derivative skewness of numerically propagated initial sinusoids with varying Gol'dberg numbers. The Earnshaw and Fay solutions are shown as solid lines, and the numerical predictions are shown in a dashed line....36
Fig. 2.8 a) Numerically propagated waveform compared with the Fay solution. b) The derivatives of the waveforms in part a). Small changes in the waveforms result in large derivative changes, which in turn result in large changes in the derivative skewness....37
Fig. 2.9 Comparison of derivative skewness values from measured waveforms in a plane wave tube with those of numerically propagated waveforms....39
Fig. 2.10 Measured noise waveforms at a) 0.4 m and b) 11.7 m, and c) the numerically predicted waveform at 11.7 m....41
Fig. 2.11 Spectra calculated from the three waveforms, segments of which were shown in Fig. 2.10. In the 11.7 m measured spectrum, high-frequency noise is present from 10-35 kHz....42

Fig. 2.12 Predicted (dashed) and measured (dots) values of the derivative skewness as a function of $\sigma_N = x/\boldsymbol{x}_N$. Values shown are for p_{rms} = 286 Pa and 200 Pa. Both cases share similar growth initially, then different behavior with increasing $\boldsymbol{\sigma}$. 44

Fig. 3.1 An example (a) shock-containing waveform, (b) wavelet transform of the waveform, and (c) coefficient of variation for each frequency. 55

Fig. 3.2 Microphone measurement positions within 38 m of the MARP. The dashed red line shows the θ= 135° radial........................57

Fig. 3.3 OASPL near an F-35A at (a) 50% ETR, (b) 75% ETR, and (c) at 150% ETR........................58

Fig. 3.4 Normalized, time-aligned waveforms at 150% ETR along the 135° radial (Red line in Fig. 2) at various distances from the MARP. 60

Fig. 3.5 Shocks in the 150% ETR waveforms from Fig. 3.4, categorized by strength........................62

Fig. 3.6 Bivariate histogram plots of pressure increases vs the maximum derivatives at (a) 19 m, (b) 28 m, (c) 38 m, (d) 76 m, (e) 152 m, and (f) 305 m at 150% ETR. Dashed lines indicate two-point shocks (Black), three-point shocks (red), and expected rise times when shock behavior is dominated by different regimes of absorption (Cyan and green)........................65

Fig. 3.7 Derivative skewness near an F-35A at (a) 50% ETR, (b) 75% ETR, and (c) 150% ETR. 68

Fig. 3.8 ASF near an F-35A at (a) 50% ETR, (b) 75% ETR, and (c) 150% ETR. 70

Fig. 3.9 SEF near an F-35A at (a) 50% ETR, (b) 75% ETR, and (c) 150% ETR. 72

Fig. 3.10 The (a) OASPL, (b) derivative skewness, (c) ASF, and (d) SEF along the peak radiation angle at 50%, 75%, and 150% ETR 77

Fig. 3.11 The (a) OASPL, (b) derivative skewness, (c) ASF, and (d) SEF at 150% ETR along radials from 120° to 150°. 79

Fig. 3.12 The SEF at an ETR of 150% and 135° as a function of distance for various shock thresholds. 80

Fig. 4.1 An F-35 flying between two cranes, each located 305 m (1000 ft) from the flight path of the aircraft. Microphones were hung from the 91.4 m cranes at multiple heights, with five heights having redundant ½" and ¼" microphones. 87

Fig. 4.2 The distance from the microphone to the aircraft $r(t)$ and angle of the microphone relative to the nose of the aircraft $\theta(t)$; for example flyover events at (a) 55% ETR and (b) 150% ETR. This microphone was located 91.4 m above ground level, hung from a crane located 305 m north of the flight path of the aircraft........................89

Fig. 4.3 Waveforms from (a) 55% ETR and (b) 150% ETR and (c) the spectra from each. Sharp compressions, or shock waves, are seen in the high-power waveform and produce the relative increase in high-frequency content. 90

Fig. 4.4 (a) The waveform measured at a location 305 m away from an F-35A flying at 55% ETR at 76.2 above the ground. (b) The PDF of the 6-dB down portion of the waveform, shown as a function of the pressure standard deviation σ. (c) The time derivative of the waveform. (d) The PDF of the derivatives from the 6-dB down portion of the waveform as a function of the derivative standard deviation $\sigma_{\partial p/\partial t}$........................92

Fig. 4.5 (a) The waveform measured at a location 305 m away from an F-35A flying at 150% ETR at 76.2 m above the ground. (b) The PDF of the 6-dB down portion of the waveform. (c) The time derivative of the waveform. (d) The PDF of the derivatives from the 6-dB down portion of the waveform. 94

Fig. 4.6 Statistics of the 55% ETR flyover waveform shown in Fig. 4.4(a), specifically the (a) OASPL, (b) derivative skewness, (c) ASF, and (d) the distance from the aircraft to the microphone, *r(t)* and the angle of the microphone relative to the aircraft nose, *θ(t)*. The 6-dB down region is highlighted in parts (a)-(c). 96

Fig. 4.7 Statistics of the 150% ETR flyover waveform in Fig. 4.5(a), specifically the (a) OASPL, (b) derivative skewness, (c) ASF, and (d) the distance from the aircraft to the microphone, *r(t)* and the angle of the microphone relative to the aircraft nose, *θ(t)*. The 6-dB down region is highlighted in parts (a)-(c). 98

Fig. 4.8 Spectra from the north tower at varying engine condition. Spectra from individual waveforms are shown in lighter lines, while the average at each engine condition is shown in a thicker, darker line. 100

Fig. 4.9 Nonlinearity metrics of waveforms recorded from different flyovers on microphones of different size, specifically the (a) derivative skewness, and (b) ASF. Statistics are calculated from the 6-dB down region of each waveform. The level and derivative skewness values increase with engine condition, and a large spread in derivative skewness values is seen at 150% ETR. 102

Fig. 4.10 Comparison of (a) a portion of the waveforms, (b) the PDF of the 6-dB down portion of the waveform, (c) the waveform derivatives, and (d) the PDF of the 6-dB down portion of the derivatives from microphones at the same location. The aircraft was operating at 150% ETR. 104

Fig. 4.11 Nonlinearity metrics of waveforms recorded from different flyovers on microphones of different size, specifically the (a) derivative skewness, and (b) ASF. Statistics are calculated from the 6-dB down region of each waveform. (c) The data for each microphone size are fit to curves overlaid on top of the data points. 107

Fig. 4.12 The importance of sampling rate when estimating nonlinear parameters of shock-containing waveforms. The (a) derivative skewness and (b) ASF of the 6-dB down portion of the waveforms from Fig. 4.4(a) Fig. 4.5(a) is calculated as the waveforms are resampled to lower sampling rates. 110

Fig. 4.13 The effects of resampling on trends for derivative skewness with two different microphone sizes. Waveforms were separated according to microphone size and then resampled to various lower sampling rates. Derivative skewness values were fit to a curve and plotted against the OASPL. Solid lines represent data from ¼” microphones, and dashed lines from ½” microphones. The 204.8 kHz and 102.4 kHz lines for ½” microphones lie almost directly on top of each other. 112

Fig. 4.14 Comparison of the (a) derivative skewness and (b) ASF for varying microphone heights, plotted against OASPL. All data shown are from ¼” microphones, with statistics calculated from the 6-dB down region. 114

Fig. 5.1 Layout for the (a) ground run-up and (b) flyover measurements. 120

Fig. 5.2 Illustration of azimuthal angle ϕ and polar angle θ relative to the flight track. 121

Fig. 5.3 Example waveform and metrics from a flyover measurement. 124

Fig. 5.4 Calculated directivity curves at a height of 76 m from (a) all microphone channels for one flyover event, colored according to the azimuthal angle ϕ, and (b) the averaged result for the flyover array’s ground microphones (-3 dB correction, black), the flyover array’s elevated microphones (red), and the ground run-up arcs at 76m (blue). 126

Fig. 5.5 Polar directivity of an aircraft at height of 305 m (a) shown for all microphones and (b) an average directivity for microphones located on and above the ground and compared with ground run-up....128
Fig. 5.6 OASPL as a function of polar angle θ and azimuthal angle ϕ during 150% ETR flyover events at aircraft heights of (a) 76 m and (b) 305 m. 129
Fig. 5.7 OASPL at a polar angle of 120° plotted against measurement distance r for flyover events at (a) 150% ETR and (b) 100% ETR....132
Fig. 5.8 Aircraft flight path relative to microphones for flyover events with aircraft height of 76 m. 135
Fig. 5.9 Comparison of OASPL at 150% ETR for (a) ground run-up and (b) flyover....136
Fig. 5.10 (a) Comparison of spectra at a distance of 76 m between ground run-up and flyover at 150% ETR and (b) relative gain in level during flight....139
Fig. 5.11 Derivative skewness comparison between (a) ground run-up and (b) flyover at 150% ETR....140
Fig. 5.12 ASF comparison between (a) ground run-up and (b) flyover at 150% ETR....142
Fig. 5.13 Average flyover directivity at an aircraft height of 76 m compared with ground run-up at (a) 75% ETR and (b) 100% ETR. 144
Fig. 5.14 Derivative skewness at 75% ETR for (a) ground run-up and (b) flyover. 146
Fig. 5.15 Derivative skewness at 100% ETR for (a) ground run-up and (b) flyover. 147
Fig. 5.16 ASF at 75% ETR for (a) ground run-up and (b) flyover....149
Fig. 5.17 ASF at 100% ETR for (a) ground run-up and (b) flyover....150
Fig. 6.1 Microphone locations for ground run-up measurements at distances of 38 m and greater relative to the MARP, located at $(x , y) = (0 , 0)$. Also shown as red squares are locations of weather stations, with weather stations present at multiple heights for the two farther locations....155
Fig. 6.2 Waveforms from the microphone located 22.8 m above the around at 610 m from the MARP along the 135° radial for three runs at 100% ETR: (a) Run 129, (b) Run 219, and (c) Run 124....160
Fig. 6.3 The (a) OASPL, (b) derivative skewness, (c) ASF, and (d) SEF are shown as a function of distance along with 135° radial for the 100% ETR runs. Standard deviation over the 9-10 runs at each measurement location is shown using error bars....162
Fig. 6.4 Spectra for measurement distances from 38.1 m to 1220 m along the 135° radial at height of 9.1 m for 100% ETR. Averaged spectrum (dB average) at each location is shown with a darker line. 164
Fig. 6.5 OASPL is shown as a function of height at a distance of 610 m at 135° for all runs at 100% ETR. Symbols denote which day the run was measured....165
Fig. 6.6 The (a) derivative skewness, (b) ASF, and (c) SEF are shown as a function of height at a distance of 610 m at 135° for all runs at 100% ETR. Symbols denote which day the run was measured. 167
Fig. 6.7 OASPL is shown as a function of height at a distance of 1220 m at 135° for all runs at 100% ETR. Symbols denote which day the run was measured....170
Fig. 6.8 The (a) derivative skewness, (b) ASF, and (c) SEF are shown as a function of height at a distance of 1220 m at 135° for all runs at 100% ETR. Symbols denote which day the run was measured. 172

Fig. 6.9 The OASPL (Normalized to average level at 0 m height at each engine condition) as a function of height for all engine conditions from 75% to 150% ETR at 135°. Colors correspond to average wind throughout the run. 174

Fig. 6.10 The OASPL (Normalized to average level at 0 m height at each engine condition) as a function of height for all engine conditions from 75% to 150% ETR at 135°. Colors correspond to measurement time. 176

Fig. 7.1 Microphone measurement positions within 38 m of the MARP. The dashed red line shows the $\theta = 135°$ radial. 181

Fig. 7.2 OTO Spectra along the 30° radial as a function of engine condition. The four plots show the OTO spectra calculated at (a) 50% ETR, (b) 75% ETR, (c) 100% ETR, and (d) 130% ETR. 187

Fig. 7.3 OTO Spectra along the 90° radial as a function of engine condition. The four plots show the OTO spectra calculated at (a) 50% ETR, (b) 75% ETR, (c) 100% ETR, and (d) 130% ETR. 189

Fig. 7.4 OTO Spectra along the 135° radial as a function of engine condition. The four plots show the OTO spectra calculated at (a) 50% ETR, (b) 75% ETR, (c) 100% ETR, and (d) 130% ETR. 190

Fig. 7.5 OTO Spectra along the 150° radial as a function of engine condition. The four plots show the OTO spectra calculated at (a) 50% ETR, (b) 75% ETR, (c) 100% ETR, and (d) 130% ETR. 191

Fig. 7.6 OTO spectra at 305 m compared with linear and nonlinear predictions for 50% ETR. Waveforms measured at $r = 76.2$ m are propagated to $r = 305$ m using both linear (blue) and nonlinear (red) propagation algorithms. The resulting OTO spectra are compared with the spectra at 305 m (black) at (a) 30°, (b) 90°, (c) 135°, and (d) 150°. 195

Fig. 7.7 OTO spectra at 305 m compared with linear and nonlinear predictions for 75% ETR. Waveforms measured at $r = 76.2$ m are propagated to $r = 305$ m using both linear (blue) and nonlinear (red) propagation algorithms. The resulting OTO spectra are compared with the spectra at 305 m (black) at (a) 30°, (b) 90°, (c) 135°, and (d) 150°. 196

Fig. 7.8 OTO spectra at 305 m compared with linear and nonlinear predictions for 100% ETR. Waveforms measured at $r = 76.2$ m are propagated to $r = 305$ m using both linear (blue) and nonlinear (red) propagation algorithms. The resulting OTO spectra are compared with the spectra at 305 m (black) at (a) 30°, (b) 90°, (c) 135°, and (d) 150°. 197

Fig. 7.9 OTO spectra at 305 m compared with linear and nonlinear predictions for 130% ETR. Waveforms measured at $r = 76.2$ m are propagated to $r = 305$ m using both linear (blue) and nonlinear (red) propagation algorithms. The resulting OTO spectra are compared with the measured spectra at 305 m (black) at (a) 30°, (b) 90°, (c) 135°, and (d) 150°. 198

Fig. 7.10 Nonlinear gain at $r = 305$ m. Waveforms measured at $r = 76.2$ m are numerically propagated to 305 m with both the linear and nonlinear algorithms described in Sec. IV A. The difference between the spectral levels of the propagated waveforms is the nonlinear gain. The nonlinear gain is plotted as a function of frequency and

angle for four engine conditions: (a) 50% ETR, (b) 75% ETR, (c) 100% ETR, and (d) 130% ETR. 201
Fig. 7.11 Comparison of (a) waveforms, (b) PDFs, and (c) spectra between a measurement at 305 m and data numerically propagated from 76 m to 305 m. 203
Fig. 7.12. Distribution of the differences in arrival times between the numerically propagated and measured waveforms shown in Fig. 7.11(a). 205
Fig. 7.13. The strongest 100 shocks in the waveform with distance. 206
Fig. 7.14 Comparison of (a) derivative skewness (b) ASF and (c) SEF between measured waveforms and numerically propagated waveforms. 208
Fig. 7.15 Numerically propagated waveforms over short distances. (a) The measured waveform at 76.2 m is compared with the same waveform numerically propagated to a distance of 76.5 and 77.7 m. (b) The PDF of derivative values is shown for the three distances. 210
Fig. 7.16 Example of measurement artifacts. Measurement at 305 m (black) is compared with a waveform numerically propagated from 76 m to 305 m (red). 211

Chapter 1

Introduction

The sound of a military jet aircraft flying overhead is an impressive reminder of the power of the aircraft itself. However, jet noise exposure can be an issue for those who work at or live near military bases, with noise levels capable of causing annoyance and producing significant hearing loss. In addition to the large noise levels, acoustic shocks further complicate the noise exposure and community annoyance.

The acoustic shocks present in the noise are a byproduct of the high noise levels produced by military jet aircraft. The small-signal assumptions that are made when dealing with acoustic propagation are violated by the extreme levels of jet noise, where the overall sound pressure level (OASPL) near the jet plume can reach over 160 dB.[1] The large pressure fluctuations associated with such a high OASPL result in local variations in sound speed, causing peaks in pressure to travel faster than troughs and form acoustic shocks. Though the idea of nonlinear propagation within jet noise is not new,[2] recently the discussion of this idea has centered on where shock formation occurs. Some have contended that shock formation is primarily a source effect, while others contend that shocks form through nonlinear propagation away from the source.

This dissertation shows that nonlinear propagation is driving shock formation in the far field and is an important factor in understanding jet noise characteristics, even at large distances of over 1000 m from the source. To do so, the basic principles of nonlinear propagation are applied to jet noise. Metrics are developed and used to understand where shock formation is present and where shocks are a significant feature of the noise. Application of these metrics occurs not only during stationary (ground run-up) measurements, but also as part of in-flight (flyover) measurements. The two scenarios are then compared to observe expected flight effects on OASPL and investigate flight effects on nonlinearity parameters. Long-range propagation effects are considered and the accuracy of numerical modeling is shown, specifically with the use of metrics to illustrate ways in which the modeling may idealize or overemphasize certain features of the waveform.

1.1 Basics of nonlinear acoustic propagation

The field of nonlinear acoustics existed long before jet noise became an issue, with many theoretical developments taking place in the 19th century. Stokes[3] initially showed a waveform steepening due to variations in sound speed, and later Earnshaw[4] developed an analytical solution showing the distortion of a waveform for an arbitrary source up until shocks, theoretical discontinuities, had formed in the noise. Later developments by Fay[5] and Blackstock[6] gave analytical solutions for distorted waveforms that were initially sinusoidal signals at distance much larger than the shock formation distance. The expected behavior can be summarized simply: the peaks of a wave travel faster than the troughs. For a finite-amplitude, initially sinusoidal signal, the sine waveform eventually steepens into a sawtooth waveform, transferring energy from the fundamental frequency to higher harmonics. In noise waveforms, steepening does not happen at a periodic interval, but energy is still transferred from peak frequency regions to both higher and lower frequencies.

The simplest model equation describing nonlinear propagation and losses due to absorption is the Burgers equation.[7] This equation, written as

$$\frac{\partial p}{\partial x} - \frac{\delta}{2c_0^3}\frac{\partial^2 p}{\partial \tau^2} = \frac{\beta p}{\rho_0 c_0^3}\frac{\partial p}{\partial \tau}, \qquad (1.1)$$

consists of three terms representing, from left to right, the change in the pressure waveform $p(\tau)$ with distance x, linear absorption, and quadratic nonlinearity. Other important terms in this equation include τ, the retarded time; β, the coefficient of nonlinearity of the material (1.2 in air); ρ_0, the ambient density; δ, the sound diffusivity; and c_0, the small-signal sound speed. Assuming a time-harmonic signal, the coefficients of the absorption and nonlinearity terms become important quantities within nonlinear acoustics when multiplied by a factor of ω for each time derivative. The thermoviscous absorption coefficient is defined as $\alpha = \delta\omega^2/2c_0^3$, and is proportional to the change in OASPL at a frequency ω with distance. It's inverse, $\ell_\alpha = 1/\alpha$, is referred to as the absorption length, and over the distance l_α the amplitude at frequency ω decreases by a factor of $1/e$. The plane-wave shock formation distance is defined as $\bar{x} = \rho_0 c_0^3/\beta\omega p_0$. An initial sinusoid of amplitude p_0, propagating in a lossless medium, first forms a theoretical discontinuity at the distance $\bar{x}$. The Gol'dberg number is the ratio of absorption length to shock formation distance, $\Gamma = \ell_\alpha/\bar{x}$. This number expresses the relative strength of nonlinear effects to absorption; $\Gamma \gg 1$ means that nonlinear effects are significant and significant shocks will form, while $\Gamma \ll 1$ means that nonlinear effects can likely be neglected. These quantities, while useful in discussing sinusoidal signals, lose some meaning when applied to noise signals with a wide frequency bandwidth. Some changes have been introduced to the traditional shock formation distance and Gold'berg number to describe shock formation when losses[2] and geometric spreading[8] are present. However, the broadband nature of noise negates the notion of a single shock formation distance[9] and other methods must be used to characterize the strength of nonlinear effects and shock formation.

1.2 Metrics that characterize shock content

The broadband nature of jet noise makes it difficult to define where shock formation is occurring and to directly compare the effects of nonlinearity and absorption. Instead, many efforts have concentrated on using single-value metrics to express the steepness of a waveform. One of the first examples of this approach comes from Ffowcs-Williams *et al.*[10] In trying to find criteria for crackle, the auditory perception of shock waves within jet noise, they suggested the skewness of the waveform, a measure of asymmetry of the pressure values, as an indicator of whether it would crackle. It has since been shown that while skewness of the pressure waveform is a property of supersonic jets, it is not a necessary or sufficient indicator of the presence of shocks within a waveform.[11] Since then, other metrics have been explored which tie more to the large positive derivative values, including the derivative skewness[12] and average steepening factor (ASF).[13]

The derivative skewness is a measure that highlights the asymmetry in derivative values that occurs as a waveform steepens through nonlinear propagation. Because peaks consistently travel faster than troughs, the time derivative of a shock-containing waveform contains larger positive values and smaller negative values, resulting in a distribution of derivative values that is positively skewed. The derivative skewness was first proposed as a metric for jet noise nonlinearity by McInerny *et al.*[12] and has since been used in many jet noise analyses. It has also shown correlation with perception of crackle.[14] However, one deficiency that has plagued the derivative skewness, as well as other metrics, is the physical interpretation of values.

Another metric that has been used in the literature is the average steepening factor (ASF)[13] and its inverse, the wave steepening factor (WSF).[15,16] This metric is defined as $\mathrm{ASF} = \langle \dot{p} \rangle_+ / |\langle \dot{p} \rangle_-|$, the average positive derivative of a waveform over the absolute value of the average negative derivative. The WSF was the metric initially used within jet noise, but it suffered from a lack of physical interpretation. It was recast as the ASF by Muhlestein *et al*.[13] to have more intuitive behavior (a greater ASF means a steeper waveform) and given a thorough analytical treatment. Muhlestein *et al*. explored the ASF for initial sinusoids and derived analytical formations of the ASF for simple solutions to the Burgers equation to help illustrate expected behavior and values. A similar analysis is performed for the derivative skewness in this dissertation to give meaning to these values.

Both the derivative skewness and ASF are exclusively time-domain metrics, focusing on the steepened waveform and presence of shocks. However, steepening in the time domain is also evident as a transfer of energy to high frequencies. Because of this, one other metric that will be considered in this dissertation is the shock energy fraction (SEF), based on the wavelet transform that gives both temporal and frequency-domain resolution. This metric is based on the crackle energy gain introduced by Baars and Tinney,[16] but with some changes to better highlight the high-energy contributions of shocks. The differences between the two are explained in detail in Chapter 3.

These three metrics emphasize different components of the waveform and can be used together to better inform about behavior of shock formation across a noisy waveform as a whole. The derivative skewness emphasizes the largest derivative values and is likely to be more influenced by larger amplitude shocks, which form quickly relative to other portions of the waveform. The ASF is more representative of general behavior and does not react as strongly to the largest shocks. The SEF, on the other hand, emphasizes the high-frequency energy associated with shocks compared with the rest of the waveform, and may better represent the perception of high-frequency energy within shocks. Comparing the behavior of these metrics together provides information about shock formation and the significance of shocks in nonlinearly propagated noise, such as around tactical military aircraft.

1.3 Nonlinearity within jet noise

Acoustic shocks within jet noise have been historically associated with the perceptual term "crackle." Steepened waveforms exist near the source,[16,17] but waveforms from full-scale aircraft continue to steepen and form shocks further away from the source due to nonlinear propagation.[18-20] One of the first indications that nonlinear propagation played a role in propagation was an apparent lack of atmospheric absorption in the far field noticed by Pernet and Payne[2] and later by Morfey and Howell.[21] The steepening of waveforms and formation of shocks was also shown by Blackstock[18] to increase at locations farther away from the jet noise source, though his analysis did not incorporate atmospheric absorption. Though nonlinear propagation has been shown to be an important contributor to waveform steepening and increased high-frequency content away from the source, some still contend that nonlinear propagation does not significantly alter the waveform away from the source.[16]

While much of the work with nonlinear propagation has been performed using stationary jets, either in laboratory or with tethered aircraft, shock content and noise exposure is important in flyover operations as well. In-flight measurements are inherently complicated by factors such as smaller integration time for metrics, uncertainty in distances between the aircraft and measurement locations, and atmospheric propagation effects.[22,23] However, the changing nature of the source between static and in-flight operations necessitates measurements during flyover events and a comparison of the two conditions. Such comparisons of OASPL have been made for both full-scale[22,23] and model-scale experiments[24,25] and agree with analytical derivations that predict effects of forward flight.[26] However, nonlinearity and shock content during flyover events is an area that has received little treatment.[27] The analyses presented in Chapter 4 represent the first peer-reviewed publication of nonlinearity metrics for in-flight military aircraft, and Chapter 5 represents the first published comparisons of OASPL and nonlinearity metrics between ground run-up and flyover measurements.

1.4 Measurement Setup

With the exception of Chapter 2, the experimental data used in this dissertation come from a measurement of the F-35A and F-35B variants which took place in September 2013 at Edwards Air Force Base, CA. Since most of the dissertation concerns data from this measurement set-up it is described here, though descriptions are also found within each chapter.

Measurements of both aircraft were made in both ground run-up (tethered to the ground) and flyover configurations in accordance with jet noise measurement standards.[28] The ground run-up measurement configuration can be seen in Fig. 1.1 for all microphones within 38 m (125 ft) of the source. The origin of this system is the microphone array reference position (MARP), located approximately 7 m behind the aircraft, as a rough estimate of source location, though the exact source location varies with frequency.[29] The majority of the microphones are located in semicircular arcs around the MARP. Additional semicircular arcs were located at 76 m, 152 m, and 305 m from the source, with measurement locations spanning from $0 - 160°$. At distances of 610 and 1220 m, microphones were located along the 120°, 135°, and 150° radials. These larger distances are considered in Chapter 6, while other chapters focus on data within 305 m.

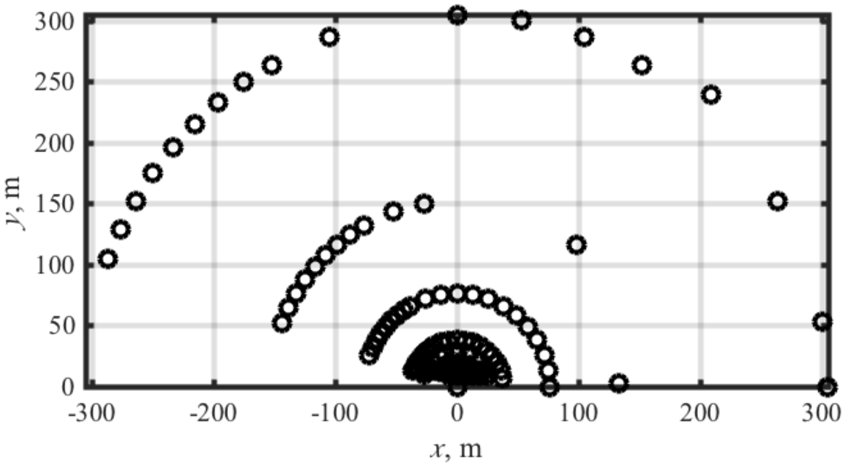

Fig. 1.1 Microphone measurement positions within 305 m of the MARP. The dashed red line shows the θ = 135° radial.

The flyover measurement setup, shown in Fig. 1.2, was also designed according to the noise measurement standard.[28] Microphones were hung from two 91 m tall cranes, located 305 m from the approximate flight path of the aircraft, the $y = 0$ line in Fig. 1.2. Microphones were also located at heights of 0, 1.5, and 9.1 m at various distances between the two cranes, with additional microphones along the flight path of the aircraft.

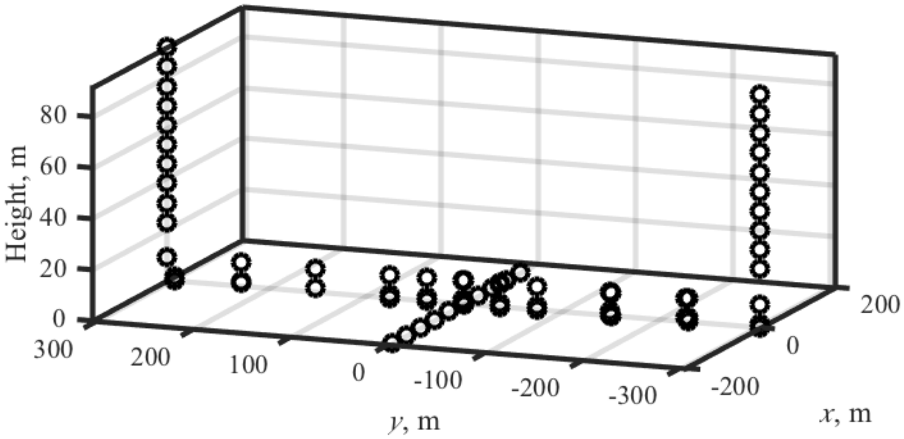

Fig. 1.2. Flyover microphone locations. The aircraft flew roughly over the *y* = 0 line at heights of 76 m or 305 m

1.5 Long-range propagation considerations

While much of the analysis in this dissertation uses data collected within 305 m from the source, propagation over longer distances is an essential step to predicting noise exposure, in particular to those living near military bases. Measurements were also collected at distances of up to 1220 m (4000 ft) in the maximum radiation region. However, small changes in weather can result in larger changes in OASPL and nonlinearity metrics at large distances. The effect of weather in nonlinear propagation, in particular, is an area that has received little study, and the ways in which atmospheric effects change shock formation is an area that is not well understood. Changes in OASPL and nonlinearity metrics are shown at large distances in Chapter 6, along with weather data that can be associated with some of the behavior at large distances.

1.6 Modeling shock formation in the far-field

The extensive measurements described in Section 1.4 can be enhanced with numerical modeling. Some of the benefits of modeling include a greater spatial resolution, the ability to directly compare nonlinear and linear effects, and the ability to extend the analyses beyond the measurement scope, in particular extending past the farthest measurement locations. The nonlinear propagation code used here is similar to that used by Gee *et al.*[30] It is a hybrid time-frequency domain algorithm based on the Generalized Burgers Equation (GBE) and incorporates geometric spreading, atmospheric absorption, and quadratic nonlinearity as well as weak shock theory developed by Pestorius and Blackstock[31] to more efficiently propagate shocks. Modeling has been used in past analyses to show shock formation and predict spectral shape in the far field.[1819]

1.7 Objectives and Scope of Work

The three main goals of this dissertation are: 1) Quantify the derivative skewness to aid in a physical understanding of values seen in other experiments. 2) Apply a better physical understanding of the values of nonlinearity metrics to understand where shock formation is occurring and where nonlinear propagation is an important factor in understanding the sound field, in both ground run-up and flyover measurements. 3) Compare the OASPL and nonlinearity metrics for ground run-up and flyover measurements to understand forward flight effects on the jet noise source and associated changes in nonlinear propagation and shock formation. In addition to these goals, chapters are devoted to long-range propagation and the effects of atmospheric conditions on nonlinear propagation and to numerical simulations.

The majority of the work contained in this dissertation comes from papers submitted by the author to journals and conference proceedings papers. A list of source material for Chapters 2-7 is found in Table 1.1 for reference.

Table 1.1. Source material for technical chapters

Chapter	Source articles
Chapter 2	Reichman *et al.*, "Evolution of the derivative skewness for nonlinearly propagating waves," J. Acoust. Soc. Am. (2016)
Chapter 3	Reichman *et al.*, "Acoustic shock formation in noise propagation during ground run-up operations of military aircraft," AIAA Paper 2017-4043 (2017)
Chapter 4	Reichman *et al.*, "Characterizing acoustic shocks in high-performance jet aircraft flyover noise," J. Acoust. Soc. Am. (2018)
Chapter 5	Reichman *et al.*, "Comparison of Noise from High-Performance Military Aircraft for Ground Run-up and Flyover Operations," Submitted AIAA Paper
Chapter 6	Will be submitted to J. Acoust. Soc. Am.
Chapter 7	Reichman *et al.*, "Modeling Far-field Acoustical Nonlinearity from F-35 Aircraft during Ground Run-up," AIAA Paper 2016-1888 (2016) Reichman *et al.*, "Acoustic shock formation in noise propagation during ground run-up operations of military aircraft," AIAA Paper 2017-4043 (2017)

Chapter 2

Evolution of the Derivative Skewness for Nonlinearly Propagating Waves

2.1 Introduction

The importance of nonlinearity during propagation has been a topic of significant debate in the jet noise community because of its tie to the growth of acoustic shocks. Many have shown evidence of nonlinear propagation for full-scale experimental data,[18,19,21,30] while some have seen evidence of nonlinear effects in model-scale jets,[32-34] and others have not.[35] Because of the difficulty in quantifying nonlinearity associated with statistical phenomena, much research has gone into the development and usage of various measures to quantify the effects and strength of nonlinearity and the presence of acoustic shocks in different situations. These measures have been developed in the time domain, using both the pressure waveform[36-38] and its first time derivative,[11,27,39,40] and in the frequency domain using higher order spectral analysis.[21,41,42] Although these various measures have been used as qualitative indicators of nonlinearity, a quantitative understanding of the values obtained has been lacking. This chapter provides quantitative insight into the meaning of skewness values of the first time derivative of the pressure waveform, using analytical, experimental, and numerical methods.

Skewness is a statistical measure of asymmetry present in a probability density function and has been used in a wide variety of fields from agriculture[43] to economics.[44] In fluid mechanics, the skewness of the streamwise derivative of both the temperature[45] and velocity[46,47] has been used to indicate an increase in vorticity in turbulent flows. The skewness of the first time derivative of the pressure waveform, i.e., derivative skewness, is a measure of the asymmetry present in the derivative values of the waveforms. The derivative skewness has been shown to be associated with the presence of acoustic shock waves[48] and has been used to investigate nonlinearity present in the propagation of jet and rocket noise.[17,20,]12 However, despite the use of this metric, a physical understanding of the connections between derivative skewness values, nonlinear propagation, and acoustic shock growth has yet to be fully investigated.

There are some examples of investigations into derivative skewness values for well-understood cases. One example, by Shepherd *et al.*[37] used the Blackstock bridging function as a solution to the Burgers equation to predict values for various statistics, including derivative skewness, for nonlinearly propagating sine waves and their evolution into sawtooth waves. They found that derivative skewness values dramatically increase during the shock formation process, in contrast to the pressure skewness, which changes only after the formation of shocks. The derivative skewness in random noise compared to sinusoidal signals has also been experimentally investigated using a plane-wave tube.[49] The preliminary analysis suggested that, for noise, the derivative skewness increased more rapidly and reached greater values.

This chapter follows a structure similar to that of Muhlestein *et al.*[50]*,* who have carried out an analytical and quantitative investigation of another time-domain metric, the average steepening factor (ASF). First, an analytical treatment of derivatives skewness is considered for the Earnshaw[4], Fubini[51], and Fay[5] solutions to the Burgers equation for initially sinusoidal signals. Included is an analysis of the effects of additive noise and sampling rate. Next, these analytical solutions are compared against those obtained using numerical propagation. Finally, numerical results are compared against experimental data from a plane-wave tube for both sinusoidal and random noise waveforms. All of these analyses combine to give a quantitative understanding of derivative skewness values observed during the formation and eventual decay of shock waves in continuous waveforms.

2.2 Derivative Skewness

2.2.1 Definition

The skewness of a random variable, y, denoted by $\mathrm{Sk}\{y\}$, is a normalization of the third central moment of the probability density function (PDF) of y and is a measure of asymmetry in a distribution. The skewness of the first time derivative of the pressure waveform is defined in terms of the expectation values, $E[\,]$, as

$$\mathrm{Sk}\left\{\frac{\partial p}{\partial \mathrm{t}}\right\} = \frac{\mathrm{E}\left[\left(\frac{\partial p}{\partial t}\right)^3\right]}{\mathrm{E}\left[\left(\frac{\partial p}{\partial \mathrm{t}}\right)^2\right]^{\frac{3}{2}}} \tag{2.1}$$

Because of the cubic power in the numerator, large values of $\partial p/\partial t$ are emphasized in the skewness calculation. It has been suggested by McInerny[12] that the skewness of the first time derivative of the pressure waveform, or derivative skewness, may be used to characterize shocks in rocket noise, and it has subsequently been used with acoustic shocks within jet noise.[11,16] These shocks have high positive derivative values and moderate negative derivative values, meaning that the pressure waveform's derivative skewness increases as shocks form during propagation. Shepherd *et al.*[37] predicted the evolution of the derivative skewness for an initially sinusoidal wave propagating without linear losses in the preshock region. Subsequently, Muhlestein and Gee[49] calculated the derivative skewness for waveforms measured in a plane-wave tube and found trends that agreed with those predicted by Shepherd *et al.* This chapter treats the evolution of the derivative skewness for an initially sinusoidal signal using analytical methods and compares the results with those obtained using numerical calculations and plane-wave tube experiments.

2.2.2 Burgers Equation

The Burgers equation models the propagation of a planar wave including thermoviscous losses and nonlinear effects. Following the notation of Blackstock *et al.*,[7] the Burgers equation is written as

$$\frac{\partial p}{\partial x} - \frac{\delta}{2c^2}\frac{\partial^2 p}{\partial \tau^2} = \frac{\beta}{\rho c^3} p \frac{\partial p}{\partial \tau} \tag{2.2}$$

where p is the acoustic pressure, x is the distance from the source, δ is a constant associated with acoustic absorption by the propagation medium, c is the small-signal sound speed, $\tau = t - x/c$ is the retarded time, β is the coefficient of nonlinearity, and ρ is the ambient density. The terms on the left-hand side in Eq. (2.2) represent the total change in pressure with x and the effect of thermoviscous absorption; the right-hand side corresponds to the changes in pressure due to quadratic nonlinear phenomena. When nonlinear effects are sufficiently strong, the absorptive term in Eq. (2.2) is negligible in comparison with the nonlinear term, resulting in the lossless Burgers equation,

$$\frac{\partial p}{\partial x} = \frac{\beta}{\rho c^3} p \frac{\partial p}{\partial \tau}. \tag{2.3}$$

Under certain assumptions, useful analytical approximations and solutions to the lossy and the lossless Burgers equation may be found which are valid in different regions. The three expressions considered in this chapter are the Earnshaw,[4] Fubini,[51] and Fay[5] solutions. These solutions are useful for our purposes because analytical forms of the time derivatives and the derivative skewness can be found for each of these solutions.

2.2.3 Earnshaw Solution

The method of characteristics may be used to directly solve the lossless Burgers equation, Eq. (2.3), implicitly. This solution, called the Earnshaw solution,[4] can be written as a parametric equation,

$$\begin{gathered} P = g(\phi) \\ \phi = t + \sigma P \end{gathered} \tag{2.4}$$

where P is the pressure normalized by some pressure amplitude p_0, ϕ is the Earnshaw phase variable, t is time, and σ is a normalized distance away from the source.[7]

The normalized distance is measured relative to the lossless shock formation distance, $\bar{x}$, which is defined for initially sinusoidal signals as

$$\bar{x} = \frac{\rho c^3}{\beta \omega p_0}. \tag{2.5}$$

In Eq. (2.5), $\omega = 2\pi f$, with f being the frequency of the initial sinusoid, and p_0 is its initial amplitude. For the remainder of this chapter, distance is represented by $\sigma = x/\bar{x}$. At $\sigma = 1$, $x = \bar{x}$, and a theoretically discontinuous shock has formed. The Earnshaw solution, which is valid for $\sigma < 1$, may be interpreted as distorting the times of arrival of the initial waveform, represented by the Earnshaw phase variable, but not modifying the pressure values, $g = g(\phi)$.

An analytical form of the derivative skewness may be found for the Earnshaw solution. For an initially sinusoidal signal, the time derivative of the Earnshaw solution is written in parametric form as

$$\left(t', \frac{\partial P}{\partial t}\right) = \left(t - \sigma\sin(t), \frac{\cos(t)}{1 - \sigma\cos(t)}\right), \tag{2.6}$$

where t' represents the retarded time of arrival and $\partial P/\partial t$ is the time derivative at the retarded time of arrival. The expectation value of the n^{th} power of the time derivative is

$$E[(\partial P/\partial t)^n] = \frac{1}{2\pi}\int_0^{2\pi}\left(\frac{\partial P}{\partial t'}\right)^n dt', \tag{2.7}$$

where $t' = t - \sigma\sin(t)$ is a retarded time that accounts for the variation in sound speed with acoustic pressure. It follows that $dt' = dt(1 - \sigma\cos(t))$. Substituting these values in Eq. (2.7) gives

$$\mathrm{E}[(\partial P/\partial t)^n] = \frac{1}{2\pi}\int_0^{2\pi}\frac{\cos^n(t)\,dt}{(1 - \sigma\cos(t))^{n-1}}. \tag{2.8}$$

This integral can be evaluated for $n = 2$ and $n = 3$ to give the analytical form of the derivative skewness, written as

$$\mathrm{Sk}\{\partial P/\partial t\} = \frac{2(1-\sigma^2)^{3/2} + 3\sigma^2 - 2}{(1-\sigma^2)^{3/4}\left(1 - \sqrt{1-\sigma^2}\right)^{3/2}}. \tag{2.9}$$

Because the Earnshaw solution assumes lossless propagation, Eq. (2.9) depends only on σ.

The expression for the Earnshaw solution-based derivative skewness results in useful approximations. For $\sigma \ll 1$, Eq. (2.9) may be approximated as

$$\mathrm{Sk}\{\partial P/\partial t\} \approx 3\sigma/\sqrt{2}, \tag{2.10}$$

indicating that the nonlinear function shown numerically by Shepherd *et al.*[37] and experimentally by Muhlestein and Gee[49] can be approximated for small σ using a linear fit. As $\sigma \rightarrow 1$, Eq. (2.9) may be approximated as

$$\mathrm{Sk}\{\partial P/\partial t\} \approx (1-\sigma^2)^{-3/4}, \tag{2.11}$$

which yields approximate values of 3.47 at $\sigma = 0.9$ and 18.9 at $\sigma = 0.99$ and then continues to increase towards infinity as $\sigma \rightarrow 1$.

2.2.4 Fubini Solution

While the Earnshaw solution is useful in certain circumstances, an explicit function is sometimes more convenient. This is especially true when constructing waveforms at specific time intervals, as is the case when discussing the effects of a finite sampling rate subsequently. One explicit solution to Eq. (2.3) is the well-known Fubini solution,[51] written as

$$P = \sum_{n=1}^{\infty} \frac{2}{n\sigma} J_n(n\sigma) \sin(nt). \tag{2.12}$$

Similar to the Earnshaw solution, the Fubini solution is only valid for $\sigma < 1$. Using the results developed in Appendix A for the skewness of an arbitrary Fourier series, an analytical form of the derivative skewness for $\sigma < 1$ can be found using the Fubini solution. The time derivative of Eq. (2.12) is an infinite cosine series, written as

$$\frac{\partial P}{\partial t} = \sum_{n=1}^{\infty} \frac{2}{\sigma} J_n(n\sigma) \cos(nt), \tag{2.13}$$

which allows the use of (A28) from Reichman *et al.*,[80]

$$\mathrm{Sk}\left\{\sum_{n} A_n \cos(nt)\right\} = \frac{3}{\sqrt{2}} \frac{\sum_{n=1}^{\infty}\sum_{m=1}^{\infty} A_n A_m A_{n+m}}{\left[\sum_{n=1}^{\infty} A_n^2\right]^{\frac{3}{2}}}. \tag{2.14}$$

Eq. (2.13) can be substituted into Eq. (2.14) and the derivative skewness can be written as

$$\mathrm{Sk}\{\partial p/\partial t\} = \frac{3}{\sqrt{2}} \frac{\sum_{n=1}^{\infty}\sum_{m=1}^{\infty} J_n(n\sigma) J_m(m\sigma) J_{n+m}\big((n+m)\sigma\big)}{\left[\sum_{n=1}^{\infty} J_n^2(n\sigma)\right]^{3/2}}, \tag{2.15}$$

where $J_n(x)$ represents the *n*th Bessel Function of the first kind.

Despite its analytical form, one disadvantage of the Fubini solution is the inability to exactly express the derivative skewness of a theoretically discontinuous shock due to the infinite series. The derivative skewness is shown in Fig. 2.1 for an initially sinusoidal waveform and the discrepancy between the values obtained using the Earnshaw and Fubini solutions, with the solid black line representing the Earnshaw solution and the remaining lines representing the Fubini solution for a varying number of terms included in the sum. The Earnshaw solution approaches infinity as $\sigma \to 1$, but bandwidth limitations in the Fubini solution limit the values seen. Thus, if a theoretically discontinuous shock has formed at $\sigma = 1$ but measurement realities limit the usable bandwidth to $10^2 \cdot f$ or $10^3 \cdot f$, the maximum derivative skewness values would be approximately 10 or 30, respectively.

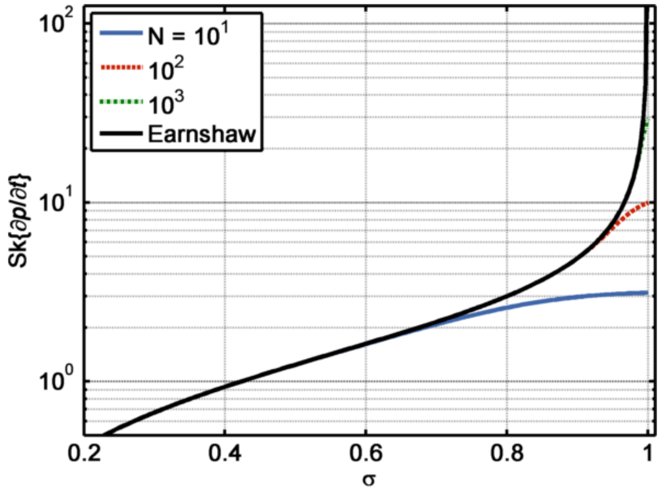

Fig. 2.1 The analytical derivative skewness of an initially sinusoidal waveform modeled by the Earnshaw solution as a function of σ along with the estimated derivative skewness of the Fubini solution for *N* terms [see Eq. (2.12)].

2.2.5 Fay Solution

For waveforms with very large amplitudes, the relative length scales of nonlinear effects are much smaller than thermoviscous absorption. For such waveforms traveling in the sawtooth regime of propagation, typically thought of as $\sigma > 3$, another solution may be found. This solution is Fay's infinite series,[5]

$$P = \frac{2}{\Gamma}\sum_{n=1}^{\infty}\frac{\sin(nt)}{\sinh(n\psi)}, \tag{2.16}$$

where $\psi = (\sigma + 1)/\Gamma$, and Γ is the Gol'dberg number, defined as $1/(\bar{x}\alpha)$, with α being the thermoviscous absorption coefficient at f_0. The Fay solution in Eq. (2.16) is valid for $\Gamma \gg 1$, signifying nonlinearity initially dominates thermoviscous losses. Similar to the Fubini solution, the time derivative of the Fay solution is a cosine series,

$$\frac{\partial P}{\partial t} = \frac{2}{\Gamma}\sum_{n=1}^{\infty}\frac{n\cos(nt)}{\sinh(n\psi)}. \tag{2.17}$$

From Eqs. (2.14) and (2.17), the derivative skewness of the Fay solution may be written as

$$\mathrm{Sk}\{\partial p/\partial t\} = \frac{3}{\sqrt{2}} \frac{\sum_{n=1}^{\infty}\sum_{m=1}^{\infty} \frac{n}{\sinh(n\psi)} \frac{m}{\sinh(m\psi)} \frac{n+m}{\sinh\left((n+m)\psi\right)}}{\left[\sum_{n=1}^{\infty} \frac{n^2}{\sinh^2(n\psi)}\right]^{3/2}}, \tag{2.18}$$

which depends, as expected, on ψ.

The derivative skewness of the Fay solution is plotted in Fig. 2.2 as a function of σ for different values of Γ. Though $N = 1000$ terms were used for all three values of Γ, the effect of including fewer terms is similar to that seen in Fig. 2.1 in that lower derivative skewness values are obtained for steepened or shock-containing waveforms. Because the effect of fewer terms has already been examined in Fig. 2.1, Fig. 2.2 instead includes multiple values of Γ. As expected, higher values of Γ have higher derivative skewness values, and lower values of Γ experience a large drop in derivative skewness values much sooner as they reach their respective old-age regimes, defined as $\sigma > \Gamma$. In the sawtooth region, for $3 < \sigma < \Gamma$, the derivative skewness drops as σ increases due to an increase in rise time in the shock, which is inversely proportional to the change in pressure over the shock.[7] It is interesting to note that a self-similar behavior is evident in the old-age regime for all three cases, as all three curves have derivative skewness values of ~1.5 at $\sigma = \Gamma$ and similar slopes when plotted on a logarithmic scale.

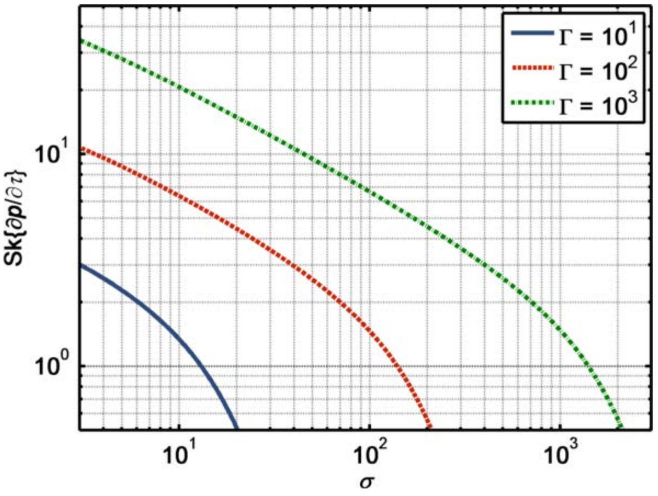

Fig. 2.2 The derivative skewness of the Fay solution as a function of σ for three values of Gol'dberg number.

2.2.6 Derivative Skewness of Acoustic Shocks

Though derivative skewness behavior differs between the Fubini and Fay solutions, it would be useful to define a rough threshold for derivative skewness, above which a wave could be considered a shock. As the waveform steepens and decays it enters and exits a region in which it is considered an acoustic shock. In most definitions of a shock, the rise time is used as the defining factor. Blackstock *et al.*[7] stated that a sinusoid remains in the sawtooth regime when the rise time, defined as the total time from the pressure minimum to the pressure maximum, is less than 20% of the period. This definition is useful but provides dissimilar results for the pre-shock and post-shock region, as the waveform shapes are significantly different. The pre-shock region contains rounded corners, while the post-shock region still maintains an N-wave shape. In an effort to accentuate the shortest rise times, Cleveland[52] and Loubeau *et al.*[53] defined rise time for impulsive signals as the time it takes for the pressure to rise from 10% to 90% of the maximum amplitude.

Because the impulsive signal definition lessens the difference between the pre and post-shock regimes, here we define a shock as occurring when the 10-90% rise time is less than 5% of the period. Waveforms for the Fubini (shock formation) and Fay (Old-age) solutions that satisfy this definition of a shock are shown in Fig. 2.3 for a portion of the period T. The derivative skewness values of the solutions are 8.9 at $\sigma = 0.96$ for the Fubini solution and 3.9 at $\sigma = 260$ for the Fay solution, providing a range of values for which acoustic shocks begin to be significant. Though an exact value cannot be set to indicate the presence of shocks, an approximate threshold of five can serve as a good approximation. Derivative skewness values below this range likely indicate that a periodic waveform does not contain shocks that fit this rise time definition, or that shock-like features are inadequately resolved due to sampling rate and noise limitations, as discussed in the following section.

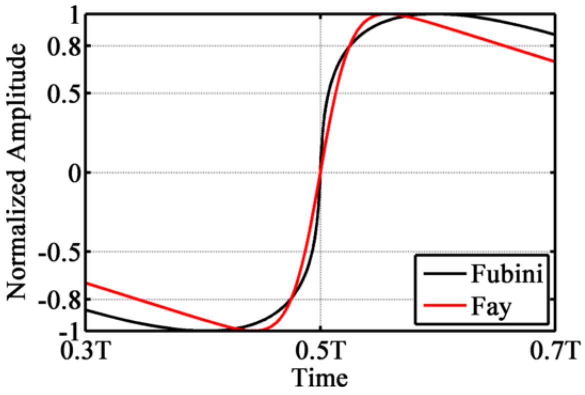

Fig. 2.3 Shock profiles for normalized Fubini (σ = 0.96) and Fay (σ = 260, Γ = 10^3) solutions with derivative skewness values of 8.9 and 3.9, respectively, shown over a section of the period *T*. See text for shock definition.

2.3 Measurement Considerations

2.3.1 Finite Sampling Rate

Defining a shock based on the duration of the rise time lends itself to the question of the importance of sampling rate. If a shock is defined such that the rise time from 10-90% is 5% of the waveform period, a sampling rate of 20 times the fundamental frequency must be used to guarantee even one point within the 5% window. However, this sampling rate is insufficient to capture the important difference in curvature between the waveforms shown in Fig. 2.3. The effects of discrete sampling on the estimate of the derivative skewness can be significant since an inaccurate measure of the derivative may be accentuated by the cubic nature of the skewness.[54]

To investigate the inaccuracies associated with a finite sampling rate for the Fubini and Fay solutions, the effect of discrete sampling on the derivative of a general Fourier sine series is shown. The general results may then be applied to the Fubini and Fay infinite series. If $f(t)$ is a Fourier sine series, written as

$$f(t) = \sum_{n=1}^{\infty} B_n \sin(nt), \tag{2.19}$$

an estimation of the first time-derivative of $f(t)$ can be obtained using a finite-difference technique. Here the series is written with B_n to be consistent with the Fubini and Fay solutions in Eq. (2.12) and Eq.(2.16), respectively. The derivatives going forward will be approximated, both analytically and numerically, using a first-order, forward-difference approximation of the first derivative. Though it is possible that a higher-order method for approximating the first derivative could produce more accurate results, it should be noted that using a central differencing method artificially lowers derivative values across a coarsely sampled shock.[54] Using a constant time step, $\Delta t = f/f_s$, the derivative of Eq. (2.19) is approximated by

$$\begin{aligned} \frac{\Delta f}{\Delta t} &= \frac{f(t+\Delta t) - f(t)}{\Delta t} \\ &= \frac{1}{\Delta t}\sum_{n=1}^{\infty} B_n \sin(nt + n\Delta t) - \frac{1}{\Delta t}\sum_{n=1}^{\infty} B_n \sin(nt) \\ &= \frac{1}{\Delta t}\sum_{n=1}^{\infty} B_n(\sin(nt + n\Delta t) - \sin(nt)). \end{aligned} \tag{2.20}$$

Using the trigonometric identity $\sin(a+b) = \sin(a)\cos(b) + \cos(a)\sin(b)$, Eq. (2.20) becomes

$$\begin{aligned}\frac{\Delta f}{\Delta t} &= \frac{1}{\Delta t}\sum_{n=1}^{\infty} B_n[\sin(nt)\cos(n\Delta t) + \cos(nt)\sin(n\Delta t) \\ &\qquad - \sin(nt)] \\ &= \sum_{n=1}^{\infty} B_n \frac{\sin(n\Delta t)}{\Delta t}\cos(nt) \\ &\qquad + \sum_{n=1}^{\infty} B_n \frac{\cos(n\Delta t) - 1}{\Delta t}\sin(nt).\end{aligned} \tag{2.21}$$

If we define

$$\begin{aligned}A_n' &= B_n \frac{\sin(n\Delta t)}{\Delta t} \\ B_n' &= B_n \frac{\cos(n\Delta t) - 1'}{\Delta t}\end{aligned} \tag{2.22}$$

then we may write (2.21) as

$$\frac{\Delta f}{\Delta t} = \sum_{n=1}^{\infty} A_n' \cos(nt) + \sum_{n=1}^{\infty} B_n' \sin(nt). \tag{2.23}$$

In the limit that $\Delta t \to 0$, we find that $A_n' \to nB_n$ and $B_n' \to 0$, which is the result obtained by assuming continuous sampling from the beginning. Thus, for a finite-sampled Fourier sine series, the first time derivative contains both sine and cosine terms. As this infinite sum involves both sine and cosine terms, we must use the skewness of a full Fourier series. Equation (2.23) is then used in conjunction with Eq. (A27) from Appendix A in Reichman *et al.*[80] to estimate the derivative skewness for the Fubini and Fay solutions while taking into account a finite sampling rate.

2.3.1.1 Fubini Solution

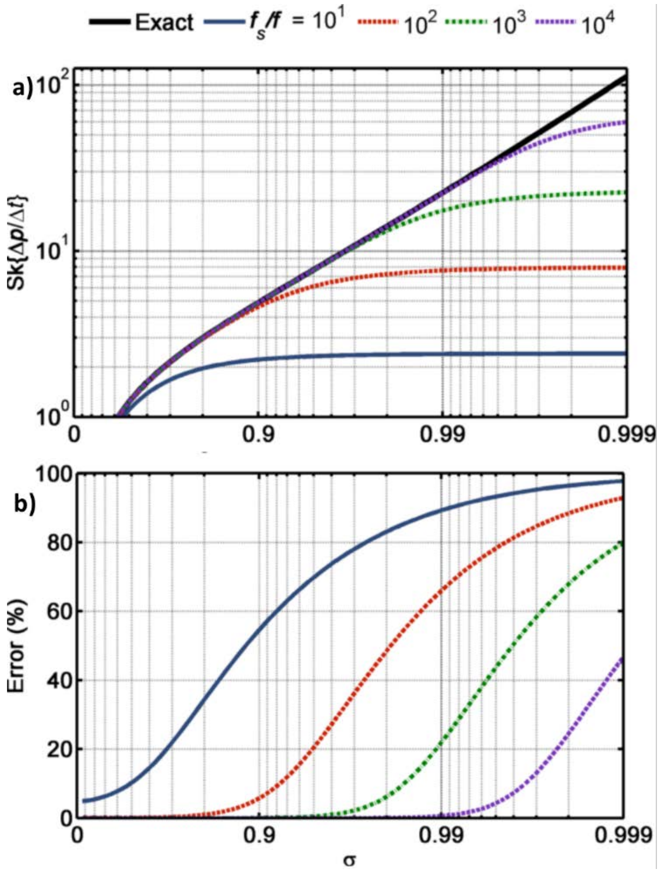

Fig. 2.4 a) Derivative skewness estimates of the Fubini solution for $f_s/f = 10^1$, 10^2, 10^3, and 10^4 along with the analytical Earnshaw calculation. For each curve, $f_s/2f$ terms were used to compute the estimates. b) Error between the Fubini estimates and the Earnshaw solution.

The effects of finite sampling rate for the Fubini solution are seen in Fig. 2.4 for various values of f_s/f, the sampling rate relative to the fundamental frequency. In Fig. 2.4a) the derivative skewness of the discretely sampled Fubini solution is plotted, while in Fig. 2.4b) the error, relative to the continuously sampled Earnshaw solution, is shown. A limiting behavior is seen as a result of the finite sampling rate. Whereas the exact solution from Eq. (2.9) continues to increase on the logarithmic scale, going to infinity as $\sigma \rightarrow 1$, the discretely sampled derivative skewness estimates in Fig. 2.4 begin to approach respective maximum values. These values are less than the theoretical maximum for a given f_s/f because of the curved shock profile in the preshock region. For greater f_s/f, shorter rise times can be resolved, resulting in larger derivative skewness estimates. The divergent nature of the exact derivative skewness suggests that a derivative skewness estimate with any reasonable sampling rate ceases to approximate the actual value for σ sufficiently close to one. The point at which the discretely sampled estimate begins to underestimate the exact value depends on f_s/f. For example, the derivative skewness obtained using $f_s/f = 10$ diverges from the continuously sampled result above $Sk\{\partial p/\partial t\} = 1$. When $f_s/f = 100$, an accurate estimate is obtained until $\mathrm{Sk}\{\partial p/\partial t\} = 5$, and for $f_s/f = 1000$ values of $\mathrm{Sk}\{\partial p/\partial t\}$ up to 12 can be accurately estimated.

2.3.1.2 Fay Solution

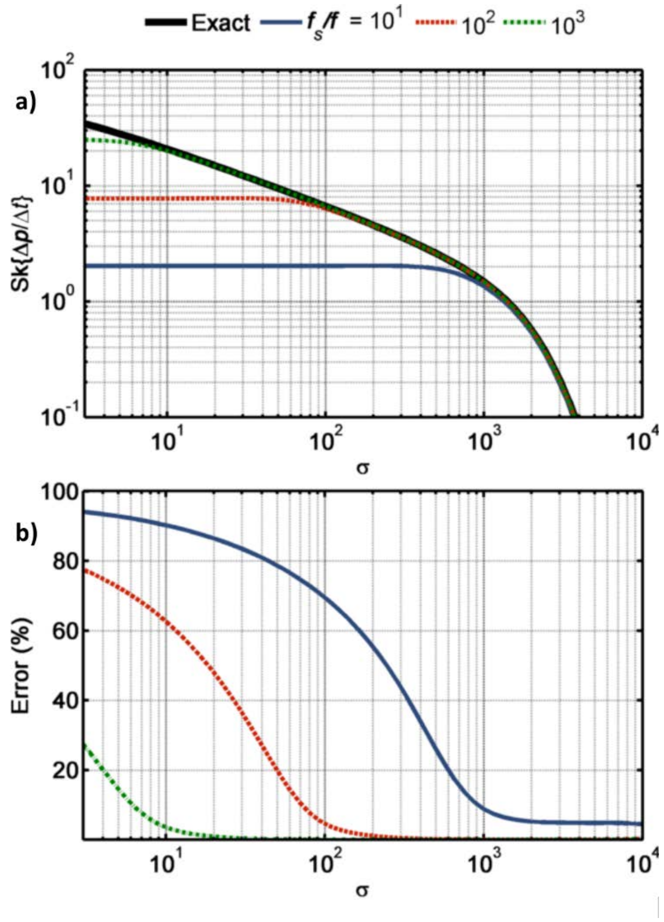

Fig. 2.5 Estimates of the derivative skewness for the Fay solution as a function of σ and f_s/f = 10^1, 10^2, 10^3, and 104, with a Gol'dberg number of 1000. To calculate the estimates, $(f_s/f)/2$ terms were used. The exact derivative skewness derived from continuous sampling is plotted for comparison.

The derivative skewness estimates of the Fay solution, shown in Fig. 2.5, show similar results to the derivative skewness estimates based on the Fubini solution. A limiting behavior is again dependent on the sampling rate relative to the fundamental frequency. However, as was discussed previously, the Fay solution has an N-wave shape and a more consistent slope than the Fubini solution, thus a lower sampling rate is required to achieve the same amount of accuracy. For example, for the $f_s/f = 100$ curve in Fig. 2.4, the derivative skewness begins to diverge at a value of 5, whereas in Fig. 2.5 the curve is accurate for derivative skewness values less than 7. As the wave enters the old-age regime, where $\sigma > \Gamma$, the shocks have decayed sufficiently that the derivative skewness values agree, even for very low relative sampling rates.

The effects of sampling rate have been identified in situations other than sinusoidal plane waves. Gee *et al.*[17] downsampled measured noise waveforms from a fighter jet aircraft and found that by slightly decreasing sampling rate, derivative skewness values decreased accordingly. Insufficient sampling rate possibly explains relatively low derivative skewness values observed in laboratory-scale jet data despite the presence of acoustic shocks.[11,39]

2.3.1.3 Recommended Sampling Rates

Though a finite sampling rate will always underestimate a theoretically discontinuous shock, an adequate sampling rate may accurately calculate derivative skewness values up to a certain threshold, so as to indicate shock formation. The Fubini solution is classified as containing a shock at $\sigma = 0.96$, with a corresponding derivative skewness values of 8.9. If this waveform is sampled at $f_s/f = 100$, there is a 28% error at this distance [see Fig. 2.4(b)]. The Fay waveform for $\Gamma = 1000$ decays to the point of no longer being a shock at $\sigma = 260$ with a derivative skewness of 3.9. At this point, $f_s/f = 10$ underestimates the derivative skewness by nearly 50%, but $f_s/f = 100$ has negligible errors [see Fig. 5(b)]. Therefore, a minimum sampling rate of $f_s/f = 100$ is recommended to accurately estimate the derivative skewness during shock formation and decay. Using this sampling rate, derivative skewness values up to five will be accurately estimated for the sinusoidal case. Greater values, up to a theoretical maximum of 9.8, may be estimated using this sampling rate, but they may underestimate the actual shock steepness. Higher sampling rates provide additional shock detail and therefore accurate $\text{Sk}\{\partial p/\partial t\}$ estimates for steeper shocks, but a minimum sampling rate of $f_s/f = 100$ is sufficient to obtain Sk$\{\partial p/\partial t\} > 5$ as an approximate threshold for the presence of acoustic shocks in the waveform.

2.3.2 Signal-to-Noise Ratio

Additive noise can also impact derivative skewness values. Though such noise occurs in different ways, each with its own characteristics and statistics, investigation into the effects of additive, Gaussian noise on derivative skewness are illustrative of the robustness of this metric. Two cases are considered: first, the case of a steepened waveform in the pre-shock region at $\sigma = 0.75$, and second, a wave in the sawtooth region, at $\sigma = 30$ and $\Gamma = 1000$.

The waveforms are calculated at each distance using the Fubini and Fay solutions, respectively, following which band-passed Gaussian noise is added to the waveform at various signal-to-noise ratios (SNR), defined as $\mathrm{SNR} = 20\log_{10}\left(\frac{p_{\mathrm{rms}}}{\mathrm{noise}_{\mathrm{rms}}}\right)$, where p_{rms} is the root-mean-square of the signal and $\mathrm{noise}_{\mathrm{rms}}$ is the root mean square of the noise. In order to avoid artifacts associated with filtering at a high sampling rate, a fourth-order Butterworth filter is used, with a center frequency of f_M and low and high cutoff frequencies of $f_L = f_M/1.41$ and $f_H = 1.41f_M$. The effect of additive noise for the steepened waveform at $\sigma = 0.75$ is displayed in Fig. 2.6a), where the derivative skewness value of the original waveform is 2.51, for $f < f_M < 50f$, where f is the fundamental frequency of the sinusoid, and $0 < \mathrm{SNR} < 50$ dB. As would be expected, a higher SNR results in a derivative skewness calculation closer to the actual value. Additive noise introduces additional variations that mask the presence of the steepened waveform resulting in lower values of $Sk\{\partial p/\partial t\}$. In addition, higher frequency noise has a greater effect than low-frequency noise on the accuracy of the derivative skewness. For $f_M = f$, a SNR of approximately 3 dB results in a measured value that is half the original derivative skewness. In contrast, the same reduction is seen at $f_M = 10f$ for SNR $\cong$ 20 dB. Higher frequency noise introduces larger amplitude derivative values, both positive and negative, than low-frequency noise of the same amplitude. These large-amplitude values are more likely to mask the larger derivative values of shocks in the expectation values used to calculate skewness. Because these expectation values are performed on a cubed quantity, the derivative skewness is likely to be less sensitive to the presence of additive noise than a metric such as the ASF,[50] where the linear average of $\partial p/\partial t$ is taken. In summary, care must be taken to maximize SNR when inspecting the derivative skewness of a waveform, as even small noise sources may artificially lower the derivative skewness values for high-frequency noise.

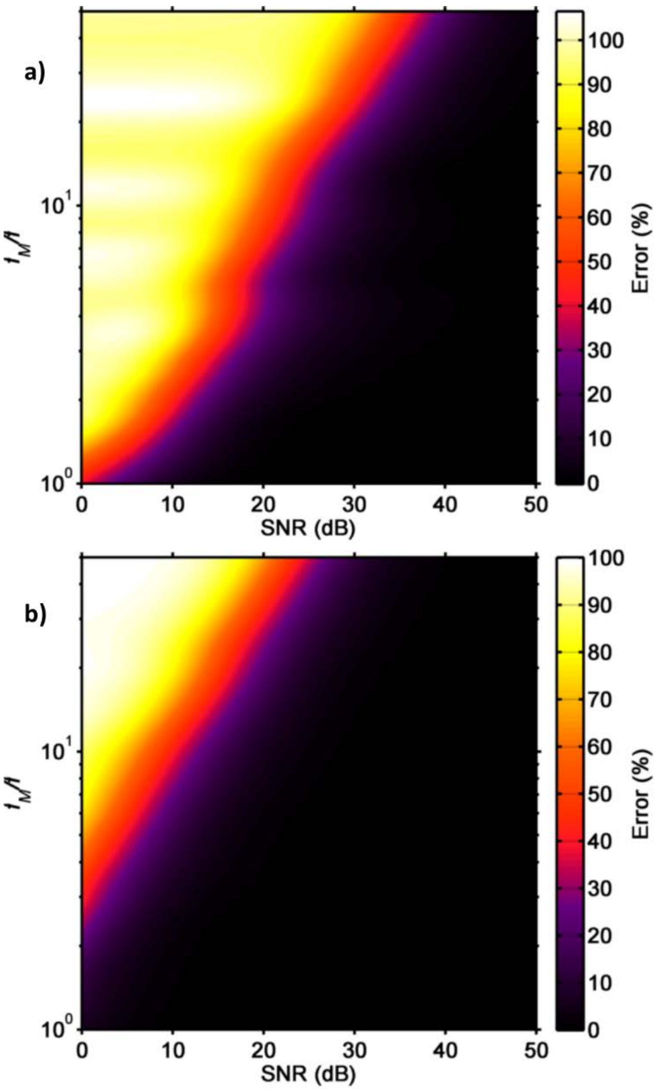

Fig. 2.6 Derivative skewness error for an initial sinusoid propagated to a distance of a) σ = 0.75 and b) σ = 30 for Γ = 1000 with band-passed noise added to the signal at various SNR. The calculated derivative skewness with infinite SNR are a) 2.51 and b) 12.23.

The results in Fig. 2.6b) are similar to those of Fig. 2.6a) but for a waveform in the sawtooth region at $\sigma = 30$. Because a shock is present in the waveform, the calculated derivative skewness is markedly higher, 12.23, and less likely to be masked in the derivative skewness by the presence of noise. In contrast with the Fubini solutions, at $f_M = 10f$ the presence of noise lowers the derivative skewness to half of the original value at SNR $\cong 7.5$. Despite the resilience of the derivative skewness when shocks are present in the waveform, it is of note that high-frequency noise can still have a noticeable effect on calculated values, even with a high SNR.

2.4 Applications

2.4.1 Numerical Case Study

Though the above results give an understanding of the behavior of derivative skewness in the shock formation, sawtooth, and old-age regimes, it is useful to have a complete grasp of the trends observed throughout the entire process. In order to do this, $Sk\{\partial p/\partial t\}$ for the spatial region between the preshock and sawtooth regimes must be calculated. Blackstock[6] presented a solution to the Burgers equation that served as a bridge between the Fubini and Fay solutions. By comparing amplitudes of the fundamental frequency as a function of σ he showed that for $\sigma > 3.6$, the difference between the "Blackstock bridging function" and the Fay solution was less than 2%.

Although an analytical representation of the derivative skewness of the Blackstock bridging function has not been found, the derivative skewness throughout the entire formation and decay of shock waves can be found using a numerical waveform propagation algorithm. The derivative skewness from the propagated waveform can be compared with the Earnshaw and Fay solutions in their regions of validity and give a complete view of $Sk\{\partial p/\partial t\}$ during shock formation and decay. For the purposes of this chapter, a propagation scheme based on the generalized Burgers equation was used which has been shown to closely follow the behavior of the Fubini and Fay solutions.[30] Sinusoids with Gol'dberg numbers ranging from $\Gamma = 0.1$ to $\Gamma = 10^4$ are numerically propagated, and their derivative skewness is compared with results obtained using the analytical solutions described earlier. In order to provide a situation similar to experimental data considered later, a 1500 Hz initially sinusoidal waveform was sampled at 204,800 Hz, giving $f_s/f = 136.5$.

This sampling rate suggests a maximum derivative skewness estimate of ~ 11.6 (see Appendix B of Reichman *et al.*[80]) for the initially sinusoidal signal. The amplitude of the initial sinusoid was varied to correspond to values of Γ ranging from 0.1 to 10,000. Although the waveform has a fundamental frequency of 1500 Hz, due to the nondimensional nature of the analysis and the assumption of thermoviscous absorption, the results show little variation with changing fundamental frequency for constant Γ and relative sampling rates.

The comparison of numerical and analytical derivative skewness values is shown in Fig. 2.7, with numerical predictions plotted as dashed lines and the analytical solutions plotted as solid lines. The Earnshaw solution is plotted for $\sigma < 1$ and the Fay for $\sigma > 3$. Values of Γ range from 10^{-1} to 10^{4}, but the Fay solution is not plotted for $\Gamma = 10^{-1}$ and 10^{0} because it is only valid for $\Gamma \gg 1$. The behavior seen using the numerical propagation of these waveforms conforms with expectations. A slight steepening of the waveform occurs, evidenced by the increase in derivative skewness, but the low initial waveform amplitude results in only minimal steepening, and absorption results in no shock formation. Both solutions diverge quickly from the Earnshaw solution as absorption dominates, but the curve for $\Gamma = 10^{0}$ reaches a much higher value than the curve for $\Gamma = 10^{-1}$. The curves for $\Gamma = 10^{1}$ and 10^{2} also show increased derivative skewness, with derivative skewness continuing to increase past $\sigma = 1$, peaking near $\sigma = \pi/2$, the theoretical location of the shock maximum amplitude. Differences seen between the numerical and analytical results are in large part due to two different effects. First, the Fay solution cannot be treated as exact for small values of σ or Γ. Second, slight error is introduced in the numerical propagation scheme due to the limited sampling rate and inability to fully characterize the acoustic shock. From past work,[52] it is recommended that 10-12 samples occur within the rise of the shock for numerical propagation, which is not achieved with the current sampling rate. The errors seen are very slight in the waveform itself, but slight changes in the waveform have a large impact on derivative values and thus $Sk\{\partial p/\partial t\}$. Increasing the sampling rate by a factor of 10 dramatically improves results for $\Gamma = 10^2$. In Fig. 2.7, there is an error of 35.1% between the numerical and analytical solutions for the $\Gamma = 10^2$ curves at $\sigma = 3$. If the sampling rate is increased by a factor of 10, this error drops to 4.6%. The numerical absorption due to the limited sampling rate is different than the maximum derivative skewness value plateau that is seen for both the $\Gamma = 10^3$ and 10^4 curves. The numerical and analytical curves for $\Gamma = 10^3$ both reach the maximum derivative skewness value defined by the sampling rate, but the numerical curve begins to decrease slightly before the analytical curve due to this numerical absorption. Though these issues are something that must be taken into account when numerically propagating shock-containing waveforms, the numerical propagation confirms the analytical results for both the Earnshaw and Fay solutions and serves as a bridge between them.

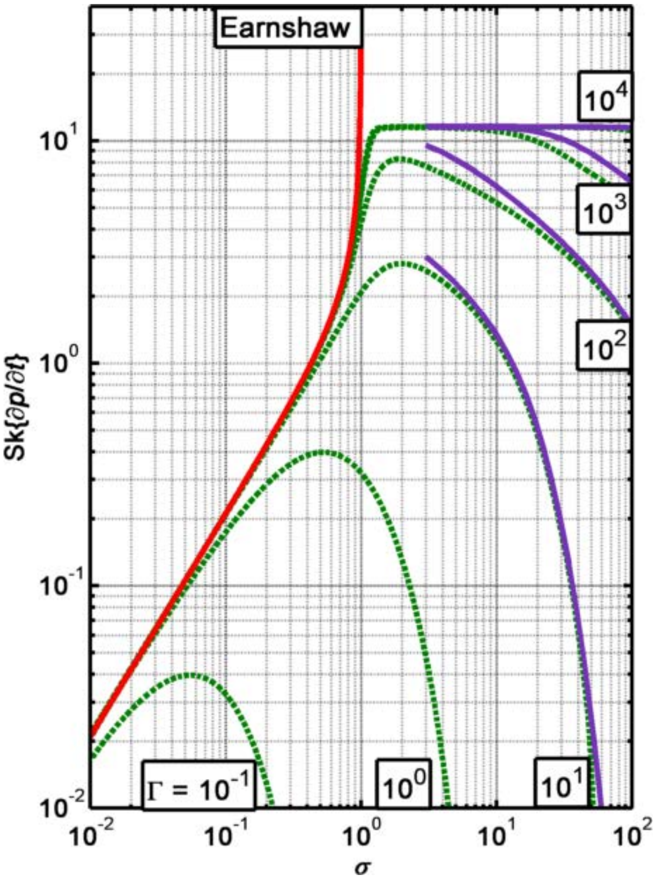

Fig. 2.7 Derivative skewness of numerically propagated initial sinusoids with varying Gol'dberg numbers. The Earnshaw and Fay solutions are shown as solid lines, and the numerical predictions are shown in a dashed line.

As an example of the sensitivity of the derivative skewness to changes in the waveform, example analytical and numerical waveforms are presented in Fig. 2.8a) for $\Gamma = 10^2$ and $\sigma = 3$. The waveforms themselves are very similar, but a very slight change in amplitude and a rounding of the edges of the shock is observed. These changes are more evident in Fig. 2.8b), which shows the derivative of the waveforms in Fig. 2.8a). The small changes in the waveforms result in larger changes in the derivative, which in turn has a large effect on the derivative skewness. The derivative skewness of the Fay solution shown is 9.53, while the numerically propagated signal has a derivative skewness of 6.18, giving an error of 35.1%. Because a small change in the waveform can have such a significant effect on derivative skewness, it is important that sampling rates be considered when numerically propagating shock-containing signals with the goal of calculating the derivative skewness.

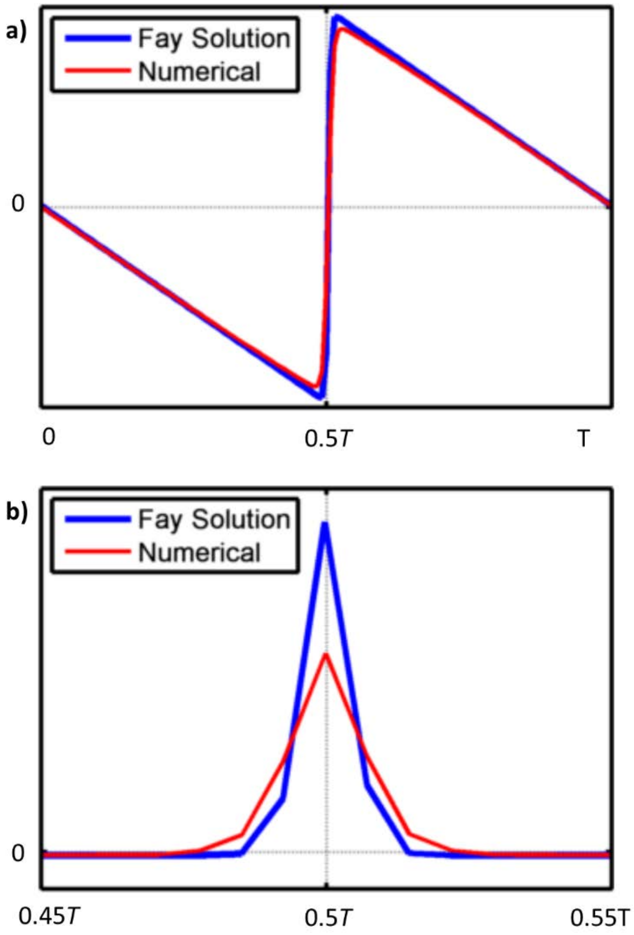

Fig. 2.8 a) Numerically propagated waveform compared with the Fay solution. b) The derivatives of the waveforms in part a). Small changes in the waveforms result in large derivative changes, which in turn result in large changes in the derivative skewness.

2.4.2 Plane Wave Tube

2.4.2.1 Initially sinusoidal signal

In addition to numerical confirmation of the analytical results, the results also have been compared against experimental data. These data were obtained through use of a plane wave tube, constructed from sections of PVC pipe, each 3.05 m (10.0 ft) long with a 2.54 cm (1.0 in) radius.

A BMS 4590 coaxial compression driver was used to excite the tube and the tube was terminated anechoically with a wedge of fiberglass insulation. Five G.R.A.S. 40DD 3.18 mm (1/8 in) microphones were mounted without gridcaps in holes drilled in the tube at distances of 0.4, 2.6, 5.6, 8.6, and 11.7 m from the driver. The microphones were flush mounted with the wall so they did not protrude and disturb the sound field. The driver was excited by a 1500 Hz signal such that the amplitude at the 0.4 m microphone was $p_0 = 547$ Pa, giving $p_{\mathrm{rms}} = 387$ Pa. This gives a lossless shock formation distance of 7.9 m, meaning that the farthest microphone is located at approximately $\sigma = 1.48$. The waveforms recorded were sampled at 204.8 kHz for approximately 6 seconds, giving $f_s/f = 136.5$, which puts the maximum derivative skewness for sawtooth waveforms at approximately 11.6. Derivative skewness values from the five waveform measurements have been calculated and compared with those predicted by numerically propagating the waveform measured at 0.4 m.

The waveforms from this experiment have been shown already by Muhlestein *et al*.[50] The figures in Ref. [50] show that the waveform steepens and forms a shock as it progresses down the tube. However, as shock waves form, a higher-frequency jitter can be observed in the waveforms, likely due to scattering of high harmonics by slight discontinuities at tube junctions. Nevertheless, the measured derivative skewness values agree well with estimates obtained through numerical propagation, as shown in Fig. 2.9. In the context of the SNR analysis above, the jitter is not of a sufficiently high frequency or amplitude to have a noticeable effect on the derivative skewness.

The close agreement between derivative skeness values seen in Fig. 2.9 is not seen in for ASF in Ref. [50]. The ASF, the ratio of the average positive derivatives to negative derivatives in the waveform and the inverse of Gallagher and McLaughlin's wave steepening factor,[55] is less sensitive to the effect of one large derivative value. The linear average causes a greater sensitivity to noise, which is seen in the form of jitter in the waveforms from Ref. [50], and causes the ASF to be underestimated. On the other hand, the cubic nature of derivative skewness suggests that although $Sk\{\partial p/\partial t\}$ can be affected by the presence of noise, its emphasis on large derivative values makes it less sensitive to noise than the ASF.

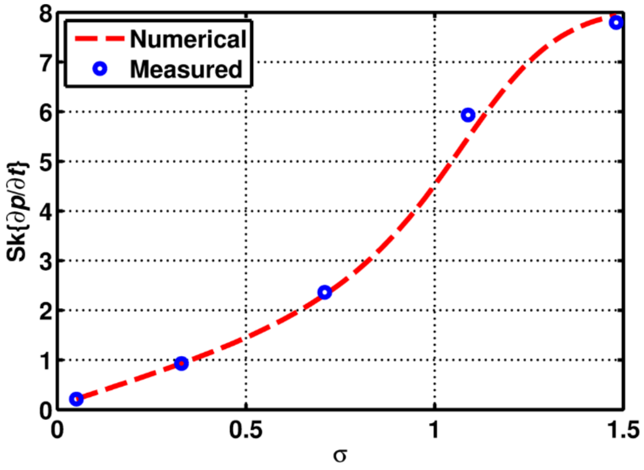

Fig. 2.9 Comparison of derivative skewness values from measured waveforms in a plane wave tube with those of numerically propagated waveforms.

2.4.2.2 Broadband noise

Though the case of an initially sinusoidal wave provides significant physical insight, of broader interest is the propagation of noise. Although the different natures and PDFs of broadband noise and sinusoids prevent an immediate quantitative comparison of derivative skewness values, insights may still be gained by comparing trends. Because of the presence of larger outliers in noise, we expect noise signals to form shocks on a smaller length scale and reach greater derivative skewness values.[49] Using the same experimental setup as in the sinusoidal case, white noise was passed through a band-pass filter (700-2300 Hz) and propagated down the tube. Because of the broadband nature of the noise, the definition of $\bar{x}$ used earlier for sinusoids in Eq. (2.5) is no longer valid. Instead, we define a nonlinear distortion length similar to that of Gurbatov and Rudenko,[56]

$$\bar{x}_N = \frac{\rho c^3}{\beta(2\pi f_c)\left(\sqrt{2}p_{\mathrm{rms}}\right)}, \tag{2.24}$$

where f_c is the characteristic frequency of the noise. While this characteristic frequency works well for a band-passed signal, other definitions may have to be used when there is no clearly defined peak frequency. Here, the $\sqrt{2}$ is included so that as the noise bandwidth approaches zero, the sinusoid shock formation distance in Eq. (2.5) is recovered. In order to differentiate between the noise and sinusoidal cases, the normalized distance is now referred to as $\sigma_N = x/\bar{x}_N$.

As an example of broadband noise propagation, noise waveforms with $f_c = 1500$ Hz and $p_{\mathrm{rms}} = 286$ Pa at $x = 0.4$ m were measured. For this case, these input conditions yield $\bar{x}_N = 9.0$ m, a slightly greater distance than the shock formation distance of the sinusoidal signal. Short waveform segments measured at 0.4 m and 11.7 m are shown in Fig. 2.10 along with the prediction made by numerically propagating the measured waveform at 0.4 m to 11.7 m. In Fig. 2.10b), a similar waveform jitter is present in the 11.7 m ($\sigma = 1.31$) waveform. However, by comparing Fig. 2.10b) and Fig. 2.10c), it can be seen that the waveforms match well aside from the previously described jitter.

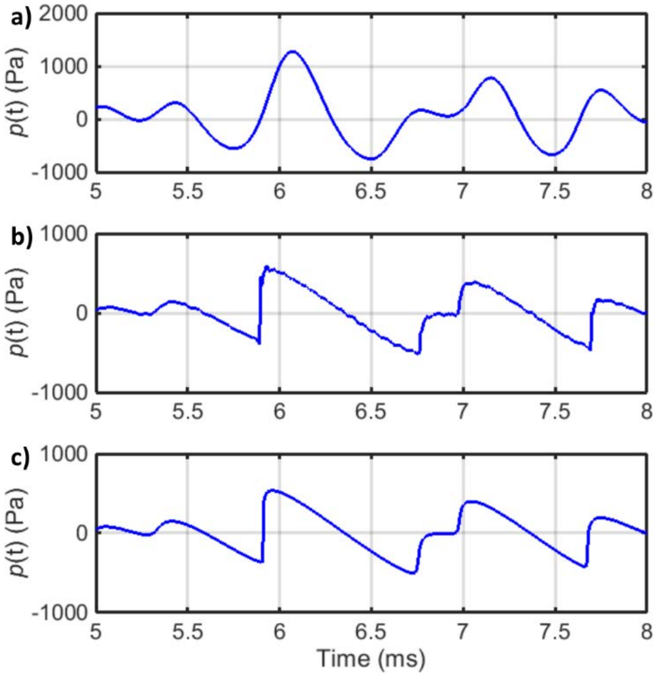

Fig. 2.10 Measured noise waveforms at a) 0.4 m and b) 11.7 m, and c) the numerically predicted waveform at 11.7 m.

To more closely examine the spectral effects, Fig. 2.11 shows the power spectral densities associated with the three waveforms in Fig. 2.10. As the waveform propagates down the tube, wave steepening results in increases in level above the original cut-off frequency, and difference-frequency generation and possible wave coalescence increase the level below.[31] The spectra of the predicted and measured waveforms at 11.7 m are very similar, aside from the 10-35 kHz noise that is 30 dB down from the spectral peak and is the frequency-domain manifestation of the waveform jitter.

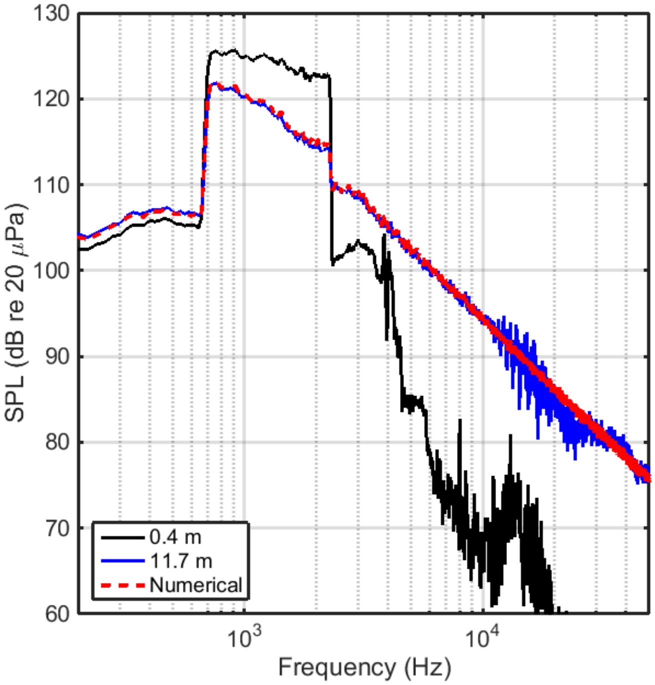

Fig. 2.11 Spectra calculated from the three waveforms, segments of which were shown in Fig. 2.10. In the 11.7 m measured spectrum, high-frequency noise is present from 10-35 kHz.

For the noise case, the waveform jitter is of sufficiently high frequency and amplitude to have a measureable difference in the derivative skewness. The measured and predicted derivative skewness values for waves of two initial amplitudes are shown in Fig. 2.12, the first with $p_{\mathrm{rms}} = 200$ Pa (140 dB re 20 μPa) and $p_{\mathrm{rms}} = 286$ Pa (143 dB re 20 μPa) for the second. These two cases in particular were chosen because for all amplitudes of 200 Pa and below the ringing noise was present, but the SNR was great enough to have a minimal effect on derivative skewness, and for all amplitudes 286 Pa and above the ringing had a noticeable effect. There are a few features of note in Fig. 2.12. First, $\mathrm{Sk}\{\partial p/\partial t\}$ reaches a higher value for the broadband noise than is possible in the sinusoidal case for the given sampling rate, as seen by comparing with Fig. 2.9. This corresponds with the initial experiment-based findings of Muhlestein *et al.*[50] Second, the derivative skewness has reached its highest value and is beginning to decrease by $\sigma_N = 1$, suggesting that the decay of shock waves is already occurring. This is likely because the definition used for $\bar{x}_N$ overestimates the actual distortion length.[49] Because broadband noise has a different PDF than sinusoidal noise, there are more outliers in terms of pressure, which are then more likely to form shocks earlier in the propagation than a sinusoid. Third, the ASF is steadily increasing throughout this range of σ, indicating that wave steepening is an ongoing process, even though the derivative skewness is decreasing. The largest shocks have already formed and started to decay, but the wave as a whole is still becoming more steepened. Fourth, for the higher amplitude case the measured derivative skewness values are markedly lower than predicted for higher values of σ_N, when shocks are likely well formed. This lower value is due to the presence of high-frequency jitter, as in the case of the sinusoidal signal. However, because the jitter is of a sufficiently high frequency and amplitude for the 286 Pa case, it creates a noticeable difference between the predicted and measured values. In contrast, the SNR is 3-5 dB higher in the low-amplitude case. In Fig. 2.6a) there is a region where a 5 dB decrease in SNR results in a substantially lower SNR, and we see similar behavior here. While Sk$\{\partial p/\partial t\}$ from both numerical and measured data agree for the lower case, a 5 dB decrease in SNR results in substantially underestimating the derivative skewness values for the high-amplitude case. Ultimately, although Sk$\{\partial p/\partial t\}$ is relatively robust to the presence of noise in the signal, high-frequency noise may still significantly alter measured values.

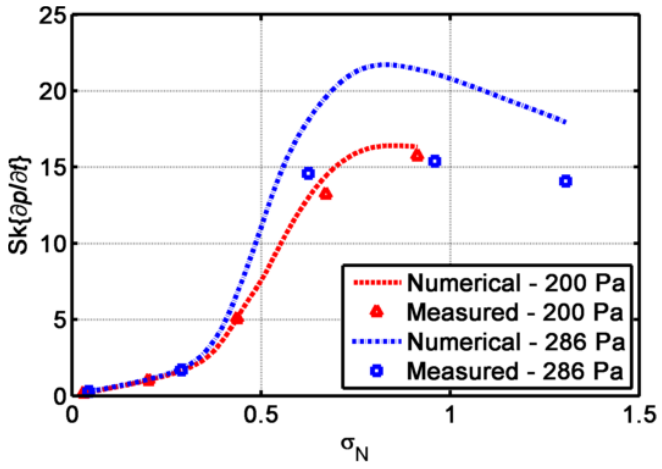

Fig. 2.12 Predicted (dashed) and measured (dots) values of the derivative skewness as a function of $\sigma_N = x/\bar{x}_N$. Values shown are for p_{rms} = 286 Pa and 200 Pa. Both cases share similar growth initially, then different behavior with increasing σ.

In the earlier discussion of sampling rates, it was suggested that $f_s/f > 100$ in order to calculate accurate derivative skewness values of at least five for sinusoidal signals. The shock content of the propagating noise waveforms provides a test for this recommendation, though this analysis is limited in scope as the noise considered is not representative of all types of noise. There are many algorithms to identify shocks in a waveform (see Ref. [16] for a recent example); here, a shock is identified as a derivative value exceeding 20 waveform derivative standard deviations to include only the largest outliers. The number of shocks matching this criterion within a 6 sec. waveform is displayed for each of the microphones in Table 2.1. The 0.4 and 2.6 m microphones have essentially no shock content for both cases, and low derivative skewness values of 0.17 and 1.01. However, differences are seen at 5.6 m. For the 200 Pa case in Fig. 2.12, shocks have begun forming and $\mathrm{Sk}\{\partial p/\partial t\} = 5.05$ and is still increasing. There are shocks present in the waveform, but fewer than at 8.6 and 11.7 m. This helps illustrate that for $\mathrm{Sk}\{\partial p/\partial t\} \geq 5$, significant shocks have formed in this waveform, providing support for a derivative skewness threshold and associated sampling requirements. These conclusions also draw support from the 286 Pa case.

Minimal shocks seen at 0.4 and 2.6 m result in derivative skewness values of 0.27 and 1.69 respectively. However, as the number of shocks greatly increases, Sk$\{\partial p/\partial t\}$ rises accordingly. While these particular cases corroborate the threshold used in sinusoidal analysis, the results are not general and therefore additional research is needed to understand the evolution of derivative skewness values in the context of random noise.

Table 2.1. The number of shocks present in two waveforms of different amplitudes, calculated from the waveforms measured at each of the five microphones. For this table a shock has been defined as a derivative exceeding 20 standard deviations of the waveform derivative.

	Mic Locations	0.4 m	2.6 m	5.6 m	8.6 m	11.7 m
200 Pa	σ_N	0.031	0.203	0.437	0.671	0.913
	Derivative Skewness	0.17	1.01	5.05	13.2	15.7
	Number of Shocks	0	0	61	305	452
286 Pa	σ_N	0.045	0.290	0.625	0.960	1.31
	Derivative Skewness	0.27	1.69	14.6	15.4	14.1
	Number of Shocks	0	3	354	664	605

2.5 Conclusions

In this chapter, quantitative and physical insights into the evolution of the skewness of the first time difference of a nonlinearly evolving pressure waveform, i.e. the derivative skewness, have been obtained using analytical, numerical, and experimental methods. Analytical forms of the changing derivative skewness have been found for the Earnshaw, Fubini, and Fay solutions. The solutions reveal a sharp increase in the derivative skewness near the shock formation distance, a gradual decrease in the sawtooth region, and a more rapid decrease in the old-age region as the waveform unsteepens. Numerical studies confirm these trends and show that the derivative skewness reaches its maximum between the preshock and sawtooth regions. The effects of additive noise and reduced waveform sampling rate have been investigated; both tend to reduce estimated derivative skewness values. In comparing derivative skewness values for random noise with those of sinusoidal signals, noise will reach greater derivative skewness values over a relatively shorter distance.

The investigation has included practical considerations for nonlinear acoustic signal analysis using the derivative skewness. For sinusoids, in order to observe large derivative skewness values that occur as shocks form, a sampling rate of at least 100 times the fundamental frequency should be used. Larger sampling rates result in more accurate estimates, provided that the measurement bandwidth is commensurate with the greater sampling rate. The recommended minimum scaled sampling rate allows derivative skewness values of at least five to be estimated, which is sufficient to serve as an approximate threshold indicating that a shock is present. The preliminary experimental investigation with noise shows that a similar threshold can also indicate shock formation, though more investigation is needed. These recommendations may provide guidelines for future experiments and allow prior experiments to be more quantitatively interpreted.

Chapter 3

Acoustic shock formation in noise propagation during ground run-up operations of military aircraft

3.1 Introduction

One of the distinctive features visible in waveforms of supersonic jet noise is the presence of acoustic shocks or large sudden increases in pressure. These shocks are often associated with the auditory phenomenon called crackle[16,62] and thus serve as an additional source of annoyance within jet noise. The nature of these shocks and their evolution in the noise field is dependent on their physical properties and origins. Steepened waveforms exist near the source,[16,17] but it has also been shown that waveforms from full-scale aircraft continue to steepen and form shocks further away from the source due to nonlinear propagation.[63,69] One of the first indications that nonlinear propagation played a role in far-field effects was a lack of atmospheric absorption in the far field noticed by Pernet and Payne[2] and later by Morfey and Howell.[21] The steepening of waveforms and formation of shocks was also shown by Blackstock[18] to increase at locations further away from the jet noise source though his analysis did not incorporate atmospheric absorption. The presence of acoustic shocks in jet noise led to efforts to quantify waveform steepening, shock content, and crackle. One of the first attempts was performed by Ffowcs Williams *et al.*[10] and was based on the statistical measure of skewness of the pressure waveform distribution. Ffowcs Williams *et al.* defined a distinctly crackling waveform as having a skewness above 0.4. Since shocks may exist without affecting the skewness of the pressure waveform, defining crackle based on the skewness of the waveform leads to an insufficient definition.[17] Nevertheless, skewness-based criteria continue to be used. A better quantification of waveform steepening and shock content is needed as the ability to quantify the steepened nature of jet noise waveforms enables a correct comparison of these important characteristics between measurement locations, across engine conditions, and among different experimental datasets.

Recent work in quantifying the steepening of a waveform has concentrated on the presence of large derivative values associated with shocks.[13,80] These efforts often rely on metrics calculated from the waveforms. Such metrics may evaluate the time-domain[12] or frequency-domain[21] characteristics of the waveform, and have been applied to full-scale[17] and laboratory-scale[11,57] data. However, one of the issues that arises from the use of metrics is their interpretation. In many cases it is difficult to tell at what point a waveform has steepened sufficiently to qualify as a shock and when it has unsteepened enough to no longer be considered a shock. In addition, the numerical values associated with some metrics have been criticized as having little physical meaning, making it difficult to interpret results and compare between experiments.

Understanding these waveform steepening metrics has been enhanced recently by theoretical and experimental analyses. In model-scale work, Baars *et al.*[16] have shown values for various metrics in the near-field of model-scale supersonic jet noise in an attempt to locate the source of the shock-like behavior. Others, including Muhlestein *et al.*[13] and Reichman *et al.*[80], have tried to quantify the connection between shock content and metrics through analytical derivations involving nonlinearly propagating initially sinusoidal signals. This recent work not only helps provide context to values seen when comparing metrics, but also points to possible issues when comparing experiments, e.g., relative sampling rates and extraneous noise characteristics.

Investigation into the shock-related metrics continues in this chapter with an application to full-scale military aircraft noise measured over a large aperture. Time waveforms, associated spectra, and a wavelet analysis show steepening in waveforms continues as distance from the source increases. Metrics to be calculated and compared include the skewness of the first time-derivative of the pressure waveform, the average steepening factor (ASF), and a new wavelet-based metric called the shock energy fraction (SEF). This represents the first time the SEF wavelet analysis has been applied to military jet noise measurements. In addition, these analyses represent the first time a connection has been made between noise measured over such a large propagation distance—from geometric near field to the far field of a military aircraft. These analyses show that the noise features in the far field of the F-35 are primarily formed through nonlinear propagation.

3.2 Metrics indicative of nonlinear propagation

It is difficult to define where nonlinear propagation and shock formation occur because of the broadband, complex nature of jet noise. As such, attempts to quantify the strength of shocks within jet noise have often concentrated on nonlinearity metrics, single values expressing the shock content of a waveform. Nonlinearity metrics considered in this chapter are the time-domain metrics of derivative skewness, ASF, and SEF, a new wavelet-based metric.

3.2.1 Derivative Skewness

The skewness of the distribution of the first time derivative of the pressure waveform (estimated via finite difference) is a statistical measure that assesses the overall steepness of a waveform. Nonzero skewness values, generally, express an asymmetry in a distribution. The large derivative values associated with acoustic shocks result in a derivative distribution in which there are many slightly negative values with relatively fewer, but significantly larger positive values.

This type of distribution has a large, positive derivative skewness indicative of steepened waveforms. A positive derivative skewness has been used to show the presence of shocks in both model-scale[11,16] and full-scale[30] analyses.

An advantage of this metric, $\mathrm{Sk}\{\partial p/\partial t\}$, is that it is dependent only on the waveform shape and independent of an arbitrary definition of a shock, but it has notable disadvantages as well. First, the large positive derivative values may be underestimated if the sampling rate is not adequate, meaning low sampling rates may cause the derivative skewness values to be severely underestimated.[17,80] Second, a quantitative interpretation of derivative skewness values has proven difficult. Recent analytical work has shown the derivative skewness values for initially sinusoidal signals as the waveform steepens and unsteepens.[17] Using a criterion for classifying shocks based on the rise time of the steepened sinusoid, a wave in the pre-shock region can be considered shock-like at a derivative skewness of 8.9, while a waveform in the post-shock region thickens and is no longer classified as shock-like at a derivative skewness of 3.9. Other examples within jet noise confirm that $\mathrm{Sk}\{\partial p/\partial t\} \sim 5$ can signify the presence of shocks.[80] As such, this value of $\mathrm{Sk}\{\partial p/\partial t\} \geq 5$ will serve as a threshold to indicate significant waveform steepening and shock content, provided that the sampling frequency exceeds the characteristic frequency in the waveform by a factor of at least 100.

3.2.2 ASF

Another time-domain metric that has been used to quantify waveform steepening is the average steepening factor (ASF), defined as the average value of positive derivatives divided by the average value of negative derivatives. This quantity was originally defined as the inverse, the waveform steepening factor $\mathrm{WSF} = 1/\mathrm{ASF}$. A recent paper by Muhlestein *et al.*[13] derives analytical expressions for ASF for high-amplitude, initially sinusoidal signals, and additionally shows values for nonlinearly propagating noise in a plane-wave environment. A non-steepened waveform would have $\mathrm{ASF} = 1$, while steepened waveforms have higher values. Because the ASF is a linear mean of derivative values it represents trends within the entire waveform more than the derivative skewness, which accentuates the large positive outliers. However, the ASF is also more susceptible to the presence of extraneous noise than the derivative skewness.[13] Like the derivative skewness, ASF has been used in both model-scale[16] and full-scale[58] jet noise applications. It has been shown that in both cases an ASF value between 1.5 and 2 is indicative of the presence of shocks, with an ASF value approaching two suggesting significant shock content.[16,81]

3.2.3 Shock Energy Fraction

The steepening of shocks in the time domain results in spectral broadening in the frequency domain, as energy is transferred from the peak frequency region to higher frequencies. Although this effect is often shown using the more familiar Fourier transform, a wavelet transform has been used in lab-scale jet noise analysis as a frequency-domain technique that also gives temporal resolution.[16] The wavelet analysis involves a convolution of the waveform with a wavelet shape to give spectral information that is time-resolved as well. The absolute value of this convolution, similar to a Fourier transform, may be squared to give the wavelet power spectrum (WPS), which if averaged over time approximates the autospectrum. Many types of wavelets exist, but for this chapter the Morlet wavelet is used to mirror previous studies,[16] where the wavelet analysis was used to show the association of high-frequency noise with shock waves and to investigate the near field of model-scale jet noise for evidence of shock wave origins.[16] An example of the wavelet transform applied to a waveform is shown in Fig. 3.1. The example waveform, of F-35A noise for 150% ETR at $r = 76$ m and $\theta = 135°$, is shown in Fig. 3.1(a) and has multiple shocks visible.

The corresponding wavelet transform is shown in Fig. 3.1(b). In the WPS an increase in high-frequency energy is visible at times corresponding to rapid increases in pressure. This high-frequency energy in the WPS is indicative of acoustic shocks.

In order to also incorporate the high-frequency energy associated with shocks, Baars and Tinney[16] proposed a metric involving the wavelet transform. This metric, a percent energy gain, used a shock detection algorithm to find sharp compressive regions of the waveform. Defining such sharp compressive regions using as a threshold derivative values above $\sigma_p/\Delta t$, where σ_p is the standard deviation of the pressure waveform and Δt is the time between samples, the algorithm identified the local waveform minima and maxima before and after these large derivative values to provide temporal bounds on the shock. Their algorithm then compiled an average spectrum of the WPS at the identified shocks. The average A-weighted spectrum of the shocks was then compared with the A-weighted spectrum of the entire waveform to determine the percent increase in energy due to the presence of shocks. This method has many interesting components, but a few shortcomings result in behavior that does not agree with expected shock behavior. One potential flaw in the percent energy gain was the application of the A-weighting to both the WPS and the waveform spectrum to correlate more closely with human perception. Though the A-weighting does serve to accentuate many of the highest frequencies, it may not have the desired effect in all situations. The shock detection algorithm was also shown in their paper[16] to be invalid for some propagation angles, which likely caused anomalous results. In addition, the spectral comparisons were performed based purely on the WPS, disregarding the number of shocks present in a waveform. This means that one shock within a 10-s waveform may be given the same emphasis as a waveform with 100 shocks per second.

To rectify some of these deficiencies, a new metric is proposed, the shock energy fraction (SEF). This metric bears many similarities to the percent energy gain but with key differences. First, this new shock detection threshold is based on $\sigma_{\partial p/\partial t}$, the standard deviation of the waveform derivative values to emphasize large derivative outliers, common for acoustic shocks, while minimizing the effects of high-frequency noise that potentially contaminated the shock detection algorithm used previously. A threshold is set and portions of the waveform with derivative values above this threshold are considered to be shocks. Rather than compare spectra directly, a new approach is used that accounts for time in a manner similar to sound exposure level (SEL)[59]; both the WPS and the duration of time associated with the number and length of shocks is used to define the SEF.

The primary difference in the WPS between the shock-containing portions and the remaining sections is the prominent presence of high-frequency sound, as seen in Fig. 3.1(b). The A-weighting applied in Ref. [16] minimized the effects of low-frequency noise, which remains consistent throughout the waveform and would otherwise dominate the higher-frequency differences that occur at a much lower decibel level. In contrast, the SEF is defined as an integral, not over the entire frequency range, but starting at a low-frequency limit. The justification for this lower-frequency limit can be seen in the coefficient of variation, c_v, shown in Fig. 3.1(c) as a function of frequency *f*. This coefficient is the normalized standard deviation of a function, $C_v = \sigma/\mu$, where σ is the standard deviation and μ is the mean value. Though ill-defined for many acoustics applications due to the abundance of zero-mean processes, C_v can be useful for energy-based applications (where explicitly non-negative values can be assumed) to show variation in a quantity. For the example waveform, C_v is shown to vary little below 1 kHz, and increases more rapidly above 2 kHz; C_v increases due to the large difference in WPS values between sections of the waveform with and without shocks. Using this as motivation, the WPS is integrated only above 2 kHz, roughly 10 times the peak frequency, to show the fraction of high-frequency energy associated with shock waves present in the waveforms.

With the above considerations, the SEF is defined as

$$\mathrm{SEF} = \frac{\sum_{t_{\mathrm{shocks}}} \sum_{f_{\mathrm{min}}=2\ \mathrm{kHz}}^{f_{\mathrm{max}}} \mathrm{WPS}\, \Delta f\, \Delta t}{\sum_{t} \sum_{f_{\mathrm{min}}=2\ \mathrm{kHz}}^{f_{\mathrm{max}}} \mathrm{WPS}\, \Delta f\, \Delta t}. \tag{3.1}$$

SEF is bounded between 0 and 1: SEF = 0 means that no high-frequency energy is found in the shocks, or that no shocks are observed above the detection threshold, and SEF = 1 means that no high-frequency energy is observed outside of shock-containing regions of the waveforms. The behavior of SEF is compared to the derivative skewness and the ASF by application to the F-35 jet noise measurements described in Section 3.4.

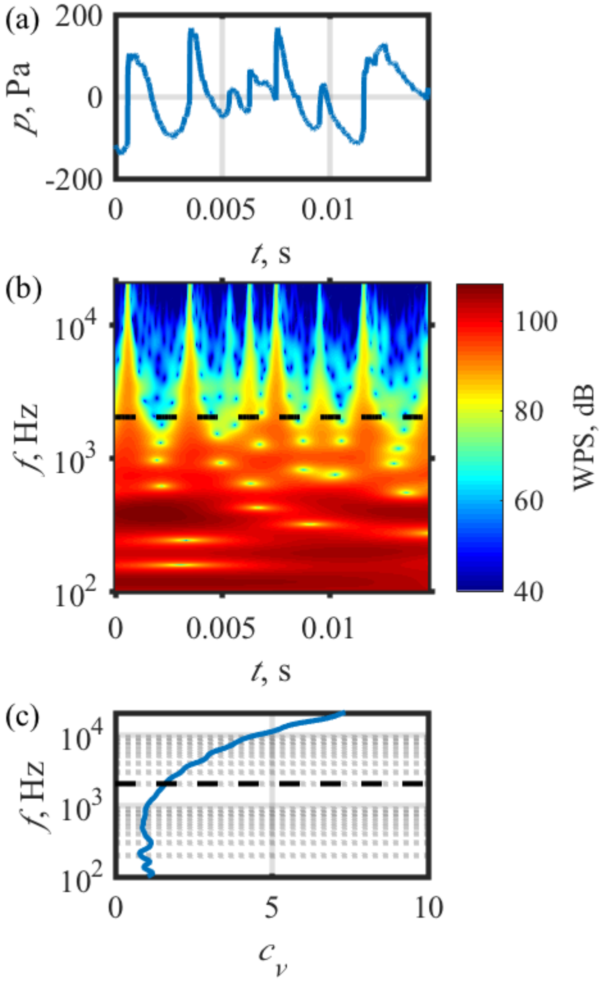

Fig. 3.1 An example (a) shock-containing waveform, (b) wavelet transform of the waveform, and (c) coefficient of variation for each frequency.

3.3 Measurement Details

3.3.1 Setup

The dataset examined in this chapter was collected at Edwards Air Force Base, September 5, 2013. The experiment has been extensively described by James *et al.*,[71] but pertinent details are given here. Noise measurements were taken as a tethered F-35A was cycled through power settings ranging from idle to 150% Engine Thrust Request (ETR), or maximum afterburner. Each engine condition was measured multiple times throughout the course of measurements. The 235 unique measurement locations, chosen in accordance with ANSI S12.75,[28] represent the largest full-scale dataset to date, with microphones located as close as 10 m from the shear layer out to 1220 m away from the microphone array reference position (MARP), located 6.6 m behind the nozzle. Microphones were arranged in either line arrays parallel to the jet centerline, or in semi-circular arcs centered at the MARP. As most of the noise generated by supersonic jets is emitted from the turbulent mixing that occurs behind the jet, the MARP represents a rough estimate of source location for many frequencies of interest. For arcs at 38 m and beyond, arc spacing of 5° between microphones was used in the direction of peak radiation, between 120° and 160°.

The microphone locations within 38 m of the aircraft are shown in Fig. 3.2, with the aircraft also included and shown to scale. Microphone locations beyond 38 m are shown in later plots. In the areas of maximum acoustic pressure, 6.35 mm (1/4”) microphones were used, with sampling rates of either 192 kHz or 204.8 kHz. At 305 m, in the forward direction, waveforms were captured at measurement locations from 0° to 40° and 60° to 80° using sound level meters. The meters recorded time-history Waveform Audio File Format (wav) files at a sampling rate of 51.2 kHz. Measurements were conducted between 3:00 and 9:00 AM local time, with temperature varying between 19.4°C and 23.1°C, relative humidity between 37.6% to 45.7%, and an average wind speed of 3.3 kts.

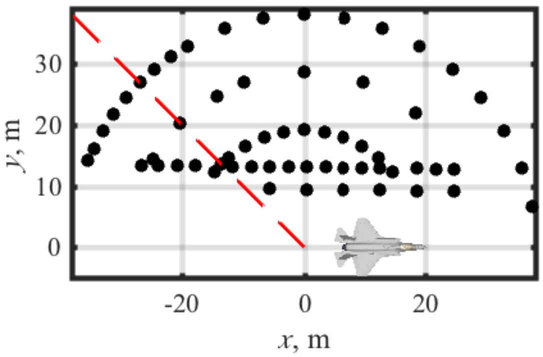

Fig. 3.2 Microphone measurement positions within 38 m of the MARP. The dashed red line shows the $\theta = 135°$ radial.

3.3.2 OASPL

The directivity of jet noise and its dependency upon engine conditions are key features of jet aircraft noise as shown in Fig. 3.3 for 50%, 75%, and 150%. Microphone locations within 38 m of the MARP are shown in Fig. 3.2, and microphone locations at 76 m, 152 m, and 305 m are shown as black dots on the plot of the overall sounds pressure level (OASPL) in Fig. 3.3. More engine conditions may be seen in James *et al.*[71] for the F-35B, which is acoustically similar to the F-35A shown here. In addition to the increase in OASPL seen at higher engine conditions, a shift in directivity is also observed. The OASPL peaks at 145° at 50% ETR, whereas the directivity shifts forward, towards the nose of the aircraft, with increasing engine power. At 75% the OASPL peaks at 135° from the aircraft nose with the origin at the MARP, while at 150% it peaks at 125°. In all cases, the far-field decay in OASPL is in line with expectations due to geometric spreading, though this will be explored further in Section 3.5.

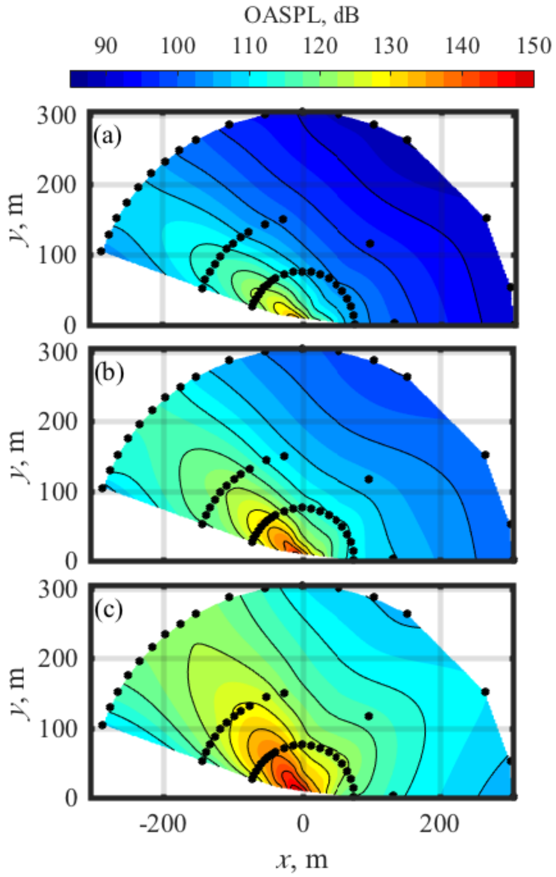

Fig. 3.3 OASPL near an F-35A at (a) 50% ETR, (b) 75% ETR, and (c) at 150% ETR.

3.4 Evidence of Shock Formation

The shock quantification metrics introduced in Section 3.2 are shown over the entire measurement aperture in this section. As the data were recorded at each engine condition multiple times, the average value between datasets is shown here, averaged over five measurements at each engine condition. The results are shown at 50%, 75%, and 150% ETR. As the nozzle diameter is on the order of 1 m, the spatial maps extends to roughly 300 nozzle diameters, farther than most laboratory-scale measurements,[16,92] though some far-field laboratory-scale measurements do exist.[33]

3.4.1 Waveform Characteristics

As an introduction to shock formation due to nonlinear propagation, normalized waveforms are considered (Fig. 3.4), at distances of 19, 29, 38, 76, and 152 m along the 135° radial, shown as a red line in Fig. 3.2. These waveforms are shown as a function of retarded time to demonstrate the evolution of waveform features with distance. Significant difference exist between the waveforms measured at 19 m and 29 m, including small shocks present at 19 m (In particular between 0.005 and 0.01 s) and other waveform shape issues that are likely due to near-field propagation effects. However, the significant features in the waveform are largely preserved from 29 m out to 305 m, and differences can mainly be seen due to nonlinear steepening. The consistency between 29 m and 305 m indicates that this measurement radial is also a propagation radial. The most noticeable change occurs near 0.015 s, as the steepened portion of the waveform forms a distinct shock by 38 m from the MARP. This shock persists all the way out to 305 m, though it does decay slightly with respect to the rest of the waveform.

Though the largest shock just after 0.015 s is well-defined by 38 m from the MARP, nonlinear propagation continues to affect the waveform out to 152 m. In particular, smaller amplitude sections of the waveform, which are clearly not shock-like at 76 m, are significantly steeper at 152 m (around 0.01 s, for example), though they begin to slightly thicken by 305 m. Similar behavior was observed in the propagation of noise from another aircraft by Gee *et al.*[60] for a lower-power engine condition—the largest features steepen and form shocks by 38 m, but smaller-amplitude sections of the waveform continue to steepen beyond this distance. These waveforms show that shock formation within noise does not occur at a specific distance from the source but is a continuous process that is dependent on the amplitude and frequency content within each section of the waveform. To accurately characterize the nonlinear propagation and shock formation of entire waveforms, it is useful to express the steepness and shock characteristics of an entire waveform in single-value metrics.

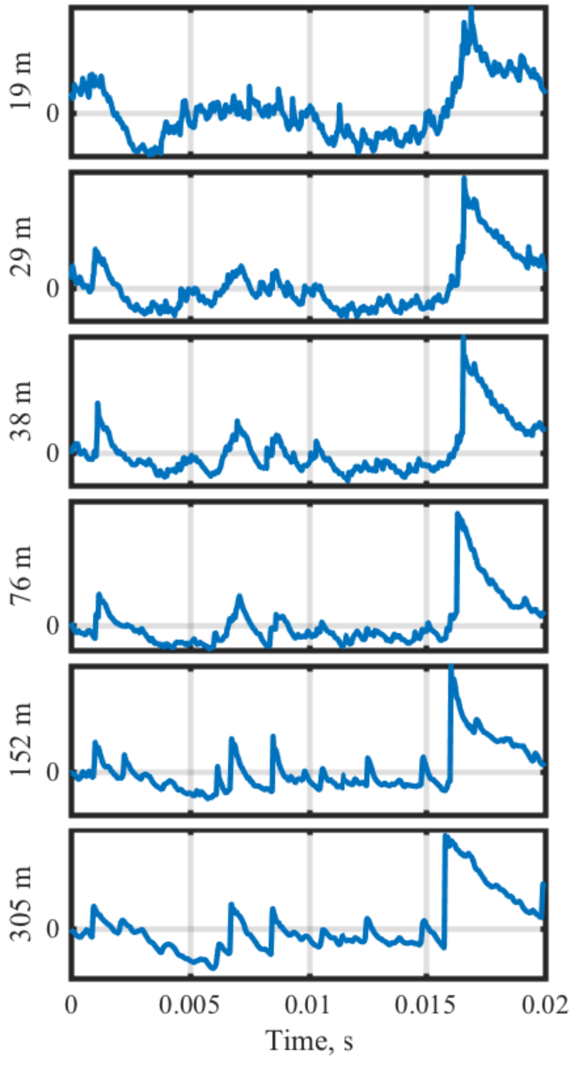

Fig. 3.4 Normalized, time-aligned waveforms at 150% ETR along the 135° radial (Red line in Fig. 2) at various distances from the MARP.

One question raised by the visual inspection of the waveforms is how to define and identify shocks. In periodic signals, a shock wave is often defined based on the rise time of the shock relative to the period of the signal. However, in noise signals this definition is not valid, and instead a shock will be defined based on how large a derivative is relative to the distribution of all derivative values. Because the most important feature of a shock is the rapid rise, a threshold based on the standard deviation of the derivative, $\sigma_{\partial p/\partial t}$, can be used as a minimum value, above which the derivative is considered a shock. To better illustrate which features are included in different shock definitions, the normalized waveforms shown in Fig. 3.4 are shown again in Fig. 3.5 with specific shocks highlighted. The shocks are color-coded according to the minimum threshold that they satisfy, i.e., a shock that satisfies the threshold $15\sigma_{\partial p/\partial t}$ also satisfies all thresholds below it. It can be seen that at the closest measurement locations more shocks are present, but that the majority of shocks are smaller, satisfying the threshold of $3\sigma_{\partial p/\partial t}$ or $5\sigma_{\partial p/\partial t}$, while at further distances such as 152 and 305 m there are fewer shocks, but they are now the most notable features of the waveform. This may suggest that although nonlinear propagation is the dominant factor behind waveform steepening in the far field, the mechanisms responsible for the shocks in the near field may be different. The shocks highlighted in Fig. 3.5 also suggest that while a threshold of $15\sigma_{\partial p/\partial t}$ does capture the most significant shocks, it may omit some significant features, and thus a threshold of $10\sigma_{\partial p/\partial t}$ is preferable.

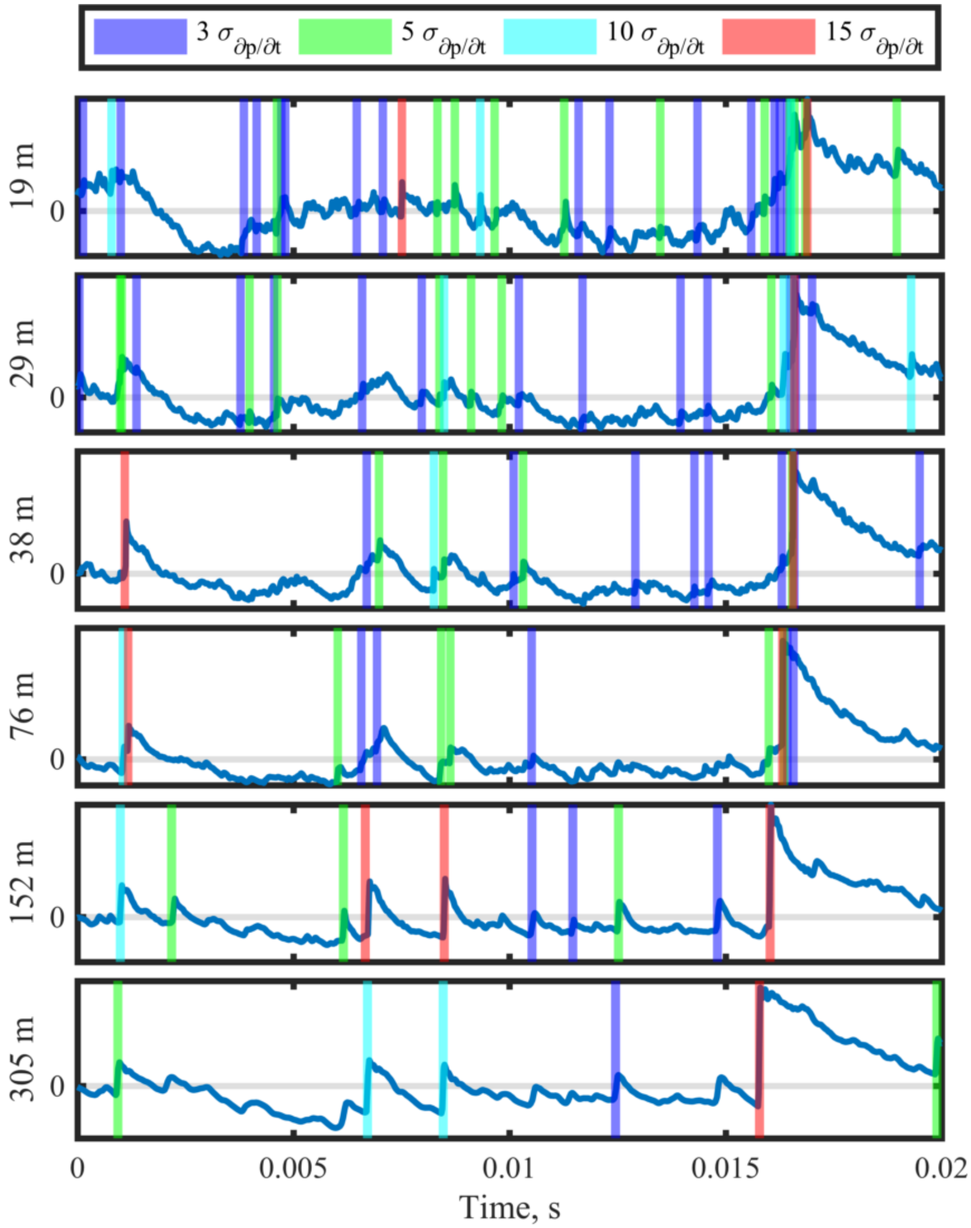

Fig. 3.5 Shocks in the 150% ETR waveforms from Fig. 3.4, categorized by strength.

While the evolution of the waveform and its time derivative provide evidence of nonlinear propagation producing shocks in the far field of jet noise, it is difficult to know if the 0.02 s portion represents the entire waveform. A way to examine the shock content of the entire (30 s) waveform was introduced by McInerny and Olcmen for rocket launch data.[54] In the plots shown Fig. 3.6, each subplot represents one waveform from Fig. 3.4. Each waveform is then broken up into positively-increasing sections. The maximum derivative within each section is plotted on the y-axis against the total pressure increase over the section, Δp, on the x axis. In a slight change from McInerny's original plots, the results here are shown in a bivariate histogram plot, similar to Muhlestein,[61] to show not only where derivative values are occurring, but also how many of them occur. The plots are also normalized according to σ_p and $\sigma_{\partial p/\partial t}$ to allow for an easy comparison between relative importance of shocks.

A few guiding lines are present in each of the subplots in Fig. 3.6 to help with understanding. The dashed black line represents a two-point shock, where the entire rise Δp occurs between two samples. Though theoretically this should be the limiting case, due to discrete bin sizes some data points are plotted above this line. For large Δp, it is safe to say that a two-point shock means that the sampling rate is inadequate to accurately characterize shock characteristics. The red dashed line, which corresponds to the line plotted by McInerny and Olcmen, is a factor of two lower than the black line and represents a three-point shock. This line is more indicative of limiting behavior for large shocks due to sampling rate and low-pass filters implemented by a data acquisition system. Finally, the cyan and green lines represent the expected rise times when shock behavior is dominated by different regimes of absorption. For the longer rise times associated with the green line, absorption is characterized by a combination of thermoviscous losses and relaxation of both nitrogen and oxygen. For shorter rise times (the cyan line) the relaxation of nitrogen can be neglected. A more detailed explanation of the phenomena can be found in McInerny and Olcmen's paper.

There are many features of note in Fig. 3.6 that illustrate the properties of shocks in jet noise. First, in Fig. 3.6(a), 19 m from the MARP, there are a small number of two-point shocks with a large amplitude Δp. These two-point shocks gradually disappear between Fig. 3.6 (a) and Fig. 3.6(d), but even out to 76 m in Fig. 3.6(d) the largest amplitude Δp are still three-point shocks, indicating that sampling rate and measurement effects are likely limiting the rise time of these largest shocks. At 76 m significantly more shocks have formed than were present at closer distances, as evidenced by the change in color. At 152 m and 305 m the shocks are below the red dashed line, indicating that sampling rate is likely sufficient for these distances. Another important behavior is the relative increase of stronger shocks. As near-field shocks disappear and coalesce at closer distances in Fig. 3.4, the remaining larger features in the far field result in a larger number of points with $\Delta P > \sigma_p$ with increasing distance. This is especially apparent in Fig. 3.6(e)-(f), where there are a large number of larger-amplitude shocks. This behavior illustrates the steepening of smaller shock features seen in Fig. 3.4 at distances of 152 and 305 m. These features show many of the behaviors identified in the discussion of Fig. 3.4, but in the context of the entire waveform, and prepare us for an informed discussion of the metrics introduced in Section 3.2.

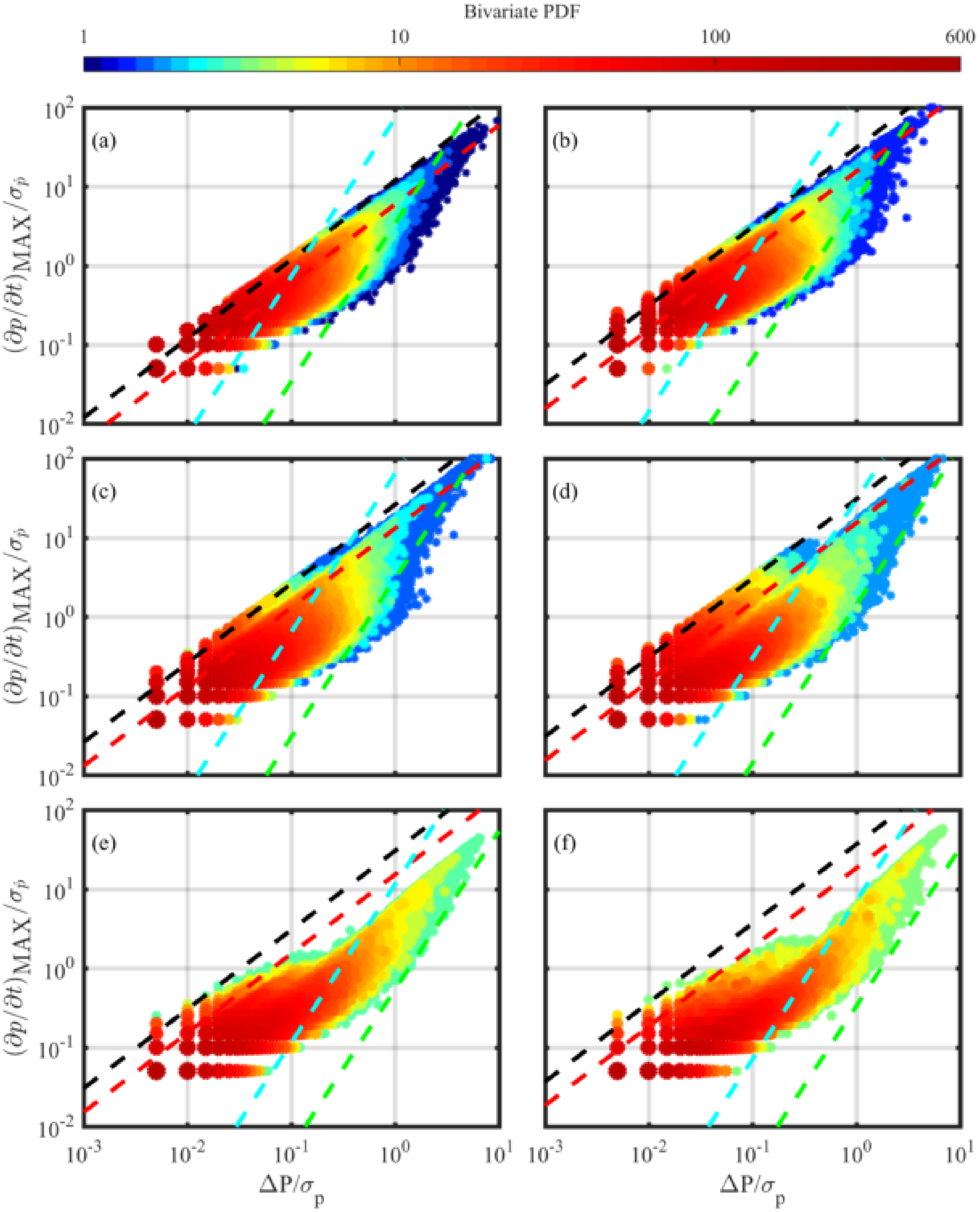

Fig. 3.6 Bivariate histogram plots of pressure increases vs the maximum derivatives at (a) 19 m, (b) 28 m, (c) 38 m, (d) 76 m, (e) 152 m, and (f) 305 m at 150% ETR. Dashed lines indicate two-point shocks (Black), three-point shocks (red), and expected rise times when shock behavior is dominated by different regimes of absorption (Cyan and green).

3.4.2 Derivative Skewness

The presence and strength of the largest acoustics shocks are readily shown by the derivative skewness, as evident in Fig. 3.7 at 50%, 75%, and 150% ETR. While the angular resolution of the data is every 5° in the peak radiation direction, the radial distribution in the far field is still rather coarse, with points at 76, 152, and 305 m. There are likely interpolation effects that accentuate the dip seen between 152 and 305 m, and more measurements are needed to precisely characterize the behavior. However, the measured behavior does indicate that at 150%, the derivative skewness decreases between 76 m and 152 m, then slightly increases between 152 m and 305 m.

The derivative skewness values shown in the near field in Fig. 3.7 are similar to those seen in other measurements of F-35 variants. Similar values were shown for the F-35B in Ref. [71]. Some differences are seen when comparing the values at 50% and 150% with those reported by Gee *et al.*[17] for the F-35 AA-1. These differences are largely explained by the differences in sampling frequencies between the current study (196 or 204.8 kHz) and for the F-35 AA-1 study (96 kHz). When the waveforms from the current study are resampled the disagreements in large part disappear. For example, at 10 m from the MARP, the resampled derivative skewness is 5.5, in agreement with findings of Gee *et al.* At 38 m the resampled derivative skewness value drops from 22 to 16, still slightly elevated from the F-35 AA-1 result of 12, but closer.

Derivative skewness values depend on the engine power conditions. The derivative skewness values at 50%, shown in Fig. 3.7(a), are not indicative of the presence of shocks. The 50% ETR power condition derivative skewness peaks at a value of $\mathrm{Sk}\{\partial p/\partial t\} = 2.5$, below the threshold of ~5 that indicates significant shock content.[80] The near-field behavior of derivative skewness at 75% and 150% ETR differ greatly from that at 50%. Although not clear in the figure, at the closest measurement locations to the MARP along the direction of peak OASPL, the derivative skewness is approximately 7 or 8 for both 75% and 150% ETR. In both cases, the derivative skewness exceeds 20 at 76 m, and then decreases. This finding is in agreement with the behavior seen in Fig. 3.4, that the largest shocks are forming by 76 m from the MARP. However, important differences remain between 75% and 150% ETR. The derivative skewness reaches a slightly higher value at 150% of 27, compared with 25 at 75%, though this difference is not likely significant. In addition, higher derivative skewness values persist over longer distances at 150%. At 305 m, the derivative skewness at 75% has dropped below a value of 10 while it remains above 15 at 150%. Both of these values, while lower than the peak derivative skewness seen at 76 m, still indicate the presence of significant shocks in the jet's far field.

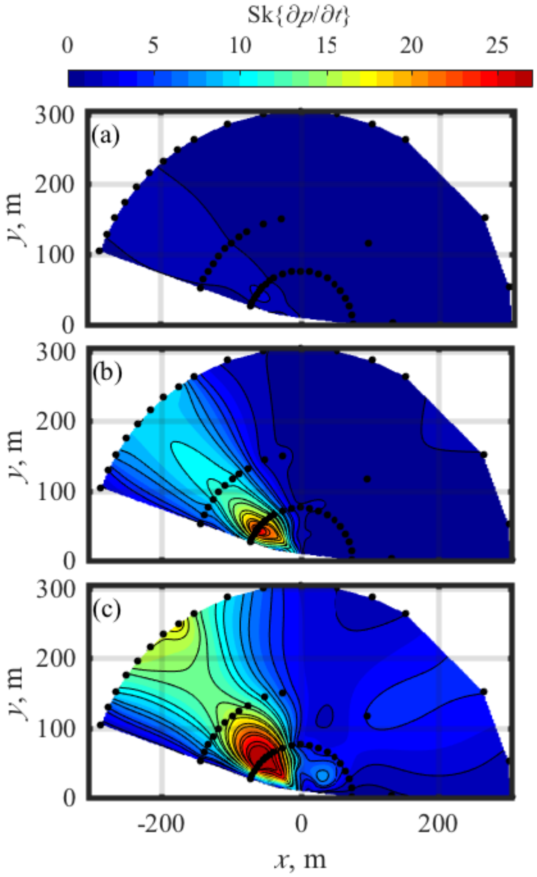

Fig. 3.7 Derivative skewness near an F-35A at (a) 50% ETR, (b) 75% ETR, and (c) 150% ETR.

3.4.3 Average Steepening Factor

While the derivative skewness accentuates the positive outliers and indicates the presence of the strongest shocks, the ASF is instead a measure of average behavior and thus, less sensitive to the less frequent but extremely large derivative values. Similar to the previous plots, at 50% ETR the low ASF values shown in Fig. 3.8(a) indicate that although the jet noise is steepening slightly, it does not contain shocks. However, at 75% the ASF (in Fig. 3.8 (b)) reaches values above 2 in the direction of peak OASPL, indicative of more significantly steepened waves. The ASF is significantly higher at 150% ETR (in Fig. 3.8(c)), reaching values of 2.5. Since ASF = 1 indicates a symmetric distribution of derivative values, a value of 2.5 is roughly 50% more than a value of 2. The peak ASF values are seen near the peak OASPL values, occurring at 140°, 130°, and 120° at 50, 75, and 150% ETR, respectively, echoing the forward shift seen in previously observed behavior.[58]

One important clarification is that the behavior of the ASF is highly dependent on the type of noise being considered. In the analytical paper describing ASF by Muhlestein *et al.*,[13] a value of 2 was reached by noise in a plane wave tube with a relatively low Gol'dberg number of $\Gamma = 3.3$. However, our effective Gol'dberg number is likely higher than the direct comparison would suggest, based on shocks present in the waveforms and the high derivative skewness values seen.

Significant changes in spatial variation in ASF are seen between the three engine conditions. At 50%, a slight increase is seen through propagation away from the jet. At 75% the increase is much more dramatic, peaking at 76 m before decreasing out to 305 m. However, at 150% the ASF continues to increase along propagation radials even out to 305 m. Because the

ASF represents a linear average of positive derivatives to the linear average of negative derivatives, it does not accentuate the largest shocks, which cause the derivative skewness to peak at 76 m. The continually increasing ASF out to 305 m at 150% ETR is due to continued nonlinear propagation, as seen by comparing the waveforms in Fig. 3.4. The nonlinear effects are evident in continued shock formation, general waveform steepening, and the persistence of shocks coupled with dissipation of high-frequency energy not associated with shocks due to atmospheric absorption. As designed, the ASF indicates the average strength of the shocks relative to the overall signal; ASF continues to increase with distance as nonlinear propagation effects continue to steepen the high-amplitude portions of the waveform and atmospheric absorption reduces the lower-amplitude, high-frequency portions of the waveform.

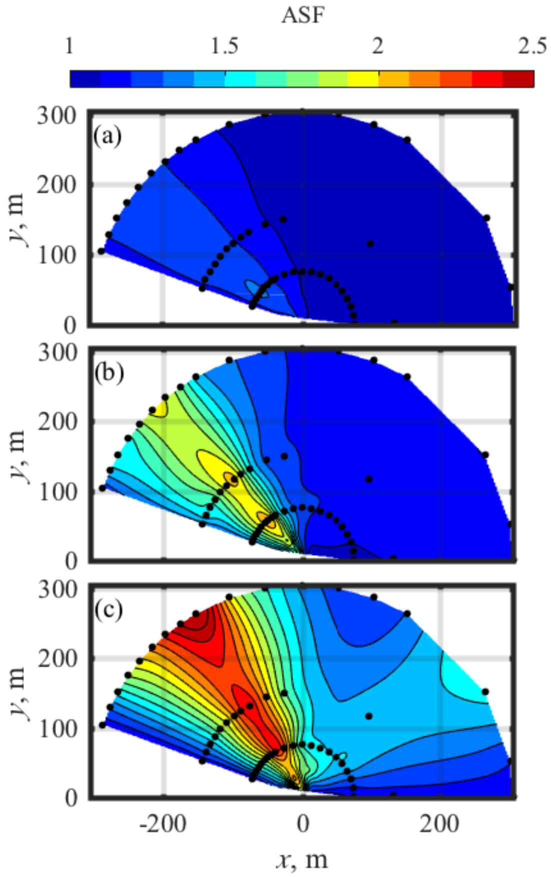

Fig. 3.8 ASF near an F-35A at (a) 50% ETR, (b) 75% ETR, and (c) 150% ETR.

3.4.4 Shock Energy Fraction

If the attenuation of high-frequency energy not associated with shocks is a cause of steadily increasing ASF values, this should be readily seen in the SEF, since the SEF shows the fraction of high-frequency energy (Above 2 kHz) associated with shocks. Spatial maps of the SEF are displayed in Fig. 3.9 at 50%, 75%, and 150% ETR. In Fig. 3.9(a), the low SEF at 50% ETR again confirms the lack of significant shocks in the waveforms, though the values are non-zero in the direction of peak OASPL. Similar to the other metrics, a large change in metric behavior is seen when comparing 50% and 75% ETR. At 75% (Fig. 3.9(b)), the increasing prominence of shocks is evident as the SEF increases with distance to values above 0.1, meaning that the infrequent shocks contribute more than 10% of the energy above 2 kHz. At 75% ETR the SEF begins to decrease from 152 to 305m, but in contrast the 150% ETR in Fig. 3.9(c) continues to increase to 305 m, where it reaches values of above 0.12. These values suggest that the acoustic shocks are a main contributor of high-frequency energy at these distances from the source; high-frequency energy not associated with the shocks has likely been significantly attenuated due to atmospheric absorption. This attenuation is also seen when comparing the closest waveforms in Fig. 3.4 with those measured at farther distances. In addition, the growth in SEF with distance points to the persistence of nonlinear propagation and continued transfer of energy to higher harmonics. If nonlinear propagation were negligible, the SEF would remain constant or decrease as high-frequency energy is absorbed at all sections of the waveform equally, similar to 50% ETR. Therefore, an increase in SEF points to continued nonlinear propagation out to 305 m from the MARP.

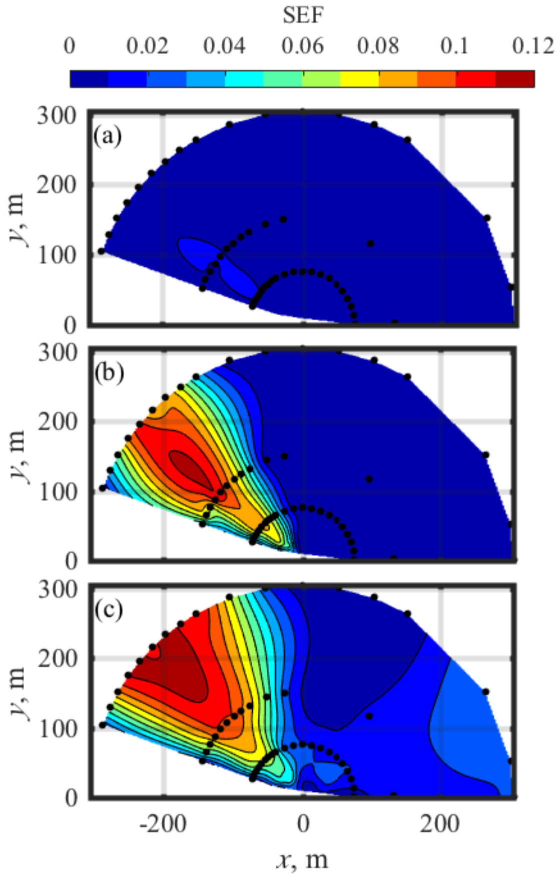

Fig. 3.9 SEF near an F-35A at (a) 50% ETR, (b) 75% ETR, and (c) 150% ETR.

3.4.5 Spatial Trend Summary

Though the above analyses all point to different aspects of shocks within jet noise, together they form a cohesive picture of continual nonlinear propagation away from the source of jet noise. At 150% ETR, all of the metrics suggest that the strongest shocks are not present immediately at the source but form through nonlinear propagation. The derivative skewness, emphasizing the largest positive outliers, peaks near 76 m, at which point the largest shocks have formed and begin decaying. However, because a noise signal is a complicated amalgamation of various frequencies rather than a simple sinusoid, shock formation is not limited to a particular spatial range. Though the largest shocks form by 152 m, overall waveform steepening and smaller shock formation continues to drive an increase in values of ASF. In addition, the rise in ASF is attributable to the decay in lower-amplitude, high-frequency energy not associated with shocks due to atmospheric absorption. This increase in the relative prominence of the shocks is also seen in the growth of SEF with distance. The evolution of these nonlinearity metrics over this large spatial aperture provides conclusive evidence that although some shocks exist in the near field of the jet noise source, the strongest acoustic shocks form by 76 m and nonlinear propagation persists out to at least 305 m from the MARP.

3.5 Nonlinearity Metrics Along Radials

Though the spatial maps presented in Section 3.4 are an efficient way to highlight trends associated with directivity and distance, there are advantages in considering propagation along individual measurement radials. Radial comparisons provide an easier way to see trends across engine conditions and show metric values at specific points without interpolation effects. Such comparisons allow for inspection of specific features, such as the dip in derivative skewness seen in Fig. 3.7, as well as a more quantitative comparison of values between engine conditions. Presented in this section are plots of the metrics considered in Section 3.4 as a function of distance along a single radial. These metric values are not from a single measurement, but an average of measurements throughout the experiment. The metric values are compared across engine condition and angle to establish and reinforce trends seen in the spatial maps, including the growth of the shocks near the jet source and continued shock formation and propagation into the far field.

3.5.1 Comparison Across ETR

This section presents plots of the various metrics as a function of r for the same three engine conditions shown above. At each engine condition, the selected radial displayed corresponds to the angle in the 305 m arc at which the greatest OASPL is measured: 145°, 135°, and 125° at 50%, 75%, and 150% ETR respectively. The different radials account for the differences in the location of data points in the plots of derivative skewness, ASF and SEF shown in Fig. 3.10, as well as the OASPL in Fig. 3.10(a). Results shown are from one 30-second measurement at each engine condition, but are representative of results and trends across the entire two-day measurement.

The derivative skewness displayed in Fig. 3.7 shows a marked peak at 76 m across all engine conditions. When each radial is inspected individually, as in Fig. 3.10(b), the same behavior is observed. Although the derivative skewness values at 50% do not suggest the presence of significant shocks, the 75% derivative skewness peaks at 76 m with a value of 20. After this point the derivative skewness decreases to 12 at 152 m and further decreases to 10 at 305 m. In contrast, the 150% derivative skewness peaks at 76 m with a value of 28, decreases to a value of 15 at 152 m, then rises again to 18 at 305 m. The large decrease between 76 m and 152 m is likely due to a combination of effects, including propagation through a refracting, turbulent atmosphere, and the presence of vegetation in the propagation path.[71] The slight increase between 152 m and 305m again points to the importance of nonlinear propagation in the far field, and this dip in derivative skewness will be investigated further in Section 3.5.2. Though the derivative skewness does not indicate the precise cause of the increase between 152 m and 305 m, three effects of nonlinear propagation are probably responsible: shock formation, waveform steepening without forming distinct shocks, and the reduction in high-frequency noise not associated with shocks. A combination of these effects results in the increase in derivative skewness at 150% ETR.

Many of the trends observed in the plots of the derivative skewness are again reinforced when considering the ASF. As shown in Fig. 3.10(c), the ASF peaks for 50% and 75% ETR at 76 m, similar to the derivative skewness. And, similar to the derivative skewness, the ASF at 75% ETR decreases consistently after 76 m, which is different than the behavior seen at 150%. The ASF at 150% ETR continues increasing with distance, from a value of 2.2 at 76 m to a value of 2.5 at 305 m. This continued increase with distance again points to nonlinear propagation in the far field of military jet aircraft.

The continued increase of ASF out to 305 m is in part due to absorption of high-frequency noise not associated with acoustic shocks. At closer distances, this "background" high-frequency noise creates large positive and negative derivatives that lower both the derivative skewness and ASF below what examination of the shock content in the waveform suggests. However, as this lower-amplitude high-frequency energy propagates and is attenuated through atmospheric absorption, the remaining shocks are accentuated in both the derivative skewness and the ASF.

The attenuation of high-frequency energy is also apparent in plots of the SEF, shown in Fig. 3.10(d). The SEF at 50% remains more or less constant, while at 75% and 150% SEF grows with distance to 152 m. At 75%, SEF decreases slightly from 152 m to 305 m; this decrease is associated with a decrease in the number of shocks. However, at 150% the SEF is, similar to the ASF in Fig. 3.10(c), increasing with distance out to 305 m, confirming the reduction in high-frequency energy not associated with shocks. One point to mention is that the SEF is higher at most distances for 75% than 150%, indicating that the shocks are more significant in terms of high-frequency contribution. This is likely due to a combination of effects, including different directivity at the two engine conditions, the number of shocks, and different spectral content. Though the derivative skewness and ASF indicate that shocks are stronger at 150% than at 75%, the SEF informs us that the shocks at 75% contribute more to the high-frequency content of the entire waveform at 152 m and closer.

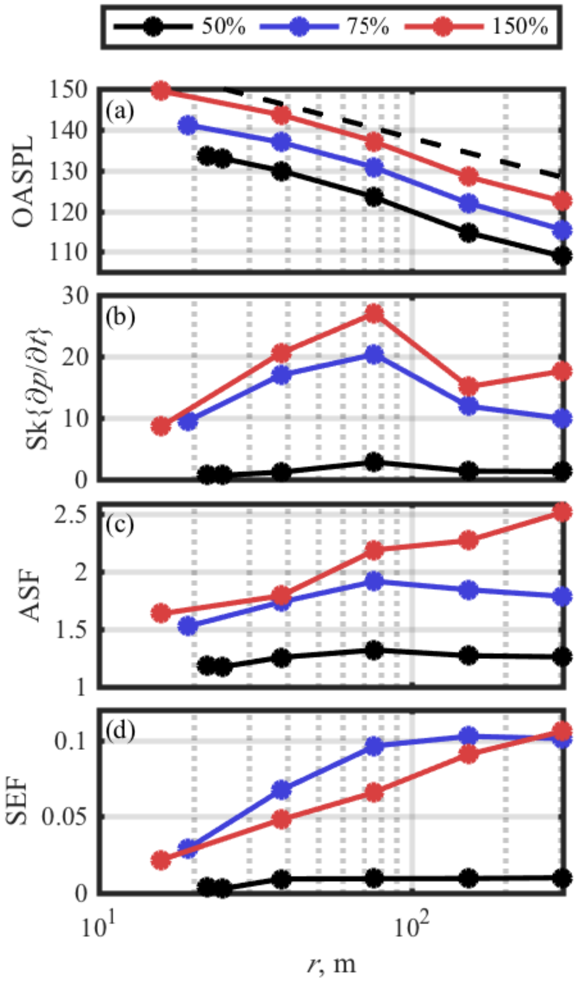

Fig. 3.10 The (a) OASPL, (b) derivative skewness, (c) ASF, and (d) SEF along the peak radiation angle at 50%, 75%, and 150% ETR

3.5.2 Angular Dependence of Nonlinearity Metrics

Some of the behavior seen in the line plots of nonlinearity metrics—In particular the fall and subsequent rise in derivative skewness seen in Fig. 3.10—raise the question as to whether the spatial trends are physical or merely the result of a single microphone with a poor response or signal-to-noise ratio. To show that the trends observed in Section 3.5.1 are physical, the metrics are plotted for various angles at 150% ETR in Fig. 3.11; the OASPL, derivative skewness, ASF, and SEF are plotted as a function of *r* for the microphones along the 120°, 130°, 140°, and 150° radials.

The OASPL shown in Fig. 3.11(a) decays close to the rate expected due to spherical spreading. This rate, 20 dB/decade or 6 dB/doubling of distance, is seen between most points. However, there is one discrepancy: all radials decrease by 8-9 dB between 76 m and 152 m. Between these distances some vegetation could have contributed to a greater than expected decay in OASPL, and it is likely that it is also in part due to meteorological effects. Between 152 m and 305 m the decay is again roughly equal to 6 dB across all radials.

The slight increase in derivative skewness between 152 and 305 m observed in Section 3.5.1 is shown in Fig. 3.11 to occur across multiple angles. The derivative skewness, shown in Fig. 3.11(b), does experience a large decrease between 76 m and 152 m, likely associated with the greater than expected decrease in OASPL. However, between 152 m and 305 m the derivative skewness either remains constant or increases across all angles in question. This points to the likelihood that past 152 m there is continued steepening and nonlinear propagation continues to play an important role.

The ASF and SEF again confirm this continued waveform steepening and importance of nonlinear propagation into the far field of the jet noise source. Across all angles, the ASF and SEF continue to increase out to 305 m. Because they are not as sensitive to large outliers, they do not experience the decrease between 76 m and 152 m seen in the derivative skewness but rather emphasize the continued steepening and presence of high-frequency energy associated with nonlinear propagation.

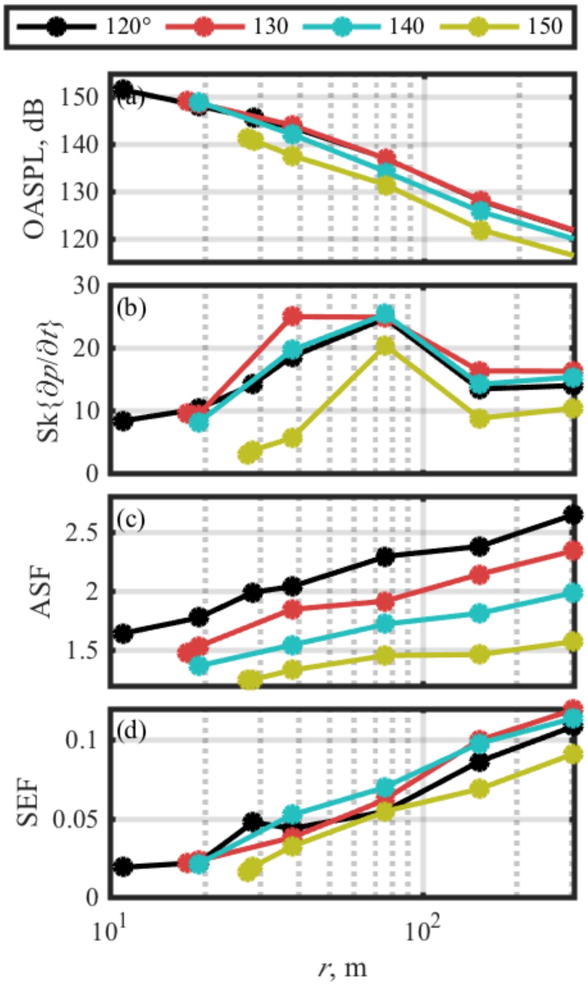

Fig. 3.11 The (a) OASPL, (b) derivative skewness, (c) ASF, and (d) SEF at 150% ETR along radials from 120° to 150°.

3.5.3 SEF and Shock Thresholds

One last point to investigate is how the behavior of the SEF changes with the definition of shock thresholds. As more or fewer sections of the waveform are identified as shocks, how does the WPS associated with shocks change? This question is answered in Fig. 3.12, where the SEF at 150% along 135° is plotted for various thresholds, ranging from $3\sigma_{\partial p/\partial t}$ to $15\sigma_{\partial p/\partial t}$. Though the SEF for higher thresholds is predictably lower as fewer points are included, the same general trends apply in all cases. The SEF continues to increase out to 305 m in all cases, with the exception of

$15\sigma_{\partial p/\partial t}$, which peaks at 76 m. This serves as evidence that even though the amplitude of the SEF may vary with threshold, the trends remain that out to 305 m shocks become relatively more important in terms of high-frequency content.

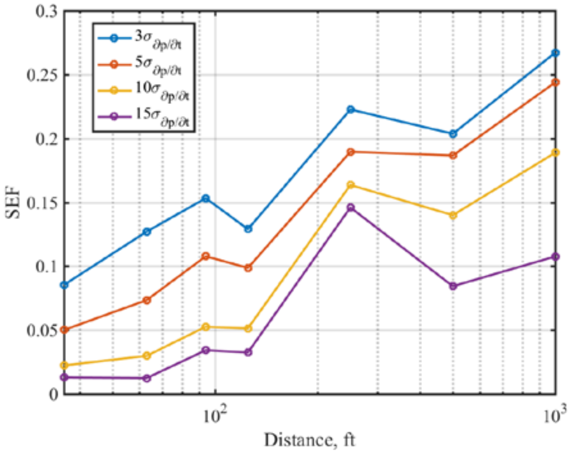

Fig. 3.12 The SEF at an ETR of 150% and 135° as a function of distance for various shock thresholds.

3.6 Conclusions

The various nonlinearity metrics considered in this chapter point to the conclusion that nonlinear propagation is an important factor in the near, mid, and far-field environments of military jet noise. Though some significant shocks exist at the closest measurement locations at a distance of roughly 10 m, the waveforms steepen and form shocks through nonlinear propagation. The derivative skewness indicates that the strongest shocks form by 76 m, then slightly thicken at greater distances. The continued growth of ASF points to nonlinear propagation out to at least 305 m, likely due to the persistent steepening of smaller features in the noise. The wavelet-base metric SEF appears to be a useful nonlinearity metric showing the relative importance of shocks in high-frequency energy. For the F-35, the increase in SEF with distance indicates that high-frequency energy not associated with shocks is attenuated through linear atmospheric absorption. The relative importance of shocks for high-frequency energy remains independent of shock threshold. These analyses show that the far-field features of jet noise are formed primarily through nonlinear propagation.

Chapter 4

Characterizing acoustic shocks in high-performance jet aircraft flyover noise

4.1 Introduction

Community annoyance of military aircraft noise is due not only to the high sound levels associated with high-performance jet noise but may also be influenced by its sound quality. One component of the noise, crackle,[10] is the perception of acoustic shocks within the waveform.[62] Due to nonlinear propagation, these shocks and the high-frequency energy associated with them persist to distances greater than expected under linear assumptions.[18,2] The nonlinear propagation of jet noise serves to steepen the waveform and form shocks, even well away from the source. Nonlinear propagation was originally identified as an explanation for the lack of atmospheric absorption in far-field full-scale jet data[21,63] and has since been confirmed through numerical modeling.[64] Modeling efforts have shown the effects of nonlinear propagation in both the temporal[19,65,66] and frequency[67,68] domains.

Many of the attempts to quantify the effects of nonlinear propagation in jet noise waveforms have revolved around statistical quantities. When the phenomenon of crackle was first discussed by Ffowcs Williams *et al.*,[10] the skewness of the pressure waveform was proposed as a metric indicating the presence of crackle, a measure that is still in use today.[69,70] However, since crackle is associated with the presence of shock waves, which have large positive derivative values, more recent work has shown that the skewness of the first time derivative of the pressure waveform, or derivative skewness, is more connected to the presence of shock waves and crackle.[12,48] The derivative skewness has since been used to show the steepened nature of nonlinearly propagated jet noise.[16,34] Other quantities, such as the average steepening factor (ASF[49,50]) or frequency-based metrics have also been used to quantify nonlinear effects. [19,21] Most of these studies utilize data collected in static jets or ground run-ups with a tethered aircraft.[71,72]

Forward flight can significantly change the noise source, but the impact of flight effects is not completely understood, in particular with regards to nonlinear propagation. Several significant studies have compared jet noise measured during flyover operations with ground run-ups or lab-scale tests. As early as the 1970s, spectra were measured during flyover events,[73] and later noise predictions were made based on static measurements.[74] Krothapalli *et al.*[75] subsequently performed model-scale tests in a wind tunnel to simulate forward flight of a heated supersonic jet and found the wind caused changes in far-field noise. Schlinker *et al.*[76] performed similar tests with installed chevrons to observe noise reduction. In recent full-scale work regarding flyover measurements, Seiner *et al.*[77] used a linear array of microphones to obtain narrowband spectra and validate noise predictions for F-18 flyover operations. In more recent work, Michel[78] analytically predicted the effects of forward flight on mixing noise, resulting in an increase in level due to "stretching of the flow field of the jet."

Fewer analyses exist examining the nonlinear characteristics of jet noise while in flight.[21,79] McInerny *et al.*[27] used a combination of time-domain and spectral methods to inspect flyover data for evidence of nonlinear propagation and to investigate effects of microphone height from ground level up to 11.9 m (39 ft) above ground level. They concluded that characteristics indicative of nonlinear propagation are seen in flyover data, and that microphones should be placed off the ground to ensure cleaner measurements.

This chapter considers the nonlinear propagation of jet noise produced by an F-35 aircraft during flyover operations. The analyses begin by considering spectra, waveforms, derivatives, and their probability density functions (PDFs) at low and high-power engine conditions. Various time-domain nonlinearity metrics are calculated for individual waveforms over multiple measurement conditions, showing time-domain evidence of nonlinear propagation at high-power conditions. Behavior of these metrics as a function of microphone size and height and sampling rate show that these measurement parameters impact the various metrics differently. Recommendations are given for future measurements and recommendations are made for standard practices[28] for high-performance military jet noise measurements.

4.2 Nonlinearity Metrics

To discuss nonlinearity and shock formation for noise waveforms, the behavior of the entire waveform must be taken into account. To gauge overall waveform behavior, metrics are often based on the probability distribution function (PDF) of the waveform or its derivative. [12,19,40] Two such metrics are used in this analysis: the skewness of the first time derivative of the pressure waveform, also known as the derivative skewness, and the average steepening factor (ASF).

The skewness of a distribution expresses asymmetry of the PDF and accentuates outliers due to the cubed nature of the numerator. The skewness of a zero-mean variable x is defined as

$$\mathrm{Sk}\{x\} = \frac{E[x^3]}{E[x^2]^{\frac{3}{2}}} \tag{4.1}$$

where $E[x]$ represents the expectation value of x. A skewness value of zero represents a symmetric distribution, while a positive number indicates the presence of a higher number of large positive values than negative. The skewness of the pressure waveform was initially used to quantify crackle, an auditory phenomenon associated with shock waves within jet noise.[10] However, to quantify shocks themselves it is more useful to use the derivative skewness, which refers to the skewness of the PDF of the first time derivative of the waveform. and expresses an asymmetry in derivative values. The derivative skewness accentuates the large derivatives (rapid pressure increases) associated with shock waves and is indicative of shocks forming due to nonlinear propagation.[48] It has been shown that a derivative skewness value greater than five is indicative of significant shocks within a waveform.[80]

The ASF[13] is also based on derivative values and defined as the average value of the positive derivatives over the average value of the negative derivatives:

$$\mathrm{ASF}\{p\} = \frac{E[\dot{p}^{+}]}{E[\dot{p}^{-}]}. \tag{4.2}$$

The ASF, which is an inverse of the previously used WSF,[15] is a linear average of derivative values, which makes it less sensitive to outliers than the derivative skewness, and thus better represents average behavior. An ASF value of one represents a waveform with no significant steepening, while a value above one represents some nonlinear steepening.[13] It has been shown that for jet noise, both full-scale[81] and model-scale,[16] that an ASF value between 1.5 and 2 is indicative of the presence of shocks, with a value approaching two suggesting significant shock content (See Section 3.2.2).

4.3 Flyover Measurement Setup

The dataset considered was part of a larger measurement of F-35 flyover events at Edwards Air Force Base in 2013. The data shown are from the F-35A but are representative of the F-35B as well.[82] The F-35A flew between two cranes, one located 305 m (1000 ft) north of the flight path, and one located 305 m (1000 ft) to the south. Flights were performed at several engine conditions, ranging from 15% engine thrust request (ETR) to 150% ETR. The height of the aircraft varied during each measurement, with some constant altitude flights at 76, 152, and 305 m (250, 500, and 1000 ft) and other flights with the aircraft climbing to maintain constant velocity at high engine power conditions.

Measurements were performed according to ANSI S12.75,[28] which outlines procedures for full-scale military aircraft noise measurements in both static and flyover cases. While this standard involves calculating directivity of the noise and requires microphones at various locations, one of the purposes of this chapter is to highlight possible variations due to measurement considerations. The measurement involved microphones of different sizes, heights and locations around the aircraft. However, at the north tower redundant ½” and ¼” microphones were placed at several heights between 0 and 91 m, giving an ideal comparison. Thus, to reduce other variations and highlight the differences in question, this chapter concentrates on microphones from the north crane, located 305 m (1000 ft) from the flight path of the aircraft. G.R.A.S. prepolarized pressure microphones were suspended at various heights from a caving ladder hanging off the crane, as shown in Fig. 4.1. All microphones were pointed directly up, giving a nearly perpendicular angle of incidence ($\pm 15°$) as the aircraft flew by at a height of 76 m (250 ft), ideal for measurements with pressure microphones to ensure accurate estimation of shock amplitude.[83] At several heights, specifically 0, 9.1, 30.5, 61.0, and 91.4 m (0, 30, 100, 200 and 300 ft), two microphones were placed side by side, roughly 0.13 m (6”) apart. The two microphones consisted of one 40BD 6.35 mm (¼”) microphone[84] with a 26CB preamplifier and one 46AO 12.7 mm (½”) microphone.[85] The 40BD microphones have a flat frequency response within 2 dB up to 70 kHz and the 46AO microphones up to 20 kHz. Though wind speeds were low (4 knots or less) during flyover events the ½” microphones had wind screens placed on them. Temperatures during the measurement ranged from 16.3°C to 34.6°C. Relative humidity ranged from 17.3% to 37.7%, while atmospheric pressure remained nearly constant at 0.92 atm.

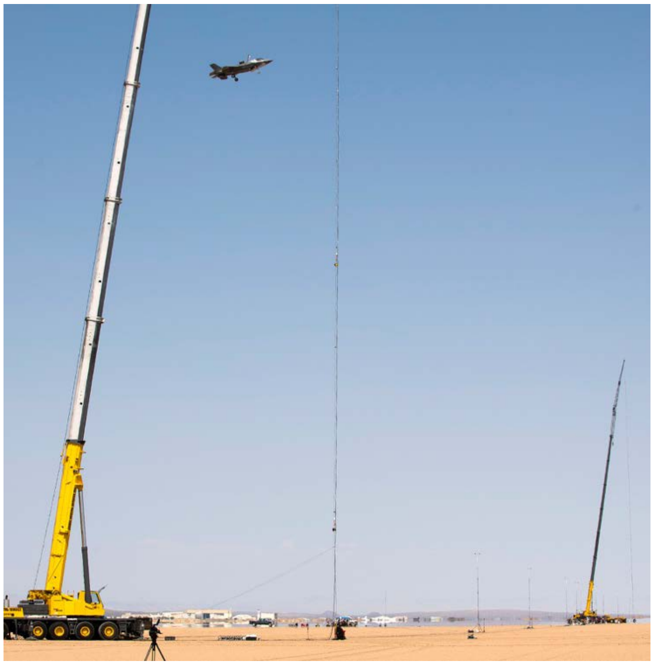

Fig. 4.1 An F-35 flying between two cranes, each located 305 m (1000 ft) from the flight path of the aircraft. Microphones were hung from the 91.4 m cranes at multiple heights, with five heights having redundant ½” and ¼” microphones.

4.4 Characterizing Nonlinearity in Flyover Waveforms

Evidence of nonlinear propagation can be found in individual waveform segments as well as statistical measures that represent the entire event. In the following sections, evidence for nonlinear propagation is found by comparing waveforms and their derivatives between engine conditions. The presence of shock waves in the waveforms themselves is shown, as well as statistical measures indicating the overall steepness of the waveforms. Waveforms and statistics are compared for both low and high-power operating conditions. The comparison is presented for a ¼” microphone located 91 m (300 ft) above the ground. The distance from this microphone to the aircraft, $r(t)$, and the angle of the microphone relative to the nose of the aircraft, θ, are shown for example flyover events in Fig. 4.2. The aircraft position is plotted relative to the time t, with $t = 0$ representing the point of closest approach between the aircraft and microphone. For both the low and high-power cases the aircraft was flying 76 m (250 ft) above ground level, giving a point of closest approach of roughly 305 m.

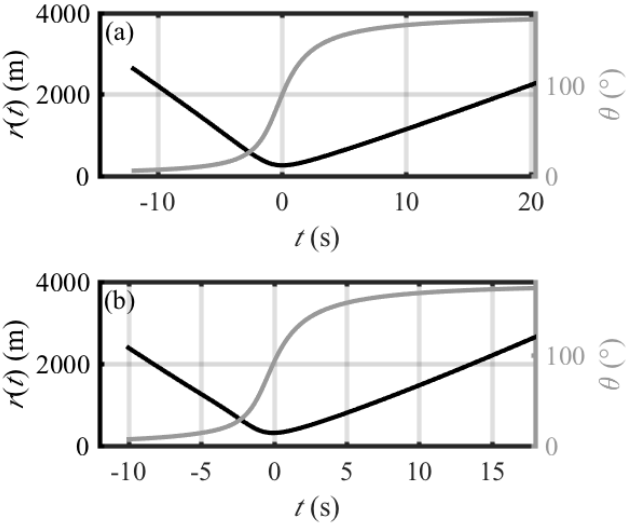

Fig. 4.2 The distance from the microphone to the aircraft *r(t)* and angle of the microphone relative to the nose of the aircraft *θ(t)*; for example flyover events at (a) 55% ETR and (b) 150% ETR. This microphone was located 91.4 m above ground level, hung from a crane located 305 m north of the flight path of the aircraft.

4.4.1 Waveforms and spectra

A comparison of characteristics of waveforms measured at various engine thrust request (ETR) settings allows for a clear indication of nonlinear behavior. A sample of each waveform at the time of maximum overall sound pressure level (OASPL) is shown in Fig. 4.3(a) for 55% ETR and in Fig. 4.3(b) for 150% ETR. The peak pressures increase by nearly a factor of ten from the 55% ETR case to 150% ETR case. In addition to the increase in pressure, sharp compressive pulses are seen for 150% ETR: the pressure increases dramatically over a short period of time. These steepened sections of the waveform are shocks, sharp increases in pressure occurring over a period on the order of tens of microseconds. Shocks have a significant impact on the spectrum, shown in Fig. 4.3(c), calculated over the 0.5-s block containing the maximum OASPL. At this distance, over 300 m from the aircraft, atmospheric absorption at high frequencies has a large effect. This is evident at 55% ETR, as the high-frequency levels decrease exponentially above 1 kHz. However, at 150% ETR, the spectral shape has changed dramatically. Although the spectrum peaks at roughly the same frequency as at 55% ETR, the same high-frequency roll-off is not observed. This apparent lack of atmospheric absorption is what initially led Pernet and Payne,[2] and later Morfey and Howell,[21] to suspect that nonlinear propagation had a significant spectral effect on jet noise.

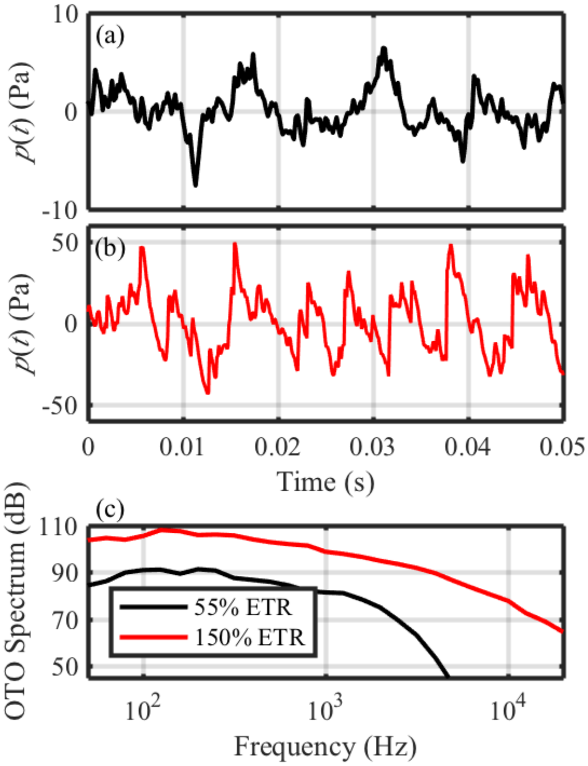

Fig. 4.3 Waveforms from (a) 55% ETR and (b) 150% ETR and (c) the spectra from each. Sharp compressions, or shock waves, are seen in the high-power waveform and produce the relative increase in high-frequency content.

4.4.2 Flyover waveforms

Although individual shocks at over 300 m from the aircraft show the steepened nature of flyover waveforms, characteristics of the entire waveform are needed to gauge overall trends. The waveform from the entire 55% ETR flyover event, its time derivative, and their respective probability density functions are shown in Fig. 4.4, for the same microphone used in Fig. 4.3. The pressure waveform is shown in Fig. 4.4(a), with the 6-dB down region highlighted in red. (The 6-

dB down region contains the times when the rms level is within 6 dB of the peak rms level.) At this distance and low engine power, the pressure peaks near 10 Pa, with a symmetric distribution centered around 0 Pa. The time derivative of the waveform, shown in Fig. 4.4(c), appears skewed, with negative values reaching -20kPa/s and positive values reaching approximately 35 kPa/s. The difference between these two distributions is more obviously seen in the plots of the probability density function[86] (PDF) of the 6-dB down portion of the waveform and its derivative, shown in Fig. 4.4(b) and (d), respectively. These plots are shown with respect to σ_p and $\sigma_{\partial p/\partial t}$, the standard deviation of the pressure waveform and its derivative, respectively. While the PDF of the pressure waveform is roughly symmetric about 0, the PDF of the derivative shows larger positive derivatives than negative. Though the slightly skewed PDF of the derivative suggests that waveforms are steepened, the difference between positive and negative derivative values is not large enough to suggest the presence of acoustic shocks, as is confirmed by a derivative skewness value of less than 1.[80]

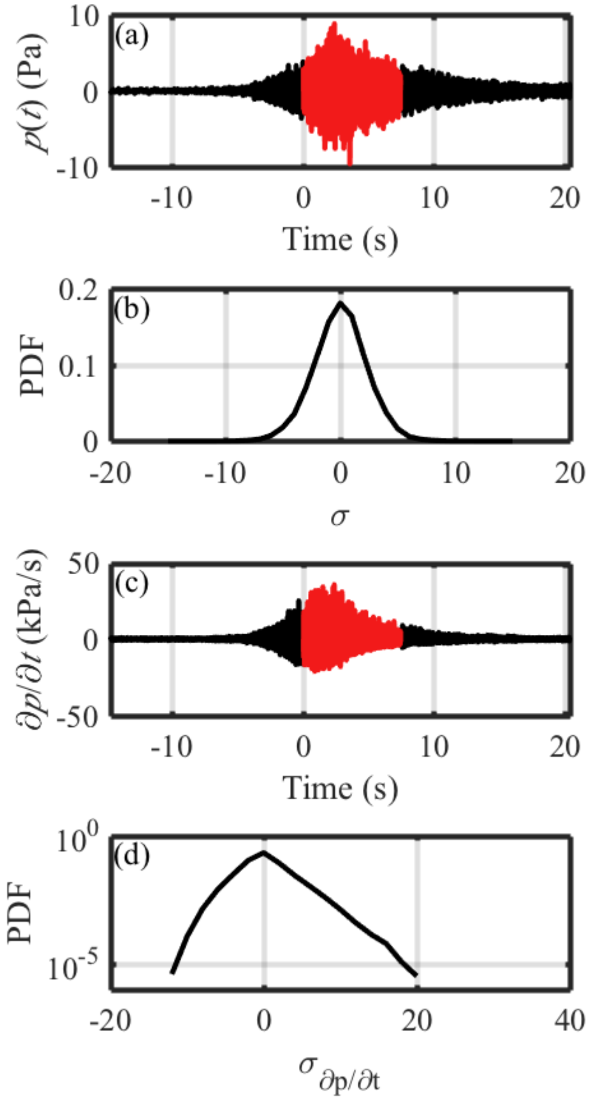

Fig. 4.4 (a) The waveform measured at a location 305 m away from an F-35A flying at 55% ETR at 76.2 above the ground. (b) The PDF of the 6-dB down portion of the waveform, shown as a function of the pressure standard deviation σ. (c) The time derivative of the waveform. (d) The PDF of the derivatives from the 6-dB down portion of the waveform as a function of the derivative standard deviation $\sigma_{\partial p/\partial t}$.

Contrasting waveforms between different engine conditions confirms the presence of nonlinear propagation at high-power engine settings. Another waveform from the same microphone as Fig. 4.4 is shown in Fig. 4.5, but with the aircraft operating at 150% ETR instead of 55%. At 150% ETR, the pressure waveform amplitude reaches values more than five times that of the lower power setting, over 50 Pa, but the starkest difference is in the derivative values. The greatest positive derivative values peak at 2 MPa/s, and although the pressure waveform PDF shown in Fig. 4.5(b) is still nearly symmetric about 0 Pa as in far-field ground run-up measurements,[87] the PDF of the waveform derivative shows a much higher positive asymmetry, with some positive derivative values reaching over 100 standard deviations.

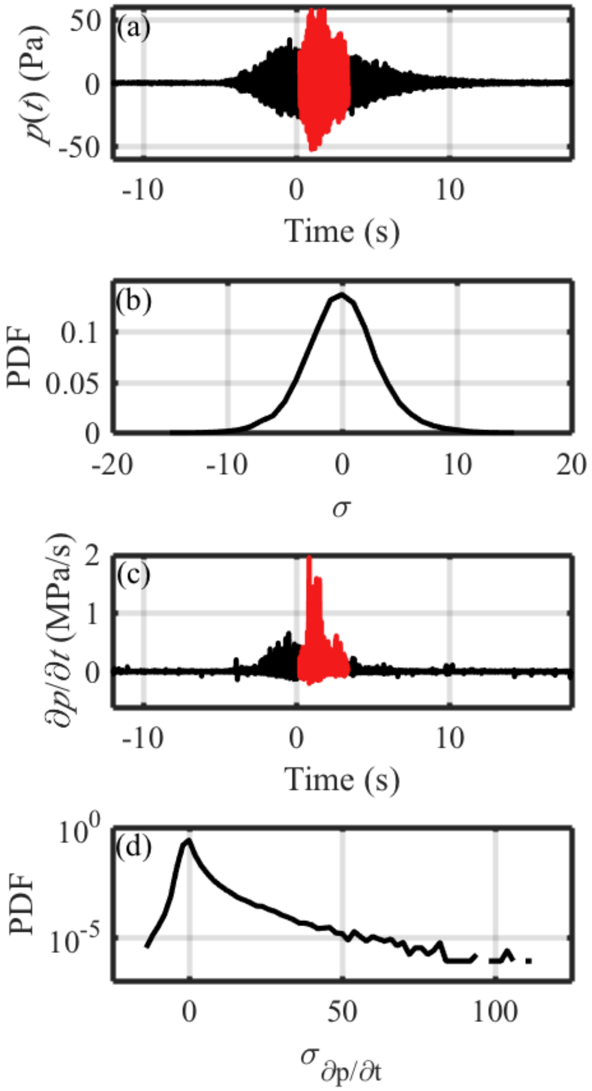

Fig. 4.5 (a) The waveform measured at a location 305 m away from an F-35A flying at 150% ETR at 76.2 m above the ground. (b) The PDF of the 6-dB down portion of the waveform. (c) The time derivative of the waveform. (d) The PDF of the derivatives from the 6-dB down portion of the waveform.

4.4.3 Metrics Characterizing Nonlinear Propagation

The quantities discussed in Section 4.2—the derivative skewness and ASF—are calculated along with OASPL from the 0.5 s blocks of the waveforms shown in Fig. 4.4 and Fig. 4.5. These statistics are investigated as a function of time, with 80% overlap between blocks, and are shown in Fig. 4.6 for 55% ETR. Fig. 4.6(a) shows the OASPL as a function of time, with the OASPL peaking shortly after the aircraft passes over. The derivative skewness and ASF of Fig. 4.6(b) and (c), respectively, both peak within this 6-dB down region, indicating steepened waveforms. The low value of the peak of the derivative skewness at $\mathrm{Sk}\{\partial p/\partial t\} = 0.8$ indicates that the waveform is steepened but does not contain significant shocks.[80] The peak ASF value of 1.22 confirms this assessment, suggesting steepened waveforms but not the presence of shocks throughout the 6-dB down region of the waveform. Thus, for this low-power case at 55% ETR, most of the statistics confirm conclusions drawn from the waveform and its PDF. Fig. 4.6(d) shows the position of the aircraft as a function of time, including both the distance $r(t)$ and the angle of the microphone with respect to the aircraft nose, $\theta(t)$. The OASPL, derivative skewness, and ASF all peak shortly after the point of closest approach, at an angle of approximately 140° due to the directivity of the jet noise source.

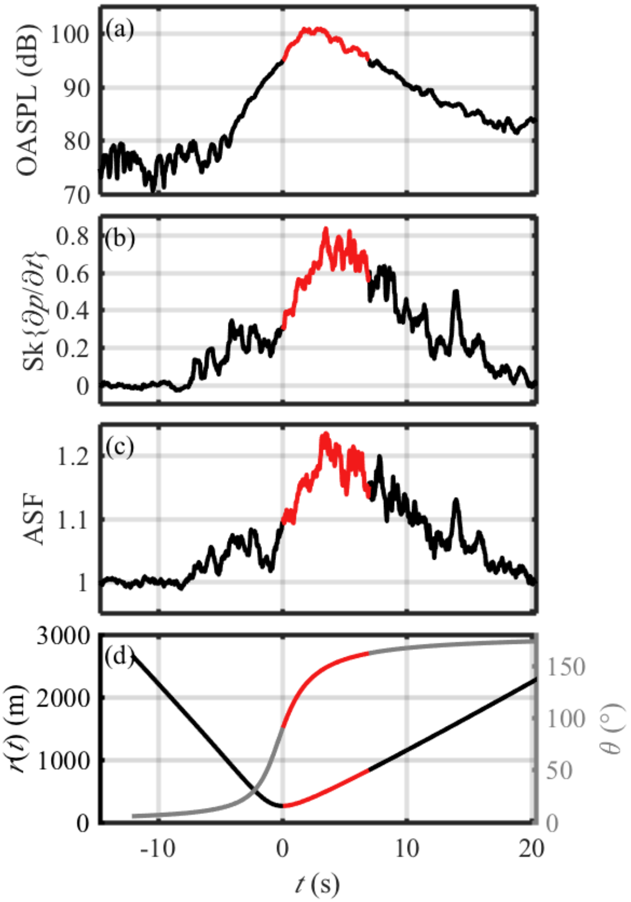

Fig. 4.6 Statistics of the 55% ETR flyover waveform shown in Fig. 4.4(a), specifically the (a) OASPL, (b) derivative skewness, (c) ASF, and (d) the distance from the aircraft to the microphone, *r(t)* and the angle of the microphone relative to the aircraft nose, *θ(t)*. The 6-dB down region is highlighted in parts (a)-(c).

In contrast with the lower-power case, high-power flight results in the presence of acoustic shocks. Fig. 4.7 shows statistics of the waveform from Fig. 4.5, when the aircraft is operating at 150% ETR. The derivative skewness in Fig. 4.7(b) reaches much higher values during this event, up to $Sk\{\partial p/\partial t\} = 14.3$, indicating the presence of significant shocks, even at 305 m from the aircraft flight path. The ASF also shows a higher peak in Fig. 4.7(c), with a value of 2.4 for the high-power case, indicative of significant shock content, versus 1.22 for the low-power case. Since the ASF is a ratio of positive derivatives to negative, a Gaussian waveform has an ASF of 1, meaning an ASF of 2.4 is much steeper than an ASF of 1.22. Also of note is the fact that the ASF peaks before the derivative skewness, meaning slightly closer in the forward direction relative to the nose of the aircraft; while the OASPL peaks when the microphone is at 115° from the nose of the aircraft, the ASF peaks at 122° and the derivative skewness at 130°. The relative angles between the peaks of the statistical metrics agree with previous findings from ground run-up analysis that the ASF peaks more in the forward direction than the derivative skewness, but these angles are roughly 10° more in the forward direction compared to ground run-up data.[19]

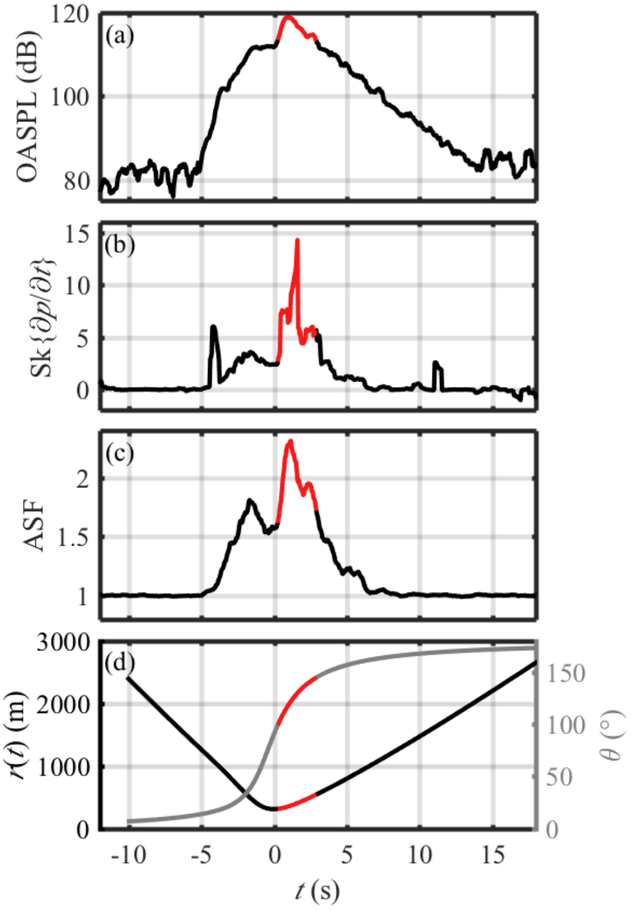

Fig. 4.7 Statistics of the 150% ETR flyover waveform in Fig. 4.5(a), specifically the (a) OASPL, (b) derivative skewness, (c) ASF, and (d) the distance from the aircraft to the microphone, *r(t)* and the angle of the microphone relative to the aircraft nose, *θ(t)*. The 6-dB down region is highlighted in parts (a)-(c).

This comparison between waveforms from the low and high-power engine conditions reveals a fundamental change in characteristics of the noise as engine power increases. The sharp, compressive shocks present at 150% ETR are noticeably absent at 55%. This analysis, which helps show nonlinear steepening as the source of high-frequency energy at large distance from the source, points to the importance of nonlinear propagation effects in the far field of flyover measurements.

4.5 Data Analysis

While the two waveforms examined in detail above provide a basis of discussion for nonlinear characteristics in flyover waveforms, a larger dataset is needed to establish more general trends. The following sections examine the OASPL, derivative skewness, and ASF from the entire course of measurements, featuring 5-6 flyover events each at 40, 55, 75, 100, and 150% ETR. Statistics are considered from microphones of different sizes, sampling rates, and heights. To present data from all of these conditions, statistics shown are calculated from the 6-dB down region of each waveform.

4.5.1 Engine Condition

A relatively well-known but important conclusion from the waveform discussion above is that the OASPL increases for higher-power operating conditions. The low-power case had a maximum OASPL of 100 dB, and the high-power case reached a maximum of 120 dB. As was also observed, the higher OASPL also results in an increase in nonlinear propagation and the presence of shocks at large distances away from the aircraft. A connection was made between nonlinear propagation and an increase in high-frequency energy in Fig. 4.3 for two example waveforms. This effect is shown for all spectra from flyover events at engine conditions ranging from 40% ETR to 150% ETR in Fig. 4.8. Microphone heights ranged from 0 to 91 m and there were 5-6 flyover events at each engine condition. Individual spectra are shown for each engine condition as thin, lighter lines, while thicker darker lines represent the energetic average from each ETR. Of particular note is the slope of the high-frequency spectrum, in particular from 2-6 kHz, which decreases steadily with increasing engine condition, from -70 dB/decade at 40 and 55% ETR to -39 dB/decade at 75%, -31 dB/decade at 100%, and only -21 dB/decade at 150% ETR.

This change in high-frequency energy, at distances of over 300 m from the source, shows that with increasing thrust comes an increase in nonlinear effects in the frequency range.

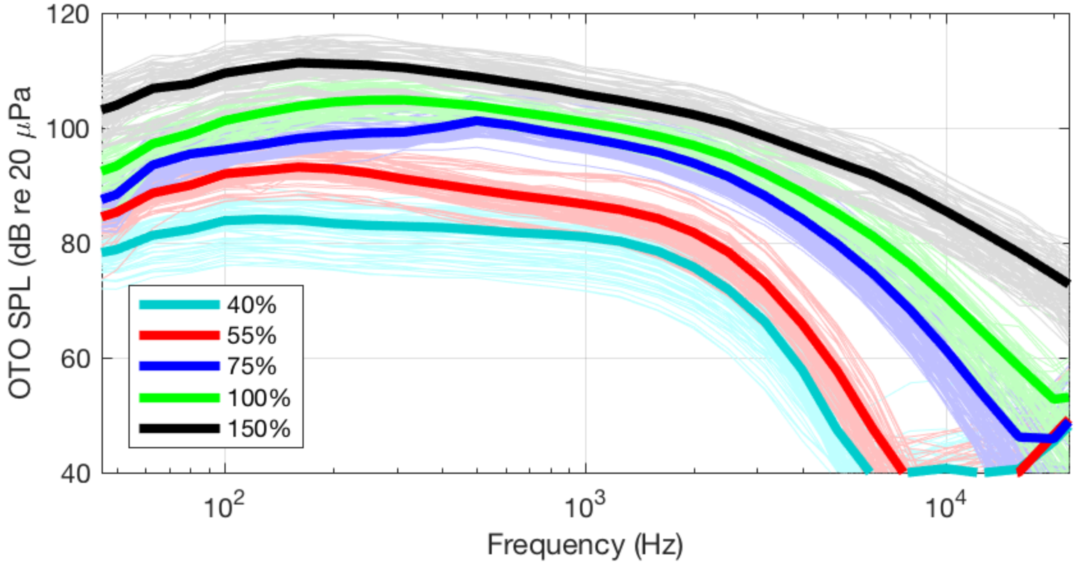

Fig. 4.8 Spectra from the north tower at varying engine condition. Spectra from individual waveforms are shown in lighter lines, while the average at each engine condition is shown in a thicker, darker line.

The increase in nonlinear effects with higher engine power is also shown by comparing nonlinearity metrics. The relationship between the increase in OASPL and increases in the nonlinearity metrics can be seen in Fig. 4.9. The derivative skewness, shown in Fig. 4.9(a), and the ASF, in Fig. 4.9(b), are plotted with respect to the OASPL, with statistics calculated from the 6-dB down region of the waveform. A clear trend is seen with increasing OASPL, as both metrics tend to increase. The increase in derivative skewness with OASPL appears almost exponential, with much larger values at 150% ETR than at 100% or below. At 100% and below, derivative skewness values are all below 5. These lower values indicate that significant shocks are not present at this location at 100% ETR and lower.[80] Interestingly, a wide spread of values is observed at

150% ETR, with derivative skewness ranging from 5 to 25. This large range of values could be due to multiple factors, including variations in distance from the aircraft to the microphone, changing weather conditions, a turbulent atmosphere changing shock characteristics,[88,89] natural variation due to the small sample size over which the statistics are calculated, and various measurement considerations. It should be noted that the cluster of data points above 120 dB are ground microphones, which have a higher OASPL due to pressure doubling with the ground reflection. However, in all cases the derivative skewness at 150% exceeds the values seen at lower ETR conditions, suggesting that the most significant shocks are likely to be found when the aircraft is operating at afterburner.

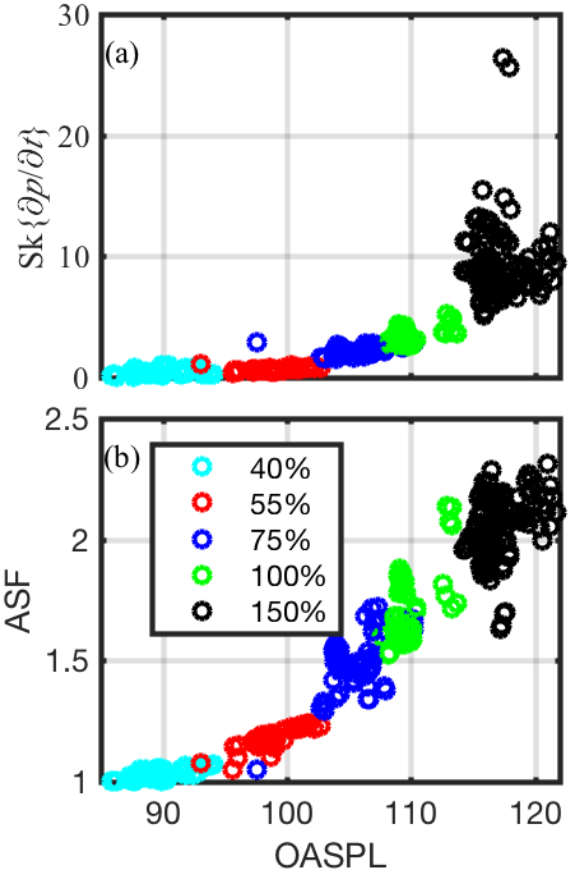

Fig. 4.9 Nonlinearity metrics of waveforms recorded from different flyovers on microphones of different size, specifically the (a) derivative skewness, and (b) ASF. Statistics are calculated from the 6-dB down region of each waveform. The level and derivative skewness values increase with engine condition, and a large spread in derivative skewness values is seen at 150% ETR.

4.5.2 Microphone size

The high-frequency energy associated with acoustic shocks may be affected by the frequency response of differently sized microphones.[28,83] For this investigation, waveforms at 150% ETR from two microphones placed 6” from each other, one ½” diameter and the other ¼”, allow for an easy comparison between similar waveforms. The similarity between the two microphones is seen in Fig. 4.10(a), where the waveforms from a ¼” microphone (same as shown in Fig. 4.4(a)) and its neighboring ½" microphone are plotted. The waveforms nearly overlay each other, and the PDFs of the pressure waveforms in Fig. 4.10(b) are nearly identical. This shows that for pressure or level-based measurements, the two microphones are essentially equivalent. However, small differences in the waveforms have a more noticeable impact on a few of the time derivative values in Fig. 4.10(c), and the PDFs of the waveform derivatives in Fig. 4.10(d) show differences for the largest derivative values. The waveform from the ¼" microphone exhibits higher derivative values, with some derivative values over 100 $\sigma_{\partial p/\partial t}$, while the highest derivative values from the waveform from the ½" microphone are at $80\sigma_{\partial p/\partial t}$. The presence of larger derivatives in the ¼" microphone show that the largest derivative values associated with acoustic shocks may be underestimated by larger microphones.

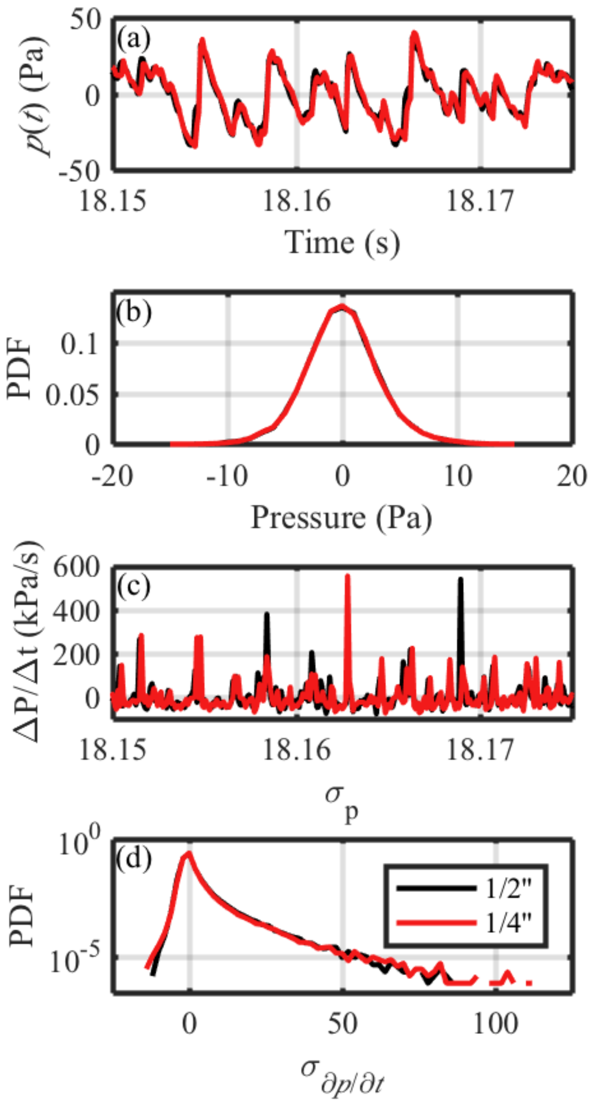

Fig. 4.10 Comparison of (a) a portion of the waveforms, (b) the PDF of the 6-dB down portion of the waveform, (c) the waveform derivatives, and (d) the PDF of the 6-dB down portion of the derivatives from microphones at the same location. The aircraft was operating at 150% ETR.

Differences in the waveforms due to microphone size also affect nonlinearity indicators. To quantify the effect of microphone size, statistics from ¼” and ½” microphones are shown in Fig. 4.11 as a function of OASPL for multiple flyover tests at engine powers ranging from 15% to 150% ETR, with more than 10 repetitions at each ETR condition. Microphones were included from five heights ranging from 0 m to 91.4 m. Although this gives a slight difference in distance between microphones, the largest difference in distance between the microphone at 91.4 m and the microphone at ground level is less than 9 m when the aircraft is flying at 76 m above ground. Statistics are calculated for the 6-dB down region for each microphone and flyover event. Fig. 4.11(b) shows that the derivative skewness measured by the ½” microphone is limited to a value of about 10 while those for the ¼” microphone tend to reach 15 (the small differences seen in the PDF of the derivative in Fig. 4.10(d) result in higher values for the derivative skewness, which accentuates the presence of outliers). At the highest engine power conditions, near 120 dB OASPL, derivative skewness values peak at 12.5 for the ½” microphones, while the derivative skewness values from the ¼” microphones reach up to 25. Thus, ¼” microphones (or smaller) should be used to measure high-power jet noise or if the source has a higher peak frequency, as is the case in model-scale jet noise, and in that case rise time is still likely to be limited by transducer size when using ¼” microphones.

It is interesting to note that the difference in microphone size does not appear to affect the ASF, shown in Fig. 4.11(c). The ASF is a linear average of derivative values, while the derivative skewness is raised to the third power and accentuates the largest derivative values. Therefore, microphone size may be less important if ASF is used to quantify waveform steepness.

The derivative skewness values shown in Fig. 4.11(a) represent a wide range of values that make a comparison between microphone sizes difficult to quantify. The difference in values is much easier to see when the derivative skewness values are fit to a curve. In this case a simple exponential fit is used because it accurately captures the behavior. Two fits were found, one from data recorded using the ½” microphones, and one from the data recorded using ¼” microphones, and plotted on top of the original data in Fig. 4.11(c). Though there is a wide spread of values for

OASPL > 115, the curve portrays a reasonable average behavior. The two curves are nearly identical below 110 dB, but above this level, which corresponds to the aircraft operating at 150% ETR, they diverge slightly. This difference, while not large, shows that microphone size has a measureable effect on the measurement of high derivative values.

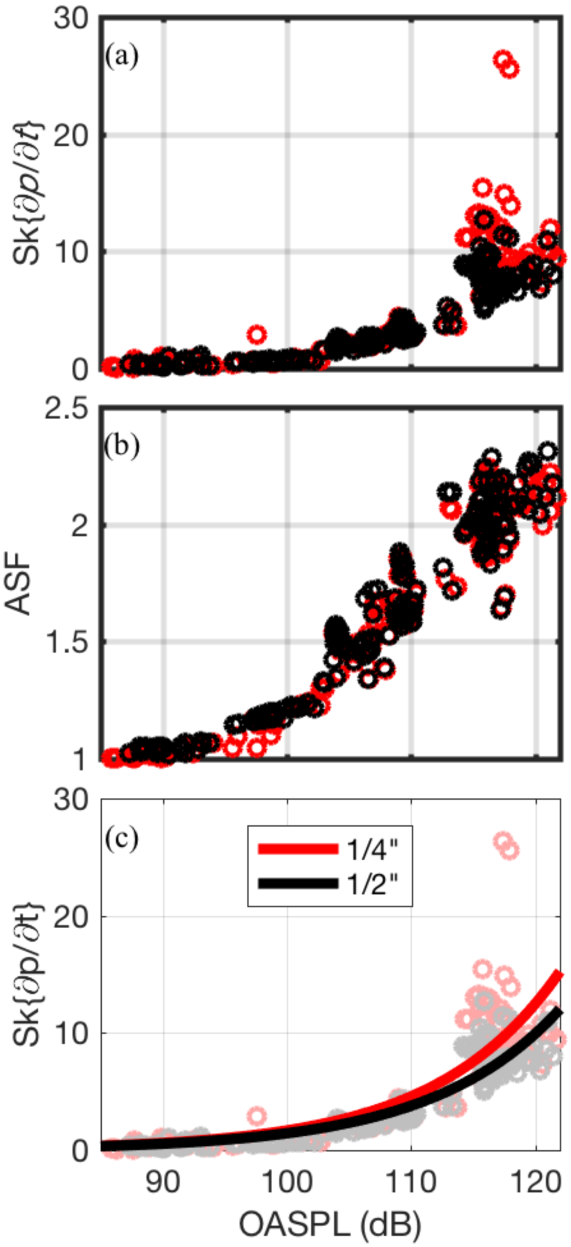

Fig. 4.11 Nonlinearity metrics of waveforms recorded from different flyovers on microphones of different size, specifically the (a) derivative skewness, and (b) ASF. Statistics are calculated from the 6-dB down region of each waveform. (c) The data for each microphone size are fit to curves overlaid on top of the data points.

4.5.3 Sampling Frequency

An important measurement detail that can have a significant impact on the estimation of nonlinearity indicators is sampling frequency. An inadequate sampling frequency not only limits bandwidth, but it also enforces a minimum resolvable rise time that may be insufficient to accurately gauge the nature of some acoustic shocks. To investigate the effects of sampling rate on derivative skewness, the 6-dB down regions of the high and low-power waveforms from Fig. 4.4(a) and Fig. 4.5(a) have been downsampled to lower sampling rates. The derivative skewness of the resampled waveforms is shown in Fig. 4.12(a) as a function of the new sampling rate. The 55% ETR case, where the waveform has slightly steepened but contains no significant shocks, was originally sampled at 102.4 kHz while the 150% ETR case was sampled at 204.8 kHz. The low-power measurement, despite the lower sampling rate, accurately captures the steepened nature of the noise, as evidenced by the fact that resampling yields very little change in derivative skewness until the sampling rate is below 20 kHz. The high-power measurement shows some change even as the sampling rate is lowered from 200 kHz to 100 kHz, as the derivative skewness drops from 8.6 to 8.1. A change this small indicates that a sampling rate of 200 kHz may be slightly underestimating the derivative skewness but is likely close to sufficient, but below 100 kHz the derivative skewness drops off more rapidly, with a value of 6.8 at 50 kHz and 4.5 at 20 kHz. Recent work by Reichman *et al.*[80] recommends a sampling rate of roughly 100 times the peak frequency of an initial sinusoid to accurately gauge derivative skewness. However, in this situation, the peak frequency of the noise is 100-200 Hz, and a sampling rate of 100 kHz may still be insufficient to observe the largest shocks. Thus, in the case of high-amplitude broadband noise, the recommendation of sampling at 100 times the peak frequency may fall short, and sampling rates of at least 500 times the peak frequency of the noise may be required to accurately calculate the derivative skewness.

While the derivative skewness, with its large emphasis on the steepest shocks, is affected significantly by a reduced sampling rate, the ASF is much more robust. The ASF of the 150% ETR waveform, shown in Fig. 4.12(b), remains at a nearly constant level as the waveform is downsampled, even to a value of 20 kHz, a tenth of the original sampling rate. This downsampling reduces the derivative skewness by more than a factor of 2, while the ASF is unchanged. Thus the importance of sampling rate depends on the behavior that needs to be identified. While the overall steepness of a waveform can be resolved with lower sampling rate, to accurately capture the largest shocks, sampling rates of 100-200 kHz should be used.

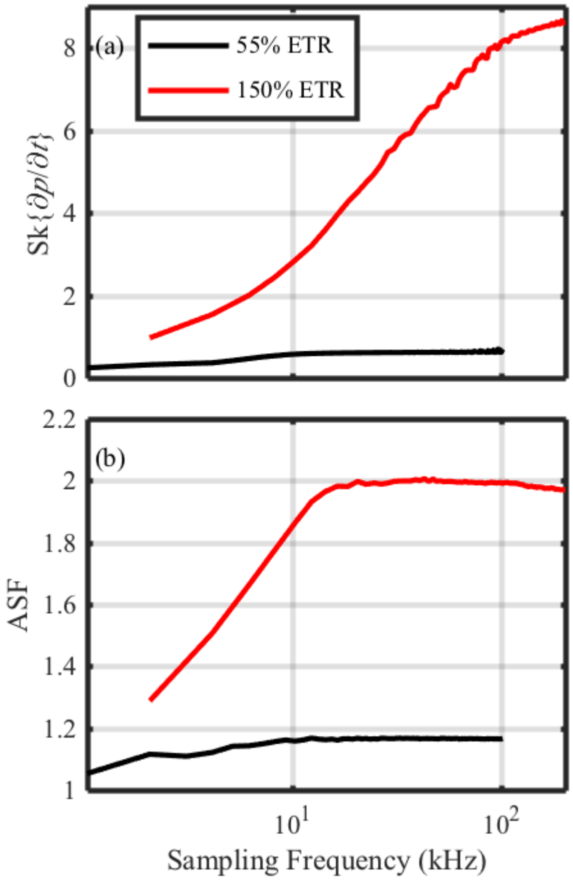

Fig. 4.12 The importance of sampling rate when estimating nonlinear parameters of shock-containing waveforms. The (a) derivative skewness and (b) ASF of the 6-dB down portion of the waveforms from Fig. 4.4(a) Fig. 4.5(a) is calculated as the waveforms are resampled to lower sampling rates.

The reduction in derivative skewness due to an inadequate sampling rate can be observed in more than a single waveform. To illustrate this for all data, the data points of derivative skewness as a function of OASPL were fit to an exponential curve, similar to the process used to create Fig. 4.11(c). All of the represented waveforms were then downsampled, the derivative skewness was calculated from the downsampled waveform, and the data points were again fit to an exponential curve. The curve fits of the downsampled data are shown in Fig. 4.13(b), for new sampling rates of $f_s = 102.4$, 51.2, 20.5, and 10.2 kHz. Solid lines represent data from ¼" microphones, while dashed lines are from ½" microphones.

As the sampling rate is reduced from 204.8 kHz to 102.4 for the data from ¼" microphones, only minimal differences are seen at the highest values. Though the individual data points are not plotted here at each sampling rate, it is worth noting that the small changes here occur at only the largest outliers, the points in Fig. 4.11(c) that have $\mathrm{Sk}\{\partial p/\partial t\} \geq 15$. As the sampling rate is further reduced to 51.2 kHz, a more noticeable decrease at the largest values is observed. Once again, this decrease is due to changes in the larger points in Fig. 4.13(a), and points that are closer to $\mathrm{Sk}\{\partial p/\partial t\} = 5$ are essentially unaffected by the resampling. For very low sampling rate of 20.5 and 10.2 kHz, drastic reductions in derivative skewness are seen, even for relatively low derivative skewness values. While these low sampling rates are not likely to be seen in practice in full-scale military jet noise, it is worth noting that 10-20 kHz is roughly 100 times the peak frequency of the signal, and thus the earlier recommendation from Reichman *et al.*[80] may fall short for the case of jet noise. The trends observed are similar for ½" microphones, but with less of a difference between 102.4 kHz and 51.2 kHz. It is important to note that sampling at a rate of 51.2 kHz with a ¼" microphone gives a similar curve to sampling at 204.8 kHz with a ½" microphone, suggesting that using a large microphone has a similar effect to reducing sampling frequency. In summary, when the amplitude and steepness of the largest shocks must be accurately characterized, such as obtaining an estimate of the derivative skewness, it is important to have a high sampling rate. However, when the ASF or similar metrics are used, sampling rate is less of an issue.

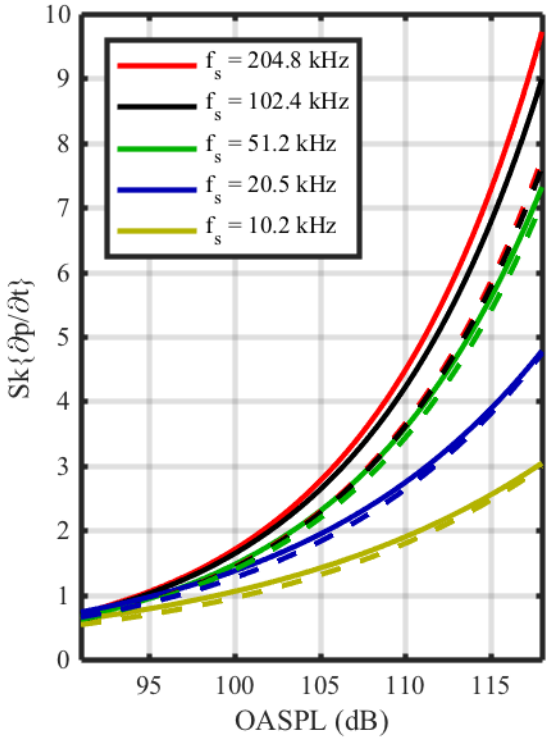

Fig. 4.13 The effects of resampling on trends for derivative skewness with two different microphone sizes. Waveforms were separated according to microphone size and then resampled to various lower sampling rates. Derivative skewness values were fit to a curve and plotted against the OASPL. Solid lines represent data from ¼” microphones, and dashed lines from ½” microphones. The 204.8 kHz and 102.4 kHz lines for ½” microphones lie almost directly on top of each other.

4.5.4 Microphone Height

According to ANSI S12.75-2012, the standard for aircraft flyover measurements, microphones at different heights are used to assess azimuthal directivity.[28] However, because the source and receiver are now both operated above ground there are multi-path interference nulls as well as other possible phenomena that may affect the presence of acoustic shocks. This brings about a need for an analysis of nonlinear indicators as a function of microphone height. The statistics of the ¼” microphones (as shown in Fig. 4.11) are identified by height in Fig. 4.14. These statistics appear to be fairly constant for heights between 9.1 m and 91 m. The derivative skewness in Fig. 4.14(a) shows an invariance with height above 9.1 m. At OASPL = 115 dB, the derivative skewness ranges from roughly 5-15, but this variation occurs at all microphone heights. The ASF exhibits a similar behavior as illustrated in Fig. 4.14(c). The similar values across all heights show that the presence of acoustic shocks is relatively unaffected by measurement height, especially above 9.1 m.

Though the behavior of these statistical metrics appears to be consistent between 9.1 m and 91 m, some slight variations are seen in the 0 m microphone. One height-dependent trend that is noticeable is the fact that data points measured at 0 m are consistently associated with an OASPL roughly 3 dB higher than other points. The ground microphone measures pressure doubling, as the incident and reflected waves are perfectly coherent across all frequencies, leading to a 6 dB increase compared to a free-field wave. However, the elevated microphone receives both the incident and reflective wave, which are emitted at different times and locations. These differences result in significantly lower spectral coherence. The resulting spectrum may have interference effects at certain frequencies, but the lower coherence allows their energies to be effectively combined incoherently, which results in an approximate 3 dB increase compared to a free-field wave. Comparing these two different reflection effects provides the observed difference of ~3 dB OASPL between the ground and elevated microphones. For the clusters of points centered at 109 and 117 dB for heights 9.1-91.4 m, the corresponding OASPL of the 0 m microphones is centered at 112 and 120 dB. Though not as noticeable, it appears that some derivative skewness values for the 0 m microphones at 120 dB are slightly lower than corresponding microphones. This behavior has been previously reported by McInerny *et al.*,[27] who showed that some of the largest derivative values were absent at microphones near the ground. This would lead to lower derivative skewness values. However, this behavior affects only the largest shocks, and the ASF is relatively unaffected.

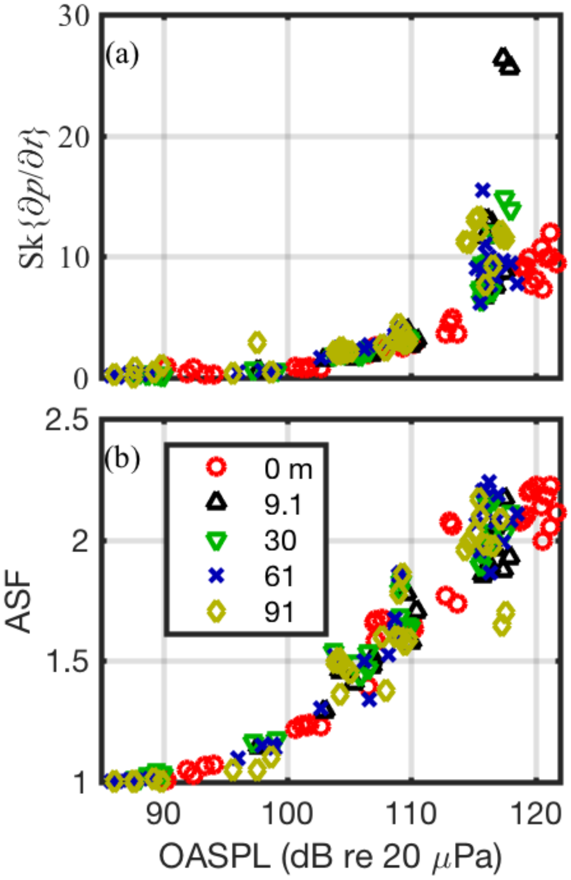

Fig. 4.14 Comparison of the (a) derivative skewness and (b) ASF for varying microphone heights, plotted against OASPL. All data shown are from ¼" microphones, with statistics calculated from the 6-dB down region.

4.6 Conclusions

Acoustic emissions from an F-35 in flight show strong evidence of acoustic shocks due to nonlinear propagation, even at distances of 305 m from the flight path. Statistical measures confirm that slight waveform steepening occurs at low engine power and significant shocks form at high engine power that persist to large distances. The ability to which these acoustic shocks can be accurately characterized depends upon sampling frequency, microphone height, and microphone size. Analysis of these trends lead to three recommendations for future measurements.

First, statistical measures of nonlinearity are relatively constant for heights above 9.1 m. This means that, while directivity concerns may necessitate higher elevated microphone, for the purposed for shock characterizations microphones should be off the ground, but do not need to be higher than 9.1 m. Second, microphone size may limit the minimum resolvable rise time for the largest shocks. In most situations, including spectral content in the audible range, either ½” or ¼” microphones may be used. However, if accurate characterization of small rise times is essential, ¼” microphones should be used. Finally it is recommended that data be sampled at 100-200 kHz. Future work is needed to consider effects of weather-related phenomena, including wind and temperature and their connection to possible turbulence, and to connect nonlinear metrics from ground run-up measurements to metrics from flyover measurements.

Chapter 5

Comparison of Noise from High-Performance Military Aircraft for Ground Run-up and Flyover Operations

5.1 Introduction

While the majority of jet noise research occurs with a static jet or aircraft, in-flight operations represent the majority of jet noise exposure from a community noise standpoint. Static measurements, either from model-scale jets or tethered aircraft, provide for a controlled environment with set locations and long exposure times. In-flight measurements are inherently complicated by factors such as smaller integration time for metrics, uncertainty in distances between the aircraft and measurement locations, and atmospheric propagation effects,[22,23]. However, the changing nature of the source between static and in-flight operations necessitates measurements during flyover events.

Jet noise can be ascribed to several different phenomena, but the dominant structure in military jet aircraft noise is caused by the turbulent mixing of the jet with the air around it. Analytical derivations and measurements of in-flight effects have shown how the turbulent mixing region is affected by a secondary flow around the jet itself.[24,26] Three main changes in the sound field are: first, the overall sound pressure level (OASPL) is reduced in the maximum radiation region. Second, the peak radiation direction is shifted forward. Third, the OASPL increases in the forward direction. These changes are confirmed through comparison with experimental results for model-scale work.[78] Analytically predicted OASPL values compare favorably with experiment, showing agreement within 1-2 dB for Michalke and Michel.[26] However, their prediction method relies on extended measurements of the OASPL at many known nozzle exit velocities and temperatures, limiting its application in military jet noise predictions as exact temperature and velocity conditions are not publicly available. In addition, the jet Mach numbers, temperatures, and flight velocities are much larger for military jet aircraft than have been used in prior analyses, and so trends observed in prior work may be of greater or lesser importance in full-scale military aircraft.

The change in levels associated with flight effects is likely to affect the importance of nonlinear propagation in the aircraft far field.[25] Nonlinear propagation in jet noise has been shown to steepen waveforms and form shocks in the far field, resulting in high-frequency energy that would otherwise not exist at large distances from the source.[18,21,90] The effects of nonlinear propagation have been shown in model-scale experiments[33,91,92] and full-scale military jet engine noise experiments,[10 ,19] but the importance of nonlinear effects is especially apparent in the far field of military jet aircraft. Viswanathan and Czech[25] showed that high-frequency energy in the far field can be attributed to nonlinear propagation for laboratory-scale jets with co-flow. McInerny *et al.*[27] and Reichman *et al.*[93] showed evidence of nonlinear propagation and the presence of shocks in the far field of military jet aircraft during flyover measurements but did not compare the effects to similar conditions on the ground. Nonlinear effects are dependent on the amplitude of the noise, so changes in OASPL-reductions in the peak radiation direction and increases in the forward direction-are likely to affect the importance of nonlinear propagation in the noise in those directions.

This chapter represents the first comparison of in-flight noise radiation with that from static or ground run-up measurements for military jet aircraft. This chapter compares OASPL, spectra, and various nonlinearity indicators to show that even for exit velocities and aircraft speeds higher than those seen in laboratory-scale experiments, some of the same general trends identified by Michalke and Michel hold for static and flying military aircraft, though these effects can be more or less apparent, depending on engine condition. In contrast with ground run-up measurements, evidence of azimuthal directivity is seen in flyover measurements. Flyover events are examined at 75%, 100%, and 150% ETR, and consistency of the results with aircraft height is shown. In addition, the nonlinearity analysis shows that the slight reduction in OASPL in the peak radiation direction does not significantly alter nonlinear propagation and shock content, but significant shocks are present in the forward direction during flyover measurements, a marked changed from the ground run-up measurements.

5.2 Measurements

The comparisons in this chapter are performed on measurements of the F-35A and F-35B variants for both ground run-up and flyover measurements. Measurements were taken in September 2013 at Edwards Air Force Base, California. The ground run-up measurement layout has already been described in detail by James *et al.*[71] but microphone locations are shown here in Fig. 5.1(a). Each location shown here has one microphone height at each location, with heights ranging from 1.5 m to 9.1 m. The origin of the coordinate system in Fig. 5.1(a) is the microphone array reference point (MARP), located 6.7 m downstream of the nozzle as an approximate source location, meaning the nozzle is located at $x = 6.7$ m and exhaust is flowing in the $-x$ direction. Measurements were made by a collaboration of the Air Force Research Laboratory; Blue Ridge

Research and Consulting, LLC; Brigham Young University; Wyle Laboratories; and the Naval Air Systems Command (NAVAIR).

While the ground run-up measurement consisted primarily of semi-circular arcs of microphones at different radii from the MARP, the flyover array consisted of linear arrays as shown in Fig. 5.1(b), which has been described by James *et al.*[71] Microphones were suspended from two cranes at a distance of 305 m on either side of the nominal flight path, at heights ranging from 0 m to 91 m. Microphones between these two cranes were arranged in a line perpendicular to the nominal flight path, and at each measurement location microphones were located at 0 m, 1.5 m, and 9.1 m. Finally, an array of microphones was located on the ground below the nominal flight path. The majority of microphones were ½” (12.7 mm), with some ¼” (6.3 mm) microphones on the crane at $y = 305$ m. Sampling rates varied between measurement systems, with sampling rates of 96, 192, and 204.8 kHz. For the flyover events used in this study the aircraft flew in the $+x$ direction nearly over the $y = 0$ line ($\pm$10 m) at a height of 76 m ($\pm$ 3 m). Data from the aircraft were used to ensure that analyses were performed only for the times at which the aircraft was operating at the desired engine condition.

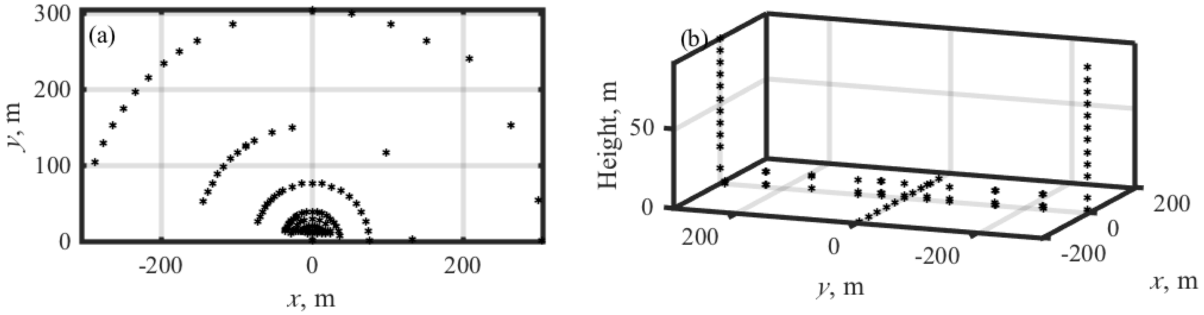

Fig. 5.1 Layout for the (a) ground run-up and (b) flyover measurements.

Directivity of the flyover noise is discussed in both the polar and azimuthal directions. As is typical in reporting jet noise, the polar angle θ is measured from the nose of the aircraft as shown in Fig. 5.2. This angle varies as the aircraft flies along the flight track for each microphone, while the azimuthal angle, ϕ, is relatively constant. An azimuthal angle of $\phi = 0$ means that the microphone is located directly under the aircraft, while $\phi = 90$ means the microphone is located at aircraft height.

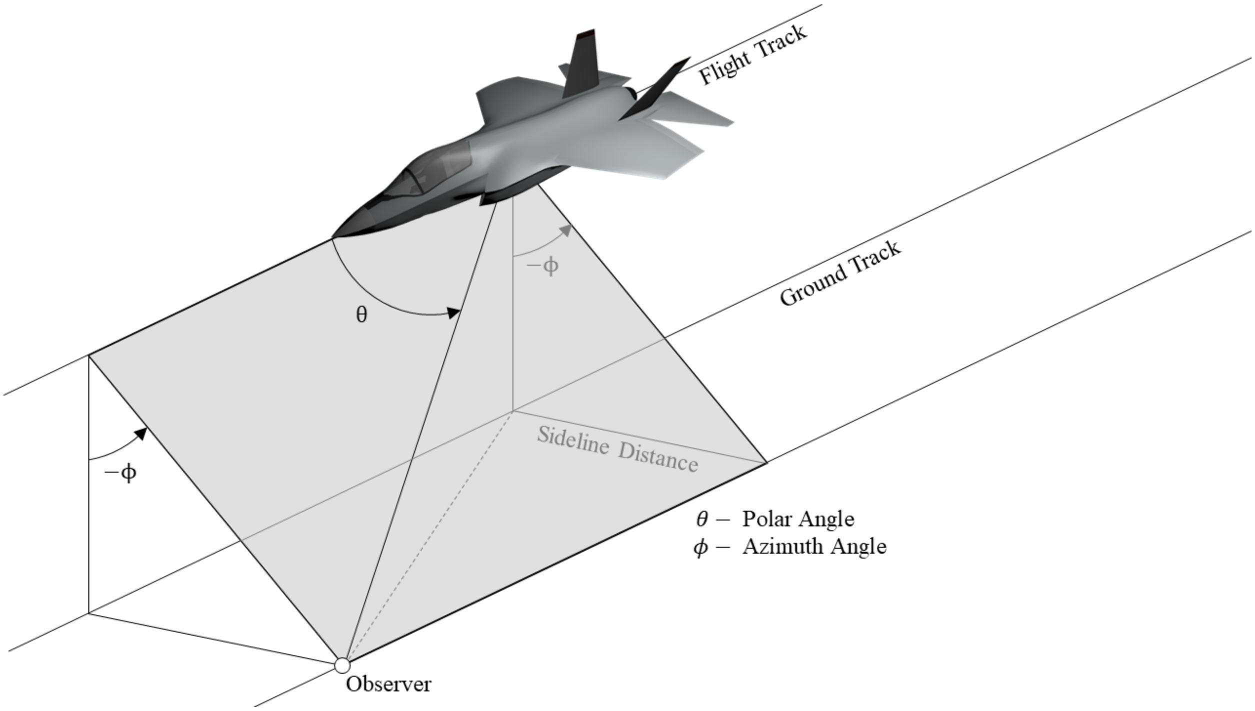

Fig. 5.2 Illustration of azimuthal angle ϕ and polar angle θ relative to the flight track.

5.3 Metrics

When comparing the sound field between ground run-up and flyover there are multiple quantities of interest. While there are many sound metrics that could be compared, this chapter concentrates on sound pressure level and two nonlinearity metrics, the derivative skewness and ASF.

5.3.1 Sound Pressure Level

Sound pressure level is the simplest quantity that can be compared between these situations, as it can be adjusted for spherical spreading. Comparisons are slightly more complicated when performed frequency-by-frequency, as atmospheric absorption and nonlinear propagation complicate distance corrections, in particular for higher frequencies and over long distances.[92] However, a comparison as a function of one-third octave (OTO) band center frequency can still be made because of the wide range of measurement locations in both ground run-up and flyover measurements.

5.3.2 Derivative Skewness

The skewness of a distribution expresses asymmetry of the PDF and accentuates outliers due to the cubed nature of the numerator. The skewness of a zero-mean variable x is defined as

$$\mathrm{Sk}\{x\} = \frac{E[x^3]}{E[x^2]^{\frac{3}{2}}}. \tag{5.1}$$

A value of $\mathrm{Sk}\{x\} = 0$ represents a symmetric distribution, while a positive number indicates the presence of a greater number of large positive values than negative. The skewness of the pressure waveform, $\mathrm{Sk}\{p\}$ was initially used to quantify crackle, an auditory phenomenon associated with shock waves within jet noise.[10] However, to quantify shocks themselves it is more useful to use the derivative skewness, $\mathrm{Sk}\{\partial p/\partial t\}$, which refers to the skewness of the PDF of the first time derivative of the waveform and expresses an asymmetry in derivative values. The derivative skewness accentuates the large derivatives (rapid pressure increases) associated with shock waves, thus, is a useful indicator of shocks forming due to nonlinear propagation.[12,48] It has been shown that a derivative skewness value greater than five is indicative of significant shocks within a waveform.[17,80]

5.3.3 Average Steepening Factor

The ASF[50] is also based on derivative values and defined as the average value of the positive derivatives over the average value of the negative derivatives:

$$\mathrm{ASF}\{p\} = \frac{E[\dot{p}^+]}{E[\dot{p}^-]}. \tag{5.2}$$

The ASF, which is an inverse of the previously used WSF,[15] is a linear average of derivative values, which makes it less sensitive to outliers than the derivative skewness, and thus better represents average behavior. An ASF value of one represents a waveform with no significant steepening, while $\mathrm{ASF} > 1$ represents some steepening. It has been shown that for jet noise, both full-scale and model-scale, that an ASF value between 1.5 and 2 is indicative of the presence of shocks, with an ASF value approaching two suggesting significant shock content.[16,81]

5.3.4 Example of flyover metrics

To show expected behavior in metrics during a flyover event, an example waveform and the calculated metrics are shown in Fig. 5.3. The waveform, which was recorded at a microphone located at $x = 0$, $y = 0$, $z = 0$ in Fig. 5.1b), is shown in Fig. 5.3(a) along with its derivative in Fig. 5.3(b), with $t = 0$ corresponding to the time of peak OASPL. Using tracking data from the aircraft, the relative position of the aircraft to the microphone in question can be calculated as a function of time; the time-dependent distance, $r(t)$, and polar angle, $\theta(t)$, are shown in Fig. 5.3(c). To describe the time-varying properties of the sound, metrics were calculated for 0.1 s sections of the waveform. Each section contained 50% overlap, meaning that the resolution is 0.05 s. The resulting 0.1 sec OASPL, derivative skewness and ASF are shown in Fig. 5.3(d)-(f), respectively.

The aircraft passes nearest the microphone shortly before the peak OASPL, at $t = -0.35$ s. The derivative skewness in Fig. 5.3(e) peaks at the same time as the OASPL ($t = 0$), but another peak is seen at $t = -0.9$ s, indicating that shocks are present in the forward direction of the aircraft. These forward shocks, which produce a noticeable effect in auralizations, are the predominant feature shaping the ASF, which peaks at $t = -1.2$ s. It is important to note that the distance to the aircraft is not constant over the duration of the flight, making it difficult to compare the ASF and derivative skewness values as a function of angle at a single microphone.

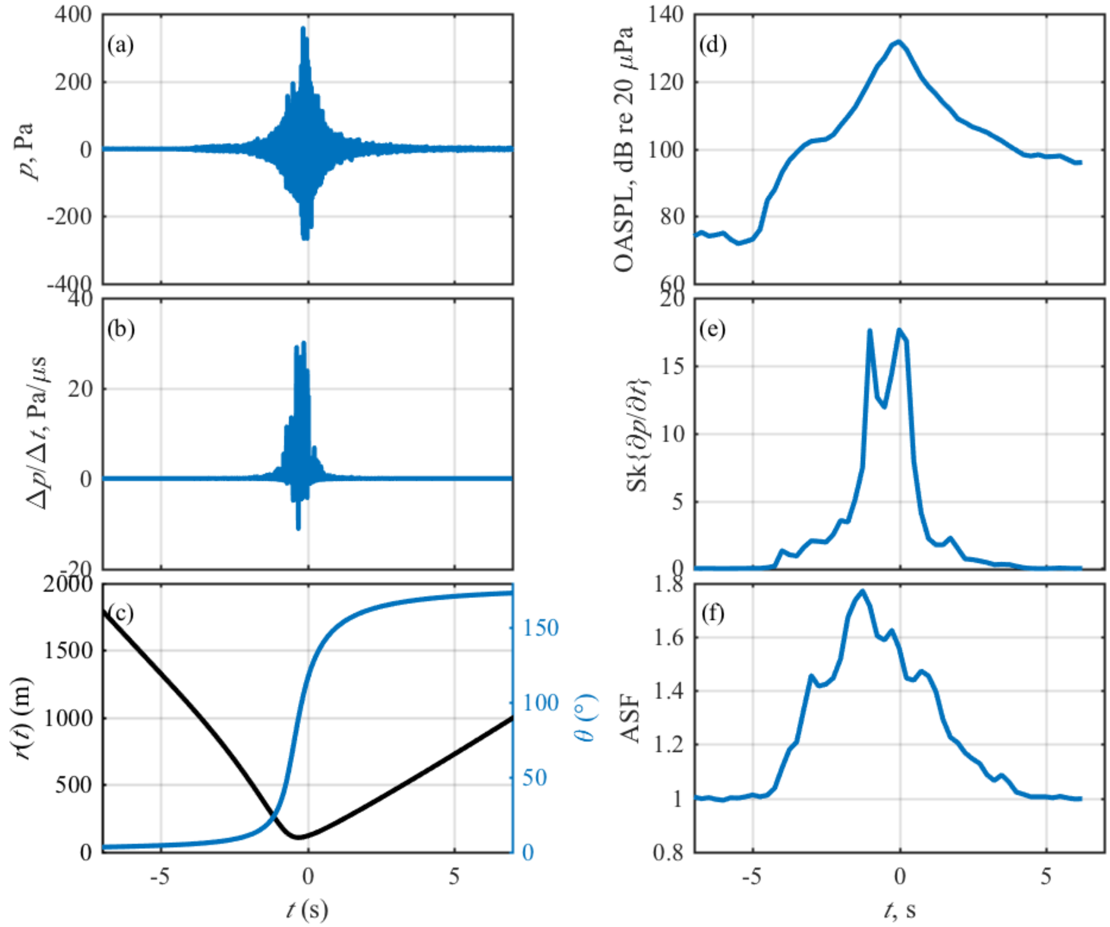

Fig. 5.3 Example waveform and metrics from a flyover measurement.

5.4 OASPL Comparison

Comparisons of OASPL and directivity of the source between ground run-up and flyover measurements have been made in previous experiments[26,73,94,95] and the subject has received an analytical treatment from Michalke and Michel.[26] As explained earlier, the three main consequences expected are (1) a decrease in OASPL in the main directivity lobe, (2) a shift towards the sideline in the main directivity lobe, and (3) an increase in OASPL in the forward direction. In this section directivity curves from flyover measurements are compared with those from ground run-up. Expected changes between the two measurements are observed, and some evidence of azimuthal variation during flyover measurements is shown.

5.4.1 Method

To compare between ground run-up and flyover measurements, we must first find common measurement locations at which to compare. The data from the ground run-up measurements provide information at various distances and angles ranging from 0° to 160°. However, in the far field where a direct comparison with flyover measurements is more likely, the measurement locations are more sparse, with microphones located only at distances of 76 m, 152 m, and 305 m from the MARP at spacing of 5-10°. In comparison with this, as the aircraft flies through the flyover measurement array, each microphone receives sound radiated at nearly all angles, but over a wide and constantly varying set of distances. However, because atmospheric absorption and nonlinear propagation have relatively small effects on OASPL (~1 dB) when compared with geometric spreading, the distances can be normalized to a standard distance assuming spherical spreading. This allows the OASPL curve shown in Fig. 5.3(d) to be compared with measurements made during ground run-up at a set distance, e.g. 76 m, over a wide range of angles

5.4.1.1 Directivity Curves

Normalizing the OAPSPL for distance gives a polar directivity curve for each microphone from the flyover measurement arrays. These curves are shown in Fig. 5.4(a) for all microphones for a single flyover event at 150% ETR, with line color corresponding to azimuthal angle ϕ, with $\phi = 0°$ corresponding to directly underneath the aircraft, and $\phi = 90°$ corresponding to a microphone at aircraft height. Though the curves exhibit a similar pattern for $\theta = 10$ to $160°$, the variation in OASPL is on the order of 5-10 dB. This variation can come from a variety of sources, including azimuthal angle and downward or upward-refracting atmospheric effects. The ground microphones experience pressure doubling due to the reflection off of the hard ground at the measurement location, while elevated microphones have a mix of destructive and constructive interference. This results in the ground microphones having an OASPL roughly 3 dB higher than the elevated microphones: Thus, 3 dB is subtracted from the ground microphone directivity curves before being plotted in Fig. 5.4(a). Taking the average after this correction results in the two curves shown in Fig. 5.4(b), where the ground and above-ground OASPL values agree within 1 dB. The corrected data will be used for all subsequent data shown.

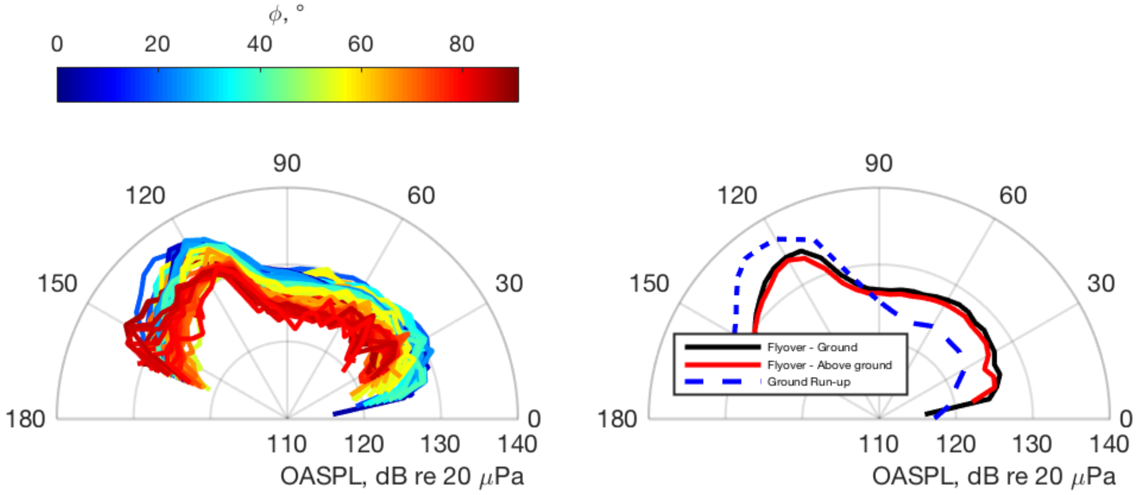

Fig. 5.4 Calculated directivity curves at a height of 76 m from (a) all microphone channels for one flyover event, colored according to the azimuthal angle ϕ, and (b) the averaged result for the flyover array's ground microphones (-3 dB correction, black), the flyover array's elevated microphones (red), and the ground run-up arcs at 76m (blue).

5.4.1.2 Comparison of Average Results

The average behavior of the flyover directivity curves in Fig. 5.4(a) exhibit the expected behavior from earlier work. The mean of the directivity curves for both on-ground microphones and above-ground microphones is shown in Fig. 5.4(b) and compared with the ground run-up measurement. This comparison exhibits many of the trends predicted analytically by Michalke and Michel.[26] The trends predicted by Michalke and Michel include a reduction in OASPL in the flyover in the maximum radiation region, as well as a shift in the maximum radiation region in the forward direction. These trends are observed in Fig. 5.4(b), with a peak directivity of 115° for the flyover results compared with 130° during ground run-up. In addition, Michalke and Michel also predicted an increase in OASPL in the forward direction, which is evident in Fig. 5.4(b) as an increase of 3-4 dB is seen from 20°-90°. Though the lack of exhaust velocity and temperature data for the F-35 prevent predictions of flyover OASPL based on ground run-up data, the trends seen in the comparison agree with other experiments and the theory set forth by Michalke and Michel.

5.4.1.3 Consistency with Aircraft Height

The results above are consistent with expectations from prior work but represent only one flyover event. To begin investigating the consistency of the results, directivity curves are shown for a flyover event at 150% ETR at an aircraft height of 305 m. These polar directivity curves confirm many of the features observed at the aircraft height of 76 m (Fig. 5.4). First, the curves in Fig. 5.5(a) show a noticeable azimuthal directivity. While azimuthal angle is limited to ~50 degrees at this aircraft height, a decrease of ~2 dB is consistent with the difference in Fig. 5.4. In addition, excellent agreement is seen in the OASPL between the two events, as shown in Fig. 5.4(b) and Fig. 5.5(b). The exact trends seen at a height of 76 m in Fig. 5.4(b), including a reduction in OASPL in the aft direction and an increase in the forward direction, are observed at 305 m, and levels agree at all observed angles to within 1 dB. These confirm the observation of previously reported behavior for the shift in polar directivity due to flight effects. However, they also point to an azimuthal variation not seen in laboratory-scale experiments.

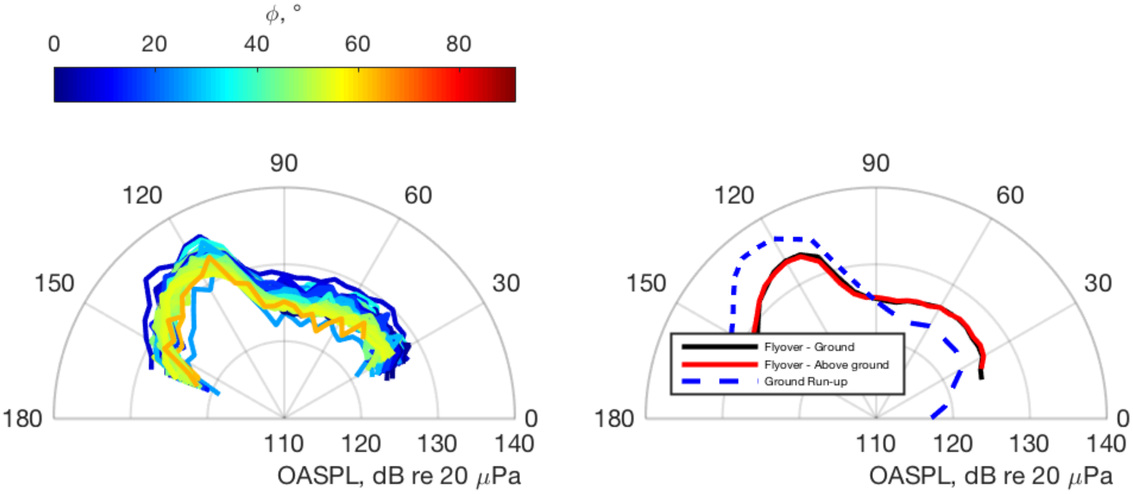

Fig. 5.5 Polar directivity of an aircraft at height of 305 m (a) shown for all microphones and (b) an average directivity for microphones located on and above the ground and compared with ground run-up.

5.4.1.4 Azimuthal Directivity

As seen in Fig. 5.4(a) and Fig. 5.5(a), differences due to azimuthal directivity during flyover events may be on the order of 3-4 dB. To investigate this possible variation, the OASPL from both flyover heights is interpolated onto a grid in θ and ϕ, and plotted as a function of θ and ϕ to show azimuthal variations. The azimuthal variations are shown in Fig. 5.6 for flyover events at (a) 76 m and (b) 305 m. It is interesting to note that the directivity maximum is not located directly under the aircraft, but roughly 20-30° to the side. A decrease in OASPL on the order of 3 dB is seen at larger angles of 70-80° in Fig. 5.6(a). However, in Fig. 5.6(b) these larger angles are not visible due to the increased aircraft height. While discrepancies exist between the directivity shown between the two heights, both show a decrease in OASPL for approximately $\phi > 50$.

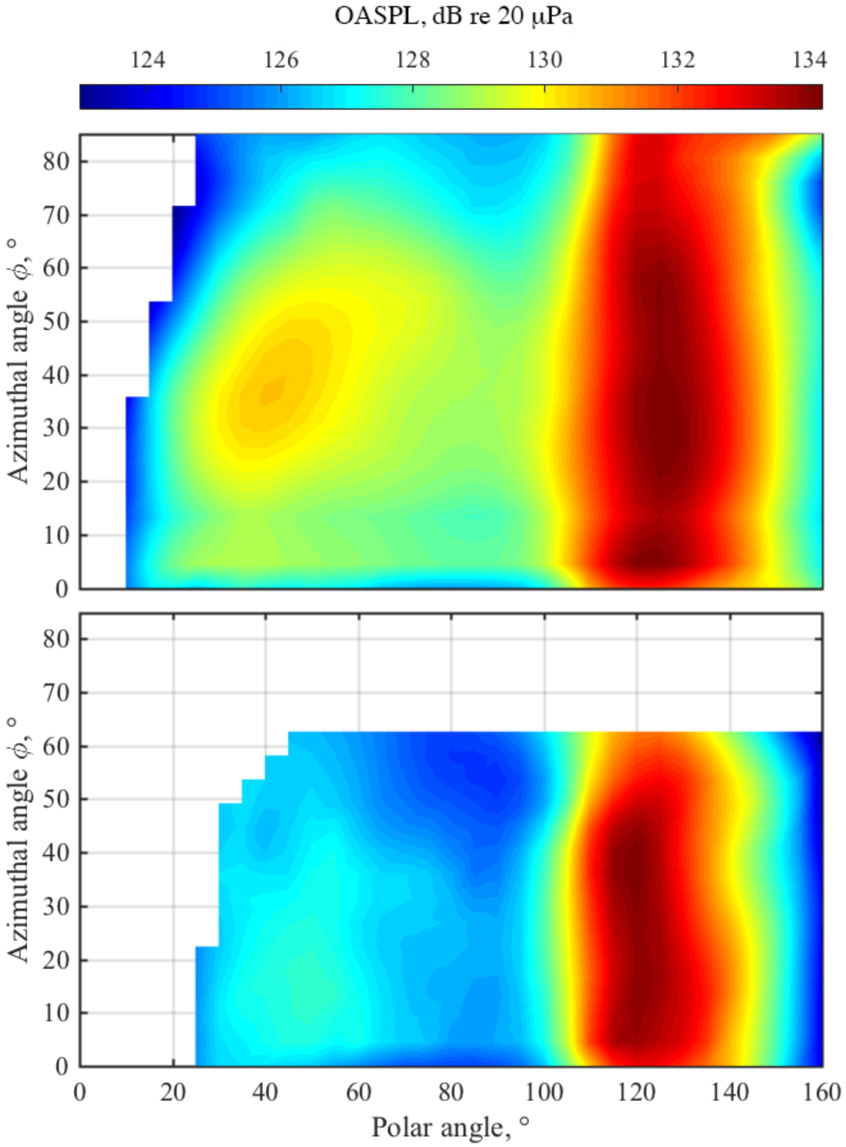

Fig. 5.6 OASPL as a function of polar angle θ and azimuthal angle ϕ during 150% ETR flyover events at aircraft heights of (a) 76 m and (b) 305 m.

Because the circular nozzle of the F-35 would not suggest any azimuthal asymmetry, the azimuthal directivity seen in Fig. 5.6 is at least in part unexpected. While factors such as flow around the aircraft and its features may produce some directivity, other factors must be estimated. One such factor that can be estimated is loss due to longer propagation distances to microphones at a higher angle ϕ. A simple way of calculating expected losses due to linear atmospheric absorption is to calculate α, the expected absorption coefficient, at the characteristic frequency of the jet noise. At a frequency of 400 Hz, roughly twice the peak frequency of the noise from an F-35, the expected loss due to atmospheric absorption over a distance of 300 m is 0.65 dB, smaller than the variation with ϕ shown in Fig. 5.6. Another possible explanation is loss due to nonlinear propagation, but previous modeling has shown that this effect should be limited to roughly 1 dB over the range of interest. Thus, it is likely that the differences seen in Fig. 5.6 are in fact due to azimuthal directivity, rather than atmospheric absorption and nonlinear propagation.

Another way of separating propagation and azimuthal effects is to consider the variation with distance at a single polar angle, as shown in Fig. 5.7. Here the OASPL, corrected for spherical spreading to a common distance of 76 m, is shown at each microphone as a function of measurement distance r for a constant polar angle of $\theta = 120°$ relative to the nose of the aircraft. These data points are taken from in Fig. 5.4 and Fig. 5.5 for the polar angle of $\theta = 120°$ for six flyover events at 76 m and 305 m at 150% ETR in Fig. 5.7(a) and 100% ETR in Fig. 5.7(b), with each data point representing the OASPL at one microphone for a single flyover event. Each data point is colored according to azimuthal angle ϕ. Clustering of the data is immediately noticeable, with the two groups of blue circles at 100 m and 400 m representing the mics closest to the flight path at the flyover heights of 76 m and 305 m. While in each group there is a wide spread of OASPL levels, the slight decrease in average behavior of the OASPL between these two groups is similar to what would normally be expected due to the longer propagation distance. In a lossless environment, these two groups should be nearly identical when corrected for spherical spreading to a common distance. Instead, a decrease of ~1.5 dB is seen when comparing average OASPL for each group. As explained above, this is likely due a combination of losses from atmospheric absorption over an additional 300 m of propagation and losses due to nonlinear propagation. A similar difference in level is seen when comparing cyan and green dots at 200 m and 450-500 m. However, the group of red and orange dots at 350 m is substantially lower than the blue dots at a similar distance. Though these two groupings are from different flyover heights, with the red dots from a flyover height of 76 m and the blue dots at a flyover height of 305 m, the propagation distances are nearly identical and long-range propagation effects should be similar. Thus, the difference between the average behavior of these two groups, on the order of 2 dB, can likely be attributed to azimuthal directivity. This behavior is not limited to a single flyover event, as the data shown here are from multiple flyover events, and the trends seen in Fig. 5.7(a) for 150% ETR are also observed in Fig. 5.7(b) at 100% ETR, showing systematic asymmetry in the azimuthal direction.

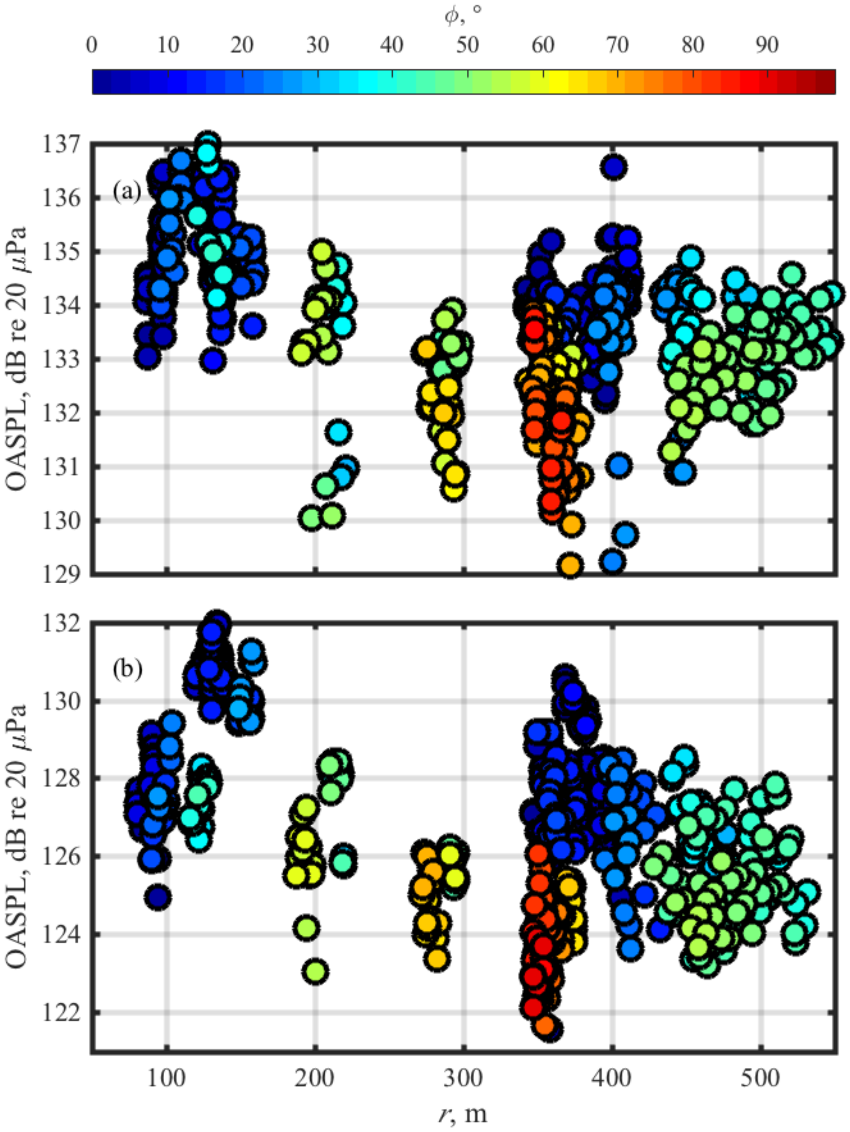

Fig. 5.7 OASPL at a polar angle of 120° plotted against measurement distance *r* for flyover events at (a) 150% ETR and (b) 100% ETR.

5.5 Field Comparisons

While the comparison of OASPL and directivity describes some of the differences in the sound field between ground run-up and flyover measurements, more comparisons are needed to understand additional characteristics of the noise. However, as other metrics are not as easily corrected for distance as the OASPL, a different approach is needed to compare spectra and nonlinearity metrics, for example derivative skewness and ASF. In this section, a method of comparing the entire field is introduced, then comparisons are shown for OASPL, nonlinearity metrics, and spectra across the field of measurement for flyover events at 76 m.

5.5.1 Method

As the aircraft flies near the measurement array, data are continuously collected at each microphone and the aircraft position is recorded every 0.1 s. Using the 0.1 s blocks mentioned in Section 5.2, we can again calculate distance and polar angle θ similar to process in Section 5.4. When the aircraft is flying at a height of 76 m, most of the microphones that can be compared with the ground run-up measurements are located near the flight path, meaning that we can assume any azimuthal variations are small for the microphones in question. With this assumption the aircraft paths, relative to each microphone, can be projected onto the same plane. In doing so, the spatial orientation given in Fig. 5.1(b) is discarded for comparison with ground run-up, and instead the spatial variables are calculated using $x = r\cos(\theta)$ and $y = r\sin(\theta)$ as the aircraft flies overhead. Doing so gives data across a wide spatial range, at distances of less than 100 m from the source and outward. The data points associated with the closest flyover locations are shown in Fig. 5.8, with each line of data points representing the aircraft flying near one of the microphones. With all the quantities of interest calculated at each point shown in Fig. 5.8, the data can be interpolated and smoothed to recreate the spatial field for various quantities.

The method above relies on some assumptions for the field recreation to be valid. First, the field must be axisymmetric. Since the comparable ground run-up measurements are primarily within 300 m of the MARP, the flyover microphones that contribute to the field recreation are all located near the flight path with an azimuthal angle near $\phi = 0$. These microphones near the flight path, though exhibiting slightly different directivities than at larger azimuthal angles, are consistent with each other and should provide a reasonable map of each parameter over the area of interest. Another important point is that the data samples are 0.1 s long to ensure the aircraft position does not vary considerably over the sample length. This short block length means that uncertainty rises, but due to the amount of data present an average behavior is displayed. A longer block size would reduce uncertainty but smear directivity effects. This method is first tested with OASPL, whose behavior is known due to the ease of correcting it for distance, and then applied to quantities that cannot be corrected for distance due to nonlinear propagation, such as spectra, derivative skewness, and ASF.

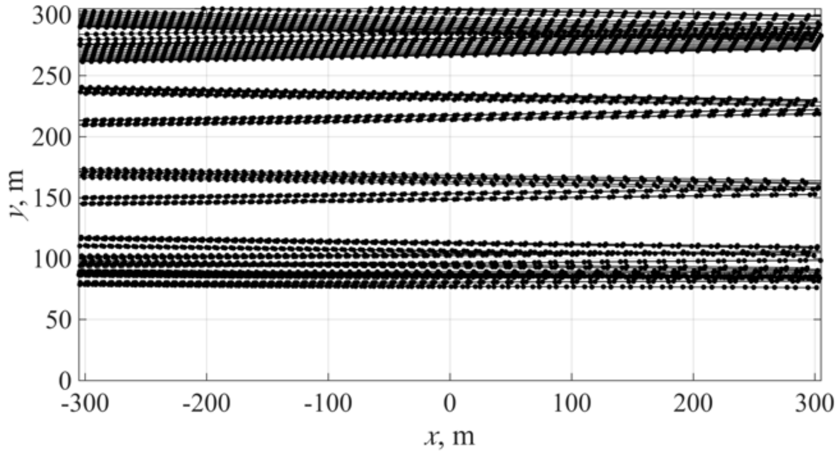

Fig. 5.8 Aircraft flight path relative to microphones for flyover events with aircraft height of 76 m.

5.5.2 OASPL

To ensure that this method provides reliable results the reconstructed field is generated for a known quantity, such as the OASPL. The reconstructed OASPL from flyover measurements is compared with ground run-up results in Fig. 5.9. The black dots shown in Fig. 5.9(a) correspond to the microphone locations at 76 m, 152 m, and 305 m from the MARP for the ground run-up measurements. The reconstructed OASPL shown in Fig. 5.9(b) agrees with the analysis above in Fig. 5.4 and Fig. 5.5. An overall reduction in level is observed in the main lobe from Fig. 5.9(a) to Fig. 5.9(b), on the order of 3-4 dB, along with a shift forward in directivity roughly 5° and an increase in OASPL of roughly 3 dB in the forward direction. This agrees with results from Fig. 5.4(b) and helps establish the validity of the field recreation.

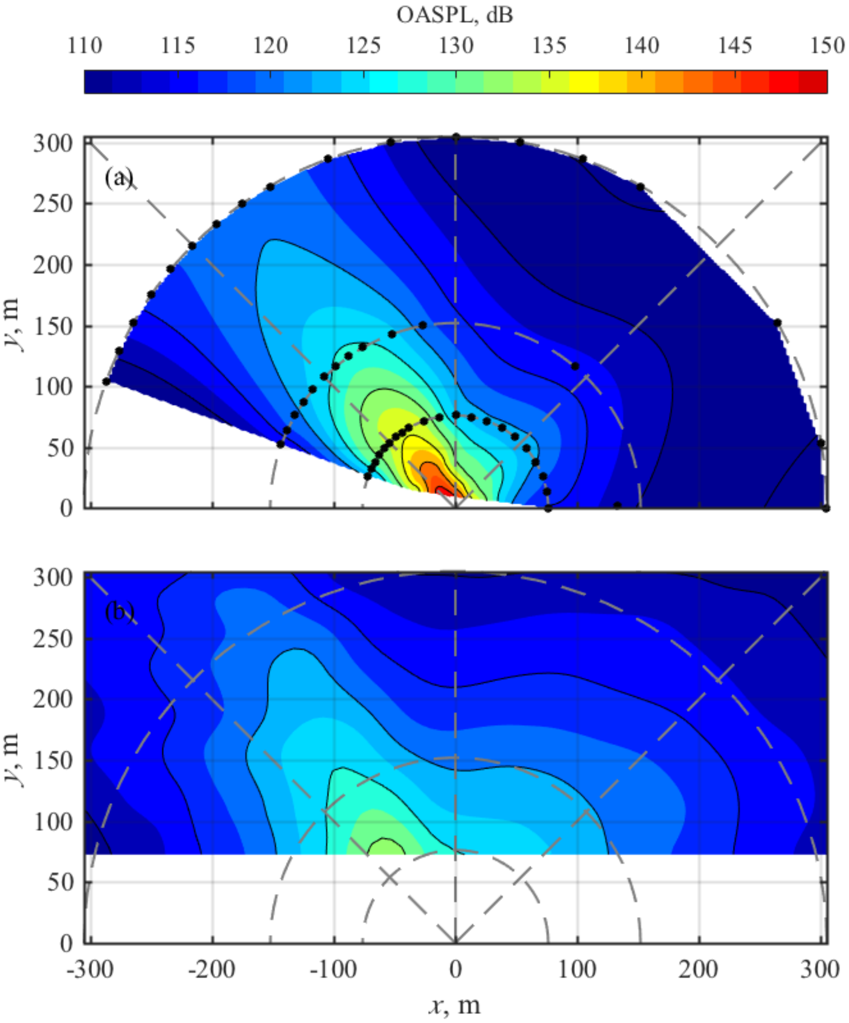

Fig. 5.9 Comparison of OASPL at 150% ETR for (a) ground run-up and (b) flyover.

5.5.3 Spectra

While the OASPL may be the most important indicator of sound exposure, important physical questions about the nature of the source can be answered by investigating the spectra. However, nonlinear propagation and atmospheric absorption make it difficult to normalize the spectra to a specific distance as can be done with OASPL, so the spatial field must be reconstructed for each frequency. The flyover field reconstruction method results for one-third octave (OTO) spectra are shown at 76 m at 30°, 90°, and 125° in Fig. 5.10(a), along with spectra from comparable ground run-up locations. Microphones from the ground run-up measurements were located at a height of 9.1 m, while the microphones used to reconstruct the flyover field were located at 0, 1.5, or 9.1 m above ground level. The same trends presented before are seen here as well—reduction in the maximum radiation region, seen as the decrease of 15 dB in the spectrum around 100 Hz at 125°, and a boost in the forward direction, seen as the increase of ~5 dB around 500 Hz at 30°. One interesting feature is that the same spectral peaks can be seen with little change in frequency between the two settings, in accordance with previous measurements.[23,25] Two peaks seen at 125° during ground run-up measurements are roughly 80-100 Hz and 315 Hz OTO bands. For the flyover measurements at the same locations, the maxima have different amplitudes but occur at close to the same frequency. Though a traditional Doppler shift would predict an increase of nearly a factor of two in the forward direction at the flyover velocity, the observed shift is in line with those shown using Eq. (70) in Michel's[26] work, on the order of half of an OTO band. This small shift in frequency has also been observed in previous measurements.[23,78] Similar behavior can be seen at both of the other angles shown, with frequency maxima remaining similar between the two measurement scenarios. However, one difference that is noticeable is the decrease in high-frequency energy seen in the maximum radiation region and the increase in high-frequency energy in the forward direction during flyover, as seen by the >20 dB increase at 10 kHz. Because peak frequency remains almost unchanged, the increased level in the forward direction during flyover likely drives an increase in waveform steepening due to nonlinear propagation effects, resulting in high-frequency energy not present in the forward direction during ground run-up. In the opposite case, the decrease in level at the peak frequency at 125° during flyover decreases the strength of the nonlinear propagation leading to less high-frequency energy due to a decrease in nonlinear propagation effects.

The increased importance of nonlinear propagation naturally brings up the question of how the spectrum changes as a function of angle. The relative gain, defined as the spectrum reconstructed from flyover events minus the measured spectrum from ground run-up, is shown in Fig. 5.10(b). As expected, an overall increase in level happens in the forward direction, and high frequencies in particular see a dramatic boost due to nonlinear propagation. As the peak frequency is consistent between the two scenarios, the degree to which nonlinear propagation is important is dependent only on amplitude. An increase of 5 dB in the peak frequency at 30° then significantly increases the high frequency content due to nonlinear propagation during flyover. The opposite trend is seen from 90-130°, where the amplitude decreases at and below 300 Hz, which in turn leads to a decrease in high-frequency noise for flyover events.

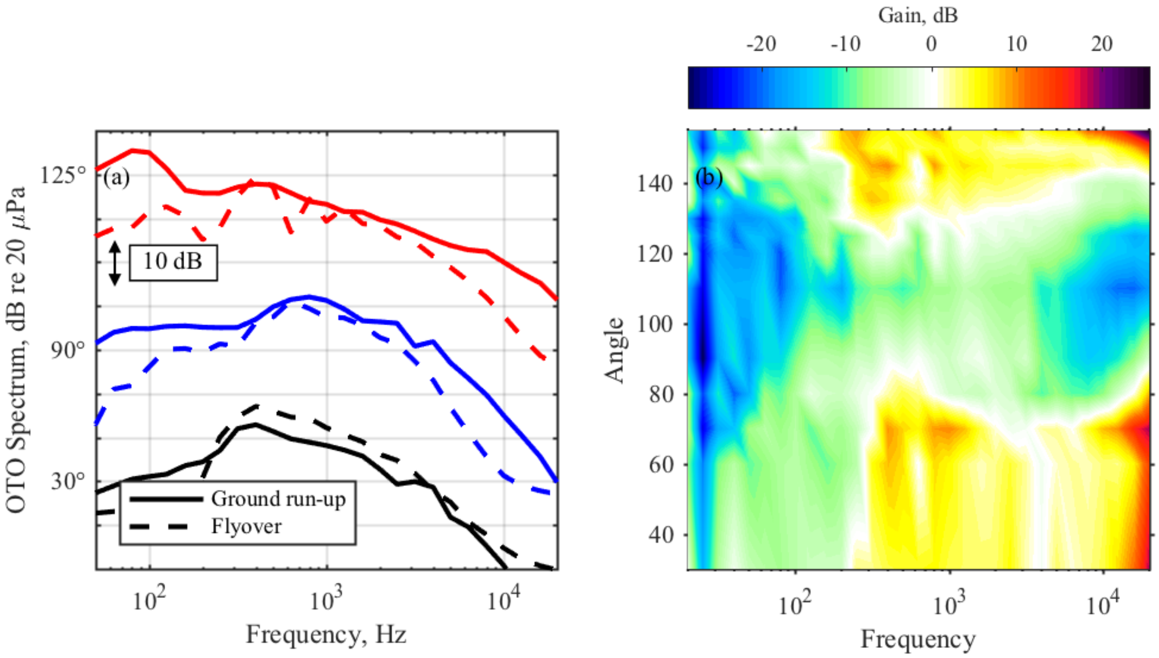

Fig. 5.10 (a) Comparison of spectra at a distance of 76 m between ground run-up and flyover at 150% ETR and (b) relative gain in level during flight.

5.5.4 Nonlinearity

The increase in high-frequency noise in the forward direction during flyover in Fig. 5.10(a-b) is similar to the increase of high-frequency energy seen due to nonlinear propagation during ground run-up measurements. If this is the case, it would be expected that the nonlinearity indicators introduced in Section 5.3 would have a relative increase from ground run-up to flyover in the forward direction, and a decrease in the maximum radiation region. Both these trends are seen in Fig. 5.11. The derivative skewness, following the trends observed in Fig. 5.9, shifts forwards, from peaking at 125° during ground run-up to peaking at 115° during flyover. The reduction in level in the maximum radiation region also leads to a decrease in derivative skewness levels, with maximum values at the 305 m radius arc reaching 10, rather than 17 as in ground run-up measurements signifying that the far-field shocks in the maximum radiation region are not as strong during flyover events. In the forward direction, however, there is a marked increase in derivative skewness for flyover, reaching a value of 13 at 30° and 152 m. This high value indicates that, in contrast to the ground run-up scenario, significant shocks can be found in the forward direction during flyover measurements.

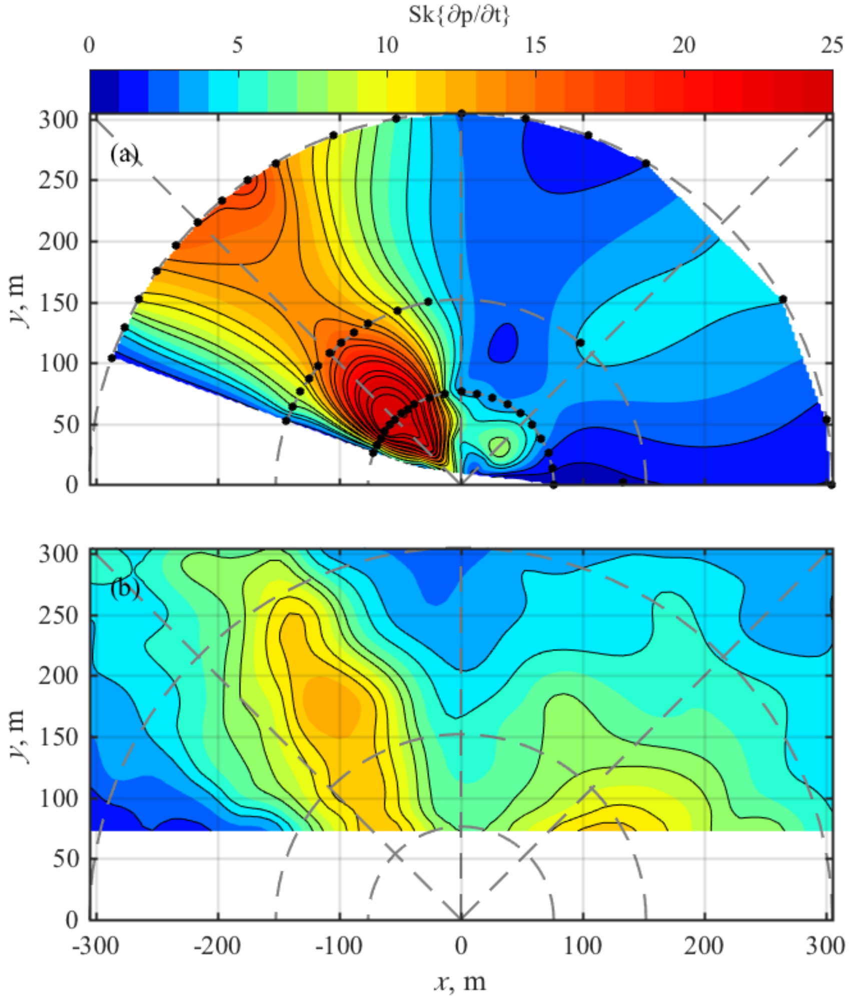

Fig. 5.11 Derivative skewness comparison between (a) ground run-up and (b) flyover at 150% ETR.

Many trends seen in the derivative skewness are also evident in the ASF in Fig. 5.12. As with derivative skewness lower values are seen in flyover in the maximum radiation region, though little to no change in directivity is observed. In both the forward and aft directions, ASF growth with distance shows that nonlinear propagation is steepening the waveforms at large distances from the source. The ASF values in the forward direction are significantly higher during flyover measurements. While the derivative skewness values in Fig. 5.11(b) suggest the strongest shocks in the forward direction at 305 m are located mainly between 20° and 55°, the ASF is higher in all forward directions. This increase indicates that although shocks may not be a significant feature of the waveform between 45° and 90°, nonlinear propagation is still a factor, leading to a steeper overall waveform.

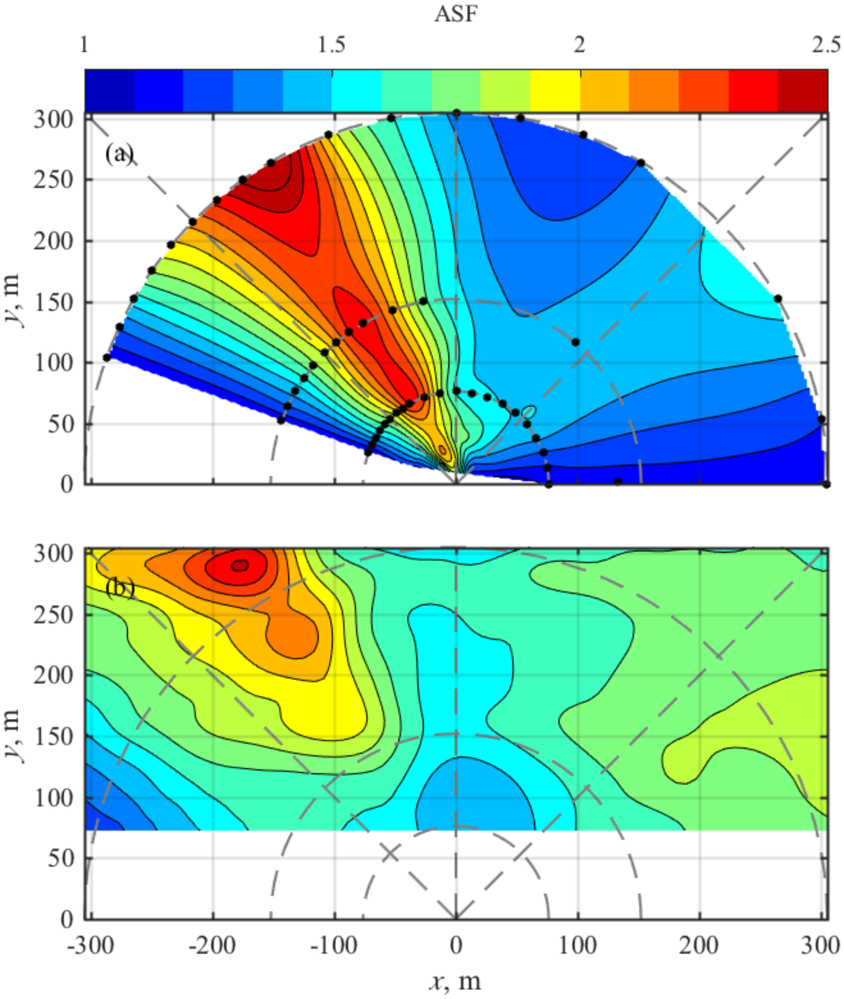

Fig. 5.12 ASF comparison between (a) ground run-up and (b) flyover at 150% ETR.

5.6 Results at Other Engine Conditions

5.6.1 OASPL

Flight effects at 150% ETR are consistent with prior work, and it is reasonable to expect that those effects are seen at other engine powers as well. Fig. 5.13 shows the OASPL comparison between ground run-up and flyover effects for (a) 75% ETR and (b) 100% ETR at an aircraft height of 76 m. The expected trends are seen here, but the effects are even more exaggerated than at 150% ETR in Fig. 5.4. In particular, at 75% ETR the OASPL in the maximum radiation region decreases from 131 to 125 dB at a distance of 76 m, while in the forward direction, from 0-160°, the OASPL increases by 10 dB, from 112 dB to 122 dB. These changes are substantial as the noise in the forward direction during flyover is comparable to the noise in the aft direction, only 3 dB lower. The changes due to flyover at 100% ETR are more noticeable than at 150% ETR, but less dramatic than those seen at 75% ETR. In the maximum radiation region, OASPL is decreased by 3 dB, while forward radiation is increased by 5 dB. The increased importance of flight effects for lower engine conditions is likely due to the fact that although exhaust velocity changes drastically between the engine conditions, aircraft speed is comparable between the three measurements. This means that the ratio of aircraft speed to jet exhaust velocity increases at lower engine conditions, leading to an increase in importance of flight effects. The significant changes in OASPL in Fig. 5.13 are likely to lead to noticeable differences in nonlinearity and shock content between ground run-up and flyover situations.

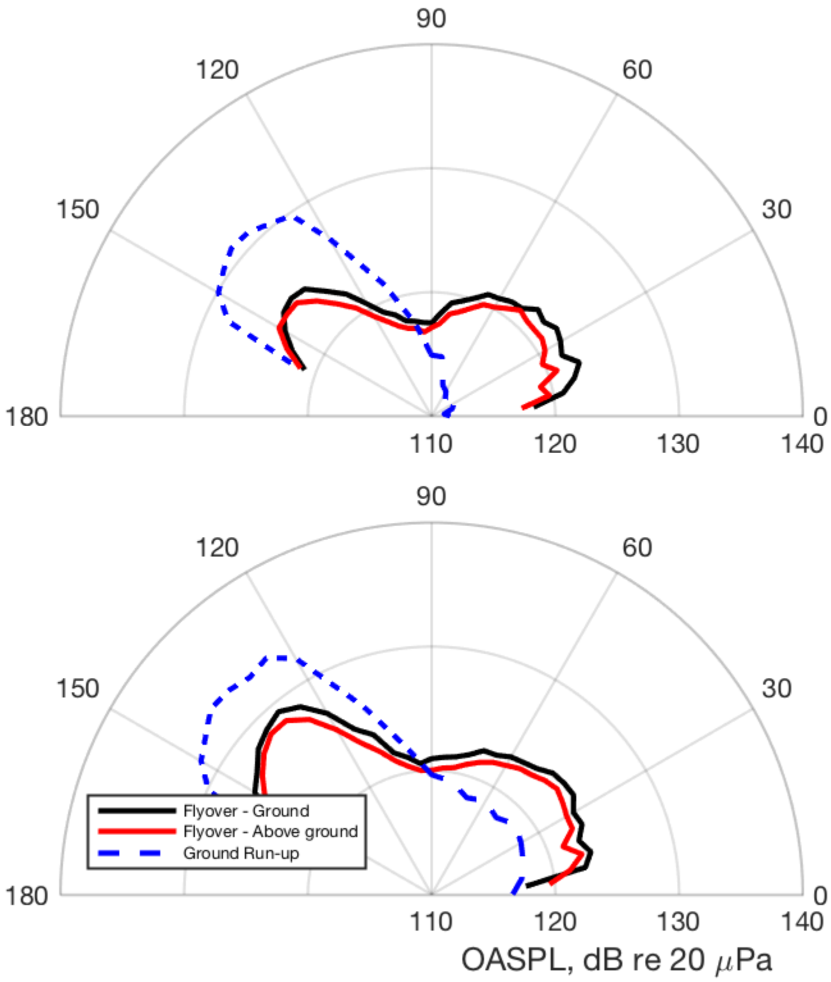

Fig. 5.13 Average flyover directivity at an aircraft height of 76 m compared with ground run-up at (a) 75% ETR and (b) 100% ETR.

5.6.2 Nonlinearity Comparisons

In the comparisons of nonlinearity metrics at 150% in Fig. 5.11 and Fig. 5.12, it was observed that the decrease in OASPL in the peak radiation direction led to a decrease in shock content, while the increase in the forward direction led to an increase in shock content, as would be expected. Since the changes seen in OASPL are more significant at 75% and 100% ETR, they are likely to have similar effects on nonlinearity to those seen at 150% ETR. This expectation is born out in Fig. 5.14 and Fig. 5.15; the derivative skewness maps are compared between ground run-up and flyover for 75% ETR in Fig. 5.14 (a) and (b) and 100% ETR in Fig. 5.15 (a) and (b). The reduction in OASPL in the maximum radiation region does lead to a decrease in derivative skewness in that direction. In the ground run-up scenario at 75% ETR, derivative skewness values peak at 20 at a distance of 76 m from the MARP, while derivative skewness values in Fig. 5.14(b) peak at a value of $\mathrm{Sk}\{\partial p/\partial t\} = 7$. Interestingly, despite the lower peak the derivative skewness values persist out to a greater distance than ground run-up, remaining above 5 out to almost 305 m. The forward direction does increase in derivative skewness, from values of $\mathrm{Sk}\{\partial p/\partial t\} < 1$ to values of $\mathrm{Sk}\{\partial p/\partial t\} > 6$, indicating the presence of significant shocks in the forward direction for the 75% ETR flyover events that were absent during ground run-up. Similar changes are seen at 100% ETR, with a significant decrease in derivative skewness in the maximum radiation region and an increase in the forward direction during flyover, although the derivative skewness values are comparable between 75% and 100% during flyover. Interestingly, the derivative skewness levels in the forward direction are similar at 75% and 100% ETR, which could be expected as the OASPL in the forward direction at 75% is within 1-2 dB of the OASPL at 100%.

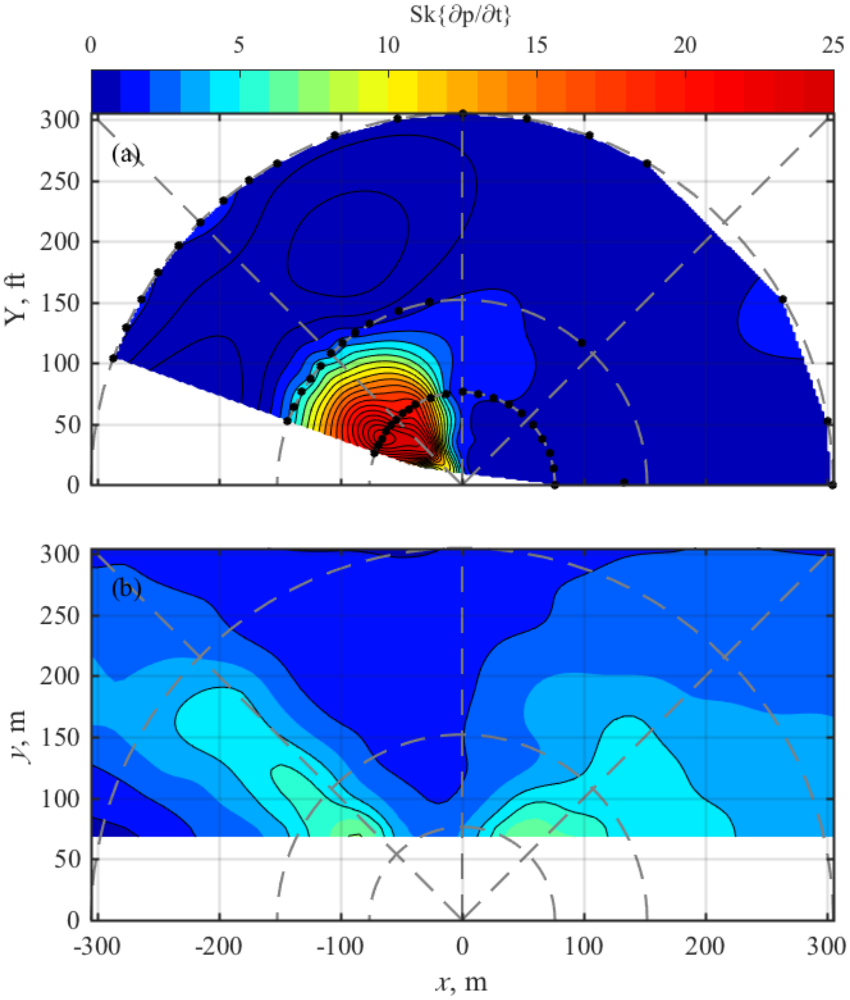

Fig. 5.14 Derivative skewness at 75% ETR for (a) ground run-up and (b) flyover.

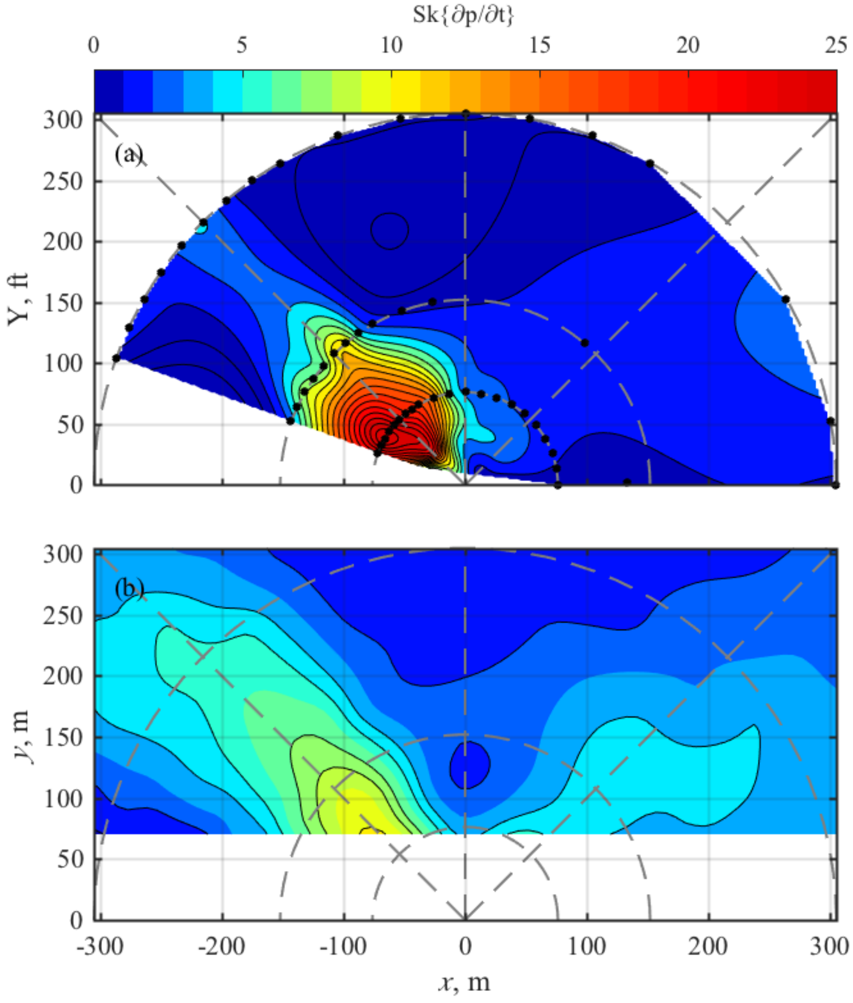

Fig. 5.15 Derivative skewness at 100% ETR for (a) ground run-up and (b) flyover.

The ASF again confirms the expected behavior of nonlinear propagation and shock content. The ASF is shown in ground run-up and flyover experiments for 75% ETR in Fig. 5.16(a) and (b) and 100% ETR in Fig. 5.17(a) and (b). Once again, a decrease in the nonlinearity indicator is seen in the maximum radiation region associated with the decrease in OASPL due to flight effects, though in all cases the ASF is increasing with distance, pointing to nonlinear propagation in the far-field for both ground run-up and flyover measurements. An increase in ASF is also seen in the forward direction in both cases, and again values in the forward direction during flyover are comparable between 75% ETR and 100% ETR.

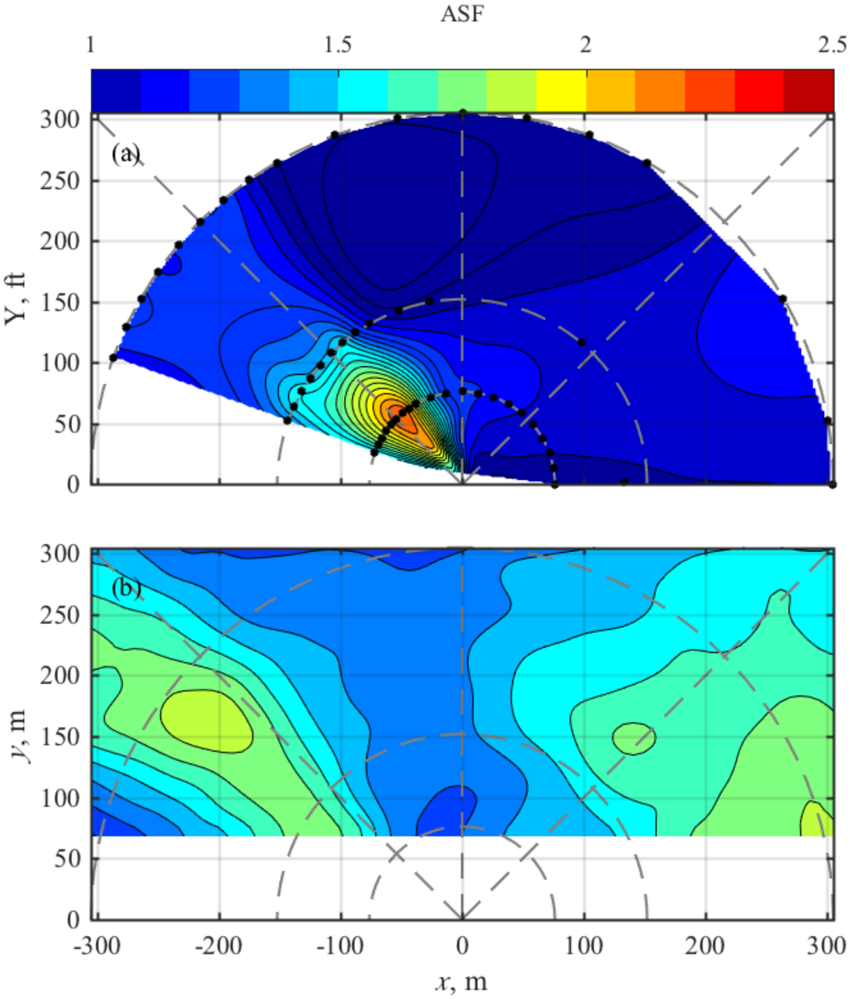

Fig. 5.16 ASF at 75% ETR for (a) ground run-up and (b) flyover.

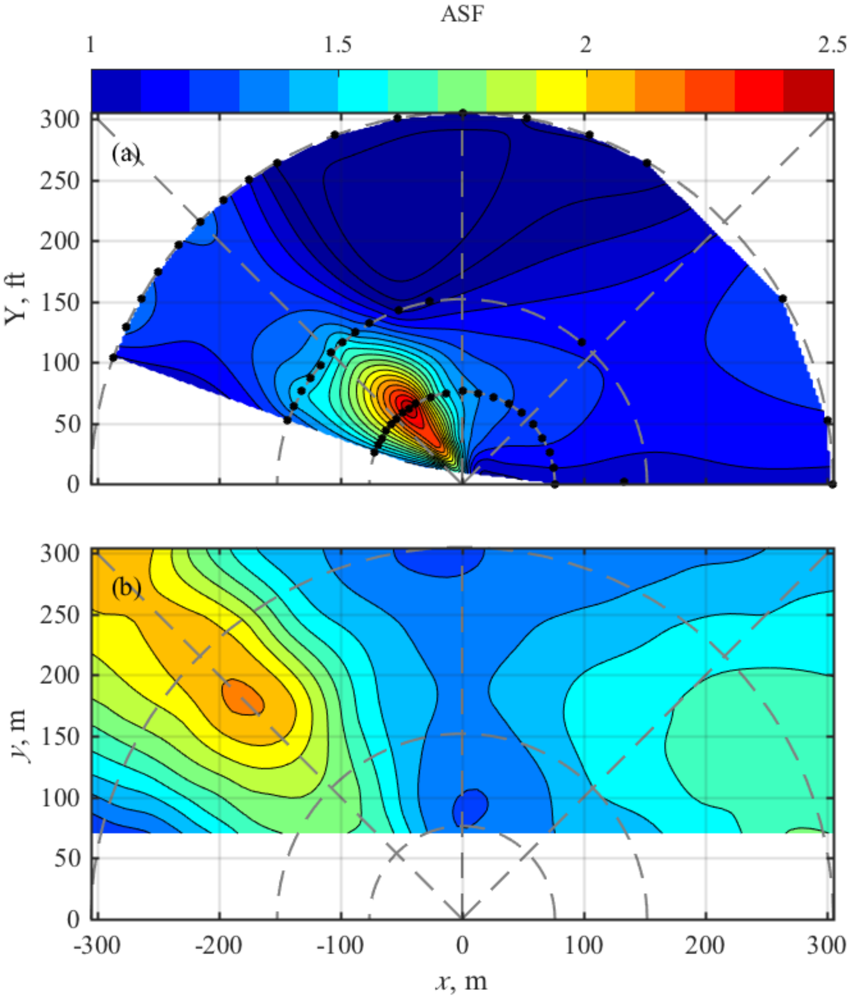

Fig. 5.17 ASF at 100% ETR for (a) ground run-up and (b) flyover.

5.7 Conclusions and Future Work

Understanding the changes in jet noise sources due to forward flight is an essential link in effective planning for jet noise exposure around military bases. Directivity, OASPL, spectra, and nonlinearity indicators have been compared between ground run-up and flyover measurements. In line with previous studies for analytical and model-scale results and predictions, the OASPL changes in three distinct ways due to forward flight effects: The maximum radiation region shifts forward, the OASPL in this region decreases slightly, and the levels in the forward direction increase. The OASPL decrease in maximum radiation region and increase in the forward direction result in lower and higher importance of nonlinear propagation, which result in lower high-frequency levels at peak radiation angles and a significant increase in high-frequency levels in the forward direction, which are due to a reduction and increase, respectively, in energy gain due to nonlinear propagation. While significant shocks are still found in the maximum radiation region during flight, shocks are also found in the forward direction at angles of less than 45°, and the increase in OASPL in the forward direction results in an overall steeper waveform.

These trends are even more evident at lower engine conditions. The increase in forward radiation is especially dramatic at 75% ETR, with a 10 dB increase over ground run-up measurements. The increase in OASPL in the forward direction does result in nonlinear propagation and shock formation at 75% and 100% ETR, but the decrease in the maximum radiation region results in a significant decrease in derivative skewness, as well as a small decrease in ASF. Overall, the trends seen here show that the flight effects create significant shock content in areas where such content is absent during ground run-up measurements.

Chapter 6

Atmospheric Conditions and Their Effects on Long-Range Nonlinear Propagation

6.1 Introduction

To predict long-range noise exposure from military aircraft, an accurate representation of far-field levels is required. To this end, recent measurements of the sound field from an F-35 included microphone locations up to 1220 m (4000 ft) away from the aircraft. However, long-range acoustic propagation introduces a number of factors that can increase uncertainty and complicate predictions.[96,97] While an ANSI jet noise measurement standard specifies a range of allowable weather conditions to help reduce some of this uncertainty, sufficient latitude still exists such that overall level, spectral shape, and waveform characteristics may vary considerably during allowable conditions.[97] This chapter demonstrates large weather-related variations in overall sound pressure level (OASPL) and nonlinearity metrics at distances beyond 305 m. Quantifying these changes is important for predicting jet noise perception.

Minor changes in atmospheric conditions can significantly affect both the propagation medium and propagation paths of sound. Variability in atmospheric pressure, humidity, and temperature can affect sound speed and atmospheric absorption, which over large distances can significantly alter high-frequency content.[98] However, larger spectral changes closer to the peak frequency region of jet noise can result from multipath effects. Multipath effects have been shown in previous chapters in the form of ground reflections, where sound arrives via a second transmission path with a slight time delay, affecting the OASPL and spectrum of the measured waveform. However, propagation distances on the order of 100 m and greater may require the consideration of more complicated multipaths due to atmospheric effects, as changes in wind speed and temperature with height can create a downward-refracting or upward-refracting atmosphere.[99,100] A downward-refracting atmosphere is often caused by a temperature inversion, when the air is colder closer to the ground.[101] The increase in sound speed with height causes sound rays to refract downward, which can result in more than two possible propagation paths to a location and produces a complicated spectrum with many interference nulls associated with different arrival times. For example, Salomons[102] showed a case of a "typical" downward refracting atmosphere that resulted in 40 possible ray paths between two sources 1000 m apart. Local variations in atmospheric conditions can also create an atmosphere where there is a combination of an upward and downward-refracting atmosphere,[101] and turbulence can further complicate predictions by smearing out interference nulls and scattering sound to shadow zones.[102,103] In addition, nonlinear propagation must be taken into account for high-power engine conditions, and little research exists showing the effect of these atmospheric conditions on shock formation and propagation.[104] Though atmospheric conditions are not available over the whole measurement area, making accurate predictions of multi-path effects impossible, examples of atmospheric effects are visible in long-range acoustic propagation measurements.

This chapter contains far-field data from measurements of a stationary F-35, and investigations into the effects of atmospheric conditions on OASPL, spectra, and nonlinearity metrics are shown. These quantities and their uncertainty are shown at distances from 39 m to 1220 m from measurements taking place over the course of two days. Spectra and nonlinearity metrics point to the importance of nonlinear propagation at large distances from the source, with significant shocks still present at 610 and 1220 m from the source. Far-field data show the presence of multipath interference effects and likely indicate that for the majority of the experiment, a downward-refracting atmosphere was present. OASPL and nonlinearity metrics are considered as a function of height at distances of 610 and 1220 m, with the surprising result that while for the bulk of the experiment OASPL tends to decrease with height, nonlinearity indicators tend to increase. Evidence is shown of a transition from a downward-refracting atmosphere to an upward-refracting atmosphere, resulting in changes of over 10 dB at microphone heights close to the ground. Occasional outliers point to the fact that some circumstances may produce significantly increased shock content.

6.2 Measurements

The microphone layout for this experiment has already been described in detail in previous papers.[71] However, as this chapter deals more with long-range propagation effects and the effects of weather conditions, certain features of the measurement array are highlighted here. In particular, six measurement locations (with two locations featuring multiple microphones at varying heights) at 610 m (2000 ft) and 1220 m (4000 ft) from the microphone array reference point (MARP, located roughly 7 m behind the jet nozzle) are shown in Fig. 6.1. These measurement locations are along the 120°, 135°, and 150° radials, allowing for comparisons in the extreme far field. The measurement locations at 120° and 150° at both distances were limited to a single microphone 9.1 m (30 ft) above the ground, while cranes were located at 135°, allowing measurements at heights of 0, 1.5, 6.1, 9.1, 22.9, and 30.5 m (0, 5, 20, 30, 75, and 100 ft) above the ground at both distances. Also shown in Fig. 6.1 are three weather measurement locations at 61, 152, and 250 m (200, 500, and 820 ft) from the MARP. A single weather station was placed 1.5 m (5 ft) above the ground at

61 m from the MARP, while the 152 m location had weather stations at heights of 1.5, 3.1, and 6.1 m and the 250 m location had weather stations at heights of 0.31, 1.5, 3.1, and 6.1 m. However, heights of individual weather stations are inconclusive due to discrepancies in the measurement documentation, so while the data represent a wide range of measurement locations, for the purposes of this chapter weather data are simply averaged.

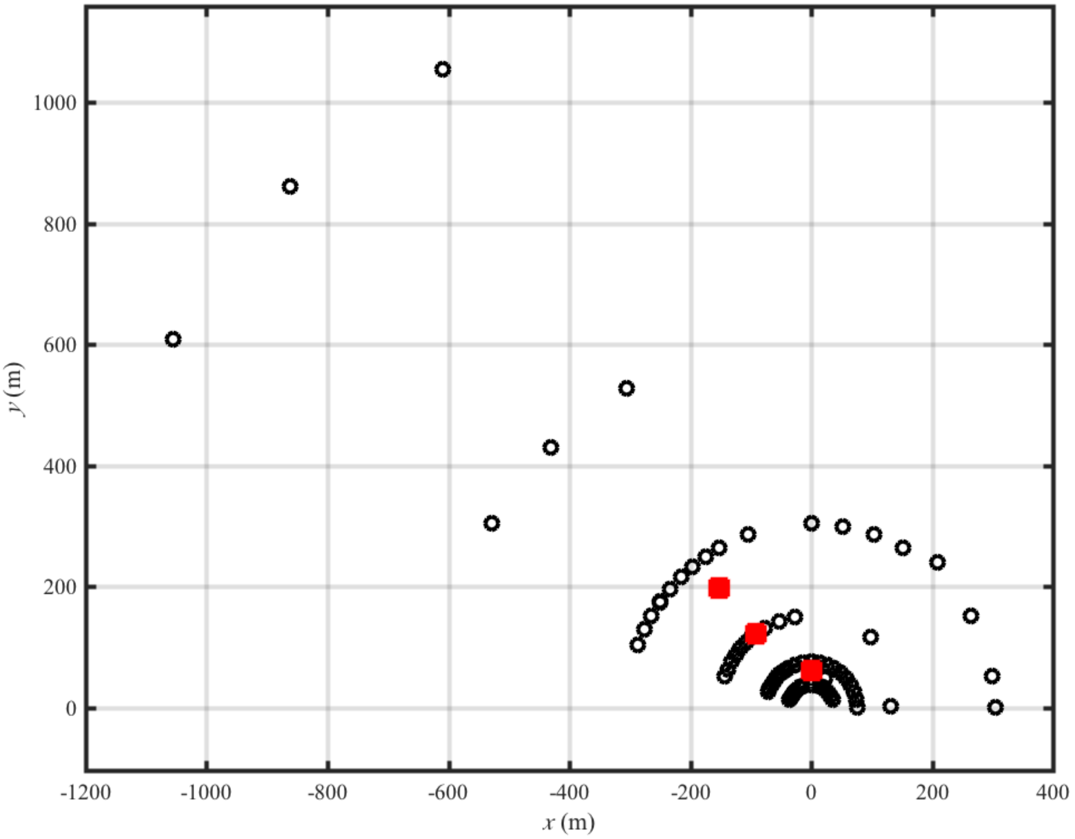

Fig. 6.1 Microphone locations for ground run-up measurements at distances of 38 m and greater relative to the MARP, located at $(x, y) = (0, 0)$. Also shown as red squares are locations of weather stations, with weather stations present at multiple heights for the two farther locations.

Individual measurements (runs) lasted roughly 30 seconds, with 9-10 runs for each engine condition. Run numbers in the 100s correspond to runs on the first day of measurements (On the F-35A) while run numbers in the 200s correspond to the second day (On the F-35B). Average weather conditions for all of the runs at 100% ETR are shown in Table 6.1, along with the required range of weather conditions allowed in the standard. This allowed range of weather values is representative of all runs measured. Most parameters were steady throughout the measurement, with temperatures ranging from 20.0-22.7°C and relative humidity staying between 40-44%. Wind varied more than these parameters, but during measurement times stayed under the threshold of a maximum wind speed of 8.0 kts. There were some more significant wind events during the first day of measurements, with some events reaching an average of over 6.0 kts. Sunrise on both measurement days occurred just before a local time of 6:30 AM, meaning that some runs took place before dawn and some after, which may be important when considering effects of a possible temperature inversion or lapse.

Table 6.1. Weather conditions for all recorded runs at 100% ETR for both measurement days and ranges given in the standard.

Run	**114**	**119**	**124**	**129**	**207**	**213**	**219**	**225**	**231**	**243**	**Standard**
Time (A.M.)	6:08	6:42	7:15	7:48	5:10	5:23	5:37	5:50	6:04	7:34	N/A
Temp. (°C)	22.7	22.0	21.7	22.2	20.9	20.9	20.9	20.5	20.0	20.3	2.2 - 35
Wind (kts)	5.7	1.3	3.2	6.5	2.4	2.4	2.0	1.8	1.4	2.0	0 - 8.0
RH (%)	41.1	43.7	42.1	40.3	41.1	42.3	42.7	42.7	44.9	40.2	10 - 95%

6.3 Metrics

The metrics that have been used in past chapters to describe nonlinearity are again considered here along with the OASPL. While a large OASPL is associated with nonlinear propagation, it is not by itself an indicator of shock content within a waveform. However, as an important acoustic quantity its changes due to long-range propagation effects are shown here, along with three nonlinearity parameters: The derivative skewness, average steepening factor

(ASF), and shock energy fraction (SEF). Variations across runs are quantified to show how OASPL and nonlinear effects are affected by long-distance variations in atmospheric propagation.

6.3.1 Derivative Skewness

To discuss nonlinearity and shock formation for noise waveforms, the behavior of the entire waveform must be taken into account. To gauge overall waveform behavior, metrics are often based on the probability distribution function (PDF) of the waveform or its derivative.[105,106] The skewness of a distribution expresses asymmetry of the PDF and accentuates outliers due to the cubed nature of the numerator. The skewness of a zero-mean variable x is defined as

$$\mathrm{Sk}\{x\} = \frac{E[x^3]}{E[x^2]^{\frac{3}{2}}} \tag{6.1}$$

where $E[x]$ represents the expectation value of x. A skewness value of zero represents a symmetric distribution, while a positive skewness indicates the presence of a higher number of large positive values than negative. The skewness of the pressure waveform was initially used to quantify crackle, an auditory phenomenon associated with acoustic shocks present within jet noise.[107] However, to quantify shocks themselves it is more useful to use the derivative skewness, $\mathrm{Sk}\{\partial p/\partial t\}$,which refers to the skewness of the PDF of the first time derivative of the waveform and expresses an asymmetry in derivative values. The derivative skewness accentuates the large derivatives (rapid pressure increases) associated with acoustic shocks, positive derivative skewness is indicative of shocks in the waveform.[108] It has been shown that an approximate threshold of $\mathrm{Sk}\{\partial p/\partial t\} \geq 5$ indicates that shocks are appearing in the waveform, while a value of $\mathrm{Sk}\{\partial p/\partial t\} \geq 9$ indicates many significant shocks present in the waveform and is associated with a high crackle rating.[14]

6.3.2 Average Steepening Factor

The ASF[109] is also based on derivative values and defined as the average value of the positive derivatives over the average value of the negative derivatives:

$$\mathrm{ASF}\{p\} = \frac{E[\dot{p}^{+}]}{-E[\dot{p}^{-}]}. \tag{6.2}$$

The ASF, which is an inverse of the previously used wave steepening factor (WSF),[110] is a linear average of derivative values, which makes it less sensitive to outliers than the derivative skewness, and thus better represents average behavior. An ASF value of one corresponds to a waveform with no significant steepening, while a value above one represents some nonlinear steepening,[109] It has been shown that for jet noise, both full-scale[111] and model-scale,[112] an ASF value between 1.5 and 2 is indicative of the presence of shocks, with a value approaching two suggesting significant shock content.

6.3.3 Shock Energy Fraction

The steepening of shocks in the time domain results in spectral broadening in the frequency domain, as energy is transferred from the peak frequency region to higher frequencies. Although spectral broadening is often shown using the more familiar Fourier transform, a wavelet transform has been used in lab-scale jet noise analysis as a frequency-domain technique that also gives temporal resolution.[112] The SEF is a metric that compares high-frequency (>2 kHz for full-scale aircraft) energy associated with shocks within the waveform to the total high-frequency energy present.[113]. A value of $\mathrm{SEF} = 0$ corresponds to no high-frequency energy associated with shocks, while a value of $\mathrm{SEF} = 1$ means that all high-frequency energy is associated with shocks.

6.4 Far-Field Variation in Metrics

Long-distance propagation introduces a level of variation not seen in near-field measurements for nearly all measured quantities. Some of these variations can be tied to atmospheric effects, such as a temperature inversion or gradients in the atmosphere that alter the path of sound and either reduce direct propagation or introduce secondary transmission paths. Other meteorological effects are not so readily connected to measurable weather conditions, and such effects on long-range, nonlinear propagation can lead to surprising results.

6.4.1 Uncertainty with Distance

The waveform changes that arise due to small atmospheric variation can be dramatic. To illustrate this, three waveforms at 100% ETR from the same microphone, 22.8 m above the ground at 610 m from the MARP at an angle of 135°, are plotted in Fig. 6.2. The three waveforms in parts (a), (b), and (c) are taken from Runs 129, 219, and 124 respectively. Though the OASPL of all three waveforms is very similar- 111.2, 111.0, and 112.5 for the three runs in order- the waveform properties themselves look very dissimilar. The waveform in Fig. 6.2(a) in particular shows several spikes that noticeably absent from the other waveforms, and are reminiscent of the waveform examples of crackle shown by Ffowcs-Williams *et al.*[10] The sharp, positively pressure skewed, double-peak features in the waveform also bear similarity to those seen in caustic focusing of sonic booms,[116] which can also occur due to atmospheric refraction. The derivative skewness for the waveform in part (a) is markedly larger than the other waveforms with a value of 18.7, compared with 4.7 and 11.0 for parts (b) and (c). Evidence of steepening is also visible in parts (b) and (c), but not nearly to the extent that it is visible in part (a). These three waveforms help show the wide disparity in shock content that is possible at the same location due to small atmospheric changes.

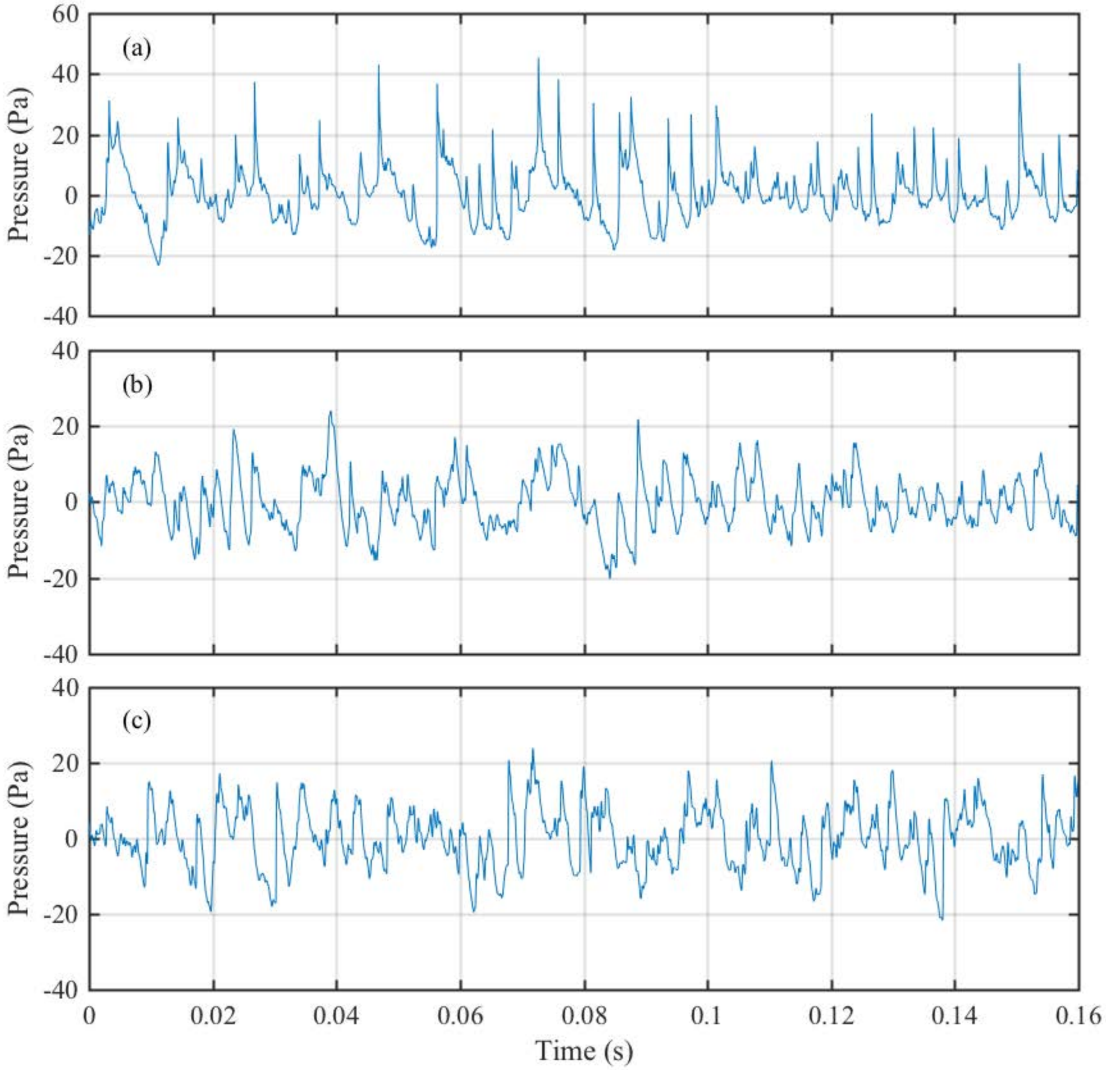

Fig. 6.2 Waveforms from the microphone located 22.8 m above the around at 610 m from the MARP along the 135° radial for three runs at 100% ETR: (a) Run 129, (b) Run 219, and (c) Run 124.

To illustrate some of the issues associated with nonlinear propagation over large distances, Fig. 6.3 shows the mean value and standard deviation for the metrics discussed above as a function of distance at 135° for a single engine condition, 100% ETR. Though microphones were available at multiple heights at 610 m and 1220 m, only the results from the 9.1 m high microphone are shown here, which is the same height as the microphones at 76, 152, and 305 m. The OASPL, shown in Fig. 6.3(a), is the metric that is most often used in noise modeling. The uncertainty in OASPL tends to increase with distance, with a standard deviation of greater than 1 dB at 610 and 1220 m. Nonlinearity metrics also tend to show greater uncertainty with distance but may appear to peak in uncertainty at 305 m before collapsing at farther distances. However, the ranges of the nonlinearity metrics and the associated perception should be taken into account when evaluating uncertainty.

Past studies[14] have shown significant differences in shock content and perception as derivative skewness values reach and exceed a value of 3, and ASF exceeds a value of 1.5, though the link between perception and ASF has yet to be quantified. The derivative skewness has a large standard deviation at 305 m, but all values are above a threshold of 9, indicating continuous crackle. On the other hand, the range of values spanned by error bars in derivative skewness at 610 m and 1220 m represent a much larger range of shock content, ranging from no significant shocks to significant shocks. The ASF values at 305 m also show a wide range of values, but all of them indicate significant shock content, while the uncertainty in ASF at 610 and 1220 m again shows that at these larger distances shock content may be significant or nearly nonexistent, depending on the run. The large uncertainty in shock content at large distances, even with weather conditions during all runs falling within the measurement standard, points to the sensitivity of long-range propagation to small variations in atmospheric conditions.

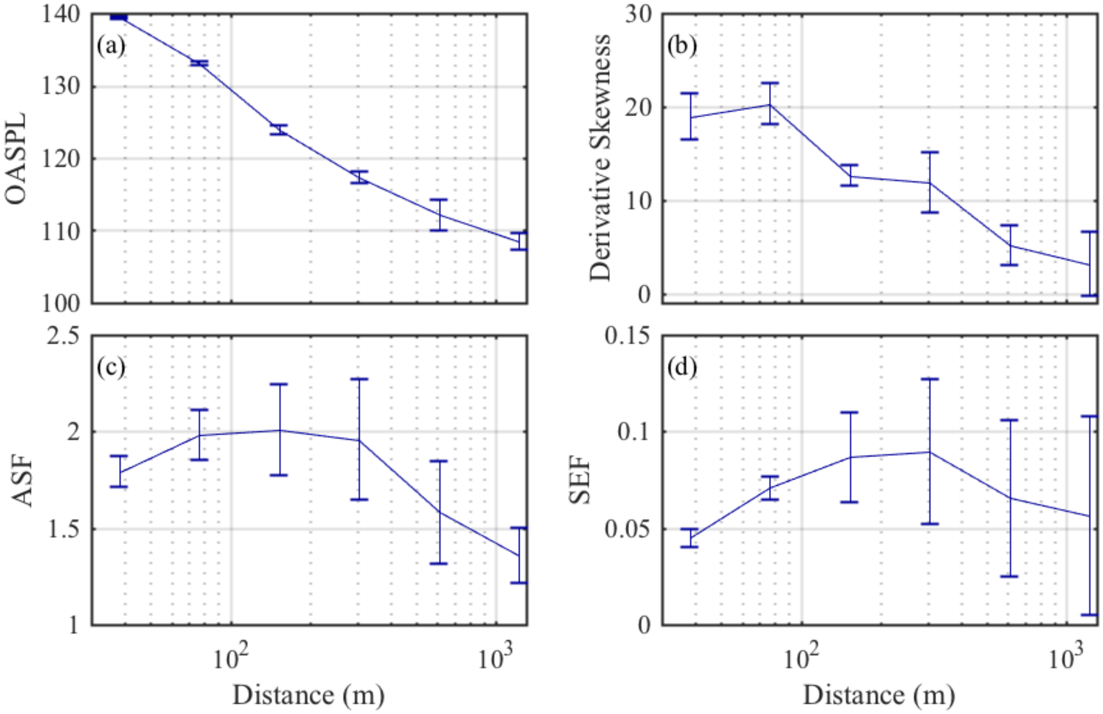

Fig. 6.3 The (a) OASPL, (b) derivative skewness, (c) ASF, and (d) SEF are shown as a function of distance along with 135° radial for the 100% ETR runs. Standard deviation over the 9-10 runs at each measurement location is shown using error bars.

Though behavior can vary in the extreme far field, in many runs the high values of derivative skewness, ASF, and SEF indicate significant shock content at distances of 610 and 1220 m from the source. However, the variation in nonlinearity metrics over runs suggests that there should be substantial differences in the high-frequency content at these distances as well: Higher nonlinearity metric values should be associated with a marked increase in high-frequency energy. The spectra from all the microphones from 38.1 m to 1220 m along the 135° radial, at a height of 9.1 m, are shown in Fig. 6.4 for all runs at 100% ETR, shown in Table 6.1. As would be expected, very little variation is seen at 38.1 m, though evidence of a ground interference null is seen near 1 kHz in some of the spectra. As distance increases, more and more variation is seen, in particular in the high-frequency regimes. At 610 m, one spectrum in particular has little high-frequency content, consistently 15-20 dB below all other spectra, even though the difference in peak level is not nearly as large. At 1220 m, differences at 200 Hz are as large as 15 dB. These dramatic differences at these low frequencies point to a secondary propagation path not due to ground reflections, as ground reflection nulls should be located near 1 kHz according to the measurement geometry. The interference nulls at frequencies too low to be caused by ground reflections suggest another secondary transmission path, possibly a downward refracting atmosphere, though more measurements are needed to confirm this. At 1220 m some runs also exhibit significantly higher SPL above 3-4 kHz. Also of note is the fact that 1220 m from the source, measurable levels exist up to 10 kHz. The level at these high frequencies should be well below the noise floor at these distances due to linear absorption, indicating that even at distances as large as 1220 m, nonlinear propagation is still a key factor in providing high-frequency energy.

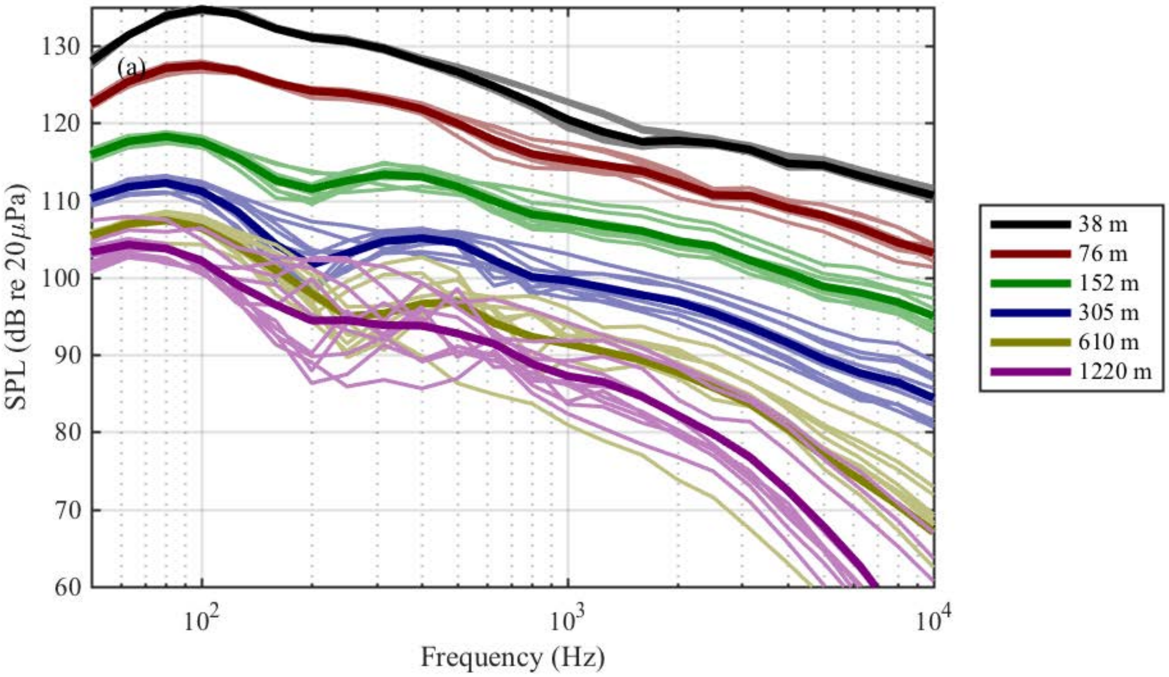

Fig. 6.4 Spectra for measurement distances from 38.1 m to 1220 m along the 135° radial at height of 9.1 m for 100% ETR. Averaged spectrum (dB average) at each location is shown with a darker line.

6.4.2 Trends at 610 m

While understanding uncertainty with distance is an important, variation with measurement height also needs to be considered. The SPL as a function of frequency, shown in Fig. 6.4 at cranes located 610 and 1220 m from the source, were solely from microphones at 9.1 m in height to match the measurement height at 76, 152, and 305 m. Though most measurement locations were limited to a single height, the 610 and 1220 m measurement locations along the 135° radial consisted of multiple microphones at heights ranging from 0 to 30.1 m off the ground. The OASPL of all microphones at 610 m is plotted in Fig. 6.5 as a function of height for all runs at 100% ETR in Table 1. One of the visible trends is that, with the exception of Run 129, OASPL tends to decrease with microphone height up to 22 m, similar to results shown by McInerny *et al.*,[114] though their results had a maximum height of 12.2 m. One possible explanation for the increase in level is that near the ground, the direct transmission from the source and the ground reflection combine constructively over the peak-frequency region, but at higher microphones the interference can be more destructive than constructive, resulting in a lower OASPL. However, the expected ground interference nulls, even at 30 m above the ground, occur at several times the peak frequency of the noise. While these ground interference nulls do affect the high-frequency shape of the spectrum, because they occur in a frequency region well below the peak, they do not affect the OASPL. This means that other long-range propagation effects due to a more complicated vertical profile in the atmosphere are the likely cause for the decrease in OASPL with microphone height.

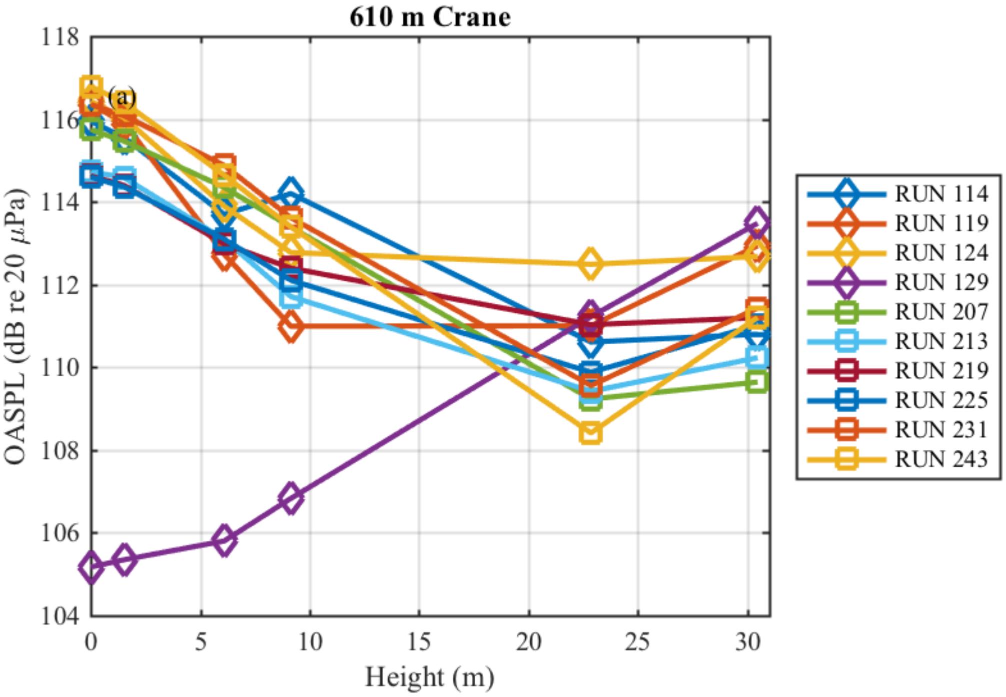

Fig. 6.5 OASPL is shown as a function of height at a distance of 610 m at 135° for all runs at 100% ETR. Symbols denote which day the run was measured.

One run stands out within these 610 m measurements, as its vertical variation in OASPL is drastically different from all others. Run 129 subverts the trend that OASPL decreases with height, with the lowest OASPL at ground level and increasing from there, similar to results shown by Gee *et al.*[115] Though not shown in Fig. 6.5, this behavior is also seen at runs at other engine conditions immediately before and after Run 129, and the significantly lower OASPL values are also seen at the 9.1 m microphone at 120° and 150° at 610 m. While it is difficult to pinpoint exactly what meteorological conditions caused such a drastic change, it is worth noting that this run was the latest time of day of all runs at 100% ETR, and it also had the highest wind speed, as shown in Table 6.1. It is possible that gradients in the atmosphere at earlier times channeled the sound towards the ground, but as the ground warmed up and a temperature lapse occurred, the sound was refracted away from the ground microphones. However, a more detailed measurement of atmospheric conditions is needed to confirm this hypothesis.

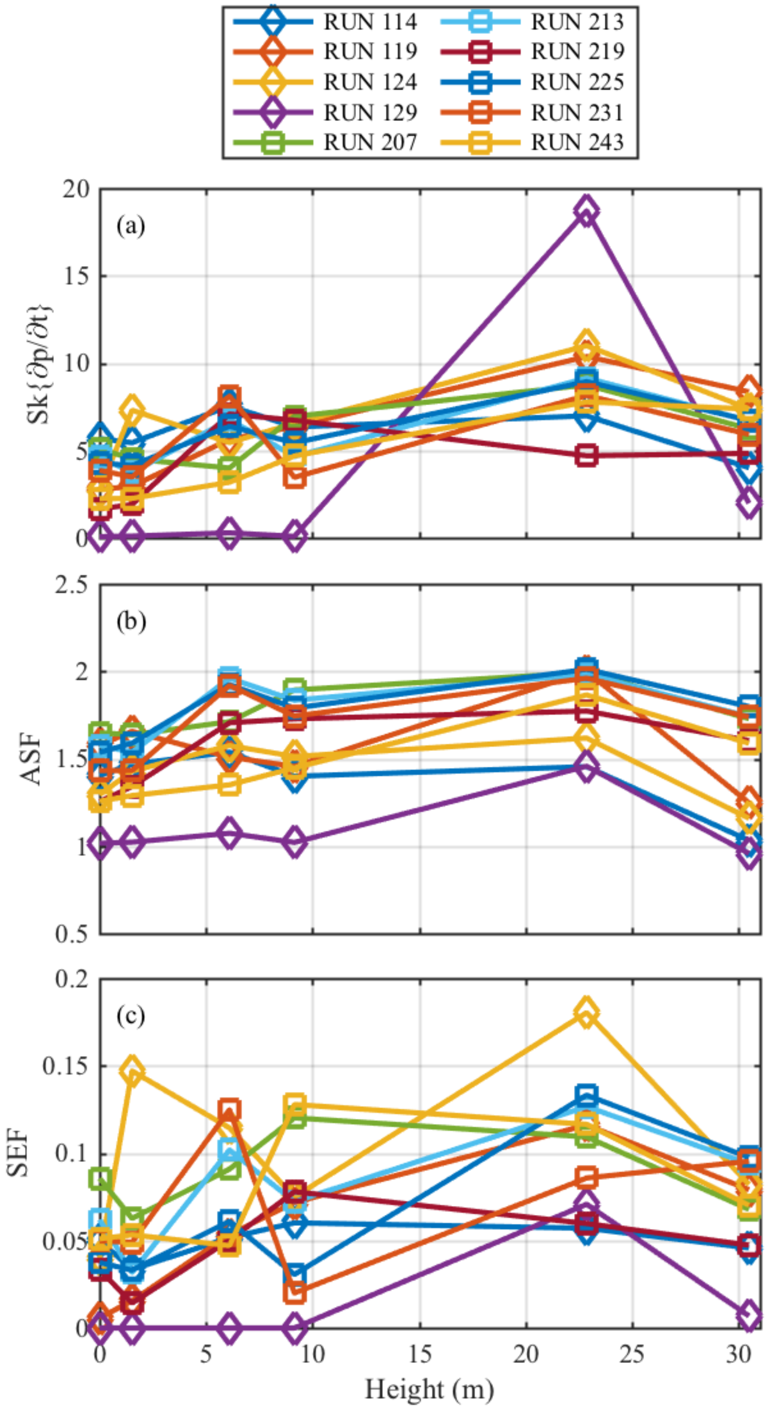

Fig. 6.6 The (a) derivative skewness, (b) ASF, and (c) SEF are shown as a function of height at a distance of 610 m at 135° for all runs at 100% ETR. Symbols denote which day the run was measured.

Since the OASPL is consistently lower at higher measurement locations it would be reasonable to assume nonlinearity metrics would exhibit height-dependent trends as well. Because peak frequency is consistent with height, one might assume that nonlinearity metrics would decrease for microphones with lower OASPL. Higher OASPL tends to drive shock formation, meaning that for these similar propagation paths, higher OASPL corresponds to higher values of nonlinearity metrics. Were this the case at the crane at 610 m, one would expect nonlinearity metrics to decrease with height. However, this is not the observed behavior, as shown in Fig. 6.6. Instead, the nonlinearity metrics tend to increase with height until 22.9 m above the ground, when they decrease as OASPL increases.

Once again, the behavior from Run 129 is drastically different from the rest. Here, the derivative skewness up to 9.1 m is negligible, while the derivative skewness at 22.9 m (Corresponding to the waveform shown in in Fig. 6.3(a)) jumps to a value of nearly 19, near the average behavior observed at 38 m and 76 m seen in Fig. 6.3. Upon listening to these samples, the difference in sound quality is stark, with the waveform at 9.1 m having no crackle, while the waveform at 22.9 m could be described as intense crackle, similar to what is heard at distances much closer to the aircraft. Just as with the OASPL behavior shown in Fig. 6.5, this larger derivative skewness at that microphone is not limited to a single run, but is also present at other engine conditions. Though it is difficult to ascribe this behavior to any particular aspect of meteorological conditions, the features appear similar to the skewed peaks produced by caustic focusing, which can be caused by a downward refracting medium,[102,116,117,118] though the effects of nonlinear propagation in a downward-refracting atmosphere have not been investigated for jet noise. However, it is important to note that nonlinear propagation can be significant at distances far from the source, and that nonlinear propagation is sensitive to small changes in the environment.

6.4.3 Trends at 1220 m

One way of confirming some of the trends seen at 610 m is looking for confirmation at other measurement locations, in this case using the crane at 1220 m. The trends at 610 m were for the most part unexpected, in particular the decrease in OASPL with height and associated increase in all three nonlinearity metrics. However, as is seen in Fig. 6.7, the decrease in OASPL with height is accentuated further at 1220 m, with a difference of 8-10 dB between the measurements at heights of 0 m and 30.5 m for most of the runs. However, some of the runs deviate from this behavior. Run 129 in particular shows an increase in OASPL at higher elevations, a trend that is present at a smaller degree in runs 119 and 124. Interestingly, the anomalous behavior is very different at 1220 m than at 610 m. While at 610 m run 129 has a 10 dB drop in OASPL at the microphones closest to the ground compared to other runs, at 1220 m the microphones near the ground are unchanged, and elevated microphones see a large increase in OASPL. This implies that the atmospheric conditions create a “shadow zone” at lower microphones at 610 m during Run 129, but the sound is again refracted toward the ground by 1220 m. Regardless, the findings from Fig. 6.7 confirm the behavior seen in Fig. 6.5, that for the course of most of the experiment the OASPL decreases with microphone heights, more so than would be expected for straight-ray propagation.

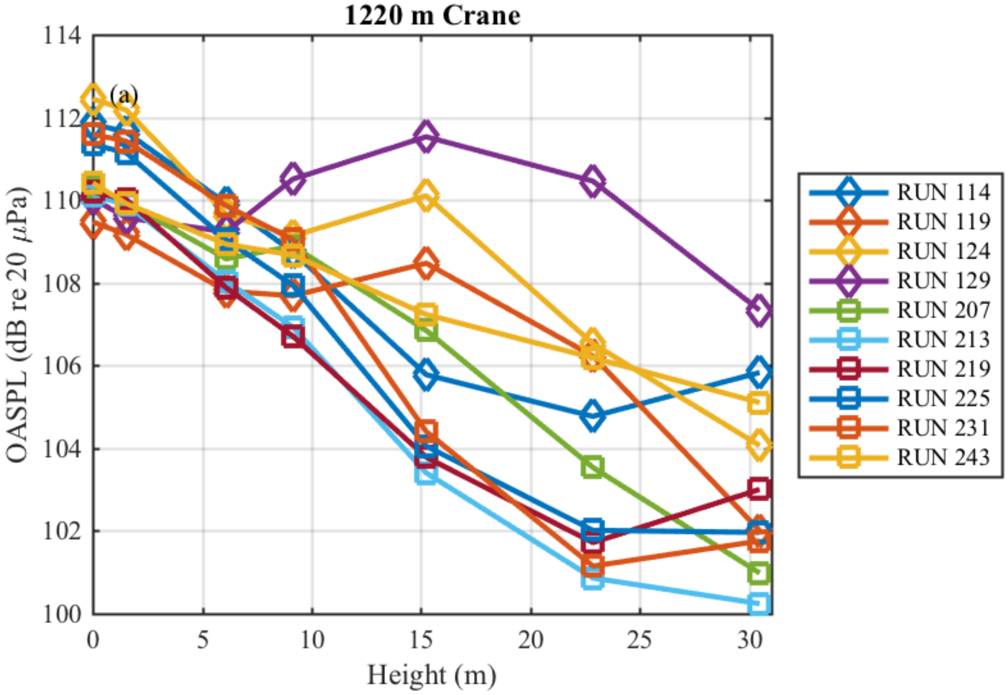

Fig. 6.7 OASPL is shown as a function of height at a distance of 1220 m at 135° for all runs at 100% ETR. Symbols denote which day the run was measured.

The other unexpected trend seen at 610 m was the increase in nonlinearity metrics corresponding to the decrease in OASPL with height. Once again, this trend is confirmed by comparing the behavior at the 1220 m crane with that of the 610 m crane. The trend seen in Fig. 6.8 is similar to the behavior in Fig. 6.6, that nonlinearity metrics tends to increase with height, though this is not as clear as in Fig. 6.6, and nonlinearity metrics peak at lower heights for many of the runs. It is also important to note that the values of the nonlinearity metrics still indicate the presence of significant shocks and crackle. While derivative skewness values vary wildly, in particular at higher microphones, values of 3-5 are seen in roughly half the runs at 22.9 and 30.5 m, indicating continuous crackle and significant shock content.[119] Also important to note is the high derivative skewness values associated with runs 129 and 243. These show the sensitivity of nonlinear propagation to weather effects over long-range propagation and point to the need for better understanding of how changes in the atmosphere within the measurement standard can lead to significantly stronger shocks at some locations.

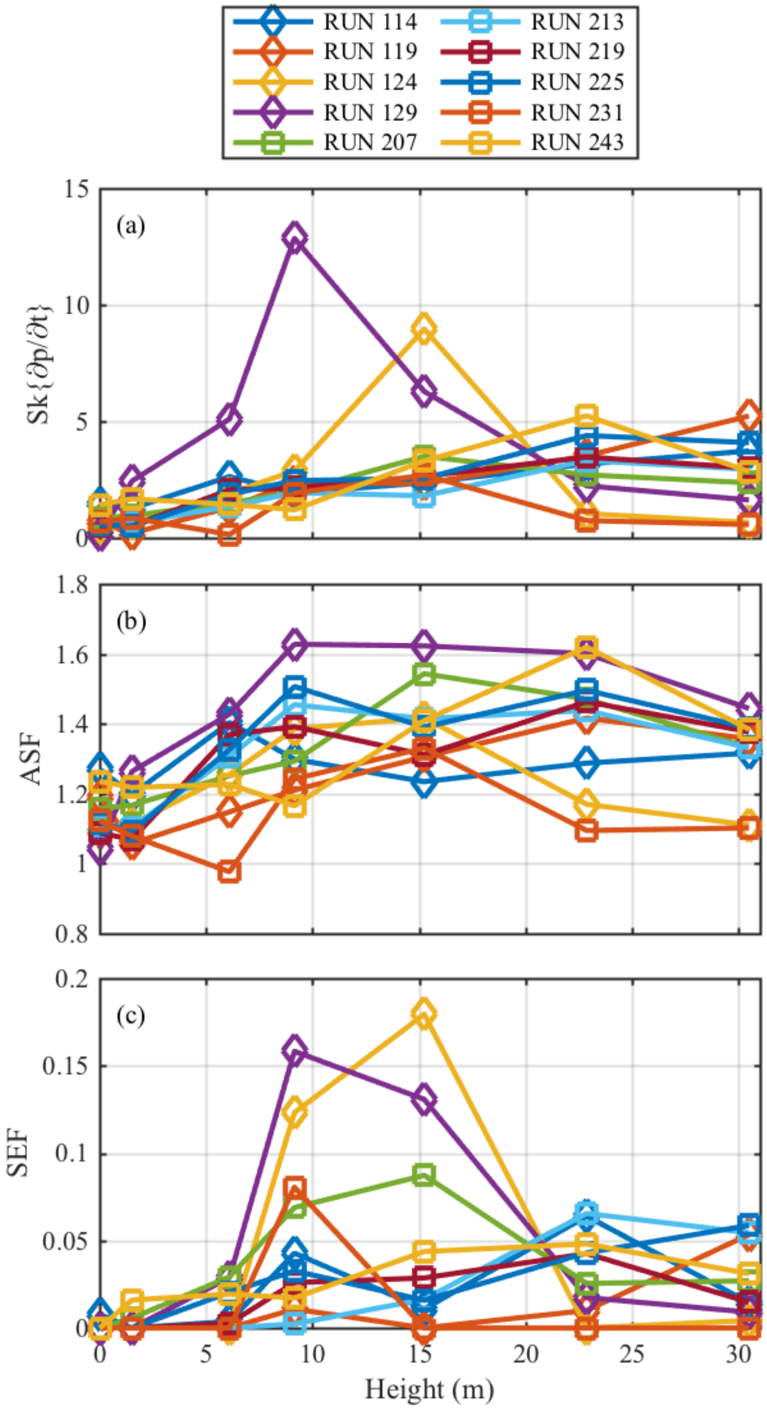

Fig. 6.8 The (a) derivative skewness, (b) ASF, and (c) SEF are shown as a function of height at a distance of 1220 m at 135° for all runs at 100% ETR. Symbols denote which day the run was measured.

6.5 Variation attributable to atmospheric conditions

Since near-field measurements of OASPL in Fig. 6.3 have a standard deviation of less than 1 dB, the larger variation in OASPL at distances far from the source is likely due to small changes in atmospheric conditions. Though a lack of atmospheric data limits analyses, a connection between weather measurements and trends in OASPL would help explain some of the result seen in Section 6.4. While the weather data collected during the experiments were limited, anomalous behavior at the 610 and 1220 m microphones can be connected to quantities such as average wind, the time of day, and a possible temperature inversion.

One of the issues in extracting trends as a function of height from the available data is the small number of runs at each ETR. While variation is seen in the OASPL values in Fig. 6.5, nine or ten runs is likely not enough to show the entire range of possible behavior. To show a larger dataset, OASPL data from all engine conditions are plotted in Fig. 6.9. To compare weather effects, rather than effects due to engine condition, these OASPL values have been normalized to the mean OASPL at a height of 0 m at each engine condition. For instance, the OASPL curves from Fig. 6.5 have had a value of 116 dB subtracted. Unfortunately, normalizing nonlinearity metrics is not as insightful given the wide range of values at each engine condition, and so the analyses in this section are confined to OASPL.

The OASPL at all microphone heights at distances of 610 m and 1220 m and over a range of engine conditions from 75% (Intermediate) to 150% ETR (Maximum afterburner) are shown in Fig. 6.9, with the color of the line corresponding to the average wind speed over the course of the run. Many of the trends seen in Fig. 6.5 and Fig. 6.7 are immediately apparent, showing they are not limited to a certain subset of the measurement. For the majority of the cases, the OASPL decreases with height, with a difference of ~5 dB between 0 and 30.5 m for the crane at 610 m and a difference of 7-10 dB at the 1220 m crane. Also apparent are a few curves that display anomalous behavior, similar to Run 129 shown in Fig. 6.5. These curves show that this behavior was not limited to a single contaminated measurement. It is interesting to note that a higher wind speed occurs during all of these events which deviate from the trend of decreasing OASPL with height observed during the rest of the measurement. However, not all high-wind events result in atypical behavior; while a high wind speed is likely related to the occurrence of the anomalous behavior, it is not enough to predict the behavior alone.

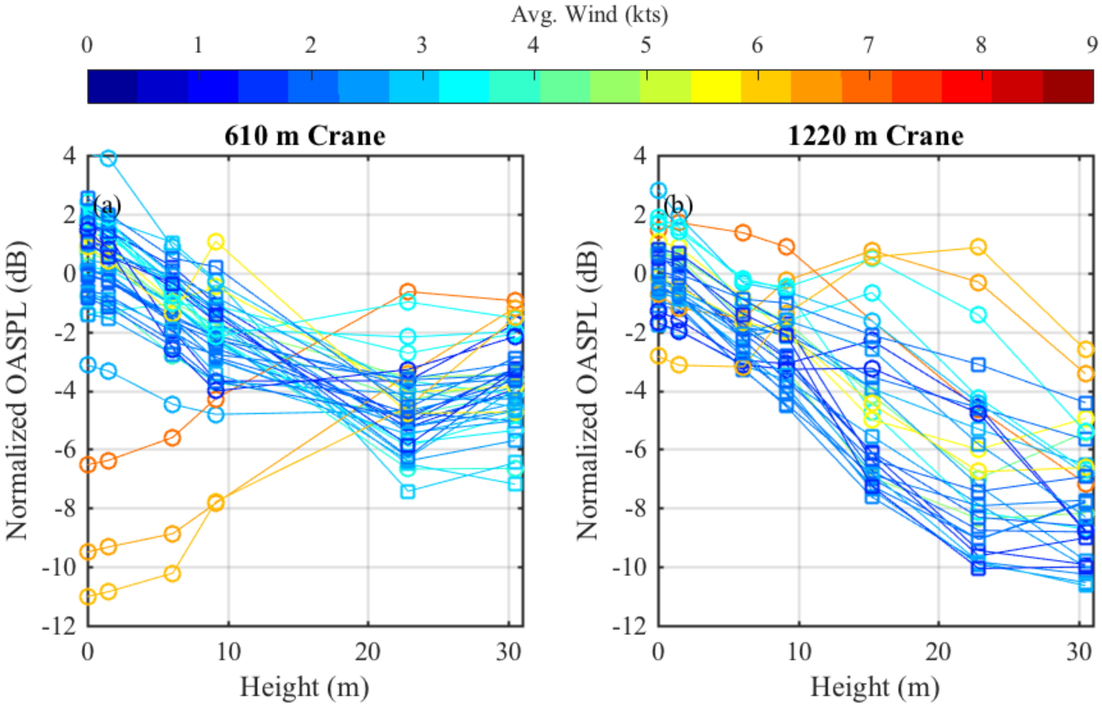

Fig. 6.9 The OASPL (Normalized to average level at 0 m height at each engine condition) as a function of height for all engine conditions from 75% to 150% ETR at 135°. Colors correspond to average wind throughout the run.

Wind is not the only factor that can have a large influence on long-range propagation. Another variable to consider is stratification of the atmosphere. While small variations in temperature are not likely to alter propagation significantly themselves, changes in temperature gradients may have a large impact. Unfortunately, the weather data from these measurements makes it difficult to say conclusively when there was a temperature inversion or lapse, though previous measurements suggest a transition to a temperature lapse occurring with the first 30 minutes after sunrise.[120] However, the time of day is likely related to changes in these atmospheric conditions, and in particular, the transition from a possible temperature inversion to a temperature lapse as the sun rises.

To help demonstrate the effect of time of day, Fig. 6.10 below shows the same OASPL curves as a function of height seen in Fig. 6.9, but the colors now correspond to local time. Sunrise occurred at 6:28 AM on both measurement days, and it is likely that if a temperature inversion were present, it would turn into a temperature lapse as the ground is heated shortly after sunrise, possibly within the first 30 minutes. Similar to the trends seen with wind in Fig. 6.9, all of the anomalous curves occur at times later in the day, with what appears to be an even stronger relationship than for wind speed. However, once again the time of day is not a perfect predictor of OASPL behavior. Long-range propagation effects are a combination of temperature and wind profiles, and more detailed weather observations are needed to uncover a relationship between atmospheric conditions and propagation effects.

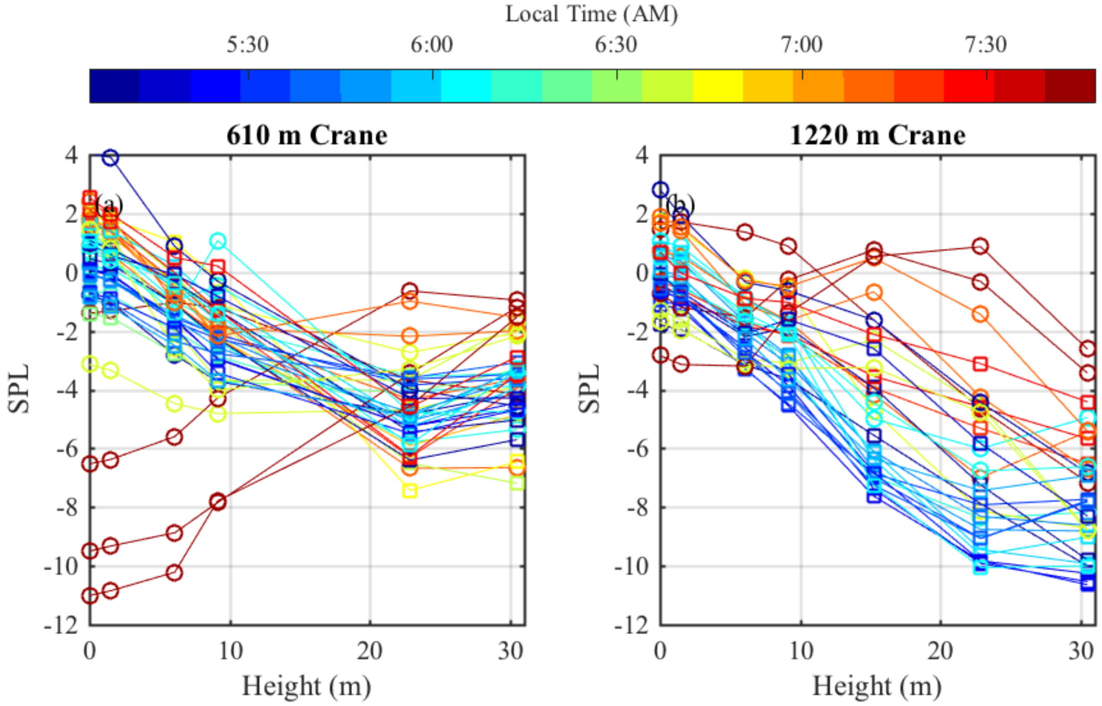

Fig. 6.10 The OASPL (Normalized to average level at 0 m height at each engine condition) as a function of height for all engine conditions from 75% to 150% ETR at 135°. Colors correspond to measurement time.

6.6 Conclusions and Future Work

This chapter illustrates difficulties in accounting for atmospheric conditions in long-range acoustic propagation for static measurements of jet aircraft and shows the importance that nonlinear propagation can have at large distances from the source. Over two days, measurements at 100% ETR, all with weather conditions within ranges allowed by the measurement standard, have consistent OASPL, spectra, and nonlinearity metrics close to the aircraft but show a wide range of behavior at distances of 305 m and greater. One fairly consistent trend seen at microphones located at 610 and 1220 m from the source is a decrease in OASPL with measurement height and an unexpected rise in nonlinearity metrics. However, some variations are seen from these trends. Atmospheric conditions occasionally produce a much lower OASPL than expected or much higher nonlinearity metrics. The anomalous behavior is not limited to a single event, but all events exhibiting the behavior do occur later in the morning on the first day of measurement and are also associated with higher wind speeds. This behavior suggests a transition from a downward-refracting atmosphere to an upward-refracting atmosphere, likely due to changes in temperature and wind shortly after sunrise. While previous measurements support this idea, more precise meteorological data is needed to associate changes in the far-field metrics with smaller atmospheric changes.

Chapter 7

Numerically modeling far-field shock formation

7.1 Introduction

The noise from high-performance military jets is a concern for military personnel who work closely with the aircraft, as well as for communities who may be exposed to such noise. In addition to the high noise levels associated with the aircraft, acoustic shocks may pose an additional risk for both annoyance and hearing loss risk. It is necessary to understand the nature and formation of the acoustic shocks to accurately understand and predict their effects in the sound field. The principles that guide the formation and decay of acoustic shock waves are outlined in nonlinear propagation theory.

The high levels associated with military fighter jet noise mean that linear propagation assumptions are no longer valid. Nonlinear effects are easily observed in the steepening of waveforms in the time domain, which results in spectral broadening and a $1/f^2$ high-frequency spectral slope[56] in the power spectral density. These effects have been observed in both laboratory[33,121] and full-scale[19,21,27,40,64] measurements, although the importance of cumulative nonlinear effects at laboratory scales has been questioned.[16,91] The nonlinear propagation of noise has been numerically modeled using many algorithms and in many situations, including military aircraft.[31,122-125] Blackstock[126] was one of the first to attempt to predict nonlinear propagation of jet noise, followed by Morfey and Howell.[21] Predictions of nonlinear behavior have been shown for multiple aircraft,[19,48] including the F-18,[125,127] and F-35.[30] Gee *et al.*[19] propagated waveforms from an military aircraft from a distance of 61 m to 305 m, along the 125° radial. They showed significantly higher levels at high frequencies compared with linear predictions and that measurements agreed closely with nonlinear predictions. A follow-on study in 2008[48] showed similar results, but broader in scope. Two measurement conditions, 90% ETR and afterburner, were shown at 90°, 125°, and 145°, and multiple propagation distances were considered. Gee *et al.* 2012[22] used a slight modification to the nonlinear propagation algorithm with data from the F-35 and showed variations in nonlinear propagation with differing weather conditions.

In this chapter the nonlinear propagation of jet noise is considered for multiple engine conditions and at a greater angular range than previously shown, including in the forward region of the aircraft. A brief overview of the experimental setup is provided, followed by an examination of time waveforms and spectral maps to show the presence of nonlinear steepening and spectral effects. Spectra at specific locations are shown and examined for nonlinear spectral broadening and other measurement effects such as multi-path interference and atmospheric absorption. Spectra from nonlinear and linear numerical predictions are compared with measurements for multiple angles and engine conditions. Nonlinearity metrics are compared between the measurements and numerical predictions and specific time-domain features of the waveforms are highlighted to illustrate difficulties in both measurement and numerical simulation. These both confirm and better quantify previous findings of significant nonlinear effects in the direction of maximum radiation and show that at high engine conditions a nonlinear transfer of energy is occurring in the forward direction as well, which may cause changes in the perceived noise.

7.2 Measurement Setup

The dataset examined in this chapter was collected at Edwards Air Force Base, September 5, 2013. The experiment has already been extensively described by James *et al.*,[71] but pertinent details are given here. Noise measurements were taken as a tethered F-35A was cycled through power settings ranging from idle to 150% ETR, or maximum afterburner. Each engine condition was measured multiple times throughout the course of the measurements. The 235 unique measurement locations, chosen in accordance with ANSI S12.75,[28] represent the largest full-scale dataset to date in terms of spatial coverage, with microphones located as close as 10 m from the shear layer out to 1220 m away from the microphone array reference position (MARP), located 6.6 m behind the nozzle. Microphones were arranged in either line arrays, parallel to the jet centerline, or in semi-circular arcs centered at the MARP. As most of the noise generated by supersonic jets is emitted from the turbulent mixing that occurs behind the jet, the MARP represents a rough estimate of source location for many frequencies of interest. For arcs from 38 m out to 305 m, arc spacing of 5° between microphones was used in the direction of peak radiation, between 120° and 160°.

The microphone locations within 38 m of the aircraft are shown in Fig. 7.1, with the aircraft also included and shown to scale. Microphone locations beyond 38 m are shown in later plots. In the areas of maximum acoustic pressure, 6.35 mm (1/4”) microphones were used, with sampling rates of either 192 kHz or 204.8 kHz. At 305 m, in the forward direction, waveforms were captured at measurement locations from 0° to 40° and 60° to 80° using sound level meters. The meters recorded time-history Waveform Audio File Format (wav) files at a sampling rate of 51.2 kHz. Measurements were conducted between 3:00 and 9:00 AM local time, with temperature varying between 19.4°C and 23.1°C, relative humidity between 37.6% to 45.7%, and an average wind speed of 3.3 kts, with a maximum windspeed of 8.0 kts during measurements.

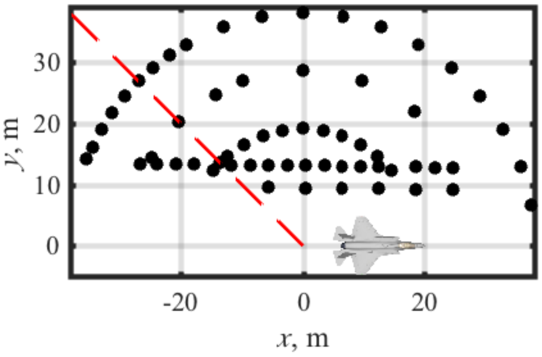

Fig. 7.1 Microphone measurement positions within 38 m of the MARP. The dashed red line shows the $\theta = 135°$ radial.

7.3 Metrics Indicative of Nonlinear Propagation

Because of the broadband, complex nature of nonlinear propagation and shock formation within jet noise, attempts to quantify the strength of shocks within jet noise have often concentrated on nonlinearity metrics, single values expressing the shock content of a waveform. Nonlinearity metrics considered in this chapter are derivative skewness, ASF, and SEF, a new wavelet-based metric.

7.3.1 Derivative Skewness

The skewness of the distribution of the first time derivative of the pressure waveform (estimated via finite difference) is a statistical measure that assesses the overall steepness of a waveform. Nonzero skewness values express an asymmetry in a distribution, and the large derivative values associated with acoustic shocks result in a distribution in which there are many slightly negative values with relatively fewer, but significantly larger positive values. This distribution results in a large positive derivative skewness indicative of steepened waveforms. Derivative skewness has been used to show the presence of shocks in both model-scale[16,10] and full-scale[22,40] analyses.

An advantage of this metric is that it is dependent only on the waveform shape and independent of an arbitrary definition of a shock, but it has notable disadvantages as well. First, sampling rate must be sufficient to adequately resolve the large positive derivatives associated with shocks and, hence, a relatively low sampling rate might cause the derivative skewness values to be severely underestimated.[17,80] A physical interpretation of derivative skewness values has also proven difficult. Recent work,[17,80] however, has shown that a threshold of derivative skewness values of approximately 5 or larger indicates significant waveform steepening and shock content, provided that the sampling frequency exceeds the characteristic frequency in the waveform by a factor of at least 100.

7.3.2 Average Steepening Factor

Another time-domain metric that has been used to quantify waveform steepening is the average steepening factor (ASF), defined as the average value of positive derivatives divided by the average value of negative derivatives. This quantity was originally defined as the inverse, the waveform steepening factor $\mathrm{WSF} = 1/\mathrm{ASF}$, and like the derivative skewness has been used in both model-scale[16] and full-scale[128] applications. A recent paper by Muhlestein *et al.*[50] derives analytical expressions for ASF for high-amplitude, initially sinusoidal signals, and additionally shows values for nonlinearly propagating noise in a plane-wave environment. A non-steepened waveform would have $\mathrm{ASF} = 1$, while steepened waveforms have higher values. The ASF of shock-containing jet noise is typically at a value of 1.5 and above.[128] Because the ASF is a linear mean of derivative values it represents trends within the entire waveform more than the derivative skewness, which accentuates the large positive outliers. However, the ASF is also more susceptible to the presence of extraneous noise than the derivative skewness.[13,80]

7.3.3 Shock Energy Fraction

The steepening of shocks in the time domain results in spectral broadening in the frequency domain, as energy is transferred from the peak frequency region to higher frequencies. Although this effect is often shown using the more familiar Fourier transform, a wavelet transform has been used in lab-scale jet noise analysis as a frequency-domain technique that also gives temporal resolution.[16] The SEF is a metric that compares high-frequency (>2 kHz) energy associated with shocks within the waveform to the total high-frequency energy present. A value of $\mathrm{SEF} = 0$ corresponds to no energy located at the shocks, while a value of $\mathrm{SEF} = 1$ means that all high-frequency energy is located at the shocks.

7.4 Spectral Analysis

A detailed analysis of the F-35 spectra at individual distances and angles can demonstrate where nonlinear propagation is occurring and to what extent. Before this analysis, linear and nonlinear propagation effects on the spectrum are discussed, following which the spectra are shown.

7.4.1 Spectral Effects

As described briefly above, waveform steepening results in a transfer of spectral energy from the peak-frequency region to higher frequencies. In a waveform containing weak shocks, the spectrum of the noise decays at $1/f^2$. For one-third-octave (OTO) spectra, which are presented here, shock-containing noise has an expected roll-off rate for high frequencies of 10 dB/decade.[17]

As the waveform continues to propagate, rise time increases and the shocks begin to thicken. As the shocks thicken the linear absorption at high frequencies has a large effect and the roll-off of the spectrum at higher frequencies increases. For initially sinusoidal plane waves this occurs when the distance, r, is equal to the absorption length, defined as

$$l_\alpha = 1/\alpha(f), \tag{7.1}$$

where $\alpha(f)$ is the absorption coefficient.[7] For sinusoidal plane waves, this distance is independent of initial source amplitude. Others have shown this transition to what is called the old-age region while incorporating geometric spreading[129] and for broadband noise.[130] When the absorption length is equal to the distance from the noise source, a steeper spectral roll-off can be expected. The distances at which far-field microphones were situated in the current experiment are listed in Table 7.1 along with the frequency associated with the absorption length at that distance. The absorption length is calculated using meteorological data from the measurements over a range of frequencies, then the data are interpolated to find the frequency with the absorption length at the microphone distances from the MARP.

Table 7.1. The frequencies with an absorption length corresponding to measurement locations. The absorption length is calculated using meteorological data from the given measurement time over a range of frequencies, then the data are interpolated to find the frequency with the absorption length at the microphone distances from the MARP.

Distance (m)	76	152	305	610	1220
Frequency (kHz)	8.0	5.5	3.8	2.4	1.5

In addition to the nonlinear effects that affect the high-frequency roll-off of the spectra, ground reflections can have a significant effect on discrete frequencies. Both the aircraft nozzle and the microphones used to record data were located off the ground, producing a minimum of two paths by which sound can travel from the noise source to the microphone, either directly through the air or after reflecting off the ground. The discrete frequencies at which the two paths will interfere destructively can be found if one assumes a point source at a height of 1.82 m and a finite ground flow resistivity.[131] In this case a value of 3,000 rayls was used, typical of hard-packed earth. Although the model gives the effect of constructive and destructive interference over a range of frequencies, Table 7.2 lists the first frequency at which destructive interference is observed. This null has the most significant effect on OTO spectra due to averaging, and the effects of higher frequency nulls are diminished due to turbulence in the atmosphere and the extended area of the ground reflection.[132,133]

Table 7.2. Microphone heights and expected interference nulls for various distances. The heights of the microphones located in arcs of various radii are listed. These microphone heights are then used with a nozzle height of 1.82 m to calculate the frequency at which an interference null would be expected using a ground flow resistivity of 3,000 rayls.

Distance (m)	19	29	39	76	152	305
Mic. Height (m)	1.52	1.52	1.52	3.66	5.49	9.14
Frequency (kHz)	0.54	0.78	0.96	0.78	0.89	0.89

7.4.2 Spectral Comparisons

With the above analyses and expected behavior concerning spectral decay, absorption length, and ground reflections, the spectra measured at specific locations can be examined for evidence of each of these phenomena. The spatial dependence of the spectra along 30°, 90°, 135°, and 150° radials are shown in Fig. 7.2-Fig. 7.5, respectively. These angles are chosen because they correspond with spatial regions where the noise properties are significantly different: forward direction, sideline of the MARP, near the maximum radiation direction and farthest downstream positions. Though some angles had microphones at a greater range of distances, at all four angles the waveforms measured at 38.1 m, 76.2 m, and 305 m from the MARP are shown for four engine conditions: (a) 50%, (b) 75%, (c) 100%, and (d) 130% ETR.

Along the 30° radial in Fig. 7.2(a), the spectrum measured at 76 m begins to sharply roll off at roughly 3 kHz, but in Fig. 7.2(c) and Fig. 7.2(d) the roll-off is much more gradual, even at frequencies as high as 20 kHz, where absorption should be having a large effect. The persistence of the shallower spectral slope at high frequencies implies that the high-frequency losses expected from atmospheric absorption (>150 dB at 10 kHz between 76 m and 305 m) are being countered by nonlinear propagation effects. Though the rate of roll-off is greater than would be expected if shocks were present, it is still smaller than would be expected if purely linear behavior is assumed. Because of this, the spectral shapes alone do not conclusively exhibit the effects of far field nonlinear propagation in the forward direction. This concept is revisited in a later section.

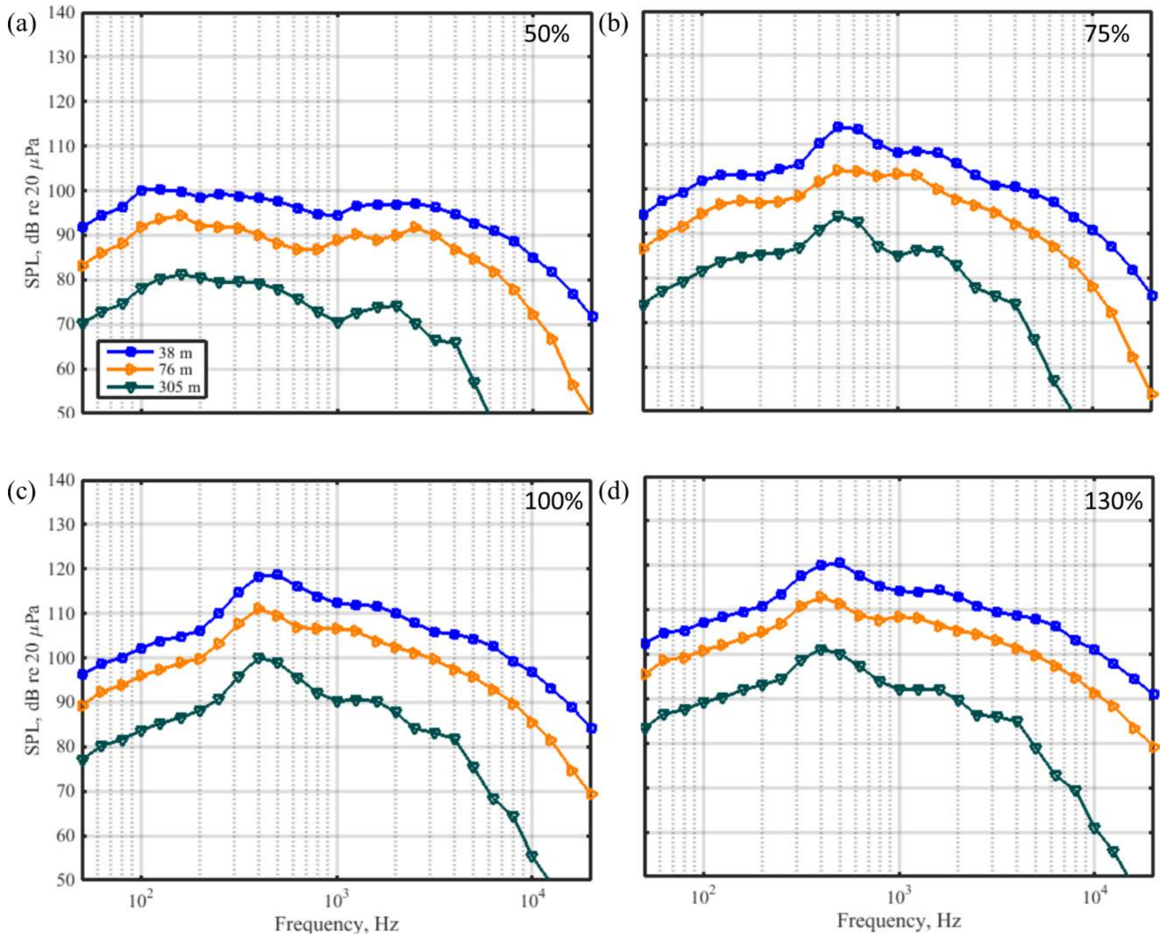

Fig. 7.2 OTO Spectra along the 30° radial as a function of engine condition. The four plots show the OTO spectra calculated at (a) 50% ETR, (b) 75% ETR, (c) 100% ETR, and (d) 130% ETR.

As the ETR increases, the spectral shape at higher frequencies (>6-7 kHz) changes for all four angles. The greatest nonlinear effects are expected in the maximum radiation direction, shown in Fig. 7.4. In this direction, the levels at frequencies of up to 12 kHz are greater than 80 dB at $r = 305$ m from the source, a level inconsistent with linear losses. In addition, from linear assumptions one would expect that between 38 m and 76 m the spectral levels at higher frequencies in Fig. 7.4(d) to have decreased relative to lower frequencies. Instead, the spectral shape is essentially unchanged, as the nonlinear transfer of energy to higher frequencies balances out the loss due to absorption. This change in the slope of the high-frequency portion of the spectral shape is most easily observed in the spectra at 76 m but can also be seen in the 152 m and 305 m spectra, indicating nonlinear propagation. If many sawtooth-like shocks are present in the waveform, the high-frequency roll-off should be roughly 10 dB/decade, and this is seen to some extent for all four ETR shown. The roll-off should also be greater at the frequencies calculated in Section 7.4.1 when the distance is on the same order of magnitude for the absorption length of that frequency, and these values do correspond with changes in the spectral shape at each distance from the source, especially at greater ETR.

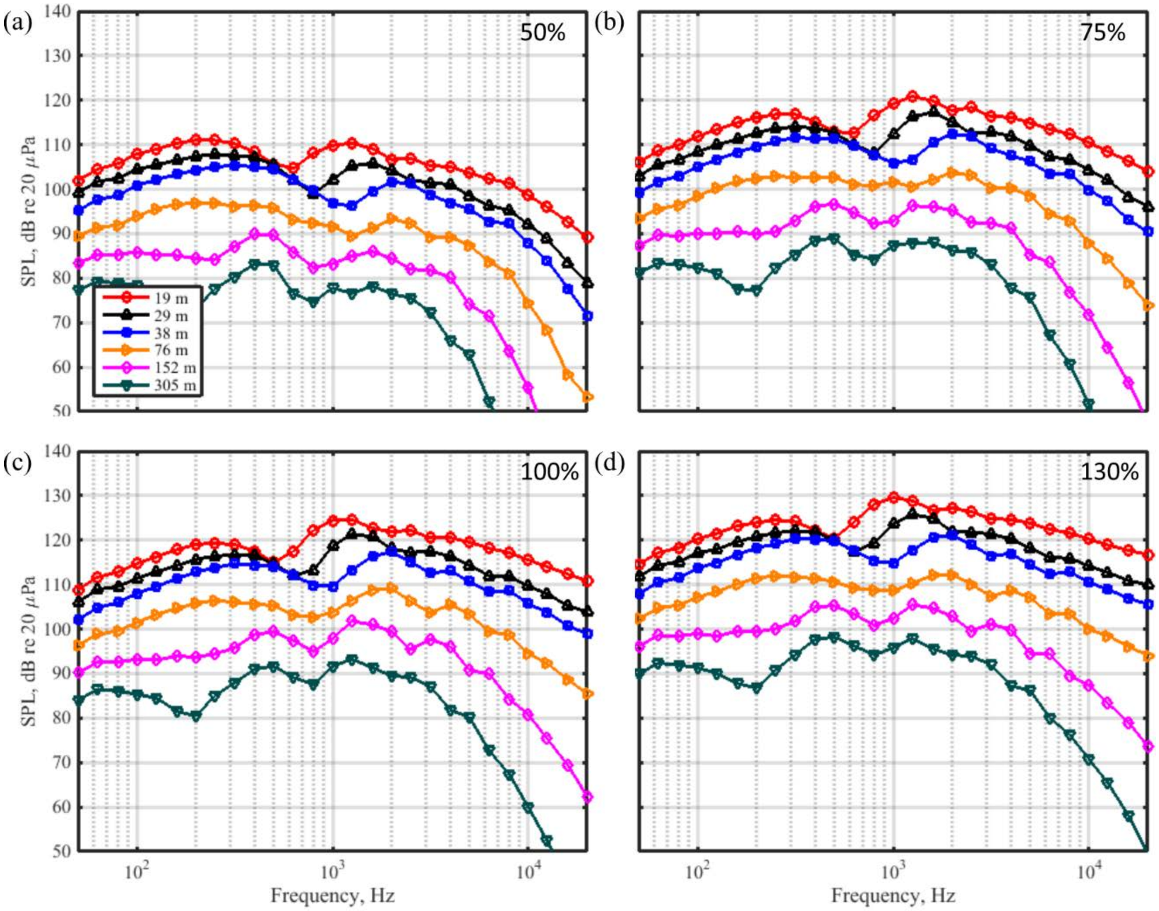

Fig. 7.3 OTO Spectra along the 90° radial as a function of engine condition. The four plots show the OTO spectra calculated at (a) 50% ETR, (b) 75% ETR, (c) 100% ETR, and (d) 130% ETR.

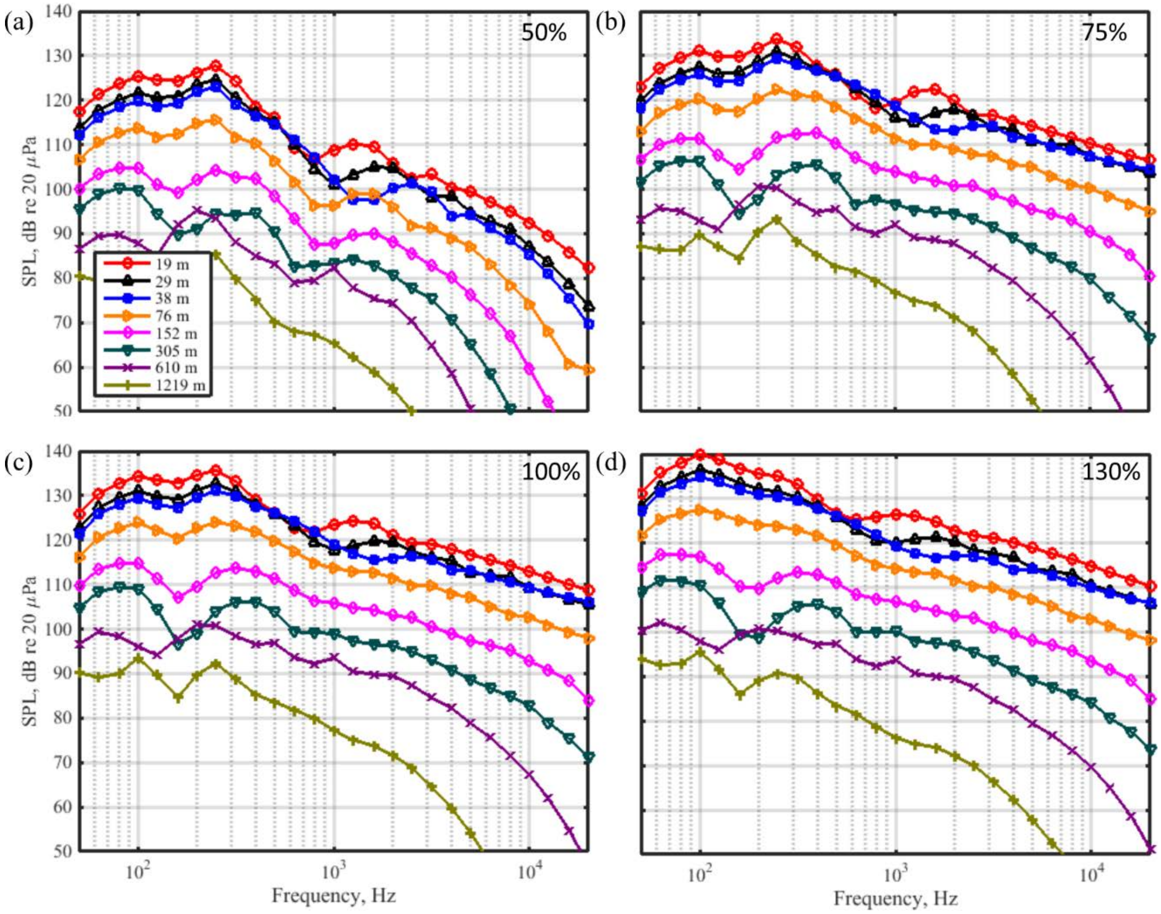

Fig. 7.4 OTO Spectra along the 135° radial as a function of engine condition. The four plots show the OTO spectra calculated at (a) 50% ETR, (b) 75% ETR, (c) 100% ETR, and (d) 130% ETR.

These same trends are seen in Fig. 7.3 and Fig. 7.5, though at a slightly lower level. Also of note is the strong evidence of a ground reflection null for all ETR in Fig. 7.3. For the spectra at 19 m, this null occurs between 500-600 Hz, precisely at the value calculated in Section 7.4.1. Also evident is the presence of interference in the spectra of microphones at 610 and 1220 m at frequencies well below those at which ground reflections would be expected. These interference nulls provide further evidence for a downward-refracting atmosphere, due to either a gradient in wind or temperature.

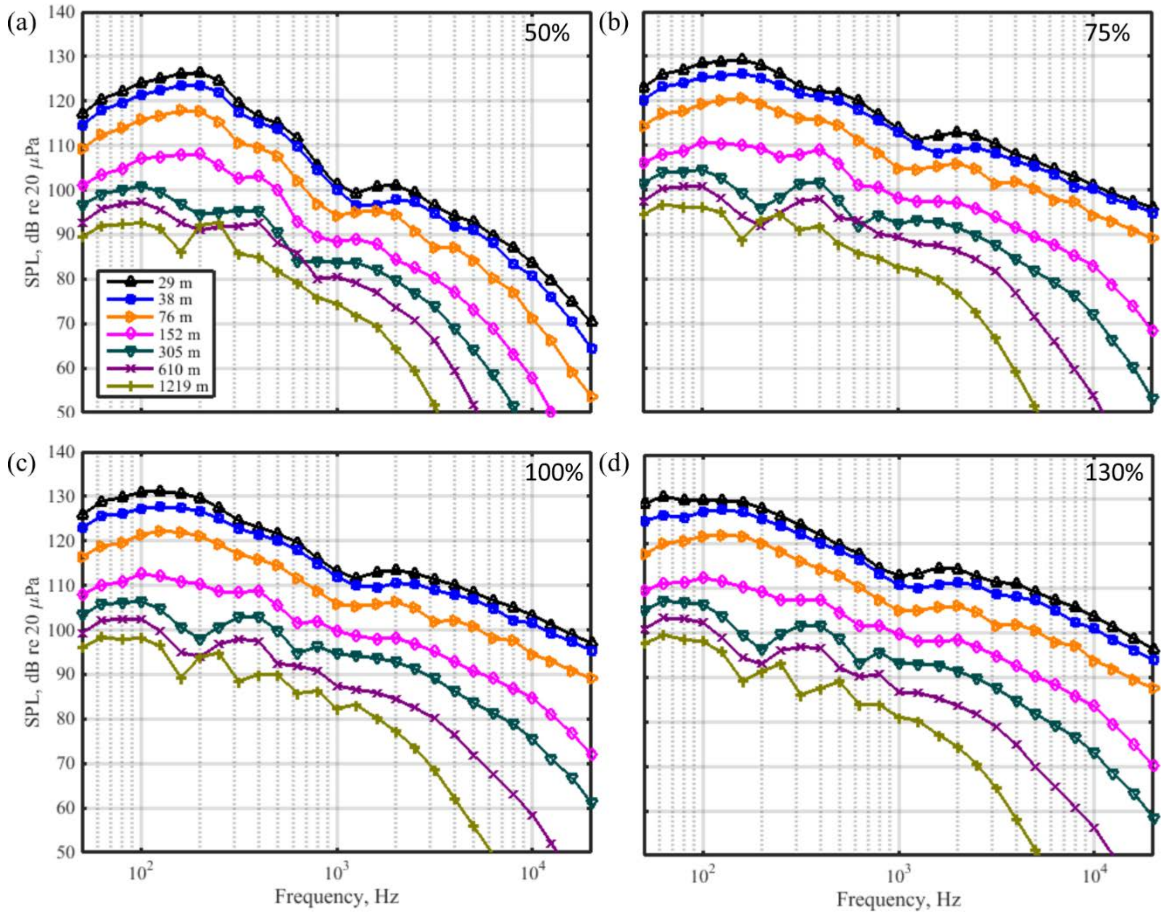

Fig. 7.5 OTO Spectra along the 150° radial as a function of engine condition. The four plots show the OTO spectra calculated at (a) 50% ETR, (b) 75% ETR, (c) 100% ETR, and (d) 130% ETR.

7.5 Nonlinear Propagation Modeling

The above spectra certainly suggest that nonlinear propagation is a factor, at the very least out to 305 m and possibly farther, and at a broad range of angles at engine conditions of 100% ETR and above. However, in order to quantify the effect that nonlinear propagation has on both the waveform and the spectrum, the nonlinear effects must be compared with a linear prediction. To do this, both linear and nonlinear propagation schemes are used to numerically propagate waveforms measured at 76.2 m to 305 m, and the resulting spectra are compared with those calculated from the measured waveform at 305 m across a wide range of angles from 0° to 160°.

7.5.1 Propagation Algorithm and Spectral Correction

The nonlinear propagation code is similar to that used by Gee *et al.*[19] It is a hybrid time-frequency domain algorithm based on the Generalized Burgers Equation (GBE) and incorporates geometric spreading, atmospheric absorption, and quadratic nonlinearity as well as weak-shock theory developed by Pestorius and Blackstock[31] to more efficiently propagate shocks. A similar code that neglects the quadratic nonlinearity is used to propagate the waveforms linearly. The spectra from these nonlinear and linear predictions can be compared against each other and against the spectrum of the measured waveforms.

Multi-path interference presents a problem in comparing numerically propagated waveforms with measurements. Measurements at 76 m from the MARP have an interference pattern due to the geometry of that location and other weather effects, but these frequency-domain patterns are still carried throughout the propagation process. However, at 305 m an entirely different interference pattern is seen, and the numerical models have no way to correct for these changes. To account for this difference in spectrum an empirical correction, developed by Gee *et al*. 2007[19] and used again in Gee *et al.* 2012[79] for meteorological and propagation environment effects not treated by the GBE model, is applied. Based on the assumption that over a short period of time, the changes in spectra due to interference effects and meteorology between the two distances are consistent, the correction is the difference between the spectra from the numerical propagation and the measurement. This correction uses the change in spectrum between the two measurement locations from a low-power measurement where nonlinear effects are minimal, in this case 50% ETR, to correct predictions at higher measurement location. The measured waveform for 50% ETR is numerically propagated to the second location, and the difference between the predicted spectrum and the measured spectrum is calculated. For higher engine power conditions, this difference is then added to the predicted linear and nonlinear spectra, such that

$$SPL_{\mathrm{HP,corr}} = SPL_{\mathrm{HP,pred}} + (SPL_{\mathrm{LP,meas}} - SPL_{\mathrm{LP,pred}}) \tag{7.2}$$

where HP indicates high power, LP low power, $SPL_{\mathrm{HP,corr}}$ is the corrected spectrum, and pred and meas refer to the predicted and measured spectra. Note that this correction is only applied below 1 kHz due to noise floor issues at 305 m above this frequency. However, this frequency range corresponds to the largest changes due to interference, and nonlinear propagation effects are small at 50% below 1 kHz.[19]

7.5.2 Nonlinear Prediction Spectral Comparison

Both the linear and nonlinear propagation algorithms are applied to waveforms measured at $r = 76.2$ m to estimate waveforms at $r = 305$ m. The empirical corrections in Eq. (7.2) are estimated separately at each angle and applied to the spectra of the numerically propagated waveforms in both the linear and nonlinear cases. The linearly and nonlinearly propagated waveforms are compared with the spectra measured at 305 m for 50% ETR in Fig. 7.6 at 30°, 90°, 135°, and 150°. For this low ETR, at both 30° and 90° there is essentially no difference between the linear and nonlinear predictions. At 135° and 150° small differences are seen but all three spectra are within a few decibels of each other.

As ETR increases, so do the differences between nonlinear and linear predictions. At 75% ETR, as shown in Fig. 7.7, nonlinear effects are evident at 135° and 150°, shown in Fig. 7.7(c) and (d), where there is a large difference among the higher frequencies. In both these cases, the measured spectrum very closely resembles the nonlinear prediction. In spite of differences in the spectra at low frequencies due to interference nulls, the nonlinear propagation code accurately characterizes the high-frequency behavior within 1-2 dB. The difference between the linear and nonlinear predictions is greater at 100% ETR, as shown in Fig. 7.8. The relative increase in high-frequency energy is again most evident at 135° and 150°, but small differences in the high frequencies can also be seen at 30° and 90° in Fig. 7.8(a) and Fig. 7.8(b).

In the discussion of Fig. 7.2 it is shown that the spectral roll-off at high frequencies could show nonlinear behavior in the forward direction. Further evidence is seen in Fig. 7.8(a) and (b), where nonlinear predictions agree with measured data more closely than linear predictions. The evidence of nonlinear propagation in the forward direction is even clearer at 130% ETR. In Fig. 7.9(a), the measured spectrum at 8 kHz is 10 dB higher than the linear prediction. Though the nonlinear method slightly overestimates the spectrum at the higher frequencies, it is more accurate than the linear prediction, indicating a degree of nonlinear propagation in the far-field forward direction.

The results show that spectra calculated from measured waveforms closely resemble those using the nonlinear propagation algorithm. In some cases, the nonlinear algorithm overpredicts the level at high frequency, but this may be in part due to terrain effects such as dense shrubbery nearby between 76 m and 152 m, which could substantially affect higher frequencies. At lower ETR the linear and nonlinear predictions are nearly aligned, but at higher conditions the measured data agrees more closely to the nonlinear predictions, even at 30°, in the forward direction of the aircraft. Because the nonlinear predictions accurately reflect changes in the spectra, in particular at high frequencies, a comparison between linear and nonlinear predictions can be used to quantify the strength of nonlinear effects as a function of angle.

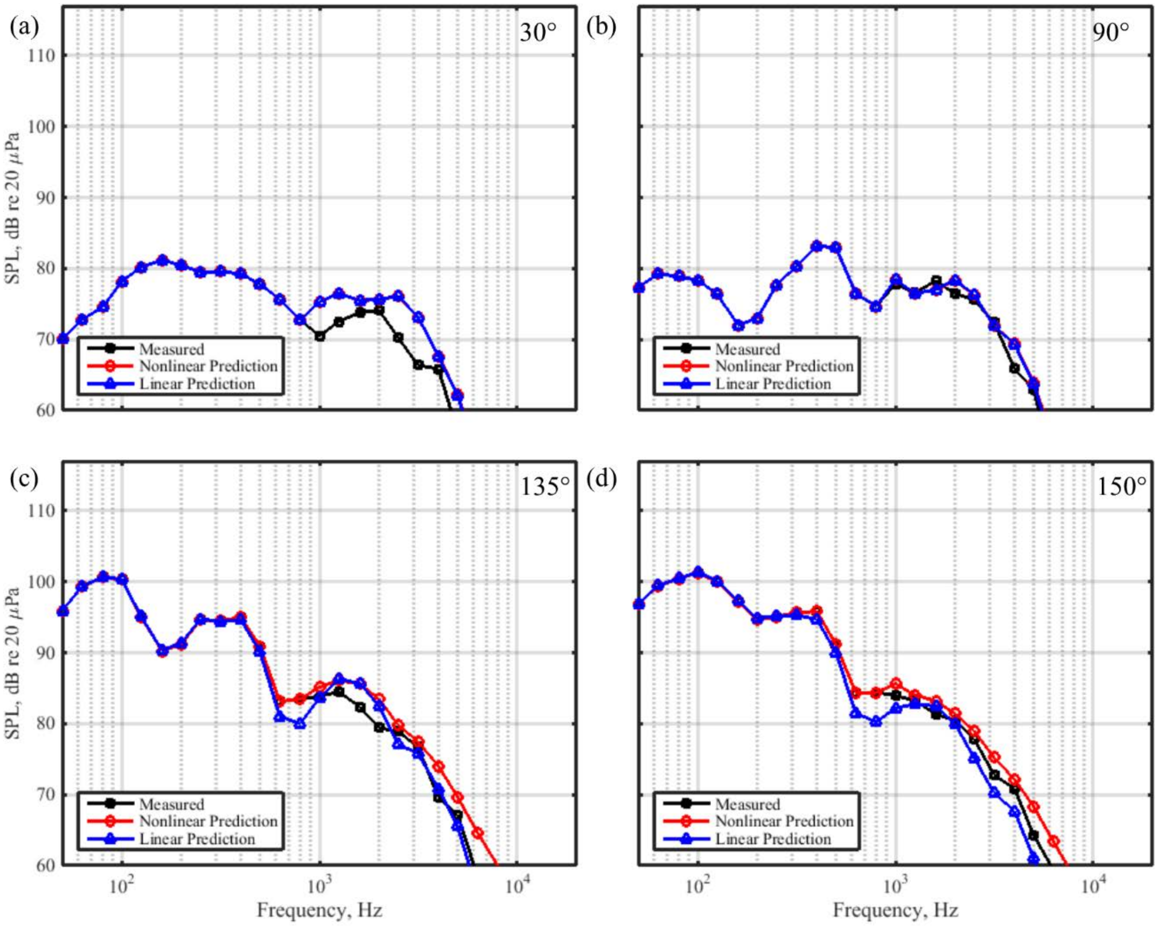

Fig. 7.6 OTO spectra at 305 m compared with linear and nonlinear predictions for 50% ETR. Waveforms measured at *r* = 76.2 m are propagated to *r* = 305 m using both linear (blue) and nonlinear (red) propagation algorithms. The resulting OTO spectra are compared with the spectra at 305 m (black) at (a) 30°, (b) 90°, (c) 135°, and (d) 150°.

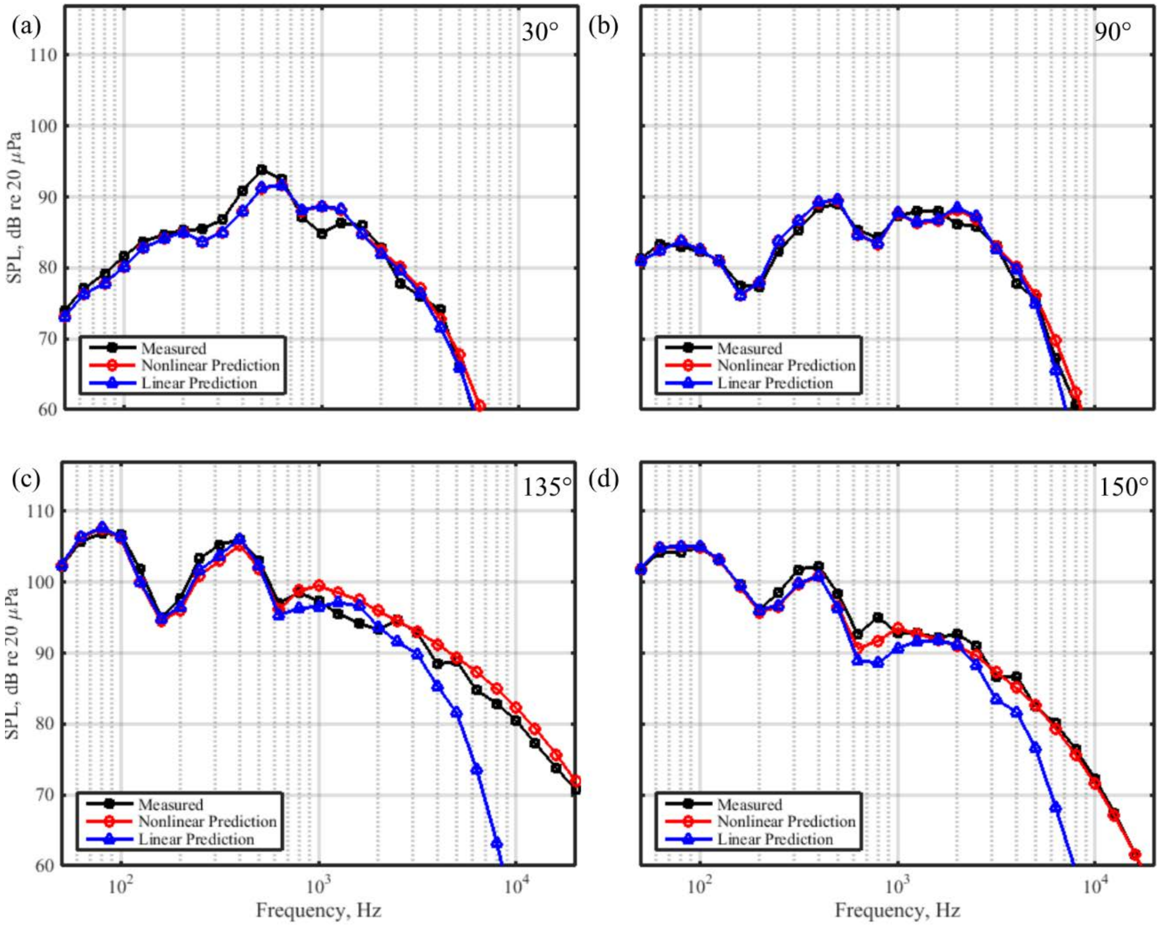

Fig. 7.7 OTO spectra at 305 m compared with linear and nonlinear predictions for 75% ETR. Waveforms measured at r = 76.2 m are propagated to r = 305 m using both linear (blue) and nonlinear (red) propagation algorithms. The resulting OTO spectra are compared with the spectra at 305 m (black) at (a) 30°, (b) 90°, (c) 135°, and (d) 150°.

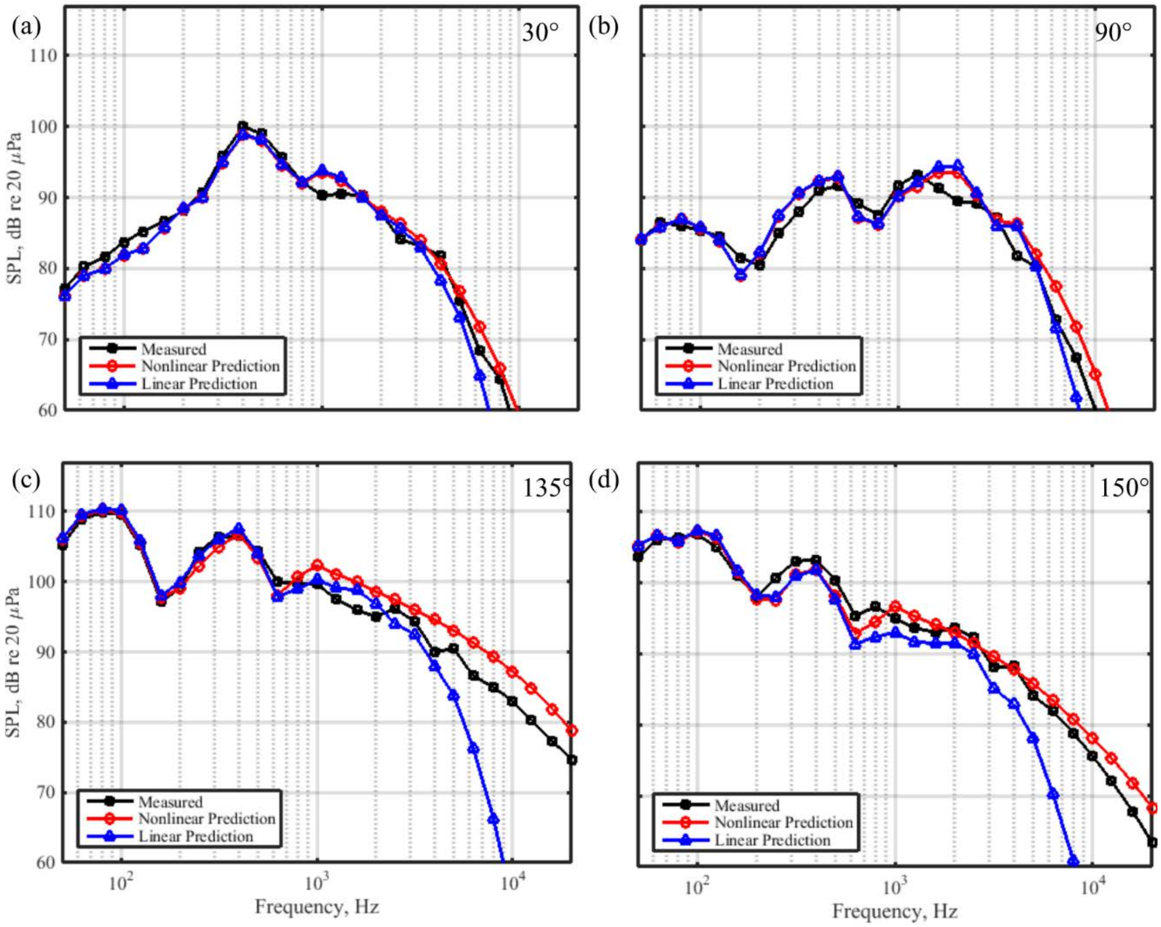

Fig. 7.8 OTO spectra at 305 m compared with linear and nonlinear predictions for 100% ETR. Waveforms measured at *r* = 76.2 m are propagated to *r* = 305 m using both linear (blue) and nonlinear (red) propagation algorithms. The resulting OTO spectra are compared with the spectra at 305 m (black) at (a) 30°, (b) 90°, (c) 135°, and (d) 150°.

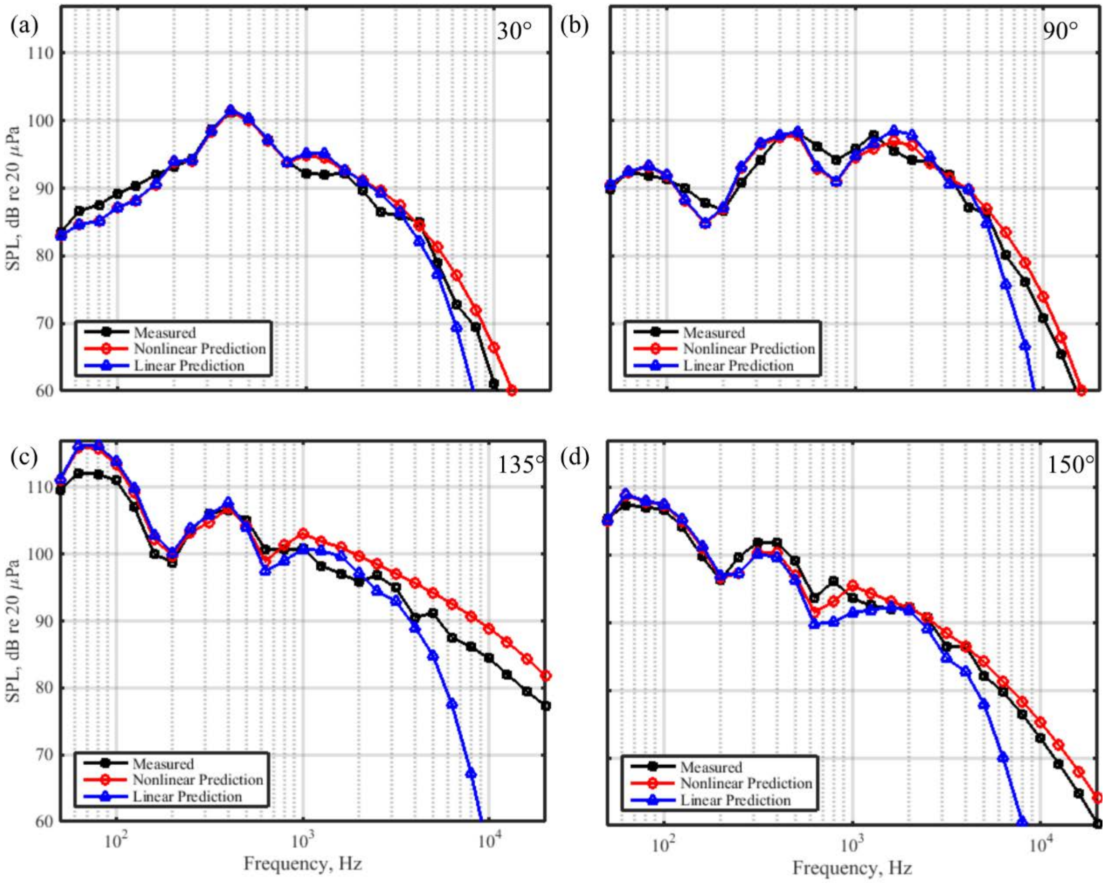

Fig. 7.9 OTO spectra at 305 m compared with linear and nonlinear predictions for 130% ETR. Waveforms measured at *r* = 76.2 m are propagated to *r* = 305 m using both linear (blue) and nonlinear (red) propagation algorithms. The resulting OTO spectra are compared with the measured spectra at 305 m (black) at (a) 30°, (b) 90°, (c) 135°, and (d) 150°.

7.5.3 Nonlinear Gain

Direct inspection of the waveforms and their spectra provides a clear view of the formation of shock waves and the presence of nonlinear propagation but fails to quantify the strength of nonlinear effects. However, this can be accomplished by computing the nonlinear gain, in decibels.[134] In order to calculate nonlinear gain, a measured waveform is propagated out to a greater distance using the Burgers-equation-based linear and nonlinear propagation algorithms used in the previous section. The OTO spectra are calculated from each of these propagated waveforms, and the difference in level between the two is the nonlinear gain. Because the nonlinearly propagated waveforms have been shown to have spectra similar to those that were measured, the nonlinear gain can accurately estimate the impact of nonlinear propagation on the spectrum. For the following discussion, the measurements at the $r = 76.2$ m arc are used as input to both models and propagated to $r = 305$ m. The angular variations in the frequency-dependent nonlinear gain are presented for the same four engine conditions as before: 50%, 75%, 100% and 130% ETR.

The nonlinear gain quantifies the difference between the nonlinearly and linearly predicted spectra and is largest in the direction of maximum level and increases as ETR increases. The nonlinear gain across angles from 0° to 160 ° is presented in Fig. 7.10. At an ETR of 50%, shown in Fig. 7.10(a), the nonlinear gain is greater than 25 dB above 10 kHz in the 135°-155° directions and greater than 45 dB at 20 kHz. This increase in high-frequency energy comes from the small decrease seen in the region from 100-200 Hz, where slightly negative values of nonlinear gain are seen. However, this increase comes in a frequency range that is much lower in level than the spectral peak. At 75% ETR, in Fig. 7.10(b), the maximum nonlinear gain is nearly 60 dB, with 30 dB or larger gain above 10 kHz in the 125°-155° directions. As the ETR increase to 100%, nonlinear gain increases as well and over a wider range of angles, as shown in Fig. 7.10(c). The nonlinear gain now has a peak value of 63 dB at 20 kHz over 120°-145°. In addition, nonlinear gain greater than 20 dB is evident for frequencies above 10 kHz from 20° to 155°, a significant increase in the forward direction.

At first glance, the nonlinear gain does not differ considerably between 100% and 130% ETR, shown in Fig. 7.10(d). The maximum nonlinear gain at 130% is only slightly larger than at 100% ETR, on the order of 1-2 dB. However, the angular aperture at which the nonlinear gain is over 25 dB above 10 kHz is larger at 130% ETR, spanning the range from 10° to 155°. In addition, the angular region over which the nonlinear gain is greater than 50 dB at 20 kHz shifts forward to 110° to 155° at 130% ETR, instead of 120° to 155° at 100% ETR. This forward shift is related to the change in the directivity with engine condition. The lack of difference in the maximum value of the nonlinear gains could indicate that an upper limit has been reached: the amount of energy that can be transferred to higher frequencies has a limit, which is governed by the spectral signature of shock waves. As pointed out earlier, the presence of shocks is tied to a $1/f^2$ high-frequency spectral slope. (10 dB/OTO decade). This limit of the slope corresponds to the upper limit on the nonlinear gain. Thus, the fact that the maximum values of the nonlinear gain are nearly identical in the maximum radiation direction for 100% and 130% ETR points to the fact that the spectral shape is still in large part determined by the presence of shocks.

The nonlinear gain, as shown in Fig. 7.10, provides a compact means of showing the importance of nonlinear propagation for the different engine conditions and angles. However, these values do not necessarily correspond with experimental values. In Fig. 7.6-Fig. 7.9 the measured spectrum often lies between the nonlinear and linear predictions, and in particular for low-power cases, the measured spectrum is often directly in the middle of the two predictions. Though the levels may not exactly correspond with measurements, the general trends still agree with those found in the discussion of Fig. 7.6-Fig. 7.9. Nonlinear gain of 35 dB can be seen at ETR as low as 50%, and the effects continue to grow, both in magnitude and spatial extent, as the ETR and corresponding SPL increase. At 130% ETR an increase of 25 dB at 10 kHz is seen over almost all angles. This nonlinear gain in the forward direction is similar to that seen in the direction of maximum radiation at 50% ETR, indicating that there is nonlinear propagation occurring, but that similar to 50%, the effects of the nonlinear propagation are small in the experimental results.

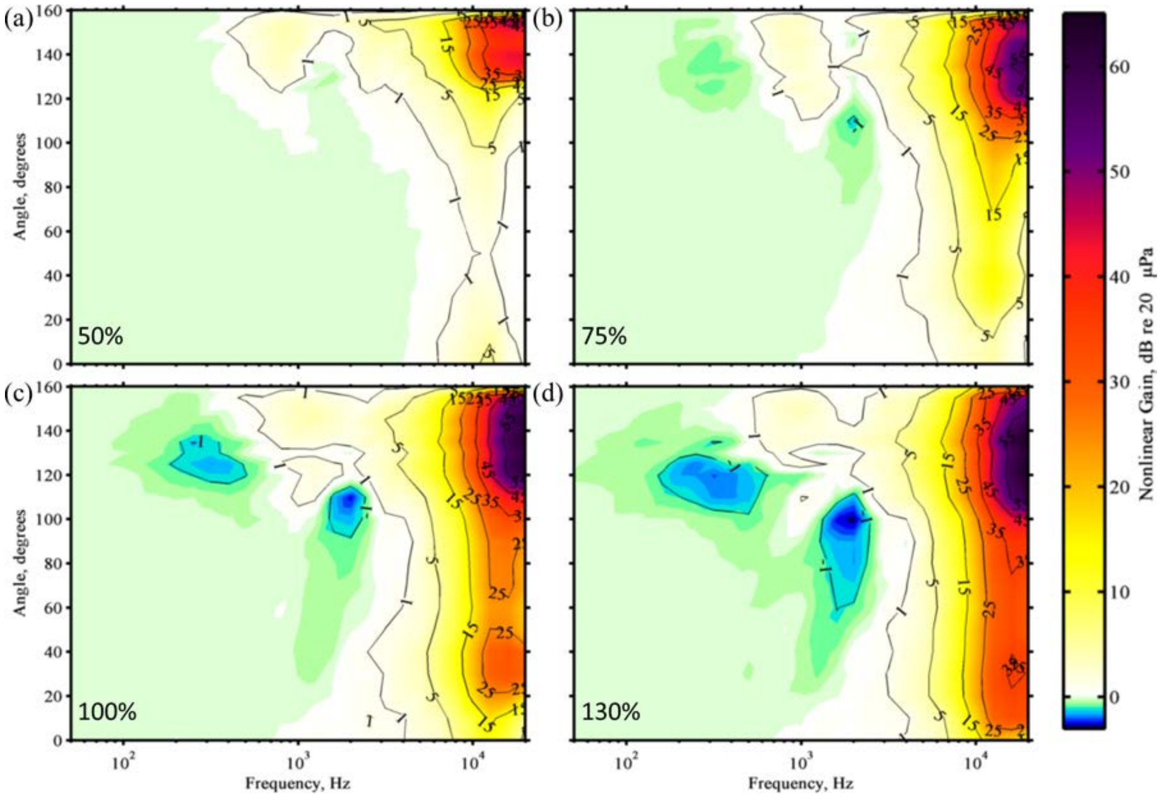

Fig. 7.10 Nonlinear gain at *r* = 305 m. Waveforms measured at *r* = 76.2 m are numerically propagated to 305 m with both the linear and nonlinear algorithms described in Sec. IV A. The difference between the spectral levels of the propagated waveforms is the nonlinear gain. The nonlinear gain is plotted as a function of frequency and angle for four engine conditions: (a) 50% ETR, (b) 75% ETR, (c) 100% ETR, and (d) 130% ETR.

7.6 Accuracy of Numerical Modeling in Waveform Characterization

The comparison above between nonlinear and linear predictions showed the large impact nonlinear propagation has on high-frequency energy within jet noise and showed that nonlinear propagation algorithms can characterize many spectral effects, including the presence of high-frequency energy at far distances from the source. Though spectral shape and high-frequency energy content are important when considering noise exposure and perception, the question remains as to how well the shocks themselves are characterized when using numerical propagation schemes. The effect of idealized numerical propagation schemes on nonlinearity metrics, which are often used to compare shock content for different waveforms, has not been explored in depth. Due to the metrics' sensitivity to small changes in derivative values, and in particular to shock amplitude and rise time, comparing nonlinearity metrics between numerically propagated data and measurements will help evaluate the robustness and accuracy of the numerical algorithms. By improving upon these algorithms in the future, predictions of far-field behavior from measurements closer to the aircraft may more accurately characterize effects seen during long-range propagation away from the aircraft.

7.6.1 Waveform Characteristics

The ability of models to capture realistic propagation can be shown by comparing the waveforms themselves and their characteristics, as shown in Fig. 7.11 for a segment of a measured (black) and a numerically propagated (red) waveform. The simulated waveform was obtained by numerically propagating the waveform measured at 76 m to 305 m using the GBE code. This code includes important effects such as geometric spreading, atmospheric absorption, and quadratic nonlinearity. However, other effects not taken into account include atmospheric turbulence and multi-path interference, such as reflections from the rigid ground or from a downward-refracting atmosphere. These discrepancies may have a noticeable effect on the time waveforms and spectral characteristics.

Despite propagation effects that are not considered, many features of the waveforms shown in Fig. 7.11(a) align closely with each other. The waveforms are time-aligned using a cross-correlation and while there are some discrepancies between the waveforms, the largest shocks and other significant features align closely.

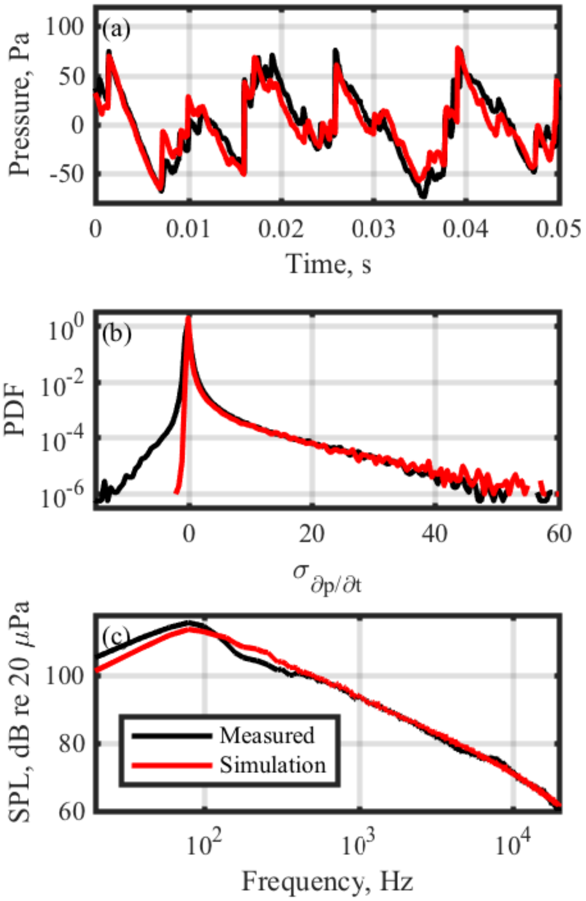

Fig. 7.11 Comparison of (a) waveforms, (b) PDFs, and (c) spectra between a measurement at 305 m and data numerically propagated from 76 m to 305 m.

Some of the discrepancies between the measured and propagated waveforms are more evident in the PDFs of the waveform derivative values, plotted in Fig. 7.11(b) as a function of the standard deviation of the derivative values, $\sigma_{\partial p/\partial t}$. Because the numerical simulation assumes an ideal atmosphere, many of the largest positive derivative values, near $50\sigma_{\partial p/\partial t}$, are higher in the numerical case than in the measured data. However, one of the largest differences occurs in the negative derivatives. The numerical propagation algorithm entirely eliminates larger negative derivative values, while the negative values in the measurement, while not as large as the positive derivative values, are significantly larger than the numerical case. These differences arise from an idealized propagation scheme, but also may arise from instrumentation effects, as is shown in 7.6.2.

These differences in the waveforms and PDFs have little effect on the spectra shown in Fig. 7.11(c). Some disagreement between the measured and predicted spectra is seen in the low-frequency regime due to multi-path interference effects. The empirical correction described earlier was not applied in this case, as the lack of phase information involved in the level correction resulted in a significantly altered waveform. Though this discrepancy can be empirically corrected in the frequency domain, the focus of this chapter is time-domain features, which are more difficult to correct for such effects. Above 400 Hz, both spectra agree remarkably well. This is due to the large amount of high-frequency energy associated with shocks, which dwarf smaller effects throughout the rest of the waveform. Though there are some differences, the numerical propagation accurately captures many of the aspects of nonlinear propagation, including the shocks present in the waveforms and the spectra.

The waveforms shown in Fig. 7.11(a) show good agreement between the numerically propagated and measured waveforms in many features, including many shock fronts which appear nearly identical. While these features do align well, there are slight differences in arrival time, on the order of less than 1 ms. Though not all shocks arrive nearly simultaneously between the numerically propagated and measured waveforms, there are many examples of waveforms that do. For all shocks with arrival times within 1 ms of each other between the two cases, the distribution of arrival times is displayed in Fig. 7.12. The average difference in arrival time is 15.8 μs, but the distribution of arrival times is nearly Gaussian around zero. The low mean difference in arrival time helps confirm that the shock speed is being accurately estimated, but the additional randomization of arrival times points to possible phenomena that could be missed by the current simplified propagation model, including turbulence, which can serve to randomize features of a waveform.

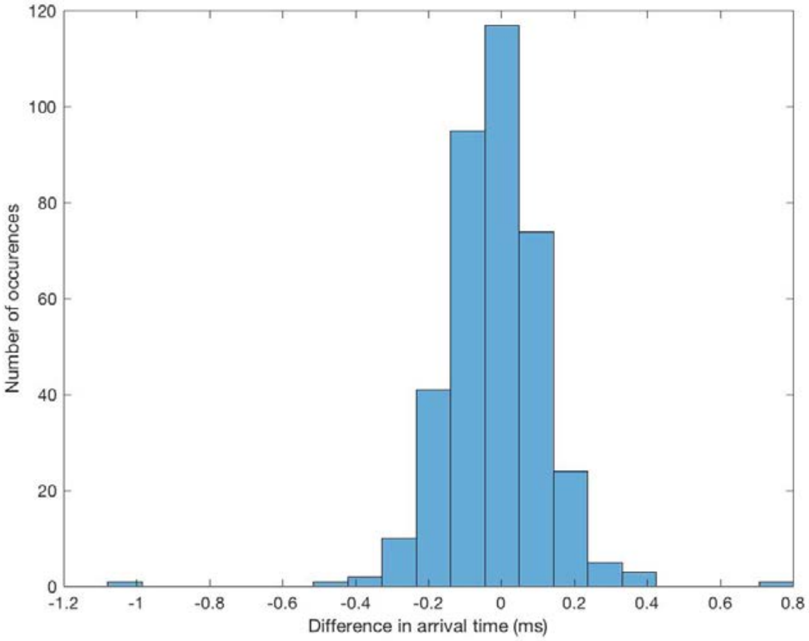

Fig. 7.12. Distribution of the differences in arrival times between the numerically propagated and measured waveforms shown in Fig. 7.11(a).

The numerical propagation algorithm provides the opportunity to inspect waveform features a much finer distance resolution than the measurement allows. One question of interest is the relative strength of shocks. Do the largest shocks remain the largest shocks through the propagation into the far-field, or are they overtaken as other shocks form and nonlinear losses cause the shock to decrease in amplitude? The relative ordering of shocks is shown in Fig. 7.13 as a waveform is propagated from 100 m to 300 m. At each distance in r, the shocks within the waveform are ordered according to total amplitude change and compared with the shocks from the previous distance to determine how the shock amplitudes have changed relative to other shocks. Each line represents one shock, and a positive slope indicates that the shock is growing larger relative to the other shocks, while a negative slope indicates it is growing smaller. While Fig. 7.13

does show some shocks that are increasing or decreasing in amplitude, for the most part the strongest shocks remain the strongest shocks, especially for the first 30-40 strongest shocks. This is in agreement with the behavior in Fig. 3.4, as the largest shock remains the largest shock after it has formed by 76 m from the source. In contrast, more variation is seen in the shocks below these strongest 30-40 shocks, indicative of other shocks forming at larger distances from the source, again in agreement with behavior shown in Fig. 3.4.

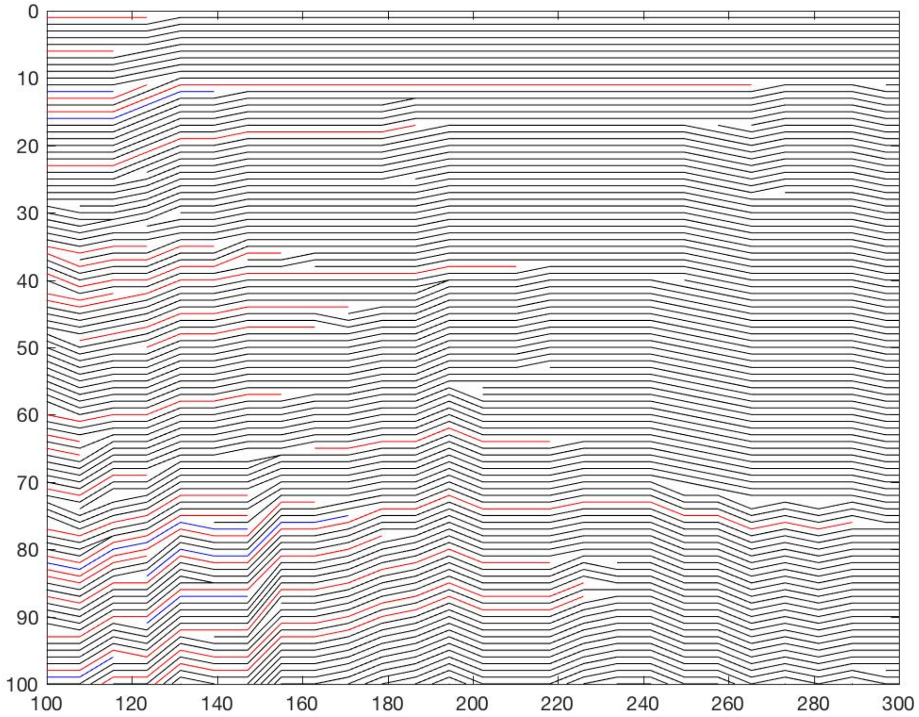

Fig. 7.13. The strongest 100 shocks in the waveform with distance.

7.6.2 Prediction of Nonlinearity Metrics

The differences in the derivative PDFs in Fig. 7.11(b) are likely to play an important role in accurately predicting the evolution of the nonlinearity metrics previously discussed. In particular, the lack of large negative derivative values affects both the derivative skewness and the

ASF of the numerically propagated waveform at distances between 76 m and 305 m. These values, in addition to the metric values calculated from the measured waveforms, are shown in Fig. 7.14. In the case of derivative skewness, the lack of large negative derivative values in the propagated waveform causes an almost immediate jump, after which the values decrease steadily out to 305 m. In the case of ASF, the lack of large negative derivatives becomes more apparent with distance as all initial high-frequency energy not associated with shock waves is linearly attenuated in the propagated waveform. This overestimation of nonlinearity metrics points to the need for improved, more realistic long-range atmospheric propagation models, including multi-path interference effects that are likely to decrease time-domain metric values. Though the current Burgers equation code accurately predicts many of the waveform characteristics, including steepening and increased high-frequency energy associated with shock formation, more accurate propagation modeling is needed to accurately predict other features of the waveforms.

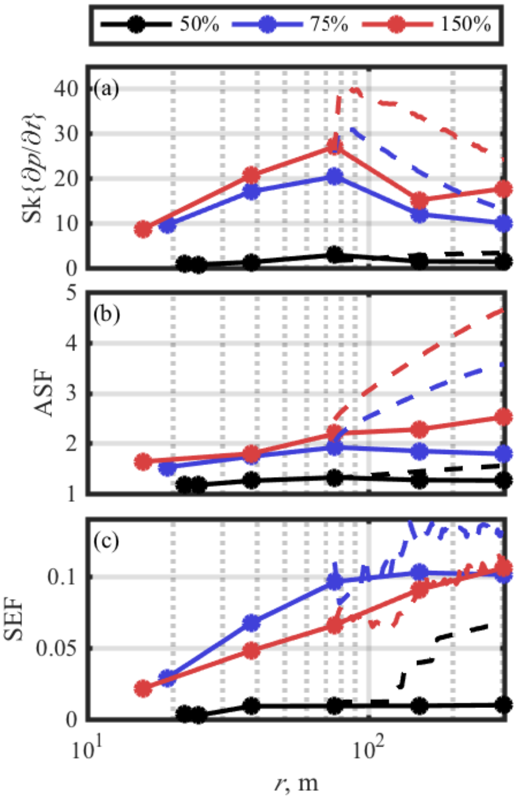

Fig. 7.14 Comparison of (a) derivative skewness (b) ASF and (c) SEF between measured waveforms and numerically propagated waveforms.

While the SEF of the numerically propagated waveform matches well with the measurements at 75% and 150% ETR, the derivative skewness and ASF are both significantly overestimated. This leads to the question of what discrepancies exist between the measured waveform and the numerically propagated waveform that lead to this issue. As these metrics are meant to express the shock content of a waveform, one of the first places that can be inspected is the shocks present in the waveform. In particular, does the numerical simulation overestimate the amplitude, rise time, or number of shocks that are present in a waveform? These quantities are compared in Table 7.3 for two waveforms, x_0 was measured at 305 m, while x_N was numerically propagated from 76 m to 305 m. The quantities shown are the number of shocks per second, the total pressure change over the shock, ΔP, and the average maximum shock derivative, $\langle (\partial p/\partial t)_{\max} \rangle$. While the number of shocks and total pressure change are comparable between the two scenarios, the average maximum derivative is considerably higher in the numerically propagated waveform. This helps quantify some of the discrepancies in the predicted metrics shown in Fig. 7.14, but does not completely resolve the issue.

Table 7.3. Shock properties in measured and numerically propagated waveforms. Quantities shown are the number of shocks per second, the total pressure change over the shock, ΔP, and the average maximum shock derivative, $\langle (\partial p/\partial t)_{\max} \rangle$.

Quantity	Shocks/sec	ΔP, Pa	$\langle (\partial p/\partial t)_{\max} \rangle$, Pa/$\mu s$
x_N	118	74	3.86
x_0	113	70	2.67

One interesting behavior seen in Fig. 7.14 is the way in which the derivative skewness and ASF of the numerically propagated waveform diverge from measurements. Specifically, the derivative skewness almost immediately increases from a value of 28.5 to over 42.3, while the difference in ASF between the measurements and numerical propagation builds gradually with distance. To help identify the cause of the immediate increase in derivative skewness for numerical propagation, the waveform initially measured at 76.2 m (250 ft) was numerically propagated to 76.5 and 77.7 m (251 and 255 ft). A section of the waveform is shown at all three distances in Fig. 7.15(a), and the PDF of the derivative values is shown in Fig. 7.15(b). Changes in the waveform and its derivative happen over small propagation distances, and these changes result in very different derivative skewness values. The derivative skewness values at 76.2, 76.5, and 77.7 m are 28.5, 31.4, and 42.3 respectively. The ASF, on the other hand, remains almost constant at values of 2.01, 2.02, and 2.05. Though the shock itself has changed very little in its steepness and amplitude, the waveform after the shock has changed significantly. This change in the waveform is seen in the PDF of the derivatives in Fig. 7.15(b), where at 77.7 m the PDF of the derivative has significantly fewer large negative derivative values. This behavior, which is also seen in Fig. 7.11(b), suggests that the large changes in the derivative skewness in the numerically propagated waveforms are not due primarily to the overestimation of shock steepness seen in Table 7.3, but rather due to the absence of the larger negative derivative values.

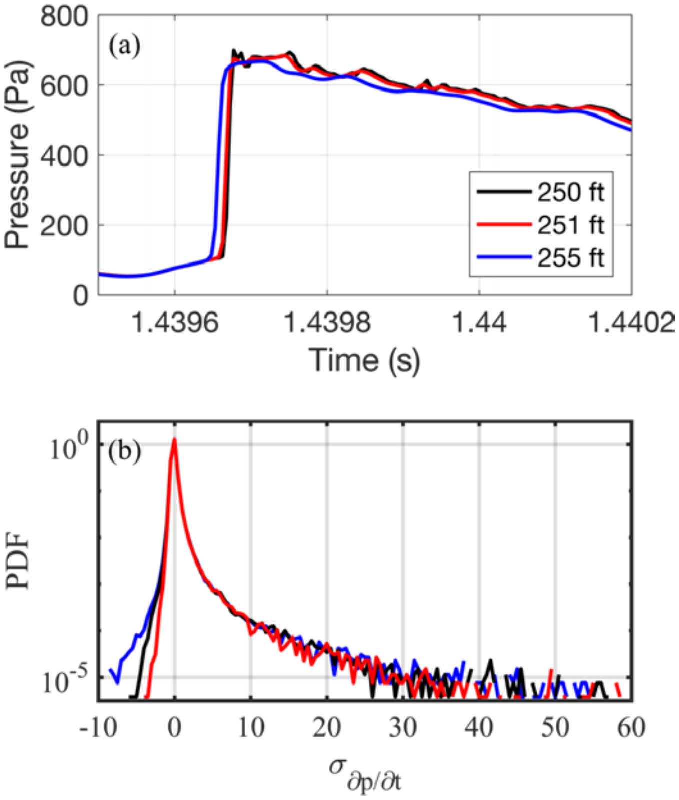

Fig. 7.15 Numerically propagated waveforms over short distances. (a) The measured waveform at 76.2 m is compared with the same waveform numerically propagated to a distance of 76.5 and 77.7 m. (b) The PDF of derivative values is shown for the three distances.

The presence of the larger negative derivative seen in the PDF in Fig. 7.15(b) is unexpected, as nonlinear propagation should serve to thicken these events. However, upon closer inspection it is likely that these instances of a large negative derivative are not physical, but measurement artifacts. When the larger negative derivative values in the PDF of Fig. 7.11(b) are identified within the waveform, all of them are located shortly after a significant shock. For example, a single shock from the waveform seen in Fig. 7.11(a) is shown in Fig. 7.16, with the shock highlighted in gray. The larger decrease in pressure is seen immediately after the large shock, which is representative of the behavior of all larger negative derivative values. The second rise shortly after this large negative derivative value is also representative of most large shock events within the waveform, and it consistently arrives roughly 1 ms after the initial shock. This likely points to measurement effects, possibly related to high-frequency reflections off the microphone itself or the microphone holder or tripod it was mounted on. This behavior is also seen in Fig. 7.15(a), but the numerical propagation immediately smears out this behavior, resulting in a larger derivative skewness. The combined understanding from Fig. 7.11, Fig. 7.15, and Fig. 7.16 help show the cause of the overestimation of derivative skewness seen in Fig. 7.14. Though the nonlinear propagation scheme does idealize the environment and overestimate shock steepness, the largest changes in the derivative distribution actually occur as measurement effects are smeared out in the numerical propagation process.

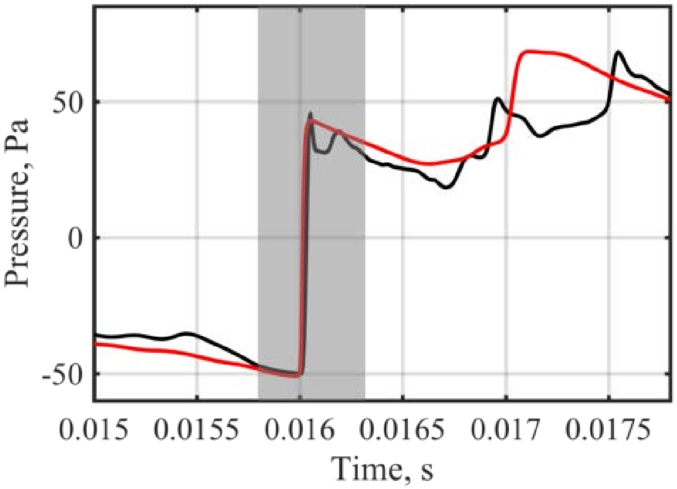

Fig. 7.16 Example of measurement artifacts. Measurement at 305 m (black) is compared with a waveform numerically propagated from 76 m to 305 m (red).

7.7 Conclusions and Future Work

Recent measurements have allowed a comparison of nonlinear propagation effects for full-scale military aircraft over a greater range of distances, angles, and operating conditions than previously. The presence of nonlinear effects is confirmed through a spectral comparison of calculated spectra with predictions made using linear and nonlinear propagation algorithms. The nonlinear propagation more closely aligns with the calculated spectra and show significant gains over the linear predictions at high frequencies, even to some extent in the forward direction. The importance of these effects is quantified using nonlinear gain. This shows that in the direction of maximum radiation the nonlinear gains at 20 kHz are nearly 50 dB, even at 50% ETR, and that at 130% ETR the nonlinear gain is greater than 25 dB over almost all angles at 305 m, relative to the 76 m measurements. These changes show that nonlinear effects have a significant effect on the spectral shape of noise, even 305 m from the source and across a wide range of angles.

The propagation algorithm successfully captures the high-frequency energy characteristic of nonlinear propagation, as well as many time-domain features. In comparing waveforms, the number and amplitude of shocks are within 5% between measured and numerically propagated waveforms, though maximum derivatives are slightly overestimated in the numerical case. Nonlinearity metrics, particularly the derivative skewness and ASF, are overestimated for the numerically propagated waveforms. This stems from the assumptions of an idealized propagation model, but also from measurement effects that introduce large negative derivatives, which are quickly smoothed in the numerical simulation. Though complicated propagation paths, a non-ideal atmosphere, and measurement effects can introduce differences between numerically propagated and measured waveforms, numerical propagation accurately captures many time-domain features of shock formation in the far-field of jet noise.

Chapter 8

Conclusions

8.1 Dissertation Summary

The three main goals of this dissertation were to: 1) Quantify the derivative skewness to aid in a physical understanding of values seen in other experiments. 2) Apply a better physical understanding of the values of nonlinearity metrics to understand where shock formation is occurring and where nonlinear propagation is an important factor in understanding the sound field, in both ground run-up and flyover measurements. 3) Compare the OASPL and nonlinearity metrics for ground run-up and flyover measurements to understand forward flight effects on the jet noise source and associated changes in nonlinear propagation and shock formation. A brief summary of this work is given below.

The derivative skewness has been quantified using analytical derivations of simple test cases in conjunction with numerical analyses and plane wave tube experiments. The derivative skewness rises as shock formation occurs then drops as the shock thickens, though derivative skewness values may remain significant until close to the old-age regime in sinusoidal signals. Estimates of the derivative skewness in measured signals are susceptible to both the presence of noise and low sampling rates, though when compared with the ASF it is more robust in the presence of noise. In order to avoid sampling rate issues, sampling rates should be at least a factor of 100 above the peak frequency of the noise in question, with a factor of 1000 more likely to give accurate results. One important result is the finding that a value of $\mathrm{Sk}\{\partial p/\partial t\} \geq 5$ is indicative of significant shocks within a waveform, a finding that appears to be consistent between sinusoidal and noise waveforms.

Nonlinear propagation effects produce noticeable waveform changes in the far-field of the F-35 during ground run-up measurements. Sample waveforms show larger features steepening into shocks within the first 76 m, while smaller features continue to steepen out to at least 305 m from the source. Metric values confirm this assessment. Derivative skewness values, which emphasize the largest shocks, peak near 76 m, while the ASF and SEF continue to increase out to distances of at least 305 m, likely showing the relative importance of shock content as other high-frequency content is absorbed by propagation through the atmosphere. Metrics are also shown over a wide range of engine conditions and angle, showing that some shocks exist in the maximum radiation region even at engine powers as low as 50% ETR, though the shocks become much more significant at 75% ETR and persist out to larger distances at higher engine power. At afterburner conditions, some shocks are also found in the forward direction, with values comparable to the maximum radiation region at 50% ETR. The metrics confirm the visual inspection of waveforms, that nonlinear propagation creates significant shocks in the far field, and that nonlinear effects must be taken into account even at distances of 305 m and farther from the source.

Acoustic shocks are significant in the far field not only for ground run-up measurements but also for flyover. Waveforms, their derivatives, and spectra show evidence of nonlinear propagation and shock formation. Even at distances of well over 305 m from the source, nonlinearity metric values indicate significant shocks, especially at an ETR of 100% or above.

The changes in source parameters between ground run-up and flyover lead to changes in shock content as well. Specifically, a decrease of 3-4 dB in the maximum radiation region can decrease nonlinearity metrics. This decrease is seen at all engine conditions but produces the biggest change at 75% ETR, when derivative skewness drops from a value of 15 or greater to a value near 5. In contrast with this, an increase in OASPL in the forward direction drives increases in the importance of nonlinear propagation, with both the derivative skewness and ASF indicating significant shock content in the forward direction at all engine conditions, a stark difference from ground run-up results.

Metric values at distances of over a kilometer still indicate the presence of significant shock content. However, the results at these distances can vary significantly with atmospheric conditions and measurement height. OASPL tends to decrease with height, with a decrease of 4-5 dB between 0 and 30.5 m at a distance of 610 m, while the decrease over the same change in height is 7-8 dB at 1220 m. Though a lower OASPL is often associated with a decrease in nonlinear propagation, while OASPL decreases with height the nonlinearity metrics tend to increase, peaking at 22.9 m above the ground. However, weather considerations must be taken into account, as a downward or upward-refracting atmosphere can significantly alter measurements. Throughout much of the measurement the data suggest the presence of a downward-refracting atmosphere, though this likely changes shortly after sunrise into an upward-refracting atmosphere, significantly decreasing the OASPL near the ground. More research is needed to show the effects of atmospheric changes on nonlinear propagation and shock formation over large distances.

8.2 Recommendations and Future Work

The results in this dissertation will provide guidance for accurately measuring shock content and interpreting results in full-scale military aircraft noise. Each of the metrics shown in this dissertation emphasize different features of the waveform, which are likely to emphasize different aspects of perception of sound. Derivative skewness is most sensitive to the largest derivative values, peaking after the most significant shocks have formed, while the ASF and SEF continue to increase out to distances of 305 m. Future work should investigate how these metric values can predict changes in human perception of noise, and which metrics accurately characterize potential annoyance or hearing loss due to the presence of shocks.

When shock content is likely to be significant, sampling rates must be a factor of 100, preferably a factor of 1000, above the peak frequency of the noise of interest. In addition, microphone size should be taken into account, with evidence that for larger shocks, larger microphones may limit bandwidth and minimum rise time. As propagation distance increases, atmospheric conditions become increasingly important, and care must be taken to ensure that results are not dominated by an upward-refracting atmosphere that may artificially lower both OASPL and nonlinearity metrics. The effect of downward and upward-refracting atmospheric conditions on shock formation should be an area of future research as it may significantly impact the presence or absence of shocks at large distances.

These recommendations are likely to be important when measuring noise from the F-35 at 75% ETR or higher. The largest shocks, which form through nonlinear propagation, are well defined by 76 m from the MARP, but nonlinear propagation steepens the waveform and shocks continue to form out to 305 m, with significant shocks persisting out in some cases out to at least 1220 m from the source in the maximum radiation region. During flight, when radiation in the forward direction is amplified, significant shocks exist in the forward direction, and are also likely to alter the sound quality and perception.

References

[1] A. T. Wall, K. L. Gee, M. M. James, K. A. Bradley, S. A. McInerny, and T. B. Neilsen, “Near-field noise measurements of a high-performance military jet aircraft,” Noise Control Eng. J. **60** (4), 421-434 (2012).

[2] Pernet, D. F., and Payne, R. C. "Non-linear propagation of signals in airs," J. Sound and Vib. Vol. 17, No. 3, 1971, pp. 383-396.

[3] Stokes, G. G., “On a difficulty in the theory of sound,” Phl. Mag. **33**, 349-356 (1848).

[4] Earnshaw, S., “On the mathematical theory of sound,” Trans. Roy. Soc. (London) **150**, 133-148 (1860).

[5] Fay, R. D., “Plane sound waves of finite amplitude,” J. Acoust. Soc. Am. **3**, 222-241 (1931).

[6] Blackstock, D. T., “Connection between the Fay and Fubini solution for plane sound waves of finite amplitude,” J. Acoust. Soc. Am. **39**, 1019-1026 (1966).

[7] Blackstock, D. T., Hamilton, M. F. and Pierce, A. D., "Progressive waves in lossless and lossy fluids," in Nonlinear Acoustics, Acoustical Society of America, Chap. 4, 65-150 (1998).

[8] W. J. Baars, C. E. Tinney, and M. F. Hamilton, “Piecewise-Spreading Regime Model for Calculating Effective Gol’dberg Numbers for Supersonic Jet Noise,” AIAA J. **54** (9), 2833-2842 (2016).

[9] M. B. Muhlestein and K. L. Gee, “Experimental investigation of a characteristic shock formation distance in finite-amplitude noise propagation,” Proc. Mtngs. Acoust. **12**, 045002 (2011); doi: 10.1121/1.3609881

[10] Ffowcs-Williams, J. E. S. , Virchis, V.J., "'Crackle': an annoying component of jet noise," J. Fluid Mech. **71**, 251-271 (1975).

[11] Gee, K. L., Neilsen, T. B., and Atchley, A. A., “Skewness and Shock Formation in Laboratory-scale Supersonic Jet Data,” J. Acoust. Soc. Am. **133**, EL 491-497 (2013).

[12] McInerny, S. A. "Launch vehicle acoustics. II - Statistics of the time domain data", J. of Aircraft **33**, 518-523 (1996).

[13] Muhlestein, M. B., Gee, K. L., Neilsen, T. B., and Thomas, D. C., “Evolution of the average steepening factor for nonlinearly propagating waves,” J. Acoust. Soc. Am. **137**, 640-650 (2015)

[14] K. L. Gee, P. B. Russavage, T. B. Neilsen, S. H. Swift, and A. B. Vaughn, “Subjective rating of the jet noise crackle percept,” J. Acoust. Soc. Am. **144**(1), EL40-EL45 (2018).

[15] Gallagher, J.,"The effect of non-linear propagation in jet noise," AIAA 20th Aerospace Sciences Meeting (1982).

[16] Baars, W. J., and Tinney, C. E. "Shock-structures in the acoustic field of a Mach 3 jet with crackle," *Journal of Sound and Vibration* Vol. 333, No. 12, 2014, pp. 2539-2553.

[17] Gee, K. L., Neilsen, T. B., Wall, A. T., Downing, J. M., James, M. M., and McKinley, R. L. "Propagation of crackle-containing jet noise from high-performance engines," *Noise Control Engineering Journal* Vol. 64, No. 1, 2015, pp. 1-12.

[18] Blackstock, D. T. "Nonlinear propagation of jet noise," *Third Interagency Symposium on University Research in Transportation Noise*. U.S. Department of Transportation, University of Utah, Salt Lake City, Utah, 1975, pp. 389-397.

[19] Paper by these authors: Kent Gee, K. L., Sparrow, V. W., James, M. M., Downing, J. M., Hobbs, C. M., Gabrielson, T. B., and Atchley, A. A. "The role of nonlinear effects in the propagation of noise from high-power jet aircraft," J. Acoust. Soc. Am. 137(6), 2008, pp. 4082-4093.

[20] Mora, P., Heeb, N., Kastner, J., Gutmark, E. J., and Kailasanath, K. "Impact of heat on the pressure skewness and kurtosis in supersonic jets," AIAA J. **52**, No. 4, 2014, pp. 777-787.

[21] Morfey, C. L., and Howell, G. P. "Nonlinear propagation of aircraft noise in the atmosphere," AIAA J.**19**, No. 8, 1981, pp. 986-992.

[22] Hoch, R., and Berthelot, M. "Use of the bertin aérotrain for the investigation of flight effects on aircraft engine exhaust noise," J. Sound and Vib. **54**, No. 2, 1977, pp. 153-172.

[23] Drevet, P., Duponchel, J., and Jacques, J. "The effect of flight on jet noise as observed on the Bertin Aérotrain," J. Sound and Vib. **54**, No. 2, 1977, pp. 173-201.

[24] Veltin, J., Day, B. J., McLaughlin, D. K., "Forward flight effect on small scale supersonic jet acoustics," AIAA Paper 2010-3924, 2010.

[25] Viswanathan, K., and Czech, M. "Measurement and modeling of effect of forward flight on jet noise," AIAA Journal Vol. 49, No. 1, 2011, pp. 216-234.

[26] Michalke, A., and Michel, U. "Prediction of jet noise in flight from static tests," J. Sound and Vib. Vol. 67, No. 3, 1979, pp. 341-367.

[27] McInerny, S., Gee, K. L., Dowing, M., and James, M. "Acoustical nonlinearities in aircraft flyover data," AIAA paper 2007-3654, 2007.

[28] "Methods for the Measurement of Noise Emissions from High Performance Military Jet Aircraft, ANSI S12.75-2012," AIAA Journal Vol. 47, No. 1, 2009, pp. 186-194.

[29] T. A. Stout, K. L. Gee, T. B. Neilsen, A. T. Wall, and M. M. James, "Source Characterization of full-scale jet noise using acoustic intensity," Noise Control Eng. J. **63** (6), 522-536 (2015).

[30] Gee, K. L., Downing, J. M., James, M. M., McKinley, R. C., McKinley, R. L., Neilsen, T. B., and Wall, A. T., "Nonlinear evolution of noise from a military jet aircraft during ground run-up," AIAA Paper No. 2012-2258 (2012).

[31] F. M. Pestorius and D. T. Blackstock, "Propagation of finite-amplitude noise," in Finite-amplitude wave effects in fluids, 24-29 (Copenhagen, 1973).

[32] Petitjean, B. P. and McLaughlin, D. K., "Experiments on the Nonlinear Propagation of Noise from Supersonic Jets," AIAA paper no. 2003-3127 (2003).

[33] Petitjean, B. P., Viswanathan, K., and McLaughlin, D. K., "Acoustic Pressure Waveforms Measured in High Speed Jet Noise Experiencing Nonlinear Propagation." Int. J. Aeroacoust. 5, 193-215 (2006).

[34] Greska, B. and Krothapalli, A., "On the far-field propagation of high-speed jet noise," Proceedings of NCAD 2008, Paper No. NCAD2008-73071 (2008).

[35] Baars, W. J., Tinney, C. E., Wochner, M. S., and Hamilton, M. F., "On Cumulative Acoustic Waveform Distortions from High-Speed Jets", J. Fluid Mech. 749, 331-366 (2014).

[36] Ffowcs-Williams, J. E., Simson, J., and Virchis, V. J., "'Crackle': An Annoying Component of Jet Noise," J. Fluid Mech. 71, 251-271 (1975).

[37] Shepherd, M. R., Gee K. L., and Hanford, A. D., "Evolution of statistical properties for a nonlinearly propagating sinusoid," J. Acoust. Soc. Am. 130, EL8-EL13 (2011).

[38] S. N.Gurbatov, A. N. Malakhov, "Statistical Characteristics of Random Quasi-Monochromatic Waves in Non-Linear Media" Soviet Physics Acoustics-Ussr 23, 325-329. (1977)

[39] P. Mora, N. Heeb, J. Kastner, E.J. Gutmark, K. and Kailasanath, “Near and Far field Pressure Skewness and Kurtosis in Heated Supersonic Jets from Round and Chevron Nozzles,” Proc. ASME Turbo Expo 2013, GT2013-95774, (2013).

[40] S.A. McInerny, M. Downing, C. Hobbs, and M. Hannon, “Metrics that Characterize Nonlinearity in Jet Noise,” Innovations in Nonlinear Acoustics (ISNA 17), AIP Conference Proceedings 838, 560-563 (2006)

[41] O.V. Rudenko and S.I. Soluyan., “Theoretical Foundations of Nonlinear Acoustics,” N.-Y., Plenum, Consultants Bureau. pp. 274 (1977).

[42] S. N. Gurbatov, A. N. Malakhov, and N. V. Pronchatov-Rubtsov, “Evolution of higher-order spectra of nonlinear random waves,” Radiophys. Quantum Electron. 29, 523–528 (1986).

[43] D. A. Hennessy, “Crop yield skewness under law of the minimum technology,” Am. J. Agr. Econ. 91, 197-208 (2009).

[44] J. Chen, H. Hong, and J. C. Stein, “Forcasting crashes: trading volume, past returns, and conditional skewness in stock prices,” J. Financ. Econ. 61, 345-381 (2001).

[45] K. R. Sreenivasan and S. Tavoularis, “On the skewness of the temperature derivative in turbulent flows,” J. Fluid Mech. 101, 783-795 (1980).

[46] S. Tavoularis, J. C. Bennett, and S. Corrsin, “Velocity-derivative skewness in small Reynolds number, nearly isotropic turbulence,” J. Fluid Mech. 88, 63-69 (1978).

[47] C. W. Van Atta and R. A. Antonia, “Reynolds number dependence of skewness and flatness factors of turbulent velocity derivatives,” Phys. Fluids 23, 252 (1980).

[48] K.L. Gee, V.W. Sparrow, A.A. Atchley, and T.B. Gabrielson, “On the Perception of Crackle in High-amplitude Jet Noise,” AIAA Journal 45, 593-598 (2007).

[49] M. B. Muhlestein and K. L. Gee, “Experimental investigation of a characteristic shock formation distance in finite-amplitude noise propagation,” Proc. Mtgs. Acoust. 12, 045002 (2014).

[50] M. B. Muhlestein, K. L. Gee, T. B. Neilsen, and D. C. Thomas, “Evolution of the average steepening factor for nonlinearly propagating waves,” J. Acoust. Soc. Am. 137, 640-650 (2015)

[51] F. Fubini, “Anomalie nella propagazione di ande acustiche de grande apiezza,” Alta Frequenza 4, 530-581 (1935). English translation: Beyer (1984), 118-177.

[52] R. O Cleveland, “Propagation of sonic booms through a real, stratified atmosphere,” Ph. D. dissertation, Dept. of Mechanical Engineering, The University of Texas at Austin, 1995.

[53] Loubeau, A., Sparrow, V. W., Pater, L. L., and Wright, W. M., “High-frequency measurements of blast wave propagation,” J. Acousti. Soc. Am. 120, EL29-EL35 (2006).

[54] S. A. McInerny and S. M. Olcmen,. “High intensity rocket noise: Nonlinear propagation, atmospheric absorption, and characterization,” J. Acoust. Soc. Am. 117, 578–591 (2005).

[55] J. A. Gallagher and D. K. McLaughlin, “Experiments on the nonlinear characteristics of noise propagation from low and moderate Reynolds number supersonic jets,” 7th Aeroacoustics Conference, 1981-2041 (1981)

[56] S. N. Gurbatov and O. V. Rudenko, “Statistical phenomena,” in Nonlinear Acoustics, edited by M. F. Hamilton and D. T. Blackstock (Academic Press, San Diego, 1998), Chap. 13, pp. 377-398.

[57] Fiévet, R., Tinney, C. E., Baars, W. J., and Hamilton, M. F. "Coalescence in the Sound Field of a Laboratory-Scale Supersonic Jet," AIAA Journal, 2015, pp. 1-12. doi: 10.2514/1.J054252

[58] Gee, K. L., Neilsen, T. B., Thomas, D. C., Reichman, B. O., Muhlestein, M., Downing, J. M., James, M. M., and McKinley, R. L. "Comparison of two time-domain measures of nonlinearity in near-field propagation of high-power jet noise," 20th AIAA/CEAS Aeroacoustics Conference. American Institute of Aeronautics and Astronautics, 2014.

[59] "Acoustics - Description, measurement and assessment of environmental noise -- Part 1: Basic quantities and assesment procedures," ISO Vol. 1996-1:2016, 2016.

[60] Gee, K. L., Sparrow, V. W., James, M. M., Downing, J. M., Hobbs, C. M., Gabrielson, T. B., and also Atchley, A. A. "The role of nonlinear effects in the propagation of noise from high-power jet aircraft," *The Journal of the Acoustical Society of America* Vol. 123, No. 6, 2008, pp. 4082-4093.

[61] Muhlestein, M. B., "Analyses of nonlinearity measures in high-amplitude sound propagation," Master's Thesis, Physics and Astronomy, Brigham Young University, 2013.

[62] A. Krothapalli, L. Venkatakrishnan, and L. Lourenco. "Crackle - A dominant component of supersonic jet mixing noise," AIAA Paper 2000-2024 (2000).

[63] D. T. Blackstock, "Once Nonlinear, Always Nonlinear," AIP Conference Proceedings 838, 601-606 (2006).

[64] K. L. Gee, V. W. Sparrow, M. M. James, J. M. Downing, C. M. Hobbs, T. B. Gabrielson, and A. A. Atchley, "Measurement and prediction of noise propagation from a high-power jet aircraft," AIAA J. 45, 3003-3006 (2007).

[65] B. O. Reichman, K. L. Gee, T. B. Neilsen, S. H. Swift, A. T. Wall, H. L. Gallagher, J. M. Downing, and M. M. James, "Acoustic shock formation in noise propagation during ground run-up operations of military aircraft," AIAA Paper 2017-4043 (2017).

[66] J. N. Punekar, "Numerical simulation of nonlinear random noise," Ph.D. thesis, University of Southampton, Southampton, UK, 1996.

[67] S. Lee, P. J. Morris, and K. S. Brentner, "Nonlinear acoustic propagation predictions with applications to aircraft and helicopter noise," AIAA Paper 2010-1384 (2010).

[68] P. Menounou and D. T. Blackstock, "A new method to predict the evolution of the power spectral density for a finite-amplitude sound wave," J. Acoust. Soc. Am. 115, 567–580 (2004).

[69] P. Mora, N. Heeb, J. Kastner, E. J. Gutmark, K. Kailasanath, "Effect of Scale on the Far-Field Pressure Skewness and Kurtosis of Heated Supersonic Jets," AIAA Paper 2013-0616 (2013).

[70] D. Buchta and J. Freund, "The near-field pressure radiated by planar high-speed free-shear-flow turbulence," Journal of Fluid Mechanics 832, 383-408 (2017). doi:10.1017/jfm.2017.671

[71] M. M. James, A. R. Salton, J. M. Downing, K. L. Gee, T. B. Neilsen, B. O. Reichman, R. L. McKinley, A. T. Wall, and H. L. Gallagher, "Acoustic Emissions from F-35 Aircraft during Ground Run-Up," AIAA Paper 2015-2375 (2015).

[72] R. H. Schlinker, S. A. Liljenberg, D. R. Polak, K. A. Post, C. T. Chipman, and A. M. Stern, "Supersonic jet noise source characteristics & propagation: Engine and model scale," AIAA Paper 2007-3623 (2007).

[73] E. Zwieback, "Flyover Noise Testing of Commercial Jet Airplanes," J. Aircraft 10, 538-545 (1973).

[74] U. Michel and A. Michalke, "Prediction of flyover jet noise spectra from static tests," J. Acoust. Soc. Am. 68.S1, S105 (1980).

[75] A. Krothapalli, P. Soderman, C. Allen, J. Hayes, and S. Jaeger, "Flight effects on the far-field noise of a heated supersonic jet," AIAA J. 35, 952-957 (1997).

[76] R. Schlinker, J. Simonich, and R. Reba, "Flight effects on supersonic jet noise from chevron nozzles," AIAA Paper 2011-2703, (2011).

[77] J. Seiner, B. Jansen, and L. Ukeiley, "Acoustic fly-over studies of F/AE/F Aircraft during FCLP mission," AIAA Paper 2003-3330 (2003).

[78] U. Michel, "Prediction of jet mixing noise in flight from static tests," Proceedings of 22nd AIAA/CEAS Aeroacoustics Conference, pp. 2807 (2016).

[79] K. L. Gee, T. B. Neilsen, M. Downing, M. M. James, and S. A. McInerny, "Characterizing nonlinearity in jet aircraft flyover data," Proceedings of Meetings on Acoustics 12, 1-9 (2013).

[80] B. O. Reichman, M. B. Muhlestein, K. L. Gee, T. B. Neilsen, and D. C. Thomas, "Evolution of the derivative skewness for nonlinearly propagating waves," J. Acoust. Soc. Am. 139, 1390-1403 (2016).

[81] K. L. Gee, T. B. Neilsen, J. M. Downing, M. M. James, R. L. McKinley, R. C. McKinley, and A. T. Wall, "Near-field shock formation in noise propagation from a high-power jet aircraft," J. Acoust. Soc. Am. 133, EL88-EL93 (2013).

[82] B. O. Reichman, A. T. Wall, K. L. Gee, T. B. Neilsen, J. M. Downing, M. M. James, and R. L. McKinley, "Modeling Far-field Acoustical Nonlinearity from F-35 Aircraft during Ground Run-up," AIAA Paper 2016-1888 (2016).

[83] T. B. Gabrielson, T. M. Marston, and A. A. Atchley, "Nonlinear propagation modeling: Guidelines for supporting measurements," J. Acoust. Soc. Am. 118, 1873-1874 (2005).

[84] http://www.gras.dk/products/measurement-microphone-cartridge/prepolarized-cartridges-0-volt/product/159-40bd, last viewed 1/26/18

[85] http://www.gras.dk/products/measurement-microphone-sets/constant-current-power-ccp/product/141-46ao, last viewed 1/26/18

[86] J. S. Bendat and A. G. Piersol, "Probability fundamentals" in *Random Data: Analysis and Measurement Procedures*, John Wiley & Sons, 1986.

[87] K. L. Gee and V. W. Sparrow, "Quantifying nonlinearity in the propagation of noise from military jet aircraft," Noise-Con 118, 1873 (2005).

[88] A. D. Pierce, ‘‘Statistical theory of atmospheric turbulence on sonic boom rise times,’’ J. Acoust. Soc. Am. 49, 906–924 (1971).

[89] B. Lipkens and D. Blackstock, "Model experiment to study sonic boom propagation through turbulence. Part I: General results," The Journal of the Acoustical Society of America 103, 148-158 (1998);

[90] Gee, K. L., Sparrow, V. W., Gabrielson, T. B., and Atchley, A. A. "Nonlinear modeling of F/A-18E noise propagation," *AIAA Paper* 2005-3089 (2005).

[91] Baars, W. J., Tinney, C. E., and Wochner, M. S. "Nonlinear Noise Propagation from a Fully Expanded Mach 3 Jet," AIAA paper 2012-1177 (2012). doi:10.2514/6.2012-1177

[92] Gee, K. L., Atchley, A. A., Falco, L. E., and Shepherd, M. R. "Nonlinearity analysis of model-scale jet noise," 19th International Symposium on Nonlinear Acoustics. Vol. 1474, AIP Publishing, Tokyo, Japan, 2012, pp. 307-310.

[93] Reichman, B. O., Gee, K. L., Neilsen, T. B., Downing, J. M., James, M. M., Wall, A. T., and McInerny, S. A., "Characterizing acoustic shocks in high-performance jet aircraft flyover noise," J. Acoust. Soc. Am. Vol. 143, No. 3, 2018, pp. 1355-1365.

[94] Howell, G., Bradley, A., McCormick, M., and Brown, J. "De-dopplerization and acoustic imaging of aircraft flyover noise measurements," J. Sound and Vib. Vol. 105, No. 1, 1986, pp. 151-167.

[95] Pott-Pollenske, M., Dobrzynski, W., Buchholz, H., Guérin, S., Saueressig, G., and Finke, U. "Airframe noise characteristics from flyover measurements and predictions," AIAA paper 2006-2567. (2006)

[96] U. Ingard, "A Review of the Influence of Meteorological Conditions on Sound Propagation," J. Acoust. Soc. Am. 25, 405 (1953); doi: 10.1121/1.1907055.

[97] J. E. Piercy, T. F. W. Embleton, and L. C. Sutherland, “Review of noise propagation in the atmosphere,” J. Acoust. Soc. Am. 61, 1403 (1977); doi: 10.1121/1.381455

[98] D. T. Blackstock, “Fundamentals of physical acoustics,” John Wiley & Sons, Inc, 2000.

[99] K. Attenborough, S. Taherzadeh, H. E. Bass, X. Di, R. Raspet, G. R. Becker, A. Güdesen, A. Chrestman, G.A. Daigle, A. L’Espérance, Y. Gabillet, K. E. Gilbert, Y. L. Li, M. J. White, P. Naz, J. M. Noble, and H. A. J. M. van Hoof, “Benchmark cases for outdoor sound propagation models,” J. Acoust. Soc. Am. 97, 173 (1995); doi: 10.1121/1.412302

[100] D. K. Wilson, “The sound-speed gradient and refraction in the near-ground atmosphere,” J. Acoust. Soc. Am. 113, 750 (2003); doi: 10.1121/1.1532028

[101] P. J. Dickinson, “Temperature inversion effects on aircraft noise propagation,” J. Sound and Vib. 47 (3), pp. 438-443 (1976).

[102] E. K. Salomons, “Computational atmospheric acoustics,” Kluwer Academic Publishers, 2001.

[103] T. F. W. Embleton, “Tutorial on sound propagation outdoors,” J. Acoust. Soc. Am. 100, 31 (1996); doi: 10.1121/1.415879.

[104] S. M. Young, K. L. Gee, T. B. Neilsen, and K. M. Leete, “Outdoor measurements of spherical acoustic shock decay,” J. Acoust. Soc. Am. 138, EL305 (2015); doi: 10.1121/1.4929928.

[105] S. A. McInerny, "Launch vehicle acoustics. II-Statistics of the time domain data," J. of Aircraft 33, 518-523 (1996).

[106] S. A. McInerny, M. Downing, C. Hobbs, M. James, and M. Hannon, "Metrics that characterize nonlinearity in jet noise," AIP Conference Proceedings 838, 560-563 (2006).

[107] J. E. S. Ffowcs-Williams, J.; Virchis, V.J., "'Crackle': an annoying component of jet noise," J. Fluid Mech. 71, 251-271 (1975).

[108] K. L. Gee, V. W. Sparrow, A. A. Atchley, and T. B. Gabrielson, "On the perception of crackle in high-amplitude jet noise," AIAA J. 45, 593-598 (2007).

[109] M. B. Muhlestein, K. L. Gee, T. B. Neilsen, and D. C. Thomas, "Evolution of the average steepening factor for nonlinearly propagating waves," J. Acoust. Soc. Am. 137, 640-650 (2015).

[110] J. Gallagher, "The effect of non-linear propagation in jet noise," AIAA 20th Aerospace Sciences Meeting (1982).

[111] K. L. Gee, T. B. Neilsen, J. M. Downing, M. M. James, R. L. McKinley, R. C. McKinley, and A. T. Wall, “Near-field shock formation in noise propagation from a high-power jet aircraft,” J. Acoust. Soc. Am. 133, EL88-EL93 (2013).

[112] W. J. Baars and C. E. Tinney, " Shock-structures in the acoustic field of a Mach 3 jet with crackle," J. Sound and Vib. 12, 2539-2553 (2014).

[113] B. O. Reichman, K. L. Gee, T. B. Neilsen, and S. H. Swift, “Acoustic shock formation in noise propagation during ground run-up operations of military aircraft,” AIAA Paper 2017-4043 (2017).

[114] S. McInerny, K. L. Gee, M. J. Downing, and M. M. James, “Acoustical Nonlinearities in Aircraft Flyover Data,” 13th AIAA/CEAS Aeroacoustics Conference (28th AIAA Aeroacoustics Conference) AIAA 2007-3654 (2007).

[115] K. L. Gee, V. W. Sparrow, M. M. James, J. M. Downing, and C. M. Hobbs, “Measurement and prediction of nonlinearity in outdoor propagation of periodic signals,” J. Acoust. Soc. Am. 120 (5), 2491 (2006)

[116] K. J. Plotkin, “State of the art sonic boom modeling,” J. Acoust. Soc. Am. 111, 530 (2002); doi: 10.1121/1.1379075

[117] R. Marchiano, F. Coulouvrat, and R. Grenon, “Numerical simulation of shock wave focusing at fold caustics, with application to sonic boom,” J. Acoust. Soc. Am. 114, 1758 (2003); doi: 10.1121/1.1610459

[118] B. Lipkens and D. T. Blackstock, “Model experiment to study sonic boom propagation through turbulence. Part I: General results,” J. Acoust. Soc. Am. 103, 148 (1998); doi: 10.1121/1.421114

[119] K. L. Gee, T. B. Neilsen, A. T. Wall, J. M. Downing, M. M. James, R. L. McKinley, “Propagation of crackle-containing jet noise from high-performance engines,” Noise Control. Enj. J. 64(1), 1-12 (2016).

[120] K. L. Gee, “Prediction of nonlinear jet noise propagation,” PhD Dissertation, Pennsylvania State University (2005).

[121] Gee, K. L., Atchley, A. A., Falco, L. E., Shepherd, M. R., Ukeiley, L. S., Jansen, B. J., and Seiner, J. M., “Bicoherence Analysis of Model-Scale Jet Noise,” *Journal of the Acoustical Society of America,* Vol. 128, No. 5, 2010, pp. EL211-EL216.

[122] R. O. Cleveland, J. P. Chambers, H. E. Bass, R. Raspet, D. T. Blackstock, and M. F. Hamilton, "Comparison of computer codes for the propagation of sonic boom waveforms through isothermal atmospheres," *Journal of the Acoustical Society of America*. 100(5), 3017-3027 (1996).

[123] M. O. Anderson, ‘‘The propagation of a spherical N wave in an absorbing medium and its diffraction by a circular aperture,’’ Masters thesis, Applied Research Laboratories, The University of Texas at Austin, 1974.

[124] H. E. Bass, R. Raspet, J. P. Chambers, and M. Kelly, "Modification of sonic boom wave forms during propagation from the source to the ground," *Journal of the Acoustical Society of America* 111(1), 481-486 (2002).

[125] H. H. Brouwer, "Numerical Simulation of Nonlinear Jet Noise Propagation," AIAA Paper No. 2005-3088 (2005).

[126] Blackstock, D. T., “Nonlinear propagation distortion of jet noise,” *Proceedings of the Third Interagency Symposium on University Research in Transportation Noise,* edited by G. Banerian and P. Kickinson, Univ. of Utah, Salt Lake City, UT, 1975, pp. 389-397

[127] S. Saxena, P. J. Morris, and K. Viswanathan, “Algorithm for the nonlinear propagation of broadband jet noise,” AIAA J. **47**(1), pp. 186-194 (2009).

[128] K. L. Gee, T.B. Neilsen, D.C. Thomas, B.O. Reichman, M.J. Muhlestein, J. M. Downing, M. M. James, and R. L. McKinley, "Comparison of two time-domain measures of nonlinearity in near-field propagation of high-power jet noise," AIAA Paper 2014-3199 (2014).

[129] Pierce, A. D. "Acoustics: An Introduction to Its Physical Principles and Applications" McGraw-Hill Book Company. *New York* (1981).

[130] Gurbatov, S. N., Demin, I. Y., Cherepennikov, V. V., and Enflo, B. O., “Behavior of intense acoustic noise at large distances,” Akusticheskil Zhurnal 53(1), pp. 55-72 (2007).

[131] Embleton, T. F. W., Piercy, J. E., and Daigle, G. A., “Effective flow resistivity of ground surfaces determined by acoustical measurements,” J. Acoust. Soc. Am., 74(4), 1239-1244 (1983)

[132] Daigle, G. A., “Effects of atmospheric turbulence on the interference of sound waves above a finite impedance boundary,” J. Acoust. Soc. Am. 65(1) (1979).

[133] Gee, K. L., Neilsen, T. B., James, M. M., “Including source correlation and atmospheric turbulence in a ground reflection model for rocket noise,” Proc. Meetings Acoust. 22, 2014

[134] K. L. Gee and V. W. Sparrow, “Asymptotic Behavior in the Numerical Propagation of Finite Amplitude Jet Noise,” AIP Conference Proceedings 838, 564 (2006); doi: 10.1063/1.2210419